Official Doctoral Programme in Information Technology and Communication

Department of Signal Theory, Telematics and Communications

University of Granada

PhD THESIS

Brain imaging biomarker normalization, analysis and classification methods to characterize the progression of neurodegenerative diseases

Written by:

Abdelbasset Brahim

Supervised by:

Dr. Javier Ramírez Pérez de Inestrosa

Dr. Dr. Juan Manuel Górriz Sáez

Editor: Universidad de Granada. Tesis Doctorales
Autor: Abdelbasset Brahim
ISBN: 978-84-9125-998-5
URI: http://hdl.handle.net/10481/44095

Programa Oficial de Doctorado en Tecnologías de la Información y la Comunicación

Departamento de Teoría de la Señal, Telemática y Comunicaciones

Universidad de Granada

TESIS DOCTORAL

Normalización, análisis y clasificación de biomarcadores de imagen cerebral para la caracterización de la progresión de las enfermedades neurodegenerativas

Realizado por:

Abdelbasset Brahim

Dirigido por:

Dr. Javier Ramírez Pérez de Inestrosa

Dr. Dr. Juan Manuel Górriz Sáez

El doctorando Abdelbasset Brahim y los directores de la tesis Javier Ramírez Pérez de Inestrosa y Juan Manuel Górriz Sáez Garantizamos, al firmar esta tesis doctoral, que el trabajo ha sido realizado por el doctorando bajo la dirección de los directores de la tesis y hasta donde nuestro conocimiento alcanza, en la realización del trabajo, se han respetado los derechos de otros autores a ser citados, cuando se han utilizado sus resultados o publicaciones.

Granada, 1 de abril de 2016

Directores de la Tesis

Dr. D. Javier Ramírez Pérez de Inestrosa Dr. Dr. D. Juan Manuel Górriz Sáez

Doctorando

D. Abdelbasset Brahim

Acknowledgements

Foremost I would like to thank Dr. Javier Ramírez Pérez de Inestrosa and Dr. Dr. Juan Manuel Górriz Sáez for supervising this work, their valuable comments and suggestions and specially for their continuous support, motivation and friendship. I would also like to express my gratitude to Dr. Carlos García Puntonet, Dr. Ignacío Alvárez Illán, Dr. Francisco Jesús Martínez Murcia, Dr. Pablo Padilla De La Torre, Dr. Diego Salas-Gonzalez and Dr. Alberto Olivares Vicente for the fruitful discussions.

Thank you Dr. Samir Sayadi and Dr. Emna Eraach for carefully reading this thesis. Their reading of the thesis has certainly improved its quality.

Special thanks go to the members of the Signal Processing and Biomedical Applications (SIPBA), who are a role model for me to become a successful researcher, for being such a nice group of people.

I would like to acknowledge the financial support of the ERASMUS MUNDUS Al-Idrisi program.

Last, but definitely not least, I would like to thank my family, friends and my lovely wife for their relentless moral assistance during these Ph.D years.

Abstract

Intensity normalization is an important pre-processing step in the study and analysis of brain functional imaging. As most automatic supervised image segmentation and classification methods base their assumptions regarding the intensity distributions on a standardized intensity range, intensity normalization takes on a very significant role. In this Thesis, new intensity normalization schemes for the detection of Parkinsonism patterns by means of Single Photon Emission Computed Tomography (SPECT) and Positron Emission Tomography (PET) images are proposed. The first normalization approach is based on a nonlinear image filtering using the Gaussian mixture model (GMM), which considers not only the intensity levels of each voxel but also its coordinates inside the so-defined spatial Gaussian functions. Normalization is achieved according to a probability threshold that measures the weight of each kernel or cluster on the striatum area. The voxels in the so-defined non-specific region are intensity normalized by removing clusters whose likelihood is negligible. The second normalization method is based on the mean-squared error (MSE) optimization which is performed by a linear intensity transformation at a voxel level. This approach is based on predicting different intensity normalization parameters that leads to the joint minimization of the squared sum errors between the template image and the optimal linear estimated image (normalized image). The third approach is a combination between the two previous methods. Thus, it is based on the minimization of the MSE between the GMM-based extracted features from each subject image and a template in the non-specific region at the cluster (of voxels) level. The fourth proposed intensity normalization approach is based on a predictive modeling using multivariate linear regression (MLR). Different intensity normalization parameters derived from this model will be used in a linear procedure to perform the intensity normalization of ^{123} I-ioflupane-SPECT and ^{18} F-DMFP PET brain images. These intensity normalization methods are compared to many widely used approaches. This comparison is performed on different databases of SPECT and PET images comprising analysis and classification stages for the development of computer aided diagnosis (CAD) system of neurological diseases, such as, idiopathic parkinsonian syndrome (Parkinson's disease) and atypical parkinsonian syndromes due to other neurodegenerative diseases, such as, multiple system atrophy (MSA) and progressive supranuclear palsy (PSP).

Resumen

La normalización en intensidad es una etapa importante de pre-procesamiento en el estudio y análisis de imágenes funcionales del cerebro. Como la mayoría de los métodos automáticos de segmentación y de clasificación supervisada de imágenes requieren que las distribuciones del nivel de gris se presenten en un rango de intensidad normalizada y comparable entre sujetos, este procedimiento adquiere un papel cada vez más importante. En la presente tesis doctoral, se proponen nuevos esquemas de normalización de la intensidad para la detección de patrones de Parkinson en tomografía computarizada de emisión de un sólo fotón (SPECT, del inglés "Single Photon Emission Tomography") y en tomografía por emisión de positrones (PET, del inglés " Positron Emission Tomography"). El primer método de normalización se basa en un filtrado no-lineal de imágenes utilizando un modelo de mezcla de Gaussianas (GMM, del inglés " Gaussian mixture model"), que considera no solo los niveles de intensidad de cada vóxel, sino también sus coordenadas dentro de las funciones Gaussianas espaciales así definidas. La normalización se consigue de acuerdo con un umbral de probabilidad que mide el peso de cada *kernel* o clúster en la zona del estriado. Los vóxeles en la región definida como no específica se normalizan en intensidad mediante la eliminación del clúster cuya probabilidad resulta no significativa. El segundo método de normalización se basa en la minimización del error cuadrático medio (MSE, del inglés " mean-squared error") que se realiza mediante una transformación lineal de intensidad a nivel de vóxel. Este enfoque se basa en la predicción de los diferentes parámetros en la normalización en intensidad que conduce a la minimización conjunta de la suma de errores cuadráticos entre la plantilla y la imagen normalizada (estimación lineal óptima bajo este criterio). El tercer enfoque es una combinación entre los dos métodos anteriores. Por lo tanto, se basa en la minimización del MSE entre las características extraídas mediante el modelo GMM de cada imagen y de una plantilla en la región no específica a nivel de clúster (de vóxeles). El cuarto enfoque de normalización de la intensidad propuesto consiste en un modelo predictivo basando en regresión lineal multivariante (MLR, del inglés " multivariate linear regression"). Los métodos propuestos se comparan con otros muchos enfoques empleados hasta la fecha en literatura médica. La comparación se realiza mediante diferentes bases de datos de imágenes SPECT y PET con el objetivo de determinar la influencia de los algoritmos de normalización de intensidad en etapas de análisis y de clasificación en la precisíon de los sistemas de diagnóstico asistido por ordenador (CAD, del inglés " computer aided diagnosis") de enfermedades neurológicas. De entre estas enfermedades destacamos el síndrome idiopático de Parkinson (enfermedad de Parkinson) y los síndromes Parkinsonianos atípicos, tales como la atrofia múltiple sistémica (MSA, del inglés " multiple system atrophy ") y la parálisis supranuclear progresiva (PSP, del inglés " progressive supranuclear palsy ").

Abbreviations

SIPBA: Signal Processing and Biomedical Applications

CAD: Computer Aided Diagnosis

SPECT: Single Photon Emission Tomography

PD: Parkinson's Disease

ECT: Emission-Computed Tomography

PS: Parkinsonian Syndrome

NC: Normal Control

DaTs: Dopamine Transporters

MRI: Magnetic Resonance Imaging

PET: Positron Emission Tomography

AD: Analog-To-Digital

PMT: Photomultiplier Tube

DLB: Dementia with Lewy Bodie

ET: Essential Tremor

MSA: Multiple System Atrophy

PSP: Progressive Supranuclear Palsy

IPS: Idiopathic Parkinsonian Syndrome

APS: Atypical Parkinsonian Syndrome

FWHM: Full Width at Half-Maximum

DOI: Depth Of Interaction

BBB:Blood-Brain Barrier

FDA: Food and Drug Administration

FBP: Filtered Backprojection

ART: Algebraic Reconstruction Technique

MLEM: Maximum Likelihood Expectation Maximization

OSEM: Ordered Subsets Expectation Maximization

SN: Spatial Normalization

3-D: Three-Dimensional

IN: Intensity Normalization

MR: Magnetic Resonance

SPM: Statistical Parametric Mapping

rCBF: regional Cerebral Blood Flow

BP: Binding Potential

BR: Binding Ratio

NS: Non-Specific

ROI: Regions Of Interest

BR$_{all}$-IN: Specific-to-non-specific binding ratio intensity normalization

Integral-IN: Integral-based intensity normalization

MKL-IN: Minimizing the Kullback-Leibler divergence intensity normalization

Hist-eq-IN: Histogram equalization for intensity normalization

PDF: Probability Density Function

Max-IN: Normalization to the maximum intensity values

α-stable-IN: α-stable distribution-based intensity normalization

GMM: Gaussian Mixture Model

FGMM: Gaussian Mixture Model-based image filtering

VOI: Voxels Of Interest

EM: Expectation Maximization

MLE: Maximum Likelihood Estimation

ML: Maximum Likelihood

BIC: Bayesian Information Criterion

AIC: Akaike Information Criterion

SNR: Signal-to-Noise Ratio

MSE: Mean-Squared Error

MLR: Multivariate Linear Regression

ED: Euclidean Distance

JD: Jeffreys Divergence

SVM: Support Vector Machines

LOO: Leave-One-Out

TP: True Positives

TN: True Negatives

FP: False Positives

FN: False Negatives

Contents

List of Figures

List of Tables

Chapter 1

Introduction

1.1 General Introduction

Imaging has been selected as one of the greatest achievements of the twentieth century by the US National Academy of Engineering (NAE) [7] because of its impact on medicine and biology [8]. In the medical field, image data are ubiquitously used in clinical practice as well as in scientific studies to infer details regarding the process under investigation whether it is a disease process or a physiological process. Hence, information provided by medical images has become a vital part of today's patient healthcare.
Beyond that, imaging has not only increased the quality of patient care, but also reduced the health care costs. In fact, imaging is a complimentary tool to the neuropsychological tests that can evaluate structural and functional abnormalities to improve the early diagnosis. Additionally, many diseases can be diagnosed in a much earlier stage of the disease progression, since it is not necessary that symptoms are apparent on the outside of the human body, as it used to be. Moreover, if a disease is detected, procedures can be performed much less invasive.
Unlike the images produced in industrial applications, the images generated in medical applications are complex and vary notably from an application to another. Thus, as one can imagine, the field of image processing and analysis has to tackle a diverse and complex set of problems. Because of its wide extent, we focus on certain topics that we consider important in the field of medicine, such as the development of computer-aided diagnosis (CAD) systems for neurodegenerative diseases. CAD is a broad concept that integrates image processing, computer vision, mathematics, physics, and statistics into computerized techniques. These techniques assist radiologists in their medical decision-making processes, as depicted in Figure 1.1. It serves as a second opinion in the detection of abnormalities, classification of lesions,

quantification of disease and anatomic structures, risk assessment, and physiologic evaluation. Moreover, CAD is a relatively young interdisciplinary technology combining elements of artificial intelligence and digital image processing in the field of radiological and nuclear medicine imaging. A typical application is the detection of a tumor. For instance, some hospitals use CAD to support preventive medical checkups in mammography (diagnosis of breast cancer), the detection of polyps in the colon, and lung cancer. This seems to indicate that CAD is beginning to be applied widely in the detection and differential diagnosis of many different types of abnormalities in medical images obtained in various examinations by use of different imaging modalities. In fact, CAD has become one of the major research subjects in medical imaging and diagnostic radiology [9–11]. Lately, some methods based on the machine learning paradigm [12, 13] and neural networks [14] have been applied to image analysis procedures, yielding to the construction of CAD systems for several neurodegenerative diseases, such as Alzheimer's disease (AD) [15–17] or Parkinson's disease (PD) [1, 18–20]. These systems not only process and analyze image data but also can determine if an image belongs to the class of normal images (healthy subjects) or pathological images (patients), performing that way an automatic diagnosis. Therefore, a typical CAD system may be made up of four main modules, as shown in Figure 1.1. Image pre-processing improves the input image quality to allow image segmentation for accurate extraction of the regions of interest. Feature extraction and selection identify a small number of mathematical features that are used by pattern-recognition and machine-learning techniques for disease identification and classification. In addition, CAD systems can be applied

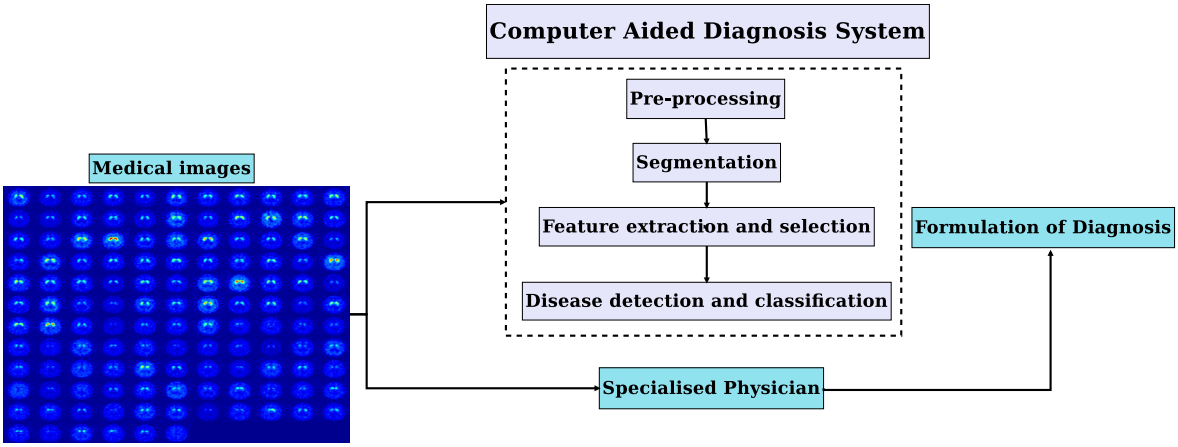

Figure 1.1: General architecture of CAD Systems for medical images.

to different nuclear medicine imaging.
Nuclear medicine is the section of science that utilizes the characteristics of radioactive drugs in order to derive clinical information of the human physiology and biochemistry. According to the examination needed for each patient, a small quantity of radioactive material, i.e., a radionuclide is attached to a pharmaceutical (tracer).

This combination is called a radiopharmaceutical or radiotracers. Then, the whole complex is administered to the patient intravenously. Thus, the radiotracer follows its physiological pathway and it is concentrated on specific place in the patient body where there could be disease or an abnormality for short periods of time. Then, the radiation emitted from the radiopharmaceutical in the human body is detected using a special camera called a gamma camera, resulting in images of the biodistribution of the radiotracer. Thus, nuclear medicine images show characteristic information about the physiological properties of the tissue or organ being investigated. In the last several decades, medical imaging systems have advanced in quantum leaps. There have been substantial improvements on their characteristics such as sensitivity, resolution and acquisition speed. Thus, advanced techniques of image processing and analysis find widespread use in medicine. Image processing methods are under continuous development in order to further improve the quality of the medical images that are used for a reliable diagnosis.
The scope of image processing and analysis applied to medical applications is to improve the quality of the acquired image and extract quantitative information (i.e., feature) from medical image data in an efficient and accurate way.
Image quality plays an important role in nuclear medicine imaging in order to provide a reliable image of the projected organ for an accurate diagnosis or therapy. The physical characteristics that are used to describe image quality are spatial resolution, contrast and noise.
Spatial resolution is defined as the ability of the imaging modality to reproduce the details of a nonuniform radioactive distribution of the tracer in the patient [21]. Thus, it refers to the ability of the imaging instrument to provide the sharpness or detail of the object. The spatial resolution is separated into intrinsic resolution (scintillator, photomultiplier tubes and electronic circuit) and system resolution (collimator, scintillator, photomultiplier tubes and electronic circuit) [22]. The intrinsic resolution depends on the thickness of scintillation crystal while the system resolution depends mainly on the distance from the emitting source to collimator (the collimator geometry) and to some extent by the septal thickness. Moreover, the resolution of a gamma camera is limited by several factors, such as, the patient motion, the statistical fluctuation in the distribution of visible photons detected, the collimators geometry, the Poisson noise in scintillation photon production, the number of photomultiplier tubes, the position-localization algorithms used and the image display or recording system [3].
Thus, intrinsic and camera spatial resolutions are parameters that inherently affect image quality and quantitative accuracy. Most modern gamma cameras have similar values for these parameters, and most of the values are close to optimal for present collimator/scintillation-crystal/photodetector technology [3].

The second physical characteristic to describe the image quality is the image contrast. It can be defined as the difference in intensity corresponding to different

concentration of activity in the patient [22]. Nuclear medicine images must be of high contrast for a good diagnostic accuracy.
Image contrast is affected by several factors, such as, the radiopharmaceutical that is used for imaging, Compton scatter, random or accidental coincidences, and detector dead time [3]. Hence, it is preferable to use a radioactive drug enabling a high uptake in the target organ. Compton scatter [23] can be reduced by energy windowing. However, to maintain high sensitivity (fewer rejected events), the energy resolution and photofraction should be high so that a narrow photopeak window will contain a high fraction of the incoming events [3]. To minimize the effect of random coincidences on image contrast, it is mandatory to have an excellent coincident time resolution and a reduced detection activity [24]. High coincident resolving time requires a fast, bright scintillation crystal or detector and low electronic noise [3]. Thus, random-coincidence and dead-time effects can be reduced if fast detectors are implemented [25, 26].
Lastly, the third physical characteristic is the noise which is the major factor in the degradation of image quality. The image noise may be divided into random and structured noise [22, 27]. Random noise, also referred as statistical noise, is the result of statistical variations in the counts being detected, which can be quite significant in positron emission tomography (PET) imaging studies [28]. Structured noise is derived from non-uniformities in the scintillation camera and overlying structures in patient brain. Structured noise may arise from the radionuclide distribution itself or caused by system artifacts [29]. Thus, the noise primarily comes from the inherent random variations in the counting of photons. Moreover, it is related to the number of photons detected and used for the image generation [29, 30]. For instance, single photon emission tomography (SPECT) images with fewer photons more typically have noise levels of about 10% [30].
Consequently, the noise can be caused on one hand, by random, uncorrelated uncertainties, including photon noise, electronic noise and noise due to scattered radiation. On the other hand, the noise can be generated by systematic, correlated uncertainties, including geometric distortion, detector non-linearity, errors due to sampling a continuous image into a discrete set of pixels and computational errors when an image is reconstructed from indirect data [31].

1.2 Motivation

Despite of the enormous progress made in imaging technology, many severe problems in using these devices are related to the artifacts of medical images for diagnostics and treatment planning. Thus, the quality of acquired images is degraded by both physical factors, such as compton scattering and photon attenuation, and system parameters, such as intrinsic and extrinsic spatial resolution of the gamma camera system. The main issue is that these image imperfections can influence the

diagnosis or in the worst case may even lead to false decisions by the physician. Therefore, the sources of artifacts have to be understood and removed during the acquisition process. However, in many cases, this cannot be achieved due to physical, financial or time issues. Then, they have to be dealt with using retrospective correction methods [32]. Moreover, in order to overcome the influence of inter-individual variability, images are processed with registration and intensity normalization steps. These steps are devoted to standardize brain volumes, spatially align anatomical regions, and recalibrate gray-level intensity so that images can be compared one to another. In this thesis, we will investigate the possibility to provide clinicians with tools that deliver useful information about emission-computed tomography (ECT) images, such as, SPECT and PET for the diagnostic process. Thus, we will mainly concentrate on a very important part of CAD system, that is intensity normalization in order to improve the overall performance in the early detection of Parkinson's disease (PD) and other neurodegenerative diseases such as multiple system atrophy (MSA) and progressive supranuclear palsy (PSP). The initial diagnoses of PD made by general neurologists have shown to be incorrect in 24% to 35% of the cases [33]. A reliable diagnostic test, which could be used to differentiate between different tremor disorders, would therefore be of great value. Thus, as a feature of PD is a marked reduction in dopaminergic neurons in the striatal region, brain imaging techniques (SPECT or PET) with specific ligands can be used as a valuable tool to evaluate PD patients [34]. These specific radio-ligands bind to the dopamine transporters in the striatum and have evolved as in vivo markers of progressive dopaminergic neuron loss in PD. Previous to any kind of image processing, the functional brain images have to be normalized in terms of intensity. Hence, the intensity normalization step is essential, as it corresponds to the initial step in any subsequent computer-based analysis. It guarantees that the differences between images of different subjects are due to physiological reasons and the brain functioning, and not due to the baseline calibration of the Gamma camera used for the acquisition among other factors [35]. The main advantage of CAD systems might be a reduction of workload for the clinicians, while providing reproducible, observer independent and reliable results. Considering longitudinal studies and treatment of patients, CAD systems may be able to detect and call the attention to early stages, prodromal cases.

1.3 Goals

The main goal of this thesis is to present four fully automated intensity normalization methodologies in order to help clinicians in the analysis of functional tomographic images of the brain. These novel approaches are based on the Gaussian Mixture Model (GMM), the mean squared error (MSE) and the predictive modeling using multivariate linear regression (MLR). The GMM-based image filtering

method will be achieved according to a probability threshold that removes the clusters whose likelihood are negligible in the non-specific region. The MSE optimization method will consist of a linear transformation that will be obtained by minimizing the MSE in the non-specific region between the intensity normalized image and the template. For the MLR approach, the normalized images will be computed by linearly transforming the voxel intensity of each image subject using a predefined model, as in the MSE approach. The proposed intensity normalization methods will be compared to widely used approaches, such as, the specific-to-non-specific binding ratio, the integral-based intensity normalization, the histogram equalization, the linear approach based on the α-stable distribution, the normalization to the maximum intensity values and the intensity normalization by minimizing the Kullback-Leiber divergence. This comparison is performed on two different image databases comprising analysis and classification stages for the development of CAD systems for idiopathic and atypical Parkinsonian syndrome (PS) detection. In addition, these proposed methods will be evaluated in the correction of spatially varying artifacts that modulate the intensity of the images.

1.4 Main contributions

The main scientific contributions of the thesis can be split into three different categories: development and implementation of standard methods for intensity normalization, development and implementation of novel intensity normalization approaches based on GMM, MSE and MLR, and utilization of the proposed intensity normalization scheme on a clinically relevant application dealing with computer-aided assessment of the early detection of PS. In the following, we will briefly introduce the major scientific contributions. For more information, we want to refer to the corresponding chapters.

- Development and implementation of state of the art algorithms for intensity normalization, which were carried out on two different imaging modalities (SPECT and PET).
- Development and implementation of a GMM-based image filtering approach, which considers not only the intensity levels, but also the coordinates of voxels inside the so-defined spatial Gaussian functions. The voxels in the reference region (non-specific region) are intensity-normalized by removing clusters whose likelihood is negligible.
- Optimization and implementation of two proposed methodologies, which are based on MSE. The first MSE optimization method consists of a linear transformation at every voxel in the brain image. This transformation is obtained by

minimizing the MSE between the intensity normalized image and the template in the so-defined non-specific (NS) region. However, the second approach is based on minimization of the MSE between the GMM-based extracted features from each subject image and the template in NS region.

- Development and implementation of a novel intensity normalization approach, which is based on a predictive modeling using MLR. Different intensity normalization parameters derived from this model will be used in a linear procedure to perform the intensity normalization of functional brain images.

- Qualitative and quantitative inter-subject variability measures are performed to evaluate the improvements provided by the proposed approaches when compared to state of the art algorithms.

- Algorithm independence of the clinical protocol.

- Improvement of the computational time, stability and repeatability of the performance for the different intensity normalization schemes.

- The development of more accurate CAD systems for the early detection of PS for two different imaging modalities (SPECT and PET).

1.5 Published works

Part of the work presented here has been published and is already available for the research community.

Articles in International Magazines:

1. A. Brahim, J. M. Górriz, J. Ramírez, L. Khedher, 'Intensity normalization of DaTSCAN SPECT imaging using a model-based clustering approach'. Journal of Applied Soft Computing, 37 (2015): 234–244, 2015, doi: 10.1016/j.asoc.2015.08.030.

2. A. Brahim, J. Ramírez , J. M. Górriz, L. Khedher and D. Salas-Gonzalez, 'Comparison between Different Intensity Normalization Methods in ^{123}I-Ioflupane Imaging for the Automatic Detection of Parkinsonism'. Journal of Plos One, 10 (6): 1–20, 2015, doi:10.1371/journal.pone.0130274.

International Conference Proceedings:

1. A. Brahim, J. M. Górriz, J. Ramírez, L. Khedher, 'Linear intensity normalization of DaTSCAN images using Mean Square Error and a model-based clustering approach', International Conference on Innovation in Medicine and Healthcare, San Sebastian, Spain, July 2014. vol.207, pp 251-260, ISBN: 978-1-61499-473-2,

2. A. Brahim, J. Ramírez , J. M. Górriz, L. Khedher, 'Linear intensity normalization of DaTSCAN images using Mean Square Error and a model-based clustering approach', 2014 IEEE International Conference on Image Processing (ICIP14), Paris, France, October 2014. vol.207, pp 3617–3621, ISBN: 978-1-4799-5751-4,

3. A. Brahim, J. M. Górriz, J. Ramírez, L. Khedher, 'Intensity Normalization of ^{123}I-ioflupane-SPECT Brain Images Using a Model-Based Multivariate Linear Regression Approach', 6th. INTERNATIONAL WORK-CONFERENCE on the INTERPLAY between NATURAL and ARTIFICIAL COMPUTATION, Elche, Spain, June 2015. vol. 9107, pp 68-77, ISBN: 978-3-319-18913-0.

Furthermore, further papers were published with collaborations in different international magazine and conference proceedings:

1. L. Khedher, J. Ramírez, J. M. Górriz, A. Brahim and F. Segovia, 'Early diagnosis of Alzheimer's disease based on partial least squares, principal component analysis and support vector machine using segmented MRI images'.Journal of Neurocomputing, 151 (1): 139–150, 2014, doi:10.1016/j.neucom.2014.09.072.

2. L. Khedher, J. Ramírez, J. M. Górriz , A. Brahim. , 'Automatic classification of segmented MRI data combining Independent Component Analysis and Support Vector Machines', International Conference on Innovation in Medicine and Healthcare (Inmed14), San Sebastian, Spain, July 2014. vol.207, pp 271–279, ISBN: 978-1-61499-473-2,

3. L. Khedher, J. Ramírez, J. M. Górriz, A. Brahim and I.A. Illán, 'Independent Component Analysis-Based Classification of Alzheimer's Disease from Segmented MRI Data', 6th. INTERNATIONAL WORK-CONFERENCE on the INTERPLAY between NATURAL and ARTIFICIAL COMPUTATION, Elche, Spain, June 2015. vol. 9107, pp 78-87, ISBN: 978-3-319-18913-0.

1.6 Structure of the document

The contents of the thesis are organized as follows:

- Chapter 2 presents an introduction to SPECT and PET imaging, their radiotracers and clinical application and an overview about various imaging artifacts that influence the image quality. In addition, it contains a medical background information about the neurodegenerative diseases that are considered along the thesis: PD, PSP and MSA. This introduction familiarizes the reader with these imaging modalities, some of its possibilities and limitations in the detection of these neurodegenerative diseases. This familiarity helps him to understand the discussions on the difficulties encountered, particularly on the intensity normalization issues.

- Chapter 3 reviews the pre-processing pipelines for the SPECT and PET data modalities that have been treated. Additionally, we present the state of the art about intensity normalization approaches adequately adapted to the nature of the PD images.

- Chapter 4 presents a novel method for automatic intensity normalization of functional brain images. The proposed methodology is based on GMMs which are used firstly for density estimation of the intensity profile of each functional medical imaging. We approximate the intensity profile of the SPECT images by a sum of Gaussians satisfying a maximum likelihood (ML) criterion. Then, the resulting mixture model is used for intensity normalization according to a cluster selection strategy. Clusters are selected by means of a normalized probability threshold that measures the weight of each kernel on the striatum area and the intensity normalization is actually carried out by only adding the relevant clusters in the image reconstruction.

- Chapter 5 addresses the correction of inter-image signal intensity variations by proposing three novel intensity normalization approaches. These methodologies are based on the extraction of intrinsic parameters from DaTSCAN SPECT and DMFP PET images, resulting in three automatic procedures for intensity normalization: MSE optimization between the intensity normalized image and the template in the NS region, MSE optimization between the GMM-based extracted features from each subject image and the template in the reference region, and finally a normalization method based on predictive modeling using MLR.

- Chapter 6 exhibits an evaluation study of the proposed intensity normalization approaches when compared to conventional IN methods adequately adapted to the nature of the PD. Thus, qualitative and quantitative inter-subject variability measures are performed. In addition, a comparison is performed using a classification system for PS detection, that may improve the development of a CAD system for PD.

- The thesis is concluded in Chapter 7 where we also discuss some possible paths for future research.

Chapter 2

The diagnosis of idiopathic and atypical parkinsonian syndromes using Functional imaging

There have been a growing number of studies showing the importance of functional imaging studies using single-photon emission tomography (SPECT) or positron emission tomography (PET) tracers in many fields, such as, neurology, nuclear imaging and in diagnostics in general. In particular, Parkinson's disease (PD) and other neurodegenerative disorders such as multiple system atrophy (MSA) and progressive supranuclear palsy (PSP) are useful disease models to understand the contribution of modern functional neuroimaging techniques in their identification and treatments. In this chapter our aim is to address the principles of SPECT and PET and also its pitfalls, with focus on the diagnosis of PD, MSA and PSP. The understanding of these molecular imaging techniques is important to be able to understand the choices we will made in treating these kind of images.

2.1 Single Photon Emission Computed Tomography (SPECT)

The neuroscientist of today disposes of a powerful instrumentarium for functional imaging that has never made more impressive advances before [36]. Thus, it helps to better understand the pathologies and the mechanisms of diseases [37]. Furthermore, its aids to develop and design drug treatment options with a superior efficacy and safety profile [38]. Among this instrumentarium, SPECT has become forerunner in the functional imaging arena, much more than functional magnetic

resonance imaging [37]. SPECT is an emission-computed tomography (ECT) imaging technique that was initially developed in the 1960s, but was not widely used in clinical practice until the 1980s [39]. The main aim of SPECT as used in brain imaging, is to measure the regional cerebral blood flow (rCBF) [40]. The earliest experiments to measure cerebral blood flow were performed in 1948 by Kety and Schmidt [41]. They used nitrous oxide as an indicator in the blood, measuring the differences between the arterial input and venous outflow, from which the cellular uptake could be determined. This could only be used to measure the global cerebral blood flow, and so in 1963 Glass and Harper [42], building on the work of Ingvar and Lassen [43], used the radioisotope ^{133}Xe (xenon), which emits gamma rays, to measure the rCBF. The development of computed tomography in the 1970's allowed the distribution mapping of the radionuclides in the brain, and led to the technique now called SPECT [44]. When structural information is insufficient to detect or monitor a functional disorder, SPECT imaging can be used [45].
SPECT is a noninvasive, three-dimensional functional imaging modality that provides clinical information regarding biochemical and physiologic processes in patients [45]. Thus, SPECT is a diagnostic imaging technique in which tomographs of a radioisotope distribution are generated from gamma photons detected at numerous positions about the distribution [3].
Thereby, SPECT imaging is an ionizing technique, where the resulting images are created by detecting nuclear radiations [46]. These radiations are emitted from the brain after injecting a radioactive pharmaceutical. The pharmaceutical is a molecule that imitates a substance which is implicated in a specific biochemical process, for example glucose or oxygen consummation. The pharmaceutical contains a radionuclide that emits gamma rays [47]. In SPECT imaging, the commonly used radionuclides are thallium (^{201} Tl), technetium (^{99m} Tc), iodine (^{123}I), gallium (^{67}Ga) and Indium (^{111} In). These radionuclides decay by emitting gamma rays for imaging with photon energies up to a few hundreds of keV, as illustrated in Table 2.1.

Table 2.1: Gamma photon emitter radionuclides with their Half-life duration and clinical applications commonly used in SPECT.

Radionuclide	Half-Life (h)	Photon energy (KeV)	Clinical applications
^{201} Tl	73	135	Cardiovascular
^{123}I	13	159	Thyroid, neurological tumor
^{99m} Tc	6	140	General and tumor
^{67}Ga	78	93, 185, 300, 304	Infections
^{111} In	68	171, 245	Infection, tumor

Figure 2.1: Brain SPECT Imaging Camera.

2.1.1 The use of the Gamma camera in SPECT imaging

The detection of Gamma rays is carried out using a gamma camera composed of a scintillation detector consisting of a collimator, a scintillation crystal, and a set of photomultiplier tubes as shown in figures 2.1 and 2.2. The purpose and functioning of the gamma camera can briefly be described as follows:

- Firstly, The photons that are emitted isotropically from within the subject are mechanically collimated. The collimator is usually a plate made of lead that absorbs photons that are not aligned with the holes drilled in it. Collimation is necessary in order to know the direction from which the photon was emitted. Thus, the collimator forms an image by selecting only the rays traveling in (or nearly in) a specific direction. To learn more about collimators and their characteristics, the reader is referred to [3].
- Secondly, The scintillation material absorbs γ photons by one or more collision processes and converts some of their energy into visible light and ultraviolet (UV) photons. This is done through a process know as scintillation.
- Then, These photons are guided toward the cathodes of the photomultiplier tubes (PMTs) where they are converted to electrons by means of the photo-

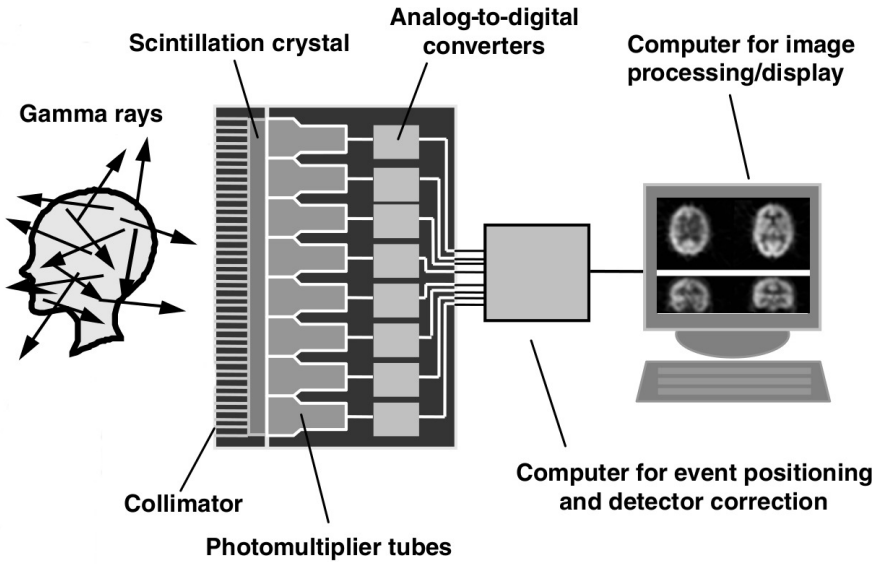

Figure 2.2: Fundamental components of a conventional gamma camera. Most gamma cameras have a collimator, a scintillation crystal, an array of photomultiplier tubes that are connected to the electronic circuits (AD converters), and a computer for acquisition, processing, and display of data and images. Modified from [3].

electric effect. From a single photoelectron, a PMT can produce a cascade of electrons, which yields a measurable electrical current. The electrons are multiplied in their flight toward the anode where they give rise to a voltage pulse.

- Lastly, The analog and digital electronic circuits (Analog-to-digital (AD) converters) measure the output voltage pulses from the photomultiplier anodes and estimate the position of the incoming gamma-ray.

2.1.2 SPECT image quality

SPECT imaging is not ideal. Inherent in SPECT imaging are degradations that distort the projection data [48]. Thus, there are many sources that influence the quality of the image, as shown previously in chapter 1. In addition, to obtain the most accurate quantitative data from SPECT images, two issues have to be resolved [3, 49]. The first issue is the photon attenuation, which can significantly reduce available counts and cause nonuniform image artifacts [49]. It is caused by the absorption of photons in the head of the subject. Thus, it depends on the distance of the cameras from the source of radiation [50]. Gamma rays emitted from deep within the head of the subject have a greater chance of being absorbed, so the effect is depth-

dependent. If not accounted for, attenuation causes the reconstructed image to appear dark in the interior of the head [51]. Therefore, to some degree, this attenuation is compensated by the fact that two cameras are used [52]. Further compensation can be made by using specialized reconstruction filters or iterative reconstruction algorithms [53, 54]. Moreover, Attenuation correction can be resolved by using the constant linear attenuation coefficient (μ) method or using the transmission source method [3, 55].
The second issue is the Compton scattering, where the photon is reduced in energy as well as deflected from its original path [56]. This is due to the interaction between a gamma ray and a free electron in the brain. Thus, it leads to lack of sharpness in the images and it is manifested as a nonlinear blurring effect in the image [3]. The scatter correction methods are based on estimation techniques using photon statistics derived from distribution models or experimental measurements [57]. In addition, in order to reduce the effect of Compton scattering it is necessary to have a camera with a high energy resolution [58]. For instance, photons with less than 140 keV, such as, those issued from a scattering event can then be filtered out [59]. Furthermore, the Compton scattering can be modeled during image reconstruction when iterative image reconstruction schemes are used [60].
SPECT imaging shows an important biochemical information tagged with specific physiology despite the poverty of SPECT images in structural information because of the attenuation and scattering problems. SPECT imaging is a proven tool in the assessment and the characterization of a tumor [45]. Also, SPECT imaging is a low-cost imaging modality compared with PET because of the lower preparation cost of the radioisotopes used in SPECT imaging. This radioisotopes have relatively long half lives (a few hours to a few days), as shown in Table 2.1, making them easy to produce and relatively cheap. Thus, this represents the major advantage of SPECT as a brain imaging technique. However, it lacks good spatial or temporal resolution, and there are safety aspects concerning the administration of radioisotopes to the subject, especially for serial studies [61].

2.2 Positron Emission Tomography

Positron emission tomography (PET) imaging modality were developed in 1970s by many researchers, such as, Ter-Pogossian and Phelps [62, 63]. PET is a nuclear medicine imaging technique that produces a three-dimensional image of functional processes in the body [64]. The PET imaging concept is based on the simultaneous detection of two 511 keV energy photons, which are emitted into near opposite directions [51]. The distinctive feature of PET imaging technique is its ability to trace radioisotope metabolized in the body tissue to provide specific information about its biochemical and physiological behavior [65]. Despite the fact that PET is based on photons emitted from a radionuclide, the underlying physics provide

an opportunity to improve beam collimation through so-called *electronic collimation* [66]. In PET, radioisotopes decay by emitting positively charged particles called positrons [57]. Positrons are short lived, of the order of 2-100 minutes (see Table 2.2), and after traveling only a short distance (typically for 1-3 mm), they interact with an electron. During this interaction, their masses are annihilated and two gamma photons with 511 keV are generated traveling in opposite directions (close to 180 degrees apart) [66]. The gamma rays are detected in coincidence by detectors that surround the patient, as shown in Figure 2.3. Thus, by detecting a large number of coincidences, the source location and distribution can be reconstructed through image reconstruction algorithms [57, 66]. In the imaging reconstruction process, it is the locations of annihilation events that are reconstructed as an image in the PET imaging technique [65]. However, the emission events distribution of positrons is considered close enough to the annihilation events distribution within a resolution limit [57].

PET scans are increasing in use for all body parts. Furthermore, PET modality is a relevant tool for the brain imaging [67]. It is challenging to get a radioactive isotope into the brain for measurement because the protection of the blood-brain barrier (BBB) [68]. The BBB makes it difficult to get most substances into the brain. Therefore, to get through the BBB and enter the brain easily, carrier-mediated transporters, such as, glucose can be used. For instance, a positron emitter, such as, the fluorine isotope ^{18}F can be inserted into a glucose molecule. Thus, the concentration of the radioactively tagged glucose is a measure of the metabolic activity level at that location in the brain [69].

The PET scanning becomes an increasingly important tool for fundamental research which provide a map of the metabolic activity level in the brain [25]. This imaging technique has been used to map the different patterns of brain activity for various activities, such as, cognitive tasks [70]. Moreover, patterns of activity associated with certain brain disorders, such as, PD may be identified [71]. The positron emitting neurotransmitters such as ^{18}F, which is administered as fluorine-labeled radiopharmaceutical called fluorodeoxyglucose (FDG), can provide useful information about the dopaminergic neuron functioning in patients with PD [72–74].

The main advantage of PET imaging is its ability to extract metabolic and functional information of the brain tissue. This is mainly due to the unique interaction of the positron with the matter of the tissue [57]. In addition, PET has major advantages over SPECT, namely better spatial resolution, greater sensitivity and it allows one to examine biological events which run much faster [75]. Radioisotopes labelled for PET have a much shorter half-life compared with those used in SPECT [76]. This means that a patient undergoing PET examination is examined more precisely and also receives a smaller dose of the harmful radiation [77]. The main drawback of PET is its very high cost because of the high costs of cyclotrons needed to produce the short-lived radionuclides for PET scanning and the need for specially adapted on-site chemical synthesis apparatus to produce the radiopharmaceuticals after radioisotope preparation [78].

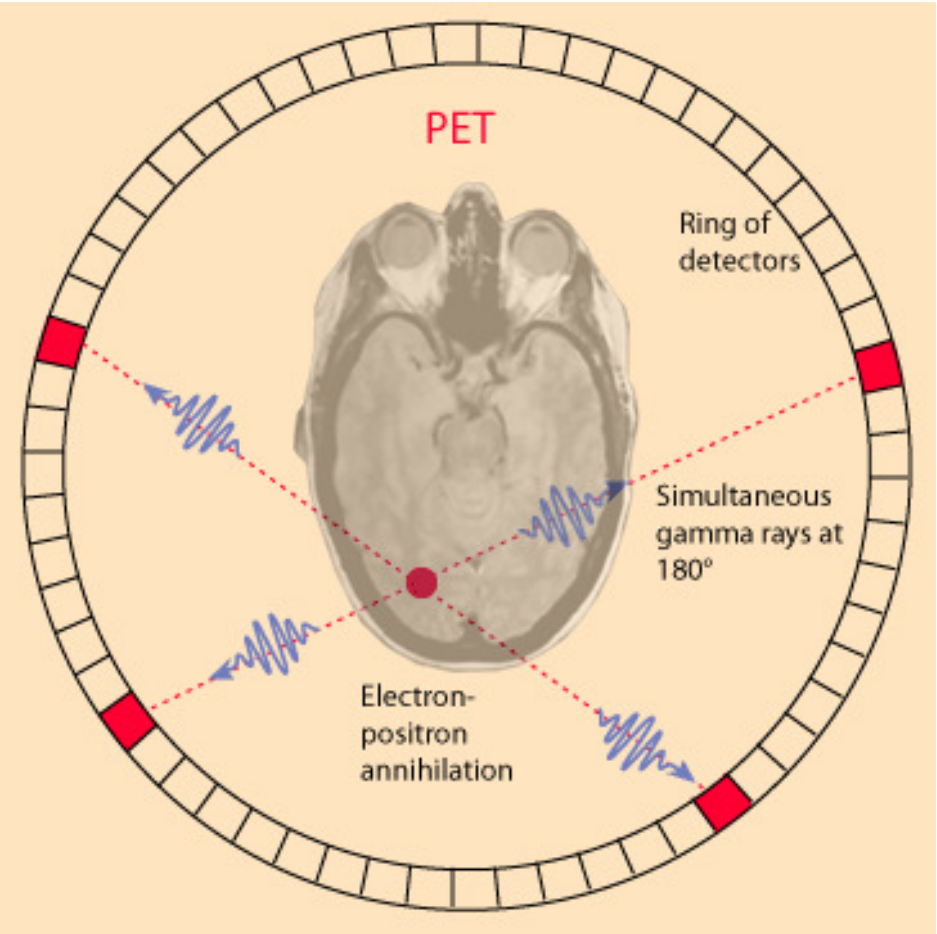

Figure 2.3: Physical principle of PET. A positron is emitted from a radioisotope in the brain. The positron annihilates with an electron, producing two photons emitted at 180 degrees to each other. Reproduced from [4].

2.2.1 PET image quality

As in SPECT scanning, PET data are affected by attenuation, scatter, and several mechanisms of blurring. These factors are generally easier to correct in PET than in SPECT [3]. The spatial resolution, contrast and sensitivity of PET imaging are significantly better than SPECT imaging mainly because of electronic collimation provided by the coincidence detection method [75]. The coincidence detection method provides a more sensitive and accurate count of the photon-emission events [79]. Moreover, the resolution of PET images does not depend on the distance between the emission source and detector as in SPECT images. In addition, The resolution of a PET scanner is influenced by some factors which depends mainly on the physical characteristics of the radionuclide and the detection system [75, 80].
Hence, the spatial resolution of PET imaging is limited by the fundamental nature of positron annihilation [81, 82]. When Positrons are emitted, they do not immediately annihilate. Instead they travel some distance in matter, depending on their initial kinetic energy and the electron density of the absorbing material [83]. These emitted positrons have a continuous distribution of kinetic energy values, ranging from zero to a maximum energy, as shown in Table 2.2. Thus, the range of positrons is not a fixed value but rather a distribution of values that can be characterized by a full width at half-maximum (FWHM). When the thermal energies are reached, the positrons interact with electrons by the formation of a hydrogen-like orbiting pair called positronium [3]. Positronium is unstable and eventually decays, via annihilation, into a pair of anti-parallel 511-keV photons (emitted at 180 degrees relative to one another) [3]. Although the radial distribution of annihilation events is sharply peaked at the origin (site of positron creation). A calculation of the radius that includes 75% of all annihilation events gives a realistic comparison of the impact of the maximum positron energy on the spatial resolution of PET imaging [84, 85].

Table 2.2 illustrates the major emitters used in PET imaging, along with positron energy and range in water (some of their relevant physical characteristics). The range is defined as the radius that includes 75% of all annihilation events.
Moreover, the non-exact collinearity of the annihilation photons also leads to a limitation of the spatial resolution of PET imaging [75]. It is a common understanding that annihilated photons travel exactly in opposite directions. However, because of the positronium has some residual momentum, annihilation photons are not emitted exactly at 180 degrees [79]. Thus, the variation in momentum of the positron results in an angular uncertainty in the direction of the 511-keV photons. This is referred to as noncolinearity [83].
A third significant factor limiting PET image resolution is the intrinsic spatial resolution of the detector [86]. A final factor affecting PET image resolution is referred to the parallax error, which results from the uncertainty of the depth of interaction (DOI) of the gamma rays in the crystal [3].

Table 2.2: Half-life and positron range of Radionuclide commonly used in PET [3].

Radionuclide	Half-Life (min)	Maximum Positron energy (KeV)	Mean Positron Range in Water (mm)
^{11}C	20.3	960	1.1
^{13}N	9.97	1190	1.3
^{15}O	2.03	1720	2.5
^{18}F	109.8	635	0.5
^{68}Ga	67.8	1899	0.8
^{82}Rb	1.26	3356	1.5

The signal-to-noise ratio (SNR) is superior in PET images to SPECT but is still affected by the dose of the positron emitter nuclide, the detector efficiency and the intensity distribution of source emission [57]. Moreover, the SNR is further improved by using retractable septa of the external collimator in multislice imaging when multiple rings of detectors are used [57]. This mode rejects any cross-plane event detection, reducing the data to only true coincidence events within the selected plane without any scattering [78].

2.3 Functional Image acquisition

The acquisition of images, both SPECT and PET is performed with the patient in supine position (lying on your back, neck in a neutral position, eyes turned to the zenith, and extended upper limbs close to the body, palms up, extended lower limbs, feet in neutral flexion and the tip of the toes up) and in a dimly lit room with no noise in which the patient must be at least 10 minutes before the start of the process [87]. Note that the obtained images will show the functions of the brain and therefore it is undesirable to have an influence of the environment that may cause more brain activity than normal (at rest). The patient's head must be immobilized and the detector must be positioned so close to the brain as possible, preferably with a radius of rotation of 14 centimeters or less from the detector surface collisions at the center of the patient's brain.
The acquisition process can start within 15 minutes of the administration of the radiopharmaceutical although it is advisable to wait between 60 and 90 minutes. During the process, the camera (or detector) is rotated around the brain and during movement is taking pictures in 2D known as projections. Typically a projection is taken every 2 degrees of rotation, making a total of 180 projections for each brain image. Finally, the three-dimensional brain image is reconstructed from the projection data using filtered back-projection algorithm (FBP) described in the following

section in combination with a Butterworth noise removal filter.
For the DaTSCAN SPECT image acquisition, the patients are injected with a gamma emitting Ioflupane-I-123 (185 MBq (5 mCi)) radioligand. During this period, the thyroid was blocked using a Lugols solution. The scans were obtained using a General Electric gamma camera, Millennium model, equipped with a dual head and general purpose collimator. A 360-degree circular orbit was made around the cranium, at three-degree intervals, leading to 60 128×128 images per interval. The brain images were reconstructed using the filtered back projection (FBP) algorithm, applying a Hanning filter (cut-off frequency equal to 0.7) and were obtained with trans-axial slices.
^{18}F-DMFP PET scans were acquired according to a standardized protocol.^{18}F-DMFP was injected as a slow intravenous bolus, and the patients were seated in a quiet room. After 55 min, the patients reclined in the scanning bed of the ECAT EXACT HR^{+} PET tomograph (Siemens/CTI), with their head comfortably immobilized within the aperture, using a foam cushion. The scanner acquired 63 contiguous trans-axial planes, simultaneously covering 15.5 cm of the axial field of view. The trans-axial and axial resolutions (FWHM) of the PET system were 4.6 and 4.0 mm, respectively, at the center of the field of view, and 4.8 and 5.4 mm, respectively, at a radial offset of 10 cm. The emission recording began at 60 min after the start of the bolus and consisted of 3 frames of 10 min each, acquired in 3-dimensional mode. Finally, a brief transmission scan was obtained using a rotating ^{68}Ge point source. Images were reconstructed as 128×128 matrices of 2×2 mm voxels by FBP using a Hanning filter with a cutoff frequency of 0.5 Nyquist and corrected for randoms, dead time, and scatter. Images were then transferred to a workstation (Hermes Medical Solutions). After verification of the absence of important head motion between frames, the 3 frames were summed for further analysis [88].

2.4 Functional Image reconstruction

The purpose of reconstruction algorithms is to calculate an accurate 3D radioactivity distribution from the acquired projections [54]. Hence, after the acquisition of projections made by the camera, it is necessary to reconstruct the transversal image slices [30, 54, 89–95]. There are two major ways to reconstruct tomographic images from acquired projections [54, 96]. The most widely used technique in clinical practice is the classical FBP algorithm [54, 97, 98]. Although many different iterative algorithms for reconstruction exist, such as, the algebraic methods like the algebraic reconstruction technique (ART) and the statistical algorithms like the maximum likelihood expectation maximization (MLEM) [92] or the ordered subsets expectation maximization (OSEM) [30, 94]. The advantage of these algorithms is that some of the error sources, such as, attenuation, Compton scatter and camera response can be explicitly modeled and taken into account during reconstruction [99, 100].

Since, all the SPECT and PET scans considered in this thesis have been reconstructed using the FBP algorithm, we will restrict to present the filtered back-projection techniques. However, in many cases iteratively reconstructed images need to be post-filtered since they tend to be noisy [54]. Therefore, filtering can also be considered as a post-processing step in iterative reconstruction [98].
The backprojection is an essential step in image reconstruction [101]. It represents the accumulation of the ray-sums of all the rays that pass through any point with coordinates (x,y) for a given projection angle θ [95]. Hence, it is the adjoint to forward projection process that forms the projections of the object. In ideal conditions, projections are a set of integrated value measurements of some object parameter along a line path. If the object is represented by a two dimensional function $f(x,y)$ and each line integral by the (θ,t) parameters, the line integral is defined as [95]:

$$P_\theta(t) = \int_{-\infty}^{+\infty}\int_{-\infty}^{+\infty} f(x,y)\delta(x\cos\theta + y\sin\theta - t)dxdy, \tag{2.1}$$

where $P_\theta(t)$ is known as the Radon transform of the function $f(x,y)$. $f(x,y)$ can be defined as the distribution of radiotracer within the slice of the body defined by the xy plane. Because an integral is basically a sum of values, the value $P_\theta(t)$ is the sum of the values $f(x,y)$ along the line t. Hence, $P_\theta(t)$ is called ray sum because it is related with the sum of radioactive counts recorded in any time interval at point t when the detector is at angle $\theta(t)$ [95].
The *Fourier Slice Theorem* is the key to tomographic imaging [102]. It is also known as the *central-section theorem* and it is a foundational relationship in analytic image reconstruction [101]. This theorem states that the Fourier transform of a one-dimensional projection is equivalent to a section, or profile, at the same angle through the center of the two-dimensional Fourier transform of the object [103]. Thus, the Fourier transform $S_\theta(w)$ of a parallel projection $P_\theta(t)$ of an image $f(x,y)$ taken at angle θ can be defined as:

$$S_\theta(w) = \int_{-\infty}^{+\infty} P_\theta(t)\exp(-j2\pi wt)dt, \tag{2.2}$$

a slice of the two-dimensional Fourier transform is given by:

$$F(u,v) = \int_{-\infty}^{+\infty}\int_{-\infty}^{+\infty} f(x,y)\exp(-j2\pi(ux+vy))dxdy, \tag{2.3}$$

subtending an angle θ with the u-axis, that is,

$$S_\theta(w) = F(u = w\cos\theta, v = w\sin\theta) \tag{2.4}$$

This result is the key of straight ray tomography. By having projections of an object function under a different angles θ_1, θ_2, ..., θ_k and taking the Fourier transform of them, the values of the two-dimensional transform $F(u,u)$ can be determined on

radial lines in the uv plane (spatial frequency domain). In practice, only a finite projections number of an object can be taken [102]. Thus, the function $F(u,v)$ is only known along a finite number of radial lines [95].
In this study, the used projection data are reconstructed using the the most commonly used FBP algorithm that is easily derived from the Fourier Slice Theorem. FBP is a mathematical technique based on an idealized model of PET and SPECT data that ignores many significant features of real data [3]. Specifically, FBP supposes that the number of detected gamma-ray events traveling along a particular direction approximates an integral of the radiotracer distribution along that line, i.e., the parallel projection defined in eq. 2.1. Thus, an image of the cross section $f(x,y)$ of an object can be recovered by:

$$f(x,y) = \int_0^{\pi} Q_\theta(x\cos\theta + y\sin\theta)d\theta, \tag{2.5}$$

where $Q_\theta(t)$ represents the filtering of the projections and it is defined as:

$$Q_\theta(t) = \int_{-\infty}^{+\infty} S_\theta(w)|w|\exp(j2\pi wt)dw \tag{2.6}$$

Therefore, the FBP algorithm consists of two steps: the backprojection process, which is taken place in spatial domain, and the filtering part, which can be visualized as a simple weighting of each projection in the frequency domain [39].
In the noise apparition, the FBP algorithm must be slightly modified by the introduction of a smoothing step [3]. The smoothing process can be implemented as a 1D filter applied to the projections prior to backprojection. Moreover, it can be implemented also as a 2D filter applied to the image after backprojection [3]. When applied to the projections, the smoothing filter is usually combined with the ramp filter [104]. In addition, the undesired amplification of the high frequency noise and its impact on reconstructed image quality, is the major drawback of FBP [95]. The causes of the noise amplification can be explained by the filtering operation or by the multiplication of $S_\theta(w)$ by $|w|$ in equation 2.6. In order to reduce the high frequency noise amplified during FBP reconstruction, various filters have been designed by including a window in them [105]. Thus, a number of window functions has been proposed. Among the widely used window functions for FBP reconstruction: *i*) cosine, *ii*) sinc (Shepp-Logan filter), *iii*) Hanning, *iv*) Hamming, and *v*) Parzen window functions. In this way, the reconstruction method described by equations 2.5 and 2.6 is normally redefined by applying a frequency window which returns to zero as the frequency tends to π. For the improvement of reconstructed image quality and therefore for the diagnostic evaluation, the noise captured by the acquisition system needs to be filtered out even when the reconstruction noise is kept low using a noise controlled FBP approach [54, 98]. Thus, in order to reduce the noise acquired by the gamma camera as well as the noise amplified during FBP reconstruction, the preprocessing stage of most automatic SPECT image processing

systems often includes prefiltering, reconstruction and postfiltering [102].
After image acquisition, when filtering and reconstruction are done, some additional preprocessing steps are needed before using functional brain images for computer aided diagnosis systems [106]. This issue will be discussed in the following chapter.

2.5 Idiopathic parkinsonian syndromes: Parkinson's di -sease (PD)

Idiopathic means that the cause of this disease is unknown. Parkinsonian syndrome (PS) or Parkinsonism is characterized by the presence of hypokinesia associated with rest tremor and/or rigidity and/or postural instability [107]. From a clinical point of view, the most common condition in this syndrome is PD [108]. PD is the second most common neurodegenerative disorder after Alzheimer's disease [109]. Incidence of the disease increases with age. The prevalence is estimated at 0.3% of the whole population in industrialized countries, rising to 1% in those over 60 years of age and to 4% of the population over 80 years of age [110]. The mean age of onset is around 60 years, although 5 – 10% of cases, classified as young onset, begin between the ages of 20 and 50 [111]. According to the Parkinson's Disease Foundation [112], approximately 60,000 Americans are diagnosed with PD each year, and this number does not reflect the many thousands of cases that go undetected.
PD is a *progressive* degenerative neurological disorder of the central nervous system. Early in the course of the disease, the most obvious symptoms are movement-related [109]. These include shaking, rigidity, tremor, slowness of movement, postural instability and difficulty with walking and gait. Later, cognitive and behavioral problems may arise, with dementia commonly occurring in the advanced stages of the disease [113, 114]. Other symptoms include sleep, sensory, and emotional problems [115]. The neuropathology of the disease is characterized by the progressive loss of dopaminergic neurons of the substantia nigra that project to the putamen, i.e., dopaminergic nigrostriatal pathway [116]. This leads to a corresponding loss of dopamine transporters (DaTs) in the striatum [117]. The DaTs are proteins situated at the presynaptic terminal of dopaminergic neurons which are responsible for the re-uptake of dopamine [118] into the presynaptic neuron.
Figure 2.4 shows that in patients with PD, nigrostriatal degeneration leads to decreased production of dopamine, which results in less synaptic dopamine, fewer axonal synapses, and ultimately fewer dopamine transporter targets for imaging [119, 120].
Thus, the nigrostriatal cell loss is responsible for the major symptoms of this disease. Although a small proportion of cases can be attributed to known genetic factors, most cases of PD are idiopathic [109]. While the etiology of dopaminergic

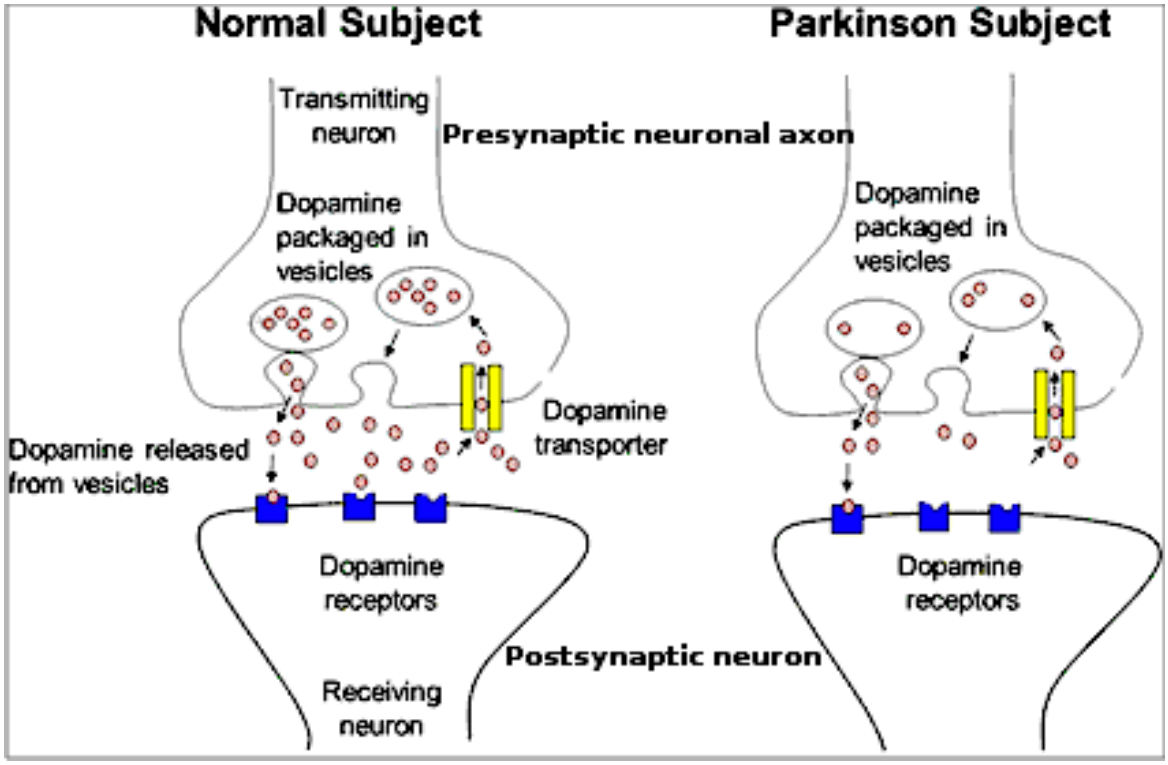

Figure 2.4: Simplified scheme of the dopaminergic synapse and dopaminergic neurotransmission [5] with dopamine transporter loss in PD: the dopamine transporters are located at the presynaptic side. They transport dopamine out of the synaptic cleft, back into the presynaptic nerve endings for either re-use or degradation [6]. Nigrostriatal dopaminergic denervation is a key pathobiological event in PD and related parkinsonian disorders. The lower number of nigrostriatal nerve terminals in PD results in decreased striatal signal on DaT imaging.

neuronal demise is elusive, a combination of genetic susceptibilities, age, and environmental factors seems to play a critical role [121].
Historically, a diagnosis of PD is usually made based on the patient's medical history and a neurological examination [122]. The physician conducts an interview specifically looking for cardinal motor symptoms while attending to other possible symptoms that would exclude a diagnosis of PD. There are four motor symptoms which are considered cardinal in PD: tremor, rigidity, slowness of movement and postural instability [123]. Common presentations of the disease are usually easily diagnosed. Diagnosis can be difficult when the symptoms are not fully typical of PD since Parkinsonism can occur due to a range of causes [124]. Furthermore, the difference with PD may be subtle, particularly in the early stages when symptoms may be mild [125, 126]. A more detailed explanation about this disease can be found in [111, 116, 123].

2.6 Atypical parkinsonian syndromes: multiple system atrophy and progressive supranuclear palsy

The atypical parkinsonian syndromes (APS) such as multiple system atrophy, progressive supranuclear palsy, and corticobasal degeneration are characterized by poor response to antiparkinsonian medication and rapid clinical deterioration, which one often confused with PD [127]. Since APS patients share the parkinsonian symptoms, the clinical distinction between PD and APS may be difficult in early phases [128]. The clinical diagnostic accuracy can be improved if specialists in movement disorders make the diagnosis [129].
However, the accurate diagnosis may take time to unveil. In MSA, and PSP there is a degeneration of dopamine neurons in substantia nigra, leading to depletion of dopamine in the nigrostriatal system, such as in PD [116].

2.6.1 Multiple system atrophy (MSA)

MSA is a sporadic progressive neurodegenerative disorder characterized by neuropathologic demonstration of CNS α-synuclein positive glial cytoplasmic inclusions with neurodegenerative changes in striatonigral or olivopontocerebellar structures [130]. It may account for up to 10% of patients with extrapyramidal diseases [131].
The disorder can present as a predominantly or exclusively cerebellar (olivoponto cerebellar atrophy) or parkinsonian (striatonigral degeneration) form associated with variable degrees of autonomic failure [132]. Depending on the predominant phenotype of the motor disorder, MSA is mainly classified into a parkinsonian type

(MSA-P) in 80% of patients and a cerebellar type (MSA-C) in 20% of patients [127]. Pathologic studies of both groups of patients have demonstrated neuronal degeneration and gliosis in many brain regions, such as, the basal ganglia, brainstem, spinal cord and cerebellum [133]. In MSA, regional cerebral blood flow and glucose metabolism are reportedly reduced in some regions, such as, the striatum, cerebellum, and in some cortical structures. This reduced metabolism in the striatum might help to distinguish MSA from PD patients [5].
The MSA-P can be reliably diagnosed only if prominent signs of autonomic failure, such as, impotence or postural hypotension develop early in the course of the disease or a clear cerebellar syndrome is also present [134]. Besides dysautonomia, other clinical characteristics can help differentiate MSA-p from PD: rapid course, early instability and falls, nocturnal stridor, stimulus sensitive myoclonus, severe dysarthria, pyramidal tract signs and insufficient or only transient response to L-dopa [135, 136]. Regarding to neuro-transmission, MSA is identified by a degeneration of the pre- and postsynaptic dopaminergic system [137]. Therefore, PET and SPECT investigations with the respective presynaptic and postsynaptic tracers have been proven to improve the differential diagnosis of IPS and MSA as well as corticobasal degeneration and PSP [88, 138]. However, the major difference between MSA and PD, is the presence of pathologic findings on the postsynaptic level. Thus, on the presynaptic level, diagnostic discrimination between MSA and PD is not reliably possible [139].

2.6.2 Progressive supranuclear palsy (PSP)

PSP, also known as Steele-Richardson-Olszewski syndrome, is a rapidly progressing degenerative disease belongs to the family of tauopathies [137]. Clinically, PSP is characterized by parkinsonism with rigidity, bradykinesia, falls, postural instability, a pseudobulbar syndrome that includes dysarthria and dysphagia and prominent frontal lobe syndrome [5, 134]. The PSP key feature is the supranuclear palsy of vertical gaze. It occurs rarely at disease onset and usually arises later [140].
Histopathologic findings of this neurodegenerative disease show cell loss and gliosis [5]. Neuropathological studies of this disease exhibit the existence of abundant tau-positive neurofibrillary tangles in different brain regions, such as, subcortical and brainstem structures [141]. Epidemiological [142] and clinicopathological [143] studies of PSP show the frequent diagnostic confusion with PD, specifically, in the early stages of this disorder before gaze abnormalities appear. Furthermore, this confusion with PD can be in patients without gaze palsy, or when full-blown parkinsonism dominates the clinical picture [134]. Otherwise, the main distinguishing features of PSP vs. MSA and PD are the decrements of glucose metabolism in the brainstem and in the midline frontal regions [137].
The neurodegeneration in PSP affects both the pre- and postsynaptic dopamine sys-

tem [144]. Therefore, the respective PET and SPECT findings are similar to those in MSA subjects, i.e., showing a reduced striatal dopamine-receptor binding on both levels [145]. Thus, PSP patients cannot be reliably separated from those with MSA neither with pre- nor postsynaptic tracers at an early stage of these diseases [139]. Nevertheless, as in the MSA disorder, the presence of pathologic PET and SPECT findings at the postsynaptic level allows the separation between PSP and PD [146].

2.7 Functional Imaging and its Role in the Differential Diagnoses of Parkinsonism

An early and correct diagnosis of PD is important for the management of patients. The diagnosis is usually based on the results of clinical assessments and clinical signs have proved to be insufficient for accurate diagnosis especially at an early stage and in elderly subjects. The initial diagnoses of PD made by general neurologists have shown to be incorrect in 24% to 35% of the cases [33]. A reliable diagnostic test, which could be used to differentiate between different tremor disorders, would therefore be of great value.

Therefore, as a feature of PD is a marked reduction in dopaminergic neurons in the striatal region, brain imaging techniques, such as SPECT or PET using pre- and postsynaptic radiotracers [5] (see Table2.3) can be used as a valuable tool to evaluate PS patients [34, 147, 148], such as I-Ioflupane (better known as DaTSCAN [34, 149] or [^{123}I]FP-CIT [1]), [^{123}I]-β-CIT, [^{123}I]iodobenzamide (IBZM) [150] and [Tc-99m]-TRODAT-1 [151]. These radiopharmaceuticals, which may examine the integrity of the nigrostriatal dopamine function with imaging techniques and bind to the dopamine transporters in the striatum, have evolved as in vivo markers of progressive dopaminergic neuron loss in PS.

In this Thesis, we focus on two specific tracers for SPECT and PET imaging for the diagnosis of PS. These tracers are [^{123}I] FP-CIT (DaTSCAN) and ^{18} F-Desmethoxyfallypride (DMFP). They have been developed to measure dopamine synthesis and transport for the PS diagnosis purpose.

Table 2.3: The most often used pre- and postsynaptic SPECT and PET tracers for investigation of the dopaminergic system.

	Parameter	SPECT	PET
Presynaptic function	Dopamine storage (dopamine decarboxylase activity)	–	^{18}F-DOPA
	Dopamine re-uptake	^{123}I-FP-CIT	^{11}C-nomifensine
		^{123}I-β-CIT	^{11}C-WIN
		^{123}IPT	^{11}C-FE-CIT
		^{123}Altropane	^{11}C-DTBZ
		^{123}PE2I	^{11}C-Cocaine
		^{99m}Tc-TRODAT-1	
Postsynaptic function	D_1 receptor density	–	^{11}C-SCH23390
			^{11}C-NNC112
	D_2receptor density	^{123}I-benzamide (IBZM)	^{11}C-raclopride
		^{123}I-Lisuride	^{11}C-methylspiperone
		^{123}IBF	^{18}F-ethylspiperone
		^{123}I-Epidepride	^{18}F-desmethoxyfallypride
			^{18}F-fallypride

2.7.1 DaTSCAN SPECT imaging

The dopamine transporter ligands, such as ^{123}I-FP-CIT (N-ω-fluoropropyl-2-β-carbomethoxy-3β-(4-[123I]iodophenyl) nortropane), Iodine-123 (^{123}I) Ioflupane (DaTSCAN) is a novel proprietary radiopharmaceutical marketed by GE Healthcare [152]. It becames commercially available following U.S. Food and Drug Administration (FDA) approval in June 2011. Prior to release in the United States, DaTSCAN had been widely used in Europe with over 100,000 recorded procedures since 2002. It is a useful tool in clinical practice to confirm diagnosis of PD and to differentiate from other diseases [107, 149, 153]. Indeed this radioligand has a high binding affinity for DaTs, particularly in the striatal regions of the brain (*putamen* and *caudate* nucleus) [117, 154, 155].

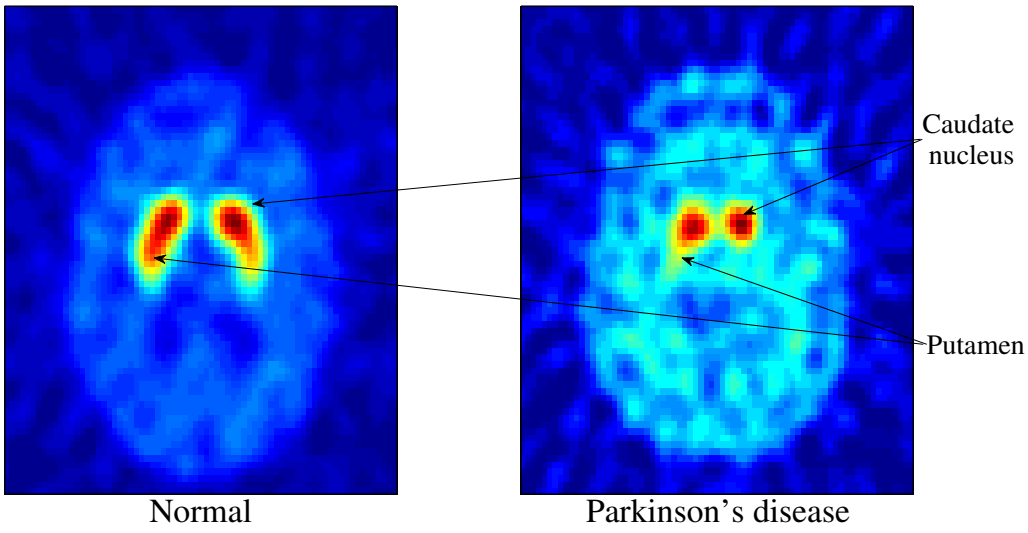

Figure 2.5: DaTSCAN measures presynaptic dopamine transporters in the nerve terminals. In a normal scan the striatum is clearly visible as symmetric, comma-shaped regions, with both the caudate and putamen showing a high intensity compared to the background. However, there is a loss of DaTs signal in PD.

In Figure 2.5, DaTSCAN shows the loss of DaTs signal in PD compared to normal subject where the striatal binding of [^{123}I]FP-CIT is symmetrical and clearly visible in both the caudate nucleus and putamen. In early PD, there is usually an asymmetrical pattern of reduced DaT binding starting in the dorsal putamen contralateral to the clinically most symptomatic body side, gradually progressing anteriorly and ipsilaterally as the disease becomes more severe.
Moreover, DaTSCAN may be used to help differentiate Essential Tremor (ET) from

tremor due to PS (idiopathic PD, MSA and PSP) [155, 156]. However, imaging with this dopaminergic marker will not reliably differentiate between PD and other neurodegenerative brain diseases such as MSA or PSP [157]. In addition, (^{123}I)Ioflupane should be used selectively for patients whose diagnosis is uncertain and for whom the result of a DaTSCAN image would make a difference [158]. While it may be helpful to exclude patients without dopamine deficiency from clinical trials, the diagnosis of PD remains predominantly clinical, and the role of molecular imaging is limited and not without controversy [159, 160].
The DaTSCAN SPECT is a nuclear medical imaging technique used for the estimation of *dopaminergic* reabsorption within the human brain to assist in the evaluation of patients with suspected PS. In cases of uncertain PS, a DaTSCAN image can help clinicians choose among medications that are most likely to provide benefit and avoid those that will not. (^{123}I)Ioflupane may be an economically advantageous diagnostic tool, avoiding costs related to inappropriate treatment of non-PD cases with expensive and unnecessary visits by medical personnel, and conversely avoiding the costs of cumulative disability related to a missed diagnosis of PD, thereby lowering the total cost of care of these patients to health economies [158].
DaTSCAN SPECT maintains all the main characteristics of SPECT described in section 2.1, using gamma cameras for detecting radioactivity level, but its application is only concerned with brain analysis, for investigating on the dopaminergic system. The scan involves injection of an intravenous radio-labelled ligand of the presynaptic DaTS, to be traced by a gamma camera for evaluating the amount of DaTs of the brain striatum.

2.7.2 DMFP PET imaging

As mentioned previously, the diagnosis of PD may be challenging for the treating physician, particularly in the early stages of disease. To aid in the differential diagnosis of PD and related Parkinsonian disorders versus, for example, ET, a presynaptic dopaminergic SPECT tracer such as ^{123} I-labelled ioflupane FP-CIT, occupying the presynaptic dopaminergic transporter, is commonly used. On the other hand, for the differential diagnosis between idiopathic parkinsonian syndrome (IPS, PD) and atypical parkinsonian syndromes (APS), such as PSP or MSA, a SPECT postsynaptic D_2 dopaminergic receptor ligand such as ^{123} I-labelled iodobenzamide (IBZM) is normally proposed [127]. Recently, some works have successfully used the radiotracer ^{18}F-Desmethoxyfallypride (DMFP) to analyze the dopamine $D_{2/3}$ receptors and it was found that this tracer is suitable to differentiate between idiopathic and non-idiopathic PS [88, 138].
In Figure 2.6, two transverse images of the striatal dopamine $D_{2/3}$ receptor binding of ^{18} F-DMFP in single representative patients with non-IPS (Right scan) and IPS (Left scan) are shown. The left-hand image shows an IPS patient with clinically left-

dominant tremor, there is slight (compensatory) increase in striatal tracer uptake, which is dominant in the right striatum. The right-hand image depicted a patient suffering from APS with clinically left-dominant tremor. The striatal tracer uptake is considerably decreased, with the lowest uptake in the left striatum. Decreased $D_{2/3}$ receptor binding, which was predominant in dorsal part of striatum, is shown in non-IPS, whereas increased $D_{2/3}$ receptor binding mainly in posterior putamen could be discerned even visually (left image). Thus, the pathologic imaging results reflect degeneration of postsynaptic fibers of the dopaminergic system within the striatum. Note that presynaptic imaging alone would not distinguish between PD and APS. Only at the postsynaptic level is there a marked difference between PD (no neurodegeneration) and APS (neurodegeneration).

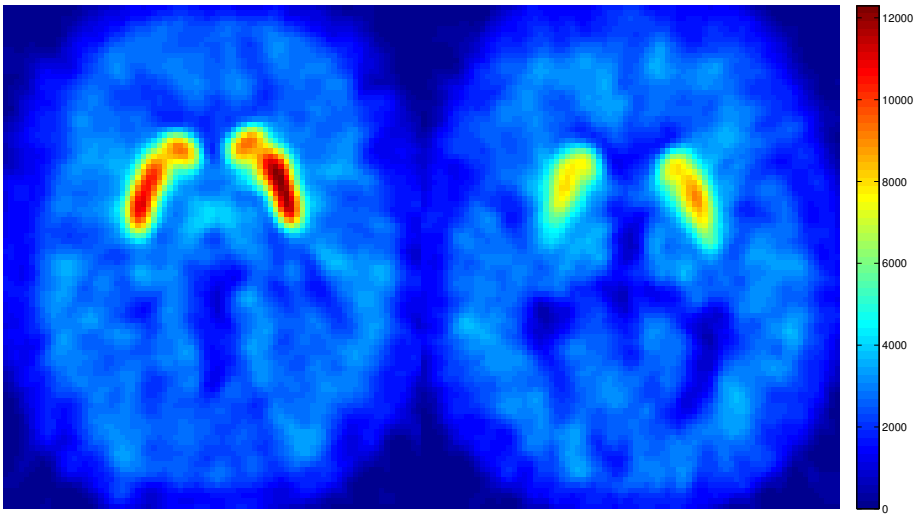

Figure 2.6: Striatal dopamine $D_{2/3}$ receptor binding of ^{18}F-DMFP in patients with IPS and APS.

First human investigations on the developed ^{18}F-fluorinated benzamide ^{18} F-desmeth-oxyfallypride [((S)-N[(1-allyl)-2-pyrrolidinyl)methyl]-5-[(3-^{18}F-fluoropropyl)-2-meth-oxybenzamide: [^{18}F]DMFP demonstrated that ^{18} F-DMFP is a highly reliable tracer for the PET imaging of dopamine D_2-like receptors, showing a comparable receptor affinity and very similar selectivity to ^{11}C-raclopride [161]. ^{11}C-raclopride is another $D_{2/3}$ receptor radiotracer. ^{18}F-DMFP presents the advantage of being labeled with fluorine-18 and therefore does not require an on-site cyclotron [162]. Moreover, this tracer compared with ^{11}C-labeled ligands, lends itself to more routine clinical use while bringing the benefits of persistently high specific activity. The benzamide antagonist ^{18}F-Desmethoxyfallypride was found to be a sensitive

agent for the differential diagnosis of patients with parkinsonism, showing high specificity and positive predictive values for the differential diagnosis of IPS and non-IPS (APS) [161], albeit in a relatively small group. Thus, [^{18}F]DMFP PET is a valuable tool for postsynaptic $D_{2/3}$ receptor quantification, differential diagnosis of idiopathic Parkinson's disease and atypical parkinsonism and can provide valuable information in unclear cases.
Whereas recent studies [88, 138] confirm the high sensitivity and specificity of [^{18}F]DMFP, but further clinical investigation will be needed, including larger patient groups and anatomopathological confirmation of the diagnostic of patients.

2.8 Conclusion

In this chapter, an overview of the SPECT and PET image formation process is given. This chapter aims to give a reader that is unfamiliar with these imaging modalities, some basic notions about these kinds of medical images and what they represent. An understanding of the image formation process is necessary in order to understand what SPECT and PET images show. The dopaminergic system plays a major role in neurological disorders, such as PD. An important neuropathological characteristic of PD is a severe loss of nigrostriatal dopamine neurons and consequently a decrease of striatal DaTs. To investigate pre- and postsynaptic function, SPECT and PET tracers, such as, [^{123}I]FP-CIT (DaTSCAN) and ^{18}F-Desmethoxyfallypride (DMFP) have been developed to measure dopamine synthesis and transport for the PS diagnosis purpose. Contrary to usual image processing problems, the resulting images are difficult to interpret. This is due to the low spatial resolution of these kind of images and because their interpretation necessitates additional expert knowledge. Furthermore, because image intensities observed in a SPECT or in PET image are not quantitative, the issue of image intensity normalization is particularly delicate. The information contained in the superimposition of two images (spatial normalization) can be used with advantage to improve such normalization as explained in the following chapter where this issue is also further discussed.

Chapter 3

Pre-processing

Recent advances in medical imaging have made possible to obtain three-dimensional (3-D) anatomical and metabolic information about the internal structure of the human body. Different medical imaging modalities provide specific information about human brain physiology and physiological processes that is often complementary in diagnosis. The complexity of brain structures and the differences between brains of different subjects make necessary the normalization of the images with respect to a common template. Thus, before being used in a statistical analysis, tomographic images must follow a process known as preprocessing ensuring that the images are comparable. This process should include both spatial and intensity normalizations, although sometimes entails more tasks, such as, skull removal, smoothing, tissue segmentation, motion correction, etc.

3.1 Spatial Normalization

To better understand physiological processes, images obtained from different modalities need to be registered [163]. For instance, anatomical images of the brain obtained from magnetic resonance imaging (MRI) modality need to be coregistered to metabolic images of the same patient obtained by positron emission tomography (PET) imaging modality in order to analyze the metabolism within the anatomical volume of a tumor. Through the comparative quantitative and qualitative analyses of anatomical and metabolic volumes of the tumor from the registered images acquired during the treatment, the response of the treatment can be evaluated. Analysis of registered 3-D multimodal images from a control group of subjects allows the study of variance of specific features for better diagnosis, the understanding of pathology, and therapeutic intervention protocols.

To make meaningful comparisons between images from different brains, extrinsic differences (position and orientation) must be removed and intrinsic differences (size and shape) minimized. A transformation process called spatial normalization (SN) [164] or *intersubject registration* is used to account for these differences by matching a set of brain features derived from a standard brain into a common space for analysis [165]. Brain position, orientation, and size provide the minimal set of global spatial features for SN in 3-D. The low resolution and the intersubject variability between [^{123}I]FP-CIT SPECT images renders them very difficult to register. For this reason, some published works performed the SN assisted by the existence of a high resolution MRI for each subject under study [166]. This strategy is the most accurate because of the high spatial resolution of anatomic images but requires the acquisition of an MRI scan for each individual undergoing DaTSCAN SPECT. Moreover, it requires an accurate registration of the DaTSCAN image onto the individual magnetic resonance (MR) image. These constraints make such an approach difficult to implement in clinical routine [167]. In the studies of this thesis, all the DaTSCAN SPECT and DMFP PET images were spatially normalized using the Statistical Parametric Mapping (SPM) 8 software [168] yielding a $73 \times 73 \times 45$ and a $79 \times 95 \times 68$ three-dimensional functional activity map for each subject. This method assumes a general affine model with 12 parameters (3 translations, 3 rotations (rigid-body), 3 shears and 3 zooms, as shown in Figure 3.1) and a Bayesian framework that maximizes the product of the prior function (which is based on the probability of obtaining a particular set of zooms and shears) and the likelihood function, derived from the residual squared difference between the template and the processed image [169]:

$$\text{CF} = \sum_i (I(\mathbf{M}\mathbf{x}_i) - \bar{I}(\mathbf{x}_i))^2, \tag{3.1}$$

where I denotes the source image and $\bar{I}$ is the template. For each voxel $\mathbf{x} = (x_1, x_2, x_3)$ in an image, the affine transformation into the coordinates $\mathbf{y} = (y_1, y_2, y_3)$ is expressed by a matrix multiplication $\mathbf{y} = \mathbf{M}\mathbf{x}$.

$$\begin{pmatrix} y_1 \\ y_2 \\ y_3 \\ 1 \end{pmatrix} = \begin{pmatrix} m_{11} & m_{12} & m_{13} & m_{14} \\ m_{21} & m_{22} & m_{23} & m_{24} \\ m_{31} & m_{32} & m_{33} & m_{34} \\ 0 & 0 & 0 & 1 \end{pmatrix} \begin{pmatrix} x_1 \\ x_2 \\ x_3 \\ 1 \end{pmatrix}. \tag{3.2}$$

After the affine normalization, a more complex non-rigid spatial transformation model is used to register the resulting image. The deformations are parameterized by a linear combination of the lowest-frequency components of the three-dimensional cosine transform bases [170]. A small-deformation approach is used and regularization is achieved by the bending energy of the displacement field.

The template $\bar{I}$ is computed by registering all control subject images to a randomly chosen one of them by affine transformations, as shown in eq. 3.2. The

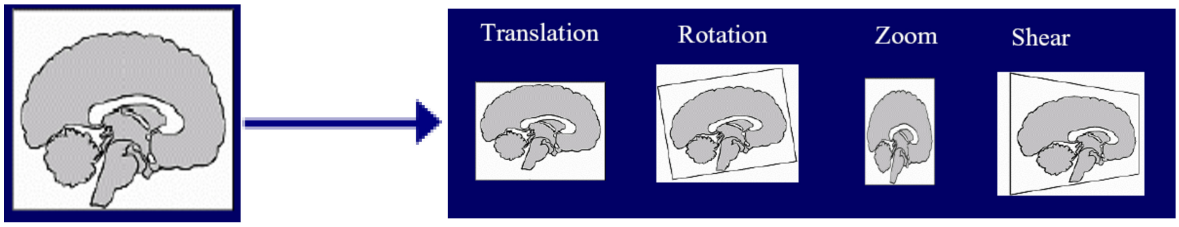

Figure 3.1: The SPM normalization procedure to match the size and position of the images.

registered images and their hemisphere midplane reflections are averaged to create the template [167], providing a symmetric image, as shown in the Figure 3.2.

$$\bar{I} = \frac{1}{N_c} \sum_{i \in X_c} (I_i(x,y,z) + I_i(-x,y,z)) \tag{3.3}$$

where X_c denotes the subset of control images, N_c the number of control images, $I_i(x,y,z)$ is the ith image and $I_i(-x,y,z)$ is its reflected image in the $x = 0$ hemisphere midplane.

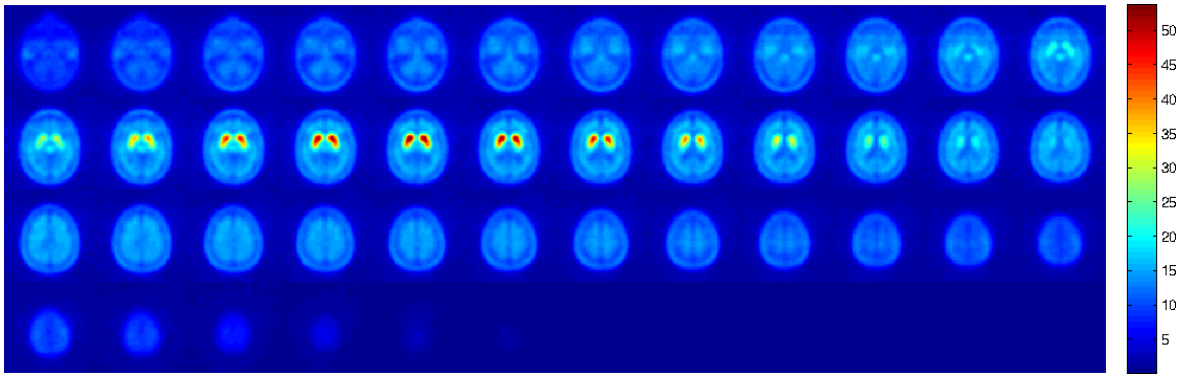

Figure 3.2: Template image generated by averaging the control subjects and symmetrizing them for DaTSCAN SPECT data.

The main reasons for building the template $\bar{I}$ by a simple averaging process of co-registered images from healthy patients [19, 171], as shown in Figure 3.3, are that DaTSCAN SPECT images provide low resolution smoothed functional maps about the uptake in the striatum area with limited morphological information. In addition, intensity normalization is aimed to correct inter-subject variability in the intensity level of the image due to a variety of reasons related to the acquisition process. Thus, high resolution morphological information is not required by intensity normalization since the algorithms are often based on descriptive statistics related to the specific and/or non-specific areas to correct global variations of the intensity. However, there are many developed methods to build the template for MRI where

the morphological changes in tissues are important for most of the applications, such as the mean shape method [172, 173].

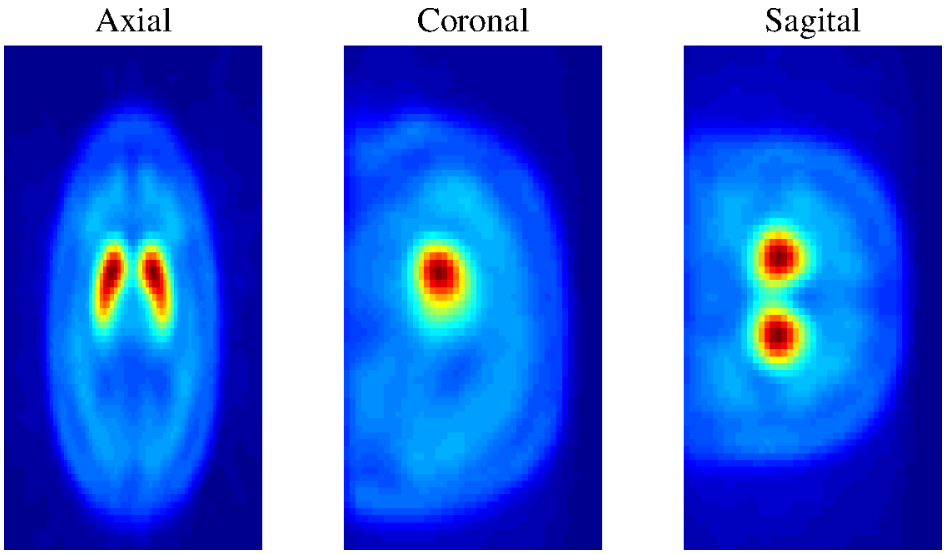

Figure 3.3: The computed template used in the intensity normalization process for DaTSCAN images.

This SN ensures that any given voxel in different images refers to the same anatomical position across the brains. This step allows us to compare the voxel intensities of the brain images of different subjects.

3.2 Intensity Normalization

Intensity normalization takes a very significant role in quantitative SPECT imaging. In order to compare the functional activity distribution between subjects or scans, the observed counts must signify absolute measures of this activity. Reporting absolute values of the regional cerebral blood flow (rCBF) also makes it possible to compare values across imaging centers. The problem of obtaining quantitative measures in emission tomography is a subject of active research.
The standard method for analyzing SPECT images is the calculation of the binding potential (BP) in the striatum. BP is a quantitative measure of specific tracer binding, and is lower in PD patients as compared to healthy subjects [153, 154]. Accurate estimation of BP can be obtained by kinetic analysis of dynamic SPECT studies [174]. Alternatively, a simplified, although somewhat biased, estimate can be obtained from a static SPECT study [175], performed after a state of pseudo-equilibrium in the tracer uptake has been reached. This specific-to-non-specific

binding ratio can then be estimated as [176]:

$$BR = \frac{C_{VOI} - C_N}{C_N} = \frac{C_{VOI}}{C_N} - 1 \tag{3.4}$$

where $\mathbf{C}_{VOI}$ is the mean count per voxel in the volume of interest (striatum, putamen or caudate nucleus) and $\mathbf{C}_N$ represents the mean count per voxel in the non-specific binding region (occipital cortex). This binding ratio is widely used in the literature for normalization purpose in different functional brain images [177–179], such as SPECT or PET images. The occipital region was chosen as reference region because of negligible density of DaTs [180]. For this purpose, clinicians often use proprietary software to delimit regions of interest (ROIs) and quantify the radiopharmaceutical uptake [181]. This procedure can be subjective and prone to error, since it relies on gross changes in transporter density throughout the ROIs to allow the differentiation between controls and pathological images. As such, it may not be sensitive to changes in the pattern of distribution that can characterize the progression of the disease [182]. In contrast, some more automatized methods have been proposed which establishes semiquantitative parameters in order to index absolute differences between specific/non-specific uptake in the tomographic examinations [183]. For this purpose, it is necessary that the images are quantitative, in the sense that the image value in each voxel is proportional to the activity concentration.
The quality of acquired images is degraded by both physical factors, such as compton scattering and photon attenuation, and system parameters, such as intrinsic and extrinsic spatial resolution of the gamma camera system. These factors result in blurred and noisy images. Most times, the blurred images present artifacts that may lead to a fault diagnosis. In order to gain a fair diagnostic of the functional brain images for the physician, it is compulsory to follow a specific series of processing, such as, scattering and attenuation correction during the image reconstruction procedure, and preferably also resolution compensation or partial volume correction [184]. In addition, the intensity normalization is a relevant preprocessing step, which guarantees that the differences between images of different subjects are due to physiological reasons and brain functioning, and not due to the baseline calibration of the gamma camera applied for the acquisition [35]. The conventional way of carrying out the intensity normalization is to consider as a reference the brain region which is not significant as a differentiating criterion between, both ill and healthy image subjects. Since the discriminant region for PD is the striatum, the occipital region is usually chosen as a reference because it is devoid of DATs and it is usually selected as the background region. However, in this thesis, the whole brain area is considered, minus the striatum, as a non-specific (NS) region[185, 186]. The main reasons for this choice are that DaTSCAN SPECT images contain considerably fewer anatomic details and omit structural details about the location of the occipital cortex (the normalization region). Furthermore, the partial volume effect causes blurring of counts from the grey matter into the ventricular space, often to such an extent that the ventricles are practically indistinguishable, sometimes making it

difficult to use confidently occipital or frontal cortex regions. The proposed use of the overall non-specific region should reduce variability as well as improve counting statistics [181]. Thus, this image preprocessing stage consists of comparing the uptake value in areas of specific activity (binding to dopaminergic transporters) to the value in areas of non-specific activity (vascular activity) between subjects.

3.3 The state of the art

There are a variety of normalization methods available in the literature for the PD image normalization [187–190]. These approaches are based on general normalization of 3D functional images and may be adapted for the normalization of a particular type of images, such as the SPECT or PET images used in this thesis for PD diagnosis. In this section, we will try to present some conventional intensity normalization methods adequately adapted to the nature of the PD images. In addition, they will be considered for comparison with our proposed approaches.

3.3.1 Specific-to-non-specific binding ratio (BR_{all}-IN):

This normalization approach is based on the computation of the radiopharmaceutical binding ratio (BR) at each voxel between high and low blood flow as a function of the tracer concentration in the blood flow [156, 176] (see eq. 3.4). This BR can be used for the normalization of functional brain images [191]. The normalization process is based on dividing each voxel intensity by the mean intensity value in the so-defined non-specific (NS) region [2]. This region includes a very large intensity range since more structural areas apart of the occipital cortex are considered. Thus, BR_{all} denotes the binding ratio calculated using all the brain voxels except those in the striatum as NS region. The main motivation for this choice is that this region is devoid of dopamine transporter-binding sites. The exact relationship between the specific-to-non-specific ratio and dopamine transporter density can be affected by a number of factors and may not be linear unless the tracer achieves a stable equilibrium during the imaging period [156].
This ratio approach is commonly used to remove the effect of global values in several imaging applications [190]. In addition, it outperforms ANCOVA, z score, residual and subject residual profile approaches [189]. For these reasons, we considered this ratio approach as a baseline for comparison with our proposed approaches. However this normalization method depends on time consuming operator-intensive work and expertise skills in manually placing the regions of interest (ROI). In addition, this approach assumes the tracer concentration in the blood to be stationary over the whole image volume.
Moreover, the size of the volumes of interest, in particular, has a direct impact on

the measurement of count concentration. This is mainly a consequence of the poor spatial resolution of functional imaging, which causes counts to be blurred out of the physical volume of the structure, i.e, partial volume effect [192], and therefore makes it difficult to evaluate count concentrations with accuracy [181].

3.3.2 Integral-based intensity normalization [1](Integral-IN):

Integral-based intensity normalization consists of the computation of an intrinsic parameter from the image, I_p. This normalization is performed by the estimation of the binding activity:

$$\hat{I} = \frac{I}{I_p} \tag{3.5}$$

where I denotes the spatially normalized image, $\hat{I}$ denotes the intensity normalized image and I_p is the integral intensity value. It can be approximated as the sum of all the intensity values of the image, giving an integral value of intensity [19]:

$$I_p = \int I(x,y,z) \approx \sum I(x,y,z) \tag{3.6}$$

Thus I_p can be seen as the mean intensity of the image [1]. The computation of this integral intensity value can be estimated in a particular reference volume in the brain for each 3D brain image. In the particular case of PD, the reference volume has to be properly defined and selected. In this thesis, it is proposed to set the reference region to the complete brain volume without the striatum region, as mentioned above.
Integral-IN preserves absolute differences in the uptake values, producing a similar measure for NS region, and differences in striatal structures with highest intensity counts [1]. This method is inexact and more sensitive to extreme values, for instance subjects with severe loss of dopamine receptors, high intra-subject differences in the binding potential, or outlier characteristics [1].

3.3.3 Intensity normalization by minimizing the Kullback-Leibler divergence (MKL-IN):

The basic idea of the method presented in [193] is to estimate a multiplicative correction field in order to match a template histogram to a reference model density. The observed image I can be expressed as:

$$I = F\hat{I} + n \tag{3.7}$$

where F is a multiplicative intensity corruption field, n is the additional acquisition noise and $\hat{I}$ is the desired correct image. After neglecting n for having only little influence on the problem of intensity normalization and solving the eq. 3.7 for $\hat{I}$, the uncorrupted image is obtained as $\hat{I} \approx F^{-1}I$. The intensity adjustment parameter F^{-1} has to be chosen in a way that the Kullback-Leibler (KL) divergence [194] between the adjusted source and target data sets is minimized. The Simultaneous Perturbation Stochastic Approximation (SPSA) is used to generate the gradient estimate and then to adjust the current solution estimate according to the gradient estimate, as shown in Appendix A.2. This approach have the following advantages [193]: i) It can be matched to a supplied histogram model which can be generated by any representative subject. This allows to proceed without assumptions about the shape of the histogram or the specific contribution of a given class of tissue. ii) Since it can be solved for a spatially varying normalization field, it is not necessary to involve a separate step for field inhomogeneity correction. However, taking into account the computational load, this normalization scheme is more demanding, as it is based on an iterative algorithm (SPSA) and it needs the optimization of many parameters, such as, the gain sequences, the maximum number of iterations, the initial intensity adjustment parameter, etc. In addition, it is necessarily constrain the estimates of F^{-1} to be of low spatial frequency. This provides a solution that improves the clustering of global image statistics while preserving the local contrast that defines the anatomical boundaries of interest.

3.3.4 Histogram equalization (Hist-eq-IN)

Histogram modeling techniques, i.e., histogram equalization provide a sophisticated method for modifying the dynamic range and contrast of an image by altering each individual voxel such that its intensity histogram assumes a desired shape [195]. A monotonic, non-linear mapping is employed by histogram equalization approach which re-assigns the intensity values of voxels in the input image such that the output image contains an uniform distribution of intensities [196]. Through this adjustment, this method is used in image comparison processes (because it is effective in detail enhancement) and in the correction of non-linear effects introduced by a digitizer or display system [197]. The gray levels in an image may be viewed as random variables in the interval [0, 1]. One of the most fundamental descriptors of a random variable is its probability density function (PDF).
Suppose that the desired or specified normalized histogram is $p_d(t)$, with the desired image being represented as d, having the normalized gray level $t = 0, 1, 2, ..., L-1$. Now, the given image f with the PDF $p_f(r)$ may be histogram-equalized by the transformation:

$$C_1(r) = \int_0^r p_f(w)dw \quad 0 \leqslant r \leqslant 1 \tag{3.8}$$

where C_1 is the cumulative sum of the image f for all intensities r, r is the gray levels of the image to be enhanced and w is a dummy variable of integration [198]. The histogram-equalizing transform for the desired image may be also driven as:

$$C_2(t) = \int_0^t p_d(w)dw \quad 0 \leqslant t \leqslant 1 \tag{3.9}$$

where C_2 is the cumulative histogram of the reference image.
For discrete values we deal with probabilities and summations instead of probability density functions and integrals. The probability of occurrence of gray level r_k in an image is approximated by:

$$p_f(r_k) = \frac{n_k}{n} \quad k = 0, 1, 2, ..., L-1 \tag{3.10}$$

where n is the total number of voxels in the image, n_k is the number of voxels that have gray level r_k, and L is the total number of possible gray levels in the image. The discrete version of the transformation function given in eq.3.8 is

$$C_1(r_k) = \sum_{j=0}^{k} p_f(r_j) = \sum_{j=0}^{k} \frac{n_j}{n} \quad k = 0, 1, 2, ..., L-1 \tag{3.11}$$

Thus, a processed (output) image is obtained by mapping each voxel with level r_k in the input image into a corresponding voxel with level $C_1(r_k)$ in the output image via eq. 3.11.
Mathematically, when a desired histogram is supplied, histogram equalization consists of choosing the grayscale transformation $\mathbf{T}$ to minimize

$$\| C_1(\mathbf{T}(t)) - C_2(t) \| \tag{3.12}$$

This minimization is subject to the constraints that $\mathbf{T}$ must be monotonic and $C_1(\mathbf{T}(a))$ cannot overshoot $C_2(a)$ by more than half the distance between the histogram counts at a given intensity value a [106]. Then, the transformation $\mathbf{T}$ will be used to map the gray levels in the image f (or the colormap) to their new values.
This non-linear normalization approach is performed for IN of functional imaging, such as, SPECT and PET imaging as follows:

- Firstly, a mask is applied in the source images in order to consider only those voxels with intensity values greater than a given threshold. This step is done to discard those image voxels that are outside of the brain.
- Secondly, the histogram of the template image is calculated.
- Finally, the histogram matching is performed and the intensity values in the source images are adjusted to the intensity values of the reference template.

The histogram equalization approach appears robust and versatile in many previous work, such as in [190]. For this reason, we will used it for comparison with our proposed approaches. In addition, we will try to implement it at a first stage on the whole image and at the second stage on the NS region. This could avoid its effect on the striatum, as it is a nonlinear normalization method.

3.3.5 Normalization to the maximum intensity values [1] (Max-IN):

This normalization method is applied individually for each scan of subject by referring each voxel to the average value of the highest intensity voxels set in [%]. Thus, the statistical comparison among different scan subjects could be permitted [186]. Moreover, this approach aims to extend the size of discriminative regions by interchanging the roles of specific/nonspecific areas of functional activity distribution between subjects [1]. This normalization approach may introduce problems in some images which can have peak intensity values due to noise [186]. These normalization errors can be removed when the intensity normalization is referred to a voxel set with the highest intensity values. The number of voxels usually considered for this intensity normalization are around 0.1% voxels [1]. Taking into account the lower intensity levels, i.e., lower activation in the case of PD patients compared to healthy subjects, this normalization method is prone to error. Furthermore, in normalization to the maximum scheme, the striatal tracer uptake is matched for all subjects, including patients and normal controls. This could lose the relation between the loss of dopamine receptors and decreased count numbers. Thus, in terms of absolute uptake values, the interpretation is lost [1].

3.3.6 The α-stable distribution-based intensity normalization [2] (α-stable-IN):

The α-stable distribution can be used for the adjustment of the functional images, such in [2, 186]. If the intensity distribution of the images without the striatum region is analyzed, a unimodal, heavy-tailed and skewed distribution is obtained, with different variance and mean values. These intensity distributions can follow an α-stable distribution [2].
The α-stable distribution is represented by the following equation [186, 199]:

$$f_{\alpha,\beta}(y|\gamma,\mu) = \frac{1}{\pi}\Re\left[\int_0^{\inf} e^{jt(y-\mu)}e^{(-\gamma t)^{\alpha}(1-j\beta\tan(\frac{\pi\alpha}{2}))}dt\right] \tag{3.13}$$

Thus, the α-stable probability density function $f_{\alpha,\beta}(y|\gamma,\mu)$ has four parameters: $\alpha \in (0,2]$ is the characteristic exponent which sets the level of impulsiveness, e.g

the "tail" of the distribution, $\beta \in [-1,+1]$ is the skewness parameter, ($\beta = 0$, for symmetric distributions and $\beta = \pm 1$ for the positive/negative stable family respectively), $\gamma > 0$ is called the scale or the dispersion parameter, and μ is the location parameter.

Figure 3.4 gives a visual impression of different parameter values. The distribution with parameters $\alpha = 1.5$, $\beta = 0$, $\gamma = 1$ and $\mu = 0$ is used as reference [2]. This figure also explain the name of the parameters: α controls the degree of impulsiveness; when α decreases, the degree of impulsiveness increases and vice versa. β controls the skewness and its sign, if the asymmetry is on the left or the right. γ controls the concentration of the samples along the bulk of the distribution: lower values of γ correspond with higher concentration of the samples. Lastly, different values of μ produce the similar probability density functions but shifted in the x-axis.

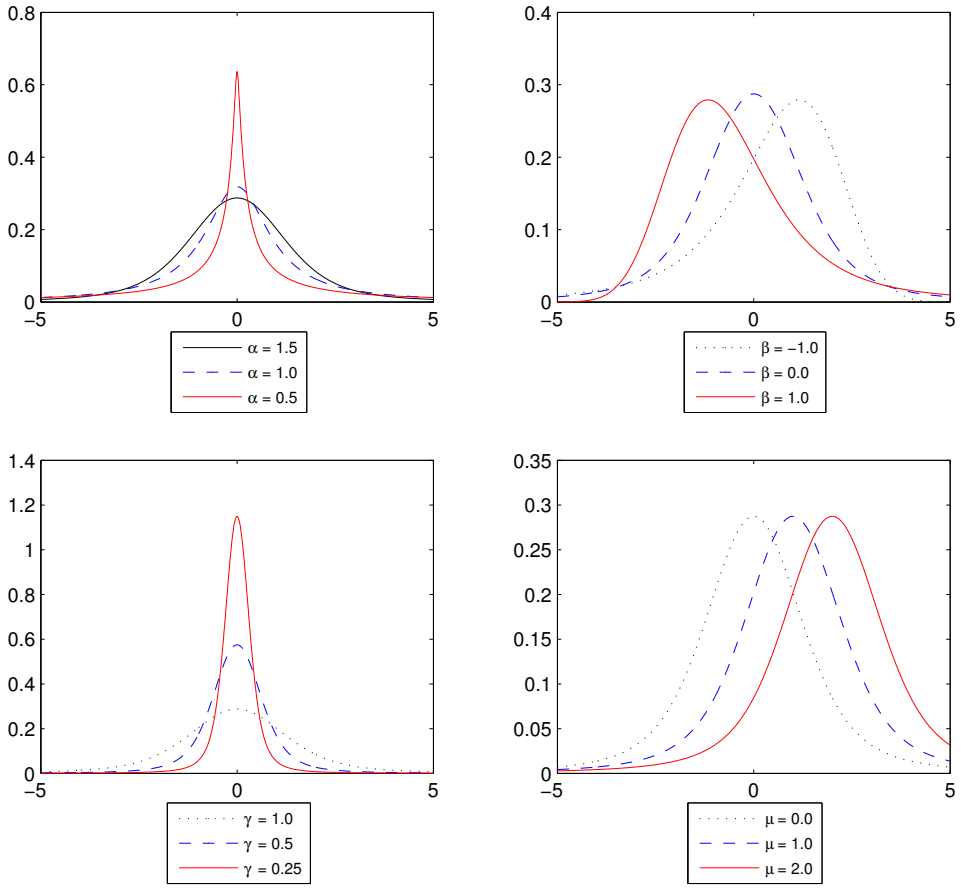

Figure 3.4: The α-stable probability density function with reference parameters $\{\alpha, \beta, \gamma, \mu\}$=$\{1.5, 0, 1, 0\}$ with changing: (a) Characteristic exponent α. (b) Skewness parameter β. (c) Dispersion γ. (d) Location parameter μ.

The intensity normalization using the α-stable is performed by transforming the vector histogram of intensity data with α-stable distribution with parameters $I \sim f_{\alpha,\beta}(y|\gamma,\mu)$ to another α-stable distribution with distribution $\hat{I} \sim f_{\alpha,\beta}(y|\gamma^*,\mu^*)$ by using the following expression

$$\hat{I} = aI + b \tag{3.14}$$

where $a = \frac{\gamma^*}{\gamma}$ and $b = \mu^* - \frac{\gamma^*}{\gamma}\mu$. Thus, the goal in this approach is to transform all the intensity values for different images i with possibly different dispersion γ_i and location μ_i parameters to another α-stable distribution with $\gamma*$ and $\mu*$ parameters using the expression in eq. 3.14 [2].

3.4 Conclusion

Data pre-processing is a very critical step in order to obtain meaningful results. The spatial normalization (registration) of the data volumes is important in order to ensure that each voxel has an equivalent meaning in all volumes. Moreover, the intensity normalization is a relevant preprocessing step, which guarantees that the differences between images of different subjects are due to physiological reasons and brain functioning, and not due to the baseline calibration of the gamma camera applied for the acquisition. Some conventional intensity normalization methods adequately adapted to the nature of the PD images are presented in this chapter. In addition, they will be considered for comparison with our proposed approaches in two different medical imaging modalities.

Chapter 4

DaTSCAN image modeling and filtering based on the Gaussian Mixture Model

The Gaussian Mixture Model (GMM) is widely used approach for regions of interest selection, density estimation and classification [200–202]. Thus, this probabilistic model could be used to describe the intensity profile of the brain image and to enhance the average intensity gap between the specific and the non-specific areas in the sense of increasing the signal-to-noise ratio (SNR) for intensity normalization purposes.

This chapter presents a novel method for intensity normalization of functional brain images based on GMMs. The proposed methodology considers not only the intensity levels, but also the coordinates of voxels inside the so-defined spatial Gaussian functions. The model parameters are obtained according to a maximum likelihood criterion employing the Expectation Maximization (EM) algorithm. First, an averaged control subject image is computed to obtain a threshold-based mask that selects only the voxels inside the skull. Then, the GMM is obtained for the DaTSCAN SPECT database, performing space quantization by populating it with Gaussian kernels whose linear combination approximates the image intensity. According to a probability threshold that measures the weight of each kernel or "cluster" in the striatum area, the voxels in the non-specific region are intensity-normalized by removing clusters whose likelihood is negligible.

The motivations of using this approach are *i)* to perform an automatic intensity normalization of FP-CIT SPECT images using GMM, *ii)* to eliminate operator-dependent manipulations [203] and *iii)* avoid the manual preselection of relevant information by means of statistical analysis [176]. In addition, the GMM has the advantage of simplifying the analytical treatment of the problem. The main novelty with respect to previous approaches, such as in [2] is that the proposed method locally decomposes the image intensity into Gaussians in the spatial domain in order to automati-

cally select ROIs. In this sense, the proposed strategy allows us to *modulate or filter* the voxel intensity in the NS region by discarding the clusters whose probability is below a normalized threshold in the specific region (striatum). We consider these deleted Gaussians as a reference region because almost all of them are located in areas with a low uptake value, i.e. the occipital cortex. Thus, GMM is used as a filtering strategy to remove artifacts and noise [54, 98], preserving the image details after the preprocessing stage.

4.1 Signal model

In general, the uptake value in the NS region should be small. Contrariwise, there is an uptake in this region for reconstructed DaTSCAN images due to an equal supply of tracer from the vascular compartment [156] and to the presence of several noise sources, such as Gaussian noise [92, 204]. The image noise may be divided into random and structured noise. For more details about this physical characteristic that is used to describe the image quality, we want to refer to the chapter 1. In this Thesis, a noise model, very similar to the one proposed in [205], is considered and assumed to be from the scanner itself:

$$I_i = \frac{\mu_{\mathbf{i}}}{\rho_{\mathbf{i}}} + N_i \tag{4.1}$$

where the observed signal (I_i) is supposed to be an un-corrupted signal (μ_i), scaled by some scanner multiplicative bias (ρ_i) with added Gaussian noise (N_i) that is independent of the bias. As a result, the real intensity μ_i for each voxel can be defined as:

$$\mu_i = \rho_i \cdot (I_i - N_i) \tag{4.2}$$

where the multiplicative bias is assumed to be inversely proportional to the mean intensity in the NS region. In the same line of reasoning, almost all the IN methods in DaTSCAN imaging, i.e. the one based on the BR, usually assume the bias to be inversely proportional to the number of count per voxel in the NS region ($\rho_i = \frac{1}{C_{NS}}$) neglecting the independent noise [2, 88]. With this definition, the BR provides the real intensity in each voxel. In this chapter the NS region, that is commonly determined by visual inspection, is automatically selected by some specific clusters, as shown in the following section.

4.2 Gaussian Mixture Models (GMMs)

GMMs are an efficient method for classification and density estimation [200–202]. The basic assumption is that the given data $\mathbf{x}_i$, $i = 1, ..., N_b$ is drawn from a probabil-

ity distribution $p(\mathbf{x})$, which is modeled by a sum of k Gaussian distributions [206]:

$$p(\mathbf{x}) = \sum_{n=1}^{k} \omega_n f_n(\mathbf{x}|\theta_n) \tag{4.3}$$

where $f_n(\mathbf{x}|\theta_n)$ is the density of the n-th Gaussian with parameter vector θ_n and the ω_n are the weight factors or mixing proportions, with $\sum_n \omega_n$=1. The normal distributions $f_n(\mathbf{x}|\theta_n)$ in d dimensions are given by:

$$f_n(\mathbf{x}|\theta_\mathbf{n} \in \{\mu_\mathbf{n}, \Sigma_\mathbf{n}\}) = \frac{1}{\sqrt{(2\pi)^d |\Sigma_\mathbf{n}|}} \times \exp[-\frac{1}{2}(\mathbf{x}-\mu_\mathbf{n})^T {\Sigma_\mathbf{n}}^{-1}(\mathbf{x}-\mu_\mathbf{n})] \tag{4.4}$$

where $\mu_\mathbf{n}$ are the expectation values and $\Sigma_\mathbf{n}$ denote the covariance matrices. Geometrical features of the components can be varied by parameterization of the covariance matrices $\Sigma_\mathbf{n}$ using the eigenvalue decomposition [207]. For our purpose, shape, volume and orientation of the Gaussians are assumed to be variable since the relevant activation areas (ROIs) could be located shapeless and with different sizes across the brain. To estimate the set of mixture parameters, the Maximum Likelihood Estimation (MLE) is usually considered since no other estimation method is asymptotically more efficient [208]. This procedure consists of adapting these parameters in order to maximize the likelihood of a mixture model with k components:

$$\mathcal{L}(\theta|\mathbf{x}) = \prod_{i=1}^{N_b} p(\mathbf{x_i}|\theta) \tag{4.5}$$

where θ=$\{\theta_\mathbf{n}\}$, for $n = 1,...,k$, and $\mathbf{x}$=$\{\mathbf{x_i}\}$, for $i = 1,...,N_b$, which corresponds to the probability to observe the given samples $\mathbf{x_i}$. If independent and identically distributed random variables are assumed [202, 209], the MLE can be used in a modified way, as shown in [210] and in the following section.
Figure 4.1 depicts a visualization of a 2 dimensional Gaussian densities on an artificial data. In this example, we plot 6 Gaussians with different parameters. Their means and covariances are randomly generated.

4.2.1 Spatial GMMs

Recently, GMMs have been successfully applied to the field of functional imaging for voxels of interest (VOI) analysis and image compression [210–212]. The main idea of this method is to assign each spatial coordinate $\mathbf{x_j}$, j=1…N_b, a probability proportionally equal to h_j/I_{tot}, where h_j is the intensity value of $\mathbf{x_j}$, and I_{tot} is the total intensity of the image:

$$I_{tot} = \sum_{j=1}^{N_b} h_j \tag{4.6}$$

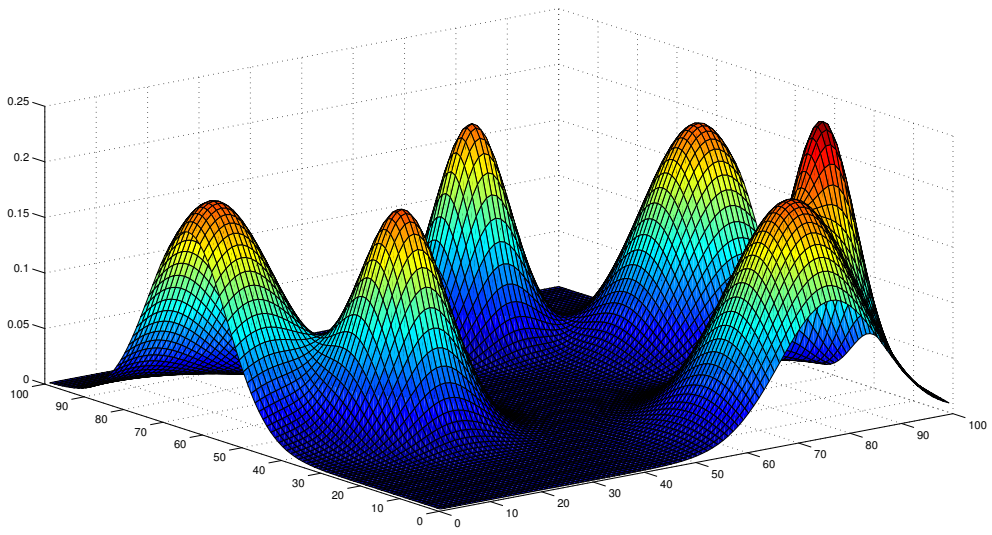

Figure 4.1: The curve of Gaussian sets with a 2-dimensional domain.

Under this assumption, the likelihood can be generalized to:

$$\mathcal{L}(\theta|\mathbf{x}) = \prod_{j=1}^{N_b} [p(\mathbf{x_j}|\theta)]^{h_j} \tag{4.7}$$

Since we have h_j i.i.d observations of data points at $\mathbf{x_j}$. Finally, the complete-data log-likelihood to be minimized using the expectation maximization (EM) algorithm [213, 214] is:

$$\ell(\theta|\mathbf{x}) = \sum_{j=1}^{N_b} \sum_{n=1}^{k} h_j \log(\omega_n f_n(\mathbf{x}|\theta_n)) \tag{4.8}$$

In the presence of hidden data, the MLE can be determined using an EM algorithm which is described in the next section.

4.2.2 The EM algorithm

The EM algorithm is widely used to maximize the likelihood [213, 214] because it is a recursive scheme with interesting monotonic convergence properties. Therefore a suitable initialization is critical in the successful application of EM. In this sense, hierarchical agglomerative clustering can be performed as an initializing step, such as in [215] in order to yield reasonable clusterings in the absence of any information about a possible clustering inherent in the data. For computational reasons, the initialization procedure are adapted to the specific data the method is intended for, as

shown in the following.
It is proved suitable to arrange the k Gaussian centers on a regular grid with $n_x \times n_y \times n_z$ grid points [87]. In order not to "pin" the Gaussian centers at local intensity maxima of the image, it is preferable to initialize the centers at low activation regions and let them evolve freely. Therefore the central subcube is used with $1/3$ of the side length of the whole brain image, where the intensity is fairly low, and distribute the Gaussian centers regularly across this region. The distances between the grid points are $l_i = L_i/(3n_i)$, with $i = x, y, z$ and L_i being the length of the brain image in the direction i. The weights are initialized with $\omega_n = 1/k$, and the covariances are chosen to be diagonal for the first step of the iteration with elements $3l_x, 3l_y$ and $3l_z$. This initialization scheme provides a regular and symmetric setup, where the Gaussians initially cover the whole central cube of the brain image and are strongly overlapping.
In Figure 4.2, the initialization of the different parameters for the EM algorithm is illustrated when using an artificial data. The initial position of the clusters are arranged on a regular grid with 11×11 grid points. This matrix represents the initial position of the clusters. Then, the MLE algorithm will change the initial positions according to the simulated data that we want to model using a GMM ($k = 121$). The covariances are chosen to be diagonal for the first step of the iteration with elements $3l_x$ and $3l_y$.

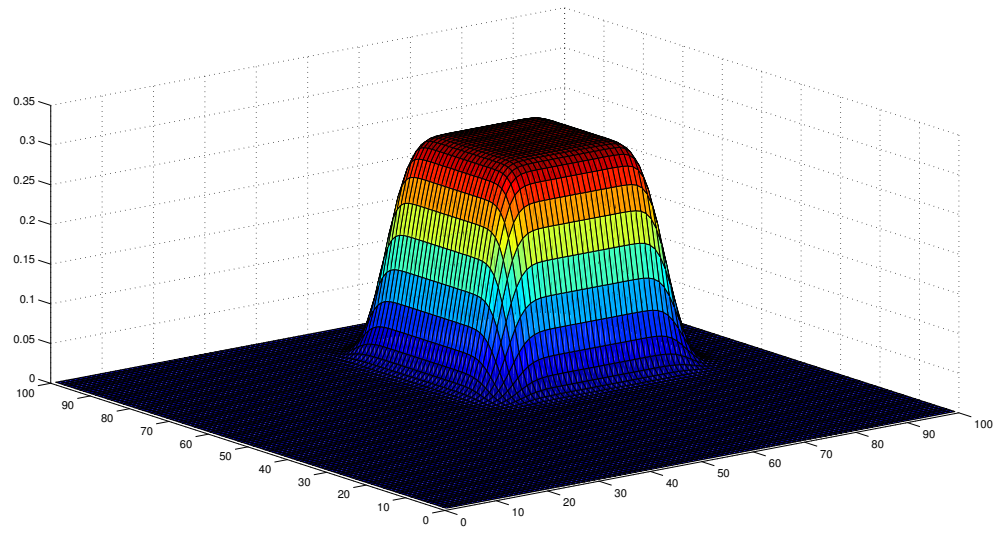

Figure 4.2: The initialization of the different parameters of the EM algorithm for a simulated data.

Along the same lines as shown for instance in reference [200] and using the

novel log-likelihood as shown in equation (4.8), we can write down the equations to update the unknown parameters ω_n, μ_n and Σ_n, where the relations are only modified by a weight factor h_j:

$$\omega_n = \frac{1}{I_{tot}} \sum_{j=1}^{N_b} h_j q_n(\mathbf{x_j}) \tag{4.9}$$

$$\mu_\mathbf{n} = \frac{1}{\omega_n I_{tot}} \sum_{j=1}^{N_b} h_j q_n(\mathbf{x_j}) \mathbf{x_j} \tag{4.10}$$

$$\Sigma_\mathbf{n} = \frac{1}{\omega_n I_{tot}} \sum_{j=1}^{N_b} h_j q_n(\mathbf{x_j})(\mathbf{x_j} - \mu_\mathbf{n})(\mathbf{x_j} - \mu_\mathbf{n})^T \tag{4.11}$$

The posterior probability $q_n(\mathbf{x})$ for a data point to belong to a specific component or cluster, entering the above equations is defined by:

$$q_n(\mathbf{x}) = \frac{\omega_n f_n(\mathbf{x})}{p(\mathbf{x})} \tag{4.12}$$

Starting with an initial guess for ω_n, μ_n and Σ_n we can recursively apply equations (4.9), (4.10) and (4.11) until convergence is reached, that is, the changes in the log-likelihood are smaller than a given threshold. Thus, The EM algorithm terminates after the difference between successive values of ℓ falls below some threshold. In the proposed GMM based method, this threshold was set to 0.00001.
In Figure 4.3, the convergence of the GMM algorithm is illustrated when it is applied to a 2D simulated data.

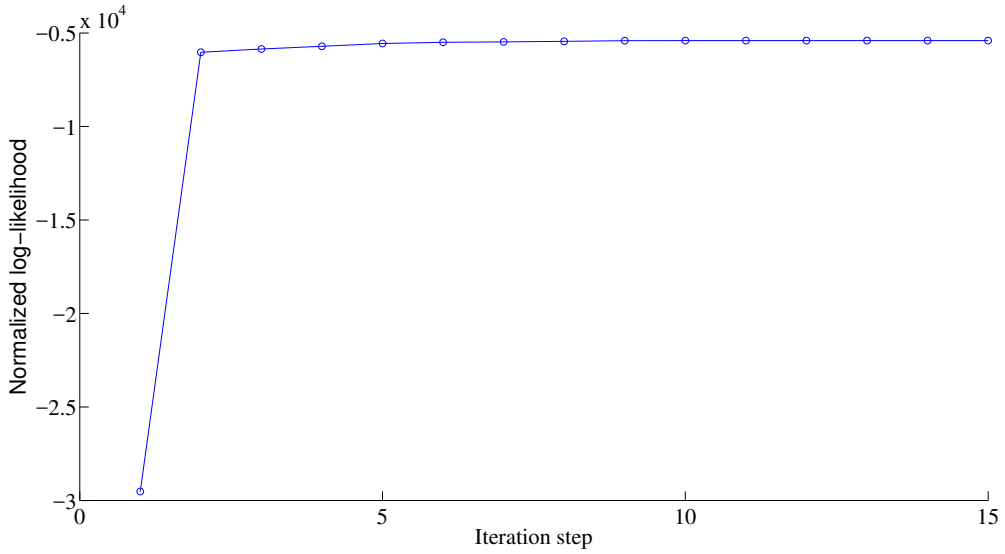

Figure 4.3: Convergence of the GMM algorithm for a simulated data. The circles represent the individual values of the log-likelihood.

Figure 4.4 depicts the location of 6 Gaussians in the resulting image after the EM convergence. In this Figure, the reconstructed image approximates the simulated data when using a number of Gaussian equal to 121 in the EM algorithm.

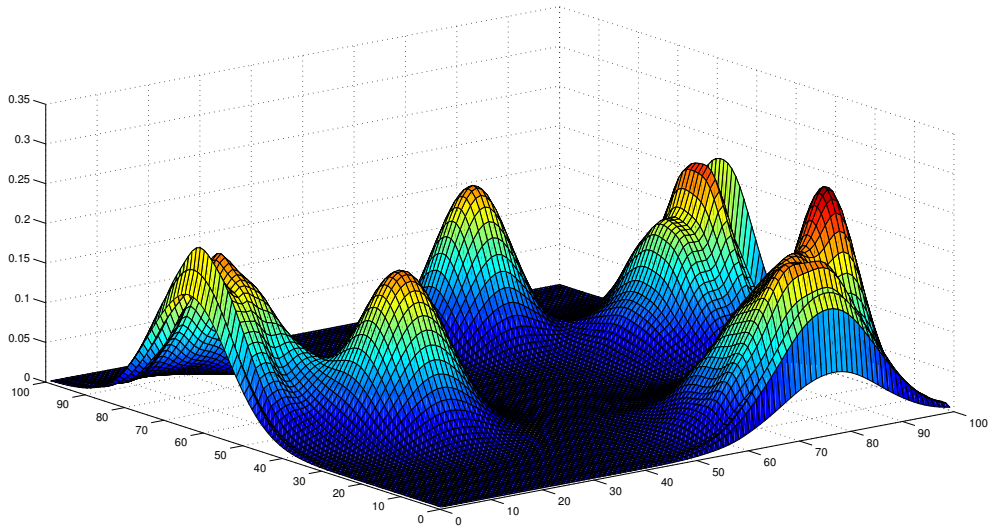

Figure 4.4: The reconstructed image from the obtained Gaussians according to eqs (4.3).

4.2.3 Model selection

In [216], the authors claimed that a key question for the GMM approach is the number of Gaussians used for modeling ROIs (parameter k in (4.3)). Several methods have been proposed to solve model selection problems, i.e. the Bayesian Information Criterion (BIC) [217] and the Akaike Information Criterion (AIC) [218], which suggest generally comparable results [219]. However the most used one is to apply several models with different pre-defined numbers of components and subsequently choose the best model according to some model selection criterion (computational requirements, required dimensionality reduction, dimension of the feature vector comparable to the number of scans, precision in defining ROIs, etc.) [201]. In this sense, our target is to model the spatial *independent sources* of any particular image [220], including those related to noise and artifacts, that perfectly reconstruct the global intensity of the raw image. This issue is major since there is a trade-off between reconstruction error and computational time. The reconstruction error, E_{rec},

has been estimated as:

$$E_{rec} = \frac{\sqrt{\frac{\sum_{i=1}^{N_b}(\mathbf{I}_i - \mathbf{I}_i^{rec})^2}{N_b}}}{I_{max}} \tag{4.13}$$

where $\mathbf{I}_i$ and $\mathbf{I}_i^{rec}$ are the intensities of i-th voxel of the original image and the reconstructed image, respectively, N_b is the number of voxels and I_{max} is the maximum intensity.
In Figure 4.5 the reconstruction error tends to stabilize when the number of Gaussians increases. Moreover, if k is large, the model will represent the image very well as the reconstruction error decreases. Thus, it can be satisfactorily reconstructed from the Gaussians, as illustrated in Figure 4.4. However, a large number of Gaussians will vastly increase the computational cost [221].

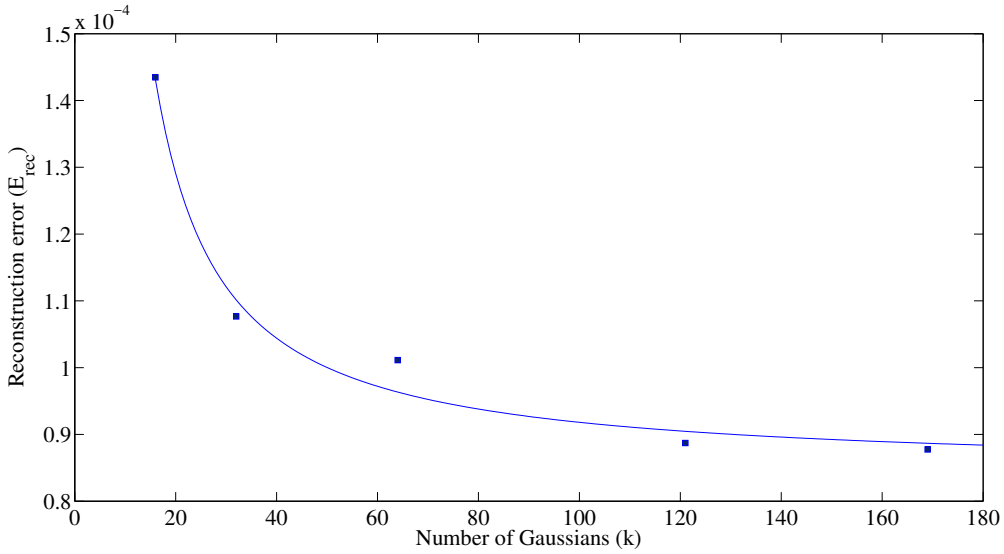

Figure 4.5: Reconstruction error of a 2D simulated data vs the number of Gaussians used in the model.

4.2.4 Density estimation of the intensity profile

Once the model parameters $\{\omega_n, \theta_n\}$ are determined, the intensity of each voxel at $\mathbf{x}$ can be recovered by:

$$I_{Gauss}(\mathbf{x}) = I_{tot} \cdot p(\mathbf{x}) = I_{tot} \cdot \sum_{n=1}^{k} \omega_n f_n(\mathbf{x}|\theta_\mathbf{n}) \tag{4.14}$$

Thus, the reconstructed images approximate the original images by conserving the total intensity through the superposition of k Gaussians. In Figure 4.6, the effect of

this modeling process is shown. The GMM method performs a space quantization of each image by populating it with Gaussian kernels whose linear combination approximates the image intensity. In principle, a histogram bin is associated to each voxel coordinate $\mathbf{x_j}$ of the DaTSCAN image, such that its intensity $I(\mathbf{x_j})$ corresponds to the histogram height h_j.

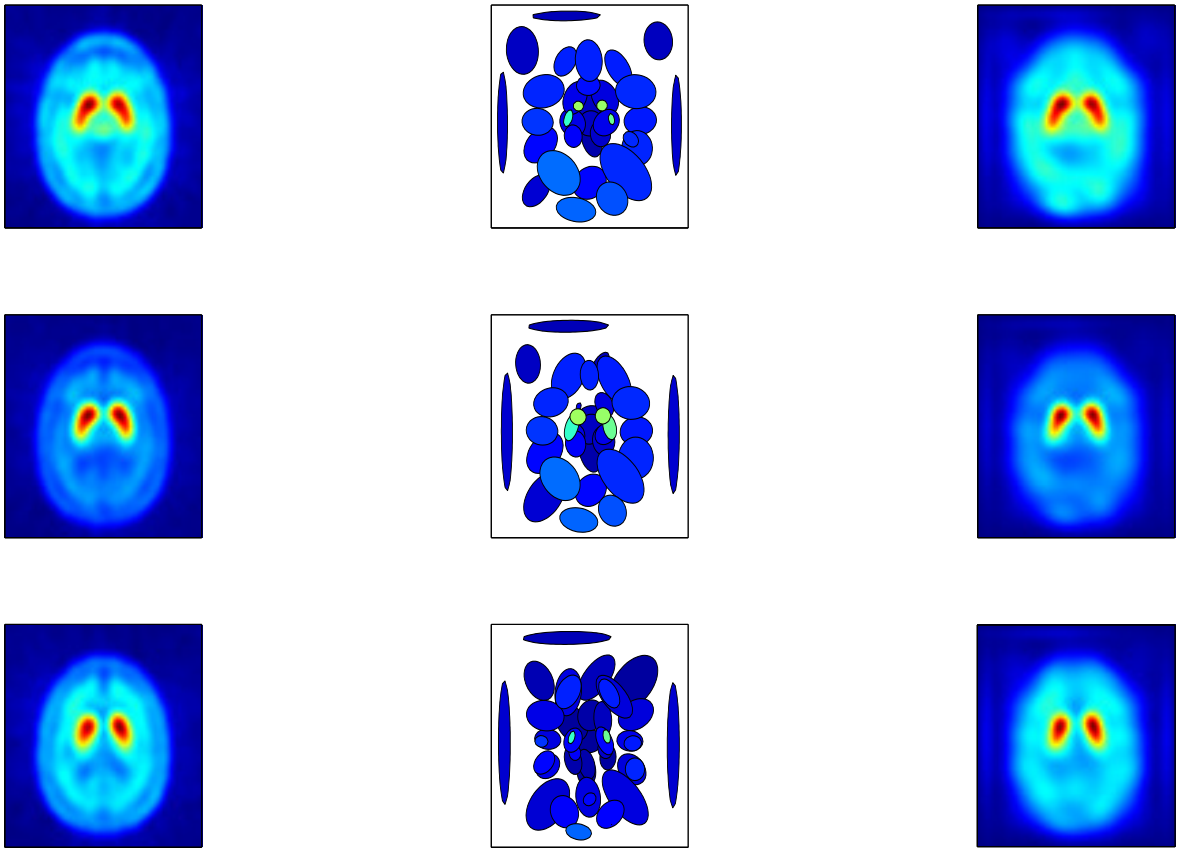

Figure 4.6: Left column: different slices of DaTSCAN image of an average normal subject. Central column: different location and intensity of the clusters with probability values larger than 50% of the total height (colors indicate intensity). Right column: reconstructed image from the obtained Gaussians according to eqs (4.3) and (4.14).

4.3 GMM-based image filtering (FGMM)

The previous GMM modulates the voxel intensity of the image as shown in (4.14). This probabilistic model can be used to enhance the average intensity gap between the specific and the non-specific areas in the sense of increasing the signal-to-noise ratio (SNR) for normalization purposes. During the image reconstruction, classical

filtering techniques can be used [107, 152], however, as the uptake is reduced in abnormal studies, the images will contain fewer counts and still appear to be noisy in DaTSCAN SPECT imaging.

Let Ω be the indexed set of Gaussians. From (4.14) the following expression can be derived by splitting Ω into two subsets:

$$I_{Gauss}(\mathbf{x}) = I_{tot} \cdot \left[\sum_{n \in \Omega_s} \omega_n f_n(\mathbf{x}|\theta_\mathbf{n}) + \sum_{n \in \Omega_N} \omega_n f_n(\mathbf{x}|\theta_\mathbf{n}) \right] \tag{4.15}$$

where Ω_s and Ω_N denote the subsets of clusters modeling the un-corrupted signal and the noise components, respectively, in (4.1). If this spatial model holds, the Gaussian noise (N_i) may be removed from (4.15) by pruning the clusters belonging to Ω_N. The whole normalization procedure is illustrated in figure 4.7. Firstly, the database is spatially normalized using the SPM software in order to ensure that any given voxel in different images refers to the same anatomical position across the brains. Secondly, a GMM approach is obtained for modeling the intensity profile of the original image. In this sense, the intensity profile of each DaTSCAN SPECT image is approximated by a sum of Gaussians (model-based clustering or *parcellation* approach [212]) by satisfying a maximum likelihood (ML) criterion. Finally, the resulting mixture model will be used for IN according to a cluster selection strategy. Clusters are selected by means of a normalized probability threshold that measures the weight of each kernel on the striatum area and the IN is actually carried out by only adding the relevant clusters in the image reconstruction. Thus, the selected clusters are used for GMM-based image filtering, which performs IN of the functional images in the NS region and provides a noise-reduced image. In this way the

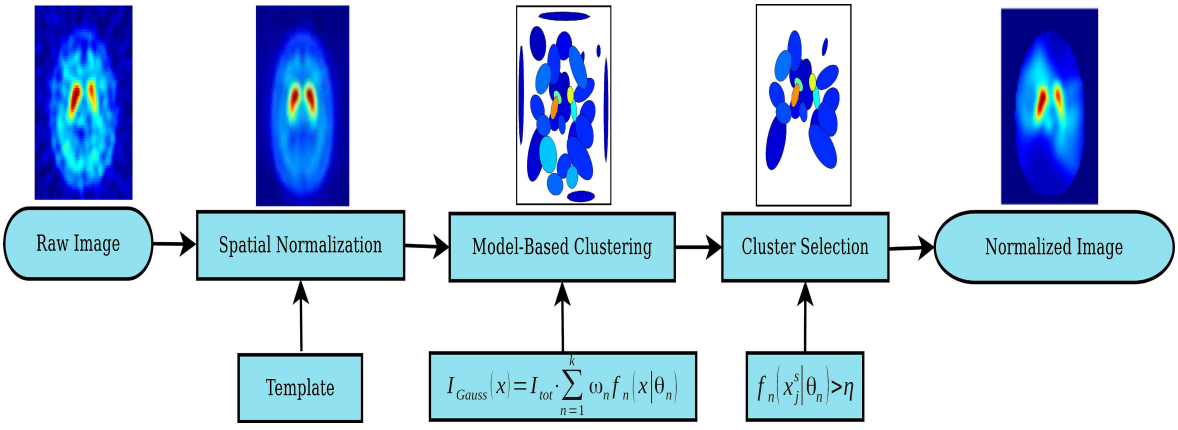

Figure 4.7: Block diagram of the IN procedure for DaTSCAN SPECT images

proposed IN method consists of the following steps:

- A striatal mask [1] (see Figure 4.8) is computed by thresholding the average image of control subjects. Then, the coordinates of each voxel belonging to the striatum, denoted by $\Gamma = \{\mathbf{x_j^s}\}$ for $j=\{1,\ldots,N_s\}$ are selected, where N_s is the number of voxels within the striatum.

- A statistical criterion is defined for the set Ω_s, that is, to determine which clusters of the GMM are relevant in Γ. If the total intensity is assumed to be uniformly distributed in the image, the probability of each coordinate is $p_u(\mathbf{x_j}) = 1/N_b \equiv \eta \cong 4 \cdot 10^{-6}$, where N_b is the total number of voxels. Thus, the partial probability value of a given voxel in Γ that satisfies:

$$f_n(\mathbf{x_j^s}|\theta_\mathbf{n}) < \eta \quad n \in \Omega \tag{4.16}$$

reflects a deviation from the uniform threshold value, that is, a negligible contribution to (4.3). A cluster $n \in \Omega_N$ is considered as irrelevant if this inequality holds for a large fraction α of N_s i.e. a fraction equal or greater than 75% (see Appendix A.1 and Figure 6.20 for further details):

$$card\{\Gamma_n\} \geq \alpha \cdot N_s \tag{4.17}$$

where Γ_n denotes the subset of non-activated voxels for the cluster n, that is, the subset of voxels that satisfies (4.16). The irrelevant clusters are removed from the probabilistic model by setting its weight ω_n to zero. Otherwise the cluster $n \in \Omega_s$ is considered as relevant (the cluster with activated voxels in Γ) and contributes to the mixture distribution.

[1] The striatal mask is a binary mask, which is applied to each volume in order to select only the high-intensity voxels of the striatum area (region of specific activity).

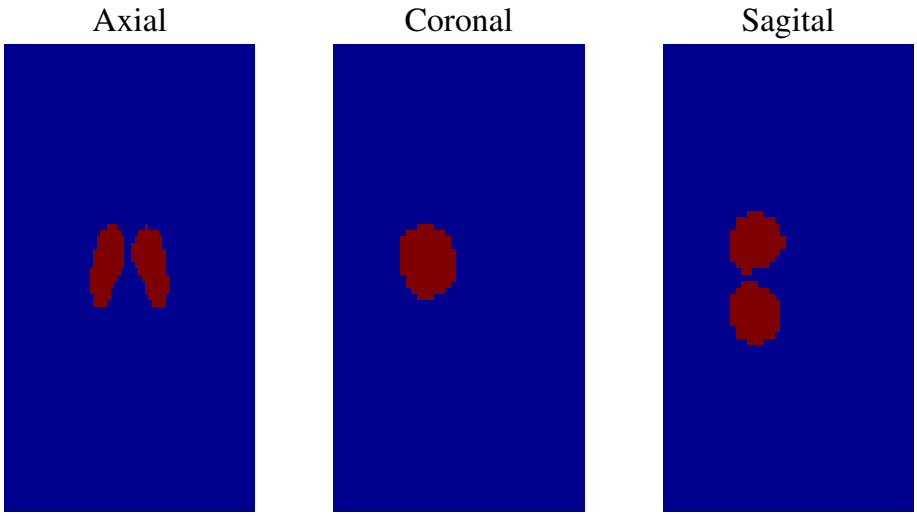

Figure 4.8: The striatum mask used in the intensity normalization process.

Figure 4.9 shows the filtering process by means of GMM, using a 2D simulated data. Here, the relevant Gaussians that contribute to the intensity of a specific region are preserved and the remaining ones are removed.

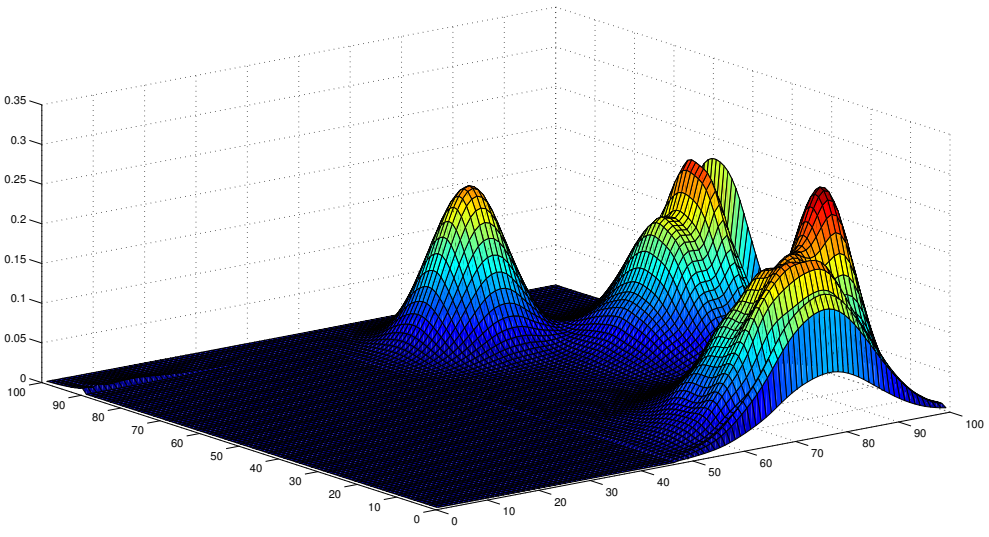

Figure 4.9: The GMM-based image filtering on a 2D simulated data.

4.4 Conclusion

The core idea of this chapter is to normalize intensity values in DaTSCAN images using a novel method based on the GMMs, which is widely used in many preprocessing techniques, such as ROI selection, density estimation, etc. In this chapter, we used the GMM method to remove the Gaussian noise from the DaTSCAN images, and to reconstruct these images by populating them with Gaussian kernels whose linear combination approximates the original image intensity. In addition, we modulated the intensity values in the NS region by filtering the GMM-reconstructed images according to a probability threshold. Using the proposed GMM-based image filtering approach, the relevant clusters that contribute to the striatum, the brain area involved in PD diagnosis, are retained. However, the non-relevant clusters selected in the normalization region (occipital cortex), are automatically removed. The proposed method was implemented using Matlab software. The principal contributions in the field of soft computing that are presented in this chapter are related to the topic "probabilistic computing" and its applications in biomedical engineering, data mining, image processing and pattern recognition. Moreover, the influence of the probabilistic computing technique shown in this chapter is evaluated within a pattern recognition system developed for computer aided diagnosis of the PD, as shown in the experimental chapter.

Chapter 5

Mean Squared Error Optimization for intensity normalization

Intensity normalization is an important pre-processing step in the study and analysis of functional imaging. As most automatic supervised image segmentation and classification methods base their assumptions regarding the intensity distributions on a standardized intensity range, intensity normalization takes on a very significant role. In this chapter, three novel intensity normalization methods are presented. These proposed methodologies are based on mean-squared error (MSE) optimization. The first MSE optimization method consists of a linear transformation at every voxel in the brain image. This transformation is obtained by minimizing the MSE between the intensity normalized image and the template in the so-defined non-specific (NS) region. However, the second approach is based on minimization of the MSE between the Gaussian Mixture Model (GMM)-based extracted features from each subject image and the template in NS region. Our approach to feature extraction consists of using the set of parameters that define the template features, such as weights, covariance matrices and mean vectors to model the remaining images by reducing, consequently their dimensionality. Finally, the third intensity normalization approach is based on a predictive modeling using multivariate linear regression (MLR). Different intensity normalization parameters derived from this model will be used in a linear procedure to perform the intensity normalization of functional brain images. This new approach is an extension of the MSE normalization method presented in our previous work in [222]. Thus, this normalization methodology can be applied to the whole medical image, not only in a NS region.

5.1 Mean Squared Error Optimization

The MSE is widely used as a metric for quality assessment of medical image [223]. In this chapter, its minimization can involve a novel intensity normalization method for functional images. To state the problem, let $I(\mathbf{x}_i)$, $\bar{I}(\mathbf{x}_i)$ and $\hat{I}(\mathbf{x}_i)$ denote the intensity values of the original, template and normalized images in the NS region (Figure 5.1).

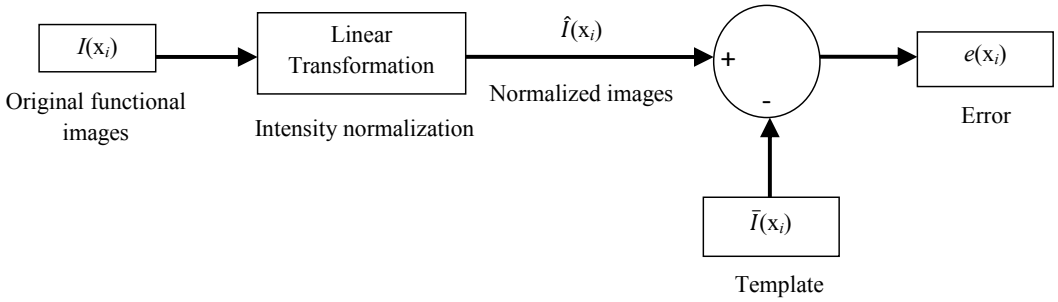

Figure 5.1: General diagram of linear intensity normalization method for functional images using the MSE approach.

In MSE optimization, an estimate $\hat{I}(\mathbf{x}_i)$ is to be found that minimizes the cost function ξ:

$$\xi = \frac{1}{N_{ns}} \sum_{i=1}^{N_{ns}} |\hat{I}(\mathbf{x}_i) - \bar{I}(\mathbf{x}_i)|^2 \tag{5.1}$$

where N_{ns} is the number of voxels in the NS region. Although the solution to this problem generally leads to a nonlinear estimator, in many cases a linear estimator is preferred [224]. In linear mean-square estimation, we assume that the image intensity levels are related by the following model:

$$\hat{I}(\mathbf{x}_i) = a\, I(\mathbf{x}_i) + b \tag{5.2}$$

where a and b are the intensity normalization parameters, they represent the scale and offset of the intensity transformation [225]. The aim of MSE optimization, is to linearly transform the intensity heterogeneity in the non-specific region for different functional brain images by jointly estimating the parameters a and b in equation 5.2. This leads to the joint minimization of a cost function ξ that is expressed as:

$$\xi = \frac{1}{N_{ns}} \sum_{i=1}^{N_{ns}} e^2(\mathbf{x}_i) \tag{5.3}$$

where e($\mathbf{x}_i$) is the estimation error, namely

$$e(\mathbf{x}_i) = \hat{I}(\mathbf{x}_i) - \bar{I}(\mathbf{x}_i) = a\ I(\mathbf{x}_i) + b - \bar{I}(\mathbf{x}_i) \tag{5.4}$$

Solving the linear mean-square estimation problem may be accomplished by differentiating ξ with respect to a and b and setting the derivatives equal to zero as follows:

$$\frac{\partial \xi}{\partial a} = \frac{1}{N_{ns}} \sum_{i=1}^{N_{ns}} \frac{\partial e^2(\mathbf{x}_i)}{\partial a} = \frac{1}{N_{ns}} \sum_{i=1}^{N_{ns}} 2\ e(\mathbf{x}_i)\ I(\mathbf{x}_i) = 0 \tag{5.5}$$

$$\frac{\partial \xi}{\partial b} = \frac{1}{N_{ns}} \sum_{i=1}^{N_{ns}} \frac{\partial e^2(\mathbf{x}_i)}{\partial b} = \frac{1}{N_{ns}} \sum_{i=1}^{N_{ns}} 2\ e(\mathbf{x}_i) = 0 \tag{5.6}$$

Note that equation 5.5 is the orthogonality principle [224] and states that for the optimum linear predictor the estimation error will be orthogonal to the data $I(\mathbf{x}_i)$. From equations 5.2, 5.4, 5.5 and 5.6, it follows that

$$a \sum_{i=1}^{N_{ns}} I^2(\mathbf{x}_i) + b \sum_{i=1}^{N_{ns}} I(\mathbf{x}_i) - \sum_{i=1}^{N_{ns}} \bar{I}(\mathbf{x}_i) I(\mathbf{x}_i) = 0 \tag{5.7}$$

$$a \sum_{i=1}^{N_{ns}} I(\mathbf{x}_i) + b\ N_{ns} - \sum_{i=1}^{N_{ns}} \bar{I}(\mathbf{x}_i) = 0 \tag{5.8}$$

Solving equations 5.7 and 5.8 for a and b we find:

$$a = \frac{\sum_{i=1}^{N_{ns}} I(\mathbf{x}_i)\bar{I}(\mathbf{x}_i) - N_{ns}\ \mathbf{m}_{\bar{I}}\ \mathbf{m}_I}{\sum_{i=1}^{N_{ns}} I^2(\mathbf{x}_i) - N_{ns}\ \mathbf{m}_I^2} \tag{5.9}$$

$$b = \mathbf{m}_{\bar{I}} - a\ \mathbf{m}_I \tag{5.10}$$

where

$$\mathbf{m}_I = \frac{1}{N_{ns}} \sum_{i=1}^{N_{ns}} I(\mathbf{x}_i); \quad \mathbf{m}_{\bar{I}} = \frac{1}{N_{ns}} \sum_{i=1}^{N_{ns}} \bar{I}(\mathbf{x}_i) \tag{5.11}$$

Substituting equation 5.10 into equation 5.2, the estimate for $\hat{I}(\mathbf{x}_i)$ may be written as:

$$\hat{I}(\mathbf{x}_i) = a\ I(\mathbf{x}_i) + (\mathbf{m}_{\bar{I}} - a\ \mathbf{m}_I) = a\ (I(\mathbf{x}_i) - \mathbf{m}_I) + \mathbf{m}_{\bar{I}} \tag{5.12}$$

As a result, the normalized image $\hat{I}(\mathbf{x}_i)$ can be expressed according to the original image $I(\mathbf{x}_i)$ and the intensity normalization parameters as:

$$\hat{I}(\mathbf{x}_i) = \frac{\sum_{i=1}^{N_{ns}} I(\mathbf{x}_i)\bar{I}(\mathbf{x}_i) - N_{ns}\ \mathbf{m}_{\bar{I}}\ \mathbf{m}_I}{\sum_{i=1}^{N_{ns}} I^2(\mathbf{x}_i) - N_{ns}\ \mathbf{m}_I^2}\ (I(\mathbf{x}_i) - \mathbf{m}_I) + \mathbf{m}_{\bar{I}} \tag{5.13}$$

After obtaining the optimum linear estimator for $\hat{I}(\mathbf{x}_i)$, the minimum MSE can be evaluated as:

$$\begin{aligned} \xi_{\mathbf{min}} &= \frac{1}{N_{ns}} \sum_{i=1}^{N_{ns}} e(\mathbf{x}_i)\ (a\ I(\mathbf{x}_i) + b - \bar{I}(\mathbf{x}_i)) = -\frac{1}{N_{ns}} \sum_{i=1}^{N_{ns}} e(\mathbf{x}_i)\ \bar{I}(\mathbf{x}_i) \\ &= \frac{1}{N_{ns}}\ (\ \sum_{i=1}^{N_{ns}} \bar{I}^2(\mathbf{x}_i) -\ b \sum_{i=1}^{N_{ns}} \bar{I}(\mathbf{x}_i) - a \sum_{i=1}^{N_{ns}}\ I(\mathbf{x}_i)\bar{I}(\mathbf{x}_i)\ ) \end{aligned} \tag{5.14}$$

In summary, this intensity normalization procedure for functional images is outlined as:

- Firstly, a non-specific mask is computed as the difference between the skull and the striatum masks of the template in a binary form, as shown in Figure 5.2. Then, it is applied to all images in order to select the brain voxels minus the striatum as non-specific region.

- Secondly, the average intensity of brain voxels $\mathbf{m}_I$ and $\mathbf{m}_{\bar{I}}$ are computed for the source $I(\mathbf{x}_i)$ and the template $\bar{I}(\mathbf{x}_i)$ images in the NS areas.

- Lastly, the intensity normalization parameters a and b are calculated using equations 5.9 and 5.10. As a result, a linear intensity transformation is applied to each source image that minimizes the MSE between the latter image and the template.

Figures 3.3 and 5.3 depict the computed templates used for normalization among the different IN approaches for DaTSCAN and DMFP images.

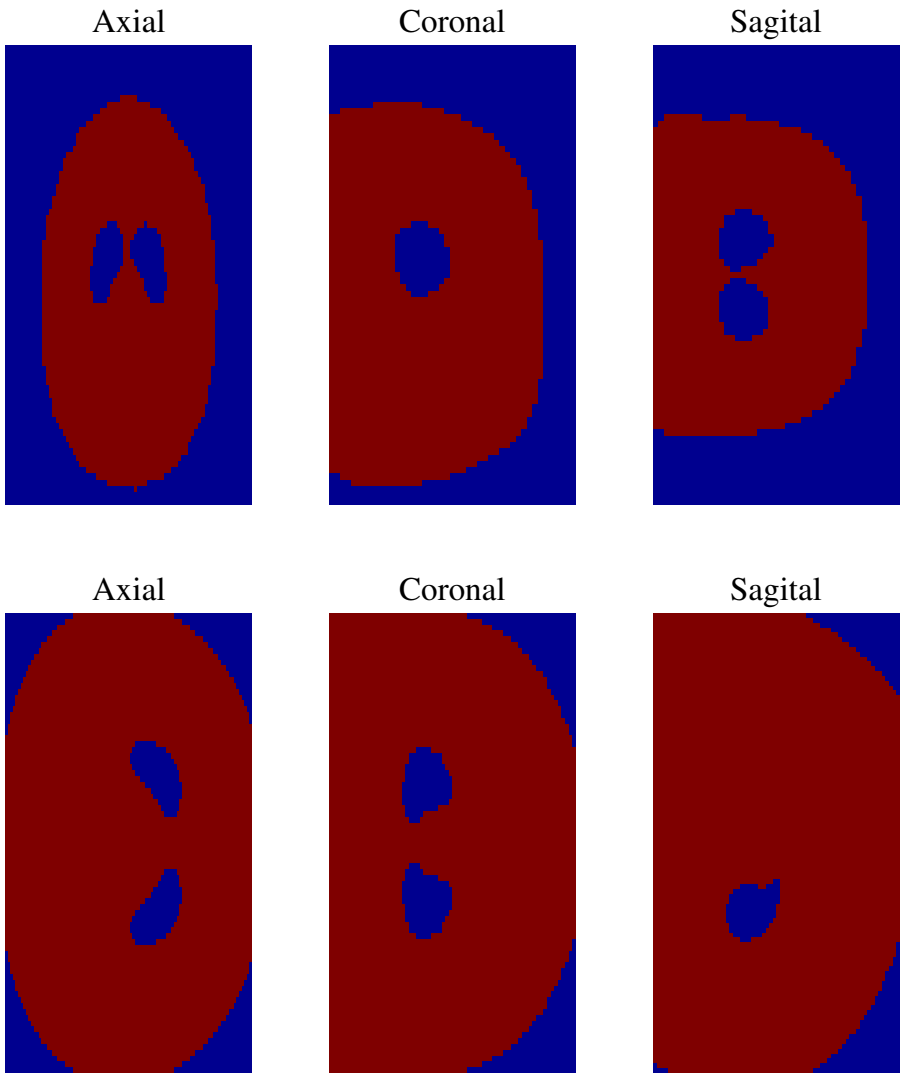

Figure 5.2: First row: the non-specific mask used in the intensity normalization process for DaTCSAN images. Second row: the non-specific mask used in the intensity normalization process for DMFP images.

5.2 Linear intensity normalization through Gaussians

In this section, a new method for intensity normalization of SPECT and PET brain images based on minimization of the MSE between the Gaussian Mixture Model (GMM)-based extracted features from each subject image and a template in the NS region is derived. The proposed approach is based on a feature extraction technique, which consists of using the set of parameters that define the template features

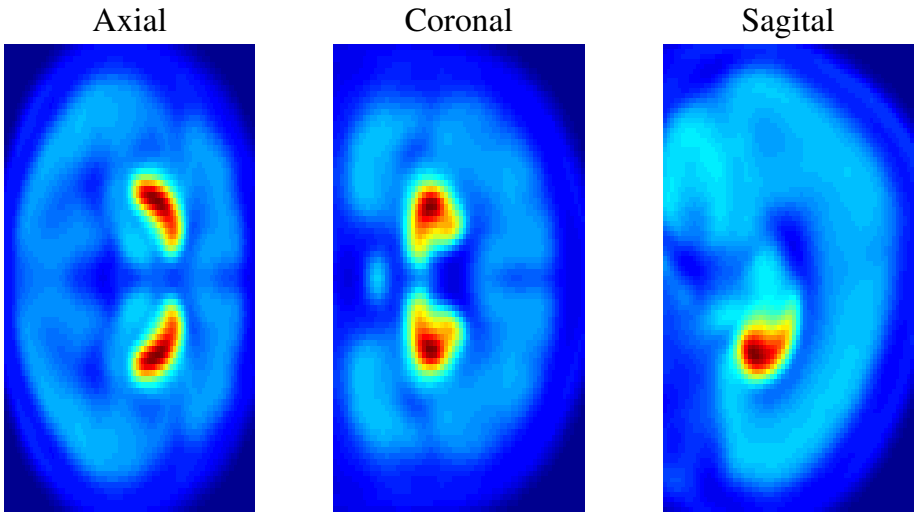

Figure 5.3: The computed template used in the MSE normalization approach for DMFP PET images.

(weights, covariance matrices and mean vectors) in order to model the remaining images. Thus reducing consequently their dimensionality. In this sense, we use the GMM-based algorithm as a feature extraction method, which enables selecting the clusters whose probability is below a probability threshold in the reference region. The proposed MSE methodology performs a linear transformation of the intensity value by estimating the different intensity normalization parameters that leads to a minimum value of the MSE between the reduced feature vectors in NS region, which represent the source and the template's images.
This normalization scheme is a combination between GMM and MSE methodologies. The main motivations of using, both GMM and MSE are to parcel or delimit the regions of interest (ROIs) on a functional image as a feature extraction method and to overcome the computational cost during the image preprocessing stage. For further details about the arguments for applying GMM to functional images, see [212]. The procedure we follow to perform intensity normalization is summarized as follows.

5.2.1 Defining ROIs and feature vectors

The GMM-based algorithm, as shown in chapter 4, is used to define the ROIs in order to normalize the functional images. The Gaussians will be extracted only once for an average normal image and we will use the obtained GMM configuration as a common mask to extract the features from all brain images. Therefore we com-

pute the average normal image using all the images of the normal subjects in the databases that yields to the GMM arrangement plotted in the right column of Figure 5.4.

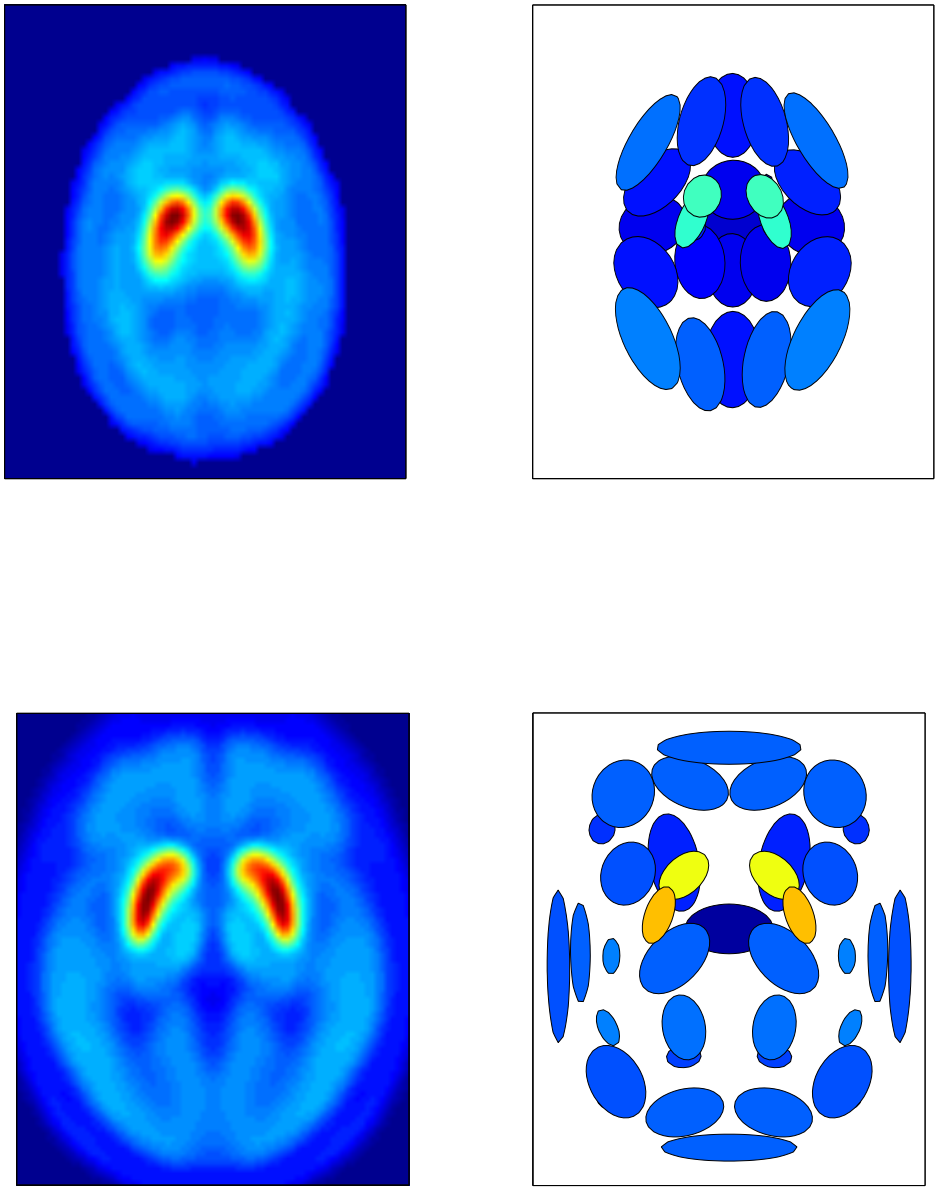

Figure 5.4: Left Column: DaTSCAN SPECT image and DMFP PET image of an average normal subject. Right Column: location of the Gaussians; the ellipses show the regions of the Gaussians with values larger than 50% of the total height and the colors indicate the intensity of the clusters. This obtained GMM configuration is used as a common mask to extract the features from all brain images.

This model is used to extract the intensities I_n of the "ROIs" for each patient, which are obtained by averaging over the intensities within the n-th Gaussian:

$$I_n = \int \mathrm{d}^3\mathbf{x}\, I(\mathbf{x}) f_n(\mathbf{x}) \tag{5.15}$$

so that the dimensionality of the feature space equals the number of clusters. The k-dimensional feature vector for each brain image is then defined by:

$$\mathbf{V} = (I_1, ..., I_k) \tag{5.16}$$

where I_i represents the activation level of the Gaussian i for image V. This approach leads to a drastic compression of the information contained in the brain image. Hence, the computational cost of the image preprocessing stage is reduced.

5.2.2 Selection of Gaussians in the reference region

In terms of probability, the selection of Gaussians for feature extraction is performed as the following. Let Ω denotes the index set of k Gaussians, Ω_s and Ω_n denote the index sets, which depend respectively on the specific and non-specific binding region, as the commonly used binding potential normalization method ($\Omega_n \cap \Omega_s = \emptyset$, $\Omega_n \cup \Omega_s = \Omega$). Furthermore, according to eqs. 4.3 and 4.14, we assume that the intensity in the reference region I_{ns} can be represented by a subset of clusters $\Omega_n \subset \Omega$:

$$I_{ns} = I \cdot \sum_{n \in \Omega_n} \omega_n f_n(\mathbf{x}|\theta_n) \tag{5.17}$$

Our aim is to select the subset of Gaussians that are located in the non-specific region. This is automatically done by thresholding in probability and following these steps:

- First, in order to select the reference region, a binary mask is computed as the difference between two binary masks that select respectively the skull and the striatum by intensity thresholding using the mean control subject image (as shown in Figure 5.2). Then, we apply this mask to all subjects computing the coordinates $\mathbf{x_j}$ of each voxel j belonging to the non-specific cortex region, where j=1, 2,..., N_{ns} and N_{ns} is defined to be the number of voxels within the mask that locates the NS region.

- Second, a statistical criterion is defined for the set Ω_n, that is, to determine which clusters of the GMM belong to the reference region. If the total intensity

is assumed to be uniformly distributed in the image, the probability of each coordinate is $p_u(\mathbf{x_j}) = 1/N \equiv \eta \cong 4 \cdot 10^{-6}$ for DaTSCAN images and $\eta \cong 2 \cdot 10^{-6}$ for DMFP images, where N is the total number of voxels in the functional image. Thus, each partial probability value of a given voxel in the reference region:

$$f_n(\mathbf{x_j}|\theta_\mathbf{n}) > \eta' \quad n \in \Omega \tag{5.18}$$

reflects a deviation from the uniform threshold value ($\eta' < \eta$, $\eta' \cong 5 \cdot 10^{-11}$ for DaTSCAN images and $\eta' \cong 2 \cdot 10^{-14}$ for DMFP images), that is, a significant contribution to the eq. 4.3 evaluated on this particular voxel. Given the reference region, a cluster $n \in \Omega_n$ if this inequality holds for a large fraction of the total number of voxels, that is, 75%, otherwise $n \in \Omega_s$.

According to this procedure, the dimensionality of the feature vectors $\mathbf{V}$ is reduced by selecting only the Gaussians that correspond to the reference region. The reduced feature vectors for each subject can be expressed as:

$$\mathbf{V}_{ns} = (I_1, ..., I_n), n \in \Omega_n \tag{5.19}$$

5.2.3 Linear intensity transformation using MSE through Gaussians

In this normalization approach, the MSE optimization is performed on the clusters that represent the NS region, not on the voxel-level information. In this sense, let $\mathbf{V}_{ns}(n)$, $\hat{\mathbf{V}}_{ns}(n)$ and $\bar{\mathbf{V}}_{ns}(n)$ denote the samples of non-specific reduced feature vectors that represent the original, normalized and template images. In mean-square estimation, an estimate $\hat{\mathbf{V}}_{ns}(n)$ is to be found that minimizes the cost function ξ', which can be derived from the GMM-based feature reduction as:

$$\xi' = \frac{1}{n_{ns}} \sum_{n=1}^{n_{ns}} |\hat{\mathbf{V}}_{ns}(n) - \bar{\mathbf{V}}_{ns}(n)|^2 \tag{5.20}$$

where $n_{ns} = |\Omega_n|$, is the number of clusters in the reference region. In linear mean-square estimation, we assume that the image intensity clusters are related by the following model:

$$\hat{\mathbf{V}}_{ns}(n) = a' \, \mathbf{V}_{ns}(n) + b' \tag{5.21}$$

where a' and b' are the intensity normalization parameters, they represent the scale and offset of the linear intensity transformation [225]. Our goal in this methodology, is to linearly transform the intensity heterogeneity in the clusters of the non-specific region to intensity inhomogeneity for normalized images using the eq. 5.21, by jointly estimating the parameters a' and b'. This leads to the joint minimization of a cost function ξ', that will be the usual sum of the squared errors:

$$\xi' = \frac{1}{n_{ns}} \sum_{n=1}^{n_{ns}} e'^2(n) \tag{5.22}$$

where e'(n) is the estimation error, namely

$$e'(n) = \hat{\mathbf{V}}_{ns}(n) - \bar{\mathbf{V}}_{ns}(n) = a'\, \mathbf{V}_{ns}(n) + b' - \bar{\mathbf{V}}_{ns}(n) \tag{5.23}$$

Solving the linear mean-square estimation problem may be accomplished by differentiating ξ' with respect to a' and b' and setting the derivatives equal to zero as follows:

$$\frac{\partial \xi}{\partial a'} = \frac{1}{n_{ns}} \sum_{n=1}^{n_{ns}} \frac{\partial e'^2(n)}{\partial a'} = \frac{1}{n_{ns}} \sum_{n=1}^{n_{ns}} 2\; e'(n)\; \mathbf{V}_{ns}(n) = 0 \tag{5.24}$$

This relationship, known as the orthogonality principle, states that for the optimum linear predictor, the estimation error will be orthogonal to the data $\mathbf{V}_{ns}(n)$.

$$\frac{\partial \xi}{\partial b'} = \frac{1}{n_{ns}} \sum_{n=1}^{n_{ns}} \frac{\partial e'^2(n)}{\partial b'} = \frac{1}{N_{ns}} \sum_{n=1}^{n_{ns}} 2\; e'(n) = 0 \tag{5.25}$$

from eqs 5.21, 5.23, 5.24 and 5.25, it follows that:

$$a' \sum_{n=1}^{n_{ns}} \mathbf{V}_{ns}^2(n) + b' \sum_{n=1}^{n_{ns}} \mathbf{V}_{ns}(n) - \sum_{n=1}^{n_{ns}} \bar{\mathbf{V}}_{ns}(n) \mathbf{V}_{ns}(n) = 0 \tag{5.26}$$

$$a' \sum_{n=1}^{n_{ns}} \mathbf{V}_{ns}(n) + b'\; n_{ns} - \sum_{n=1}^{n_{ns}} \bar{\mathbf{V}}_{ns}(n) = 0 \tag{5.27}$$

Solving eqs. 5.26 and 5.27, for a' and b' we find:

$$a' = \frac{\sum_{n=1}^{n_{ns}} \mathbf{V}_{ns}(n) \bar{\mathbf{V}}_{ns}(n) - n_{ns}\; \mathbf{m}'_{\bar{\mathbf{V}}_{ns}} \mathbf{m}'_{\mathbf{V}_{ns}}}{\sum_{n=1}^{\mathbf{n}_{ns}} \mathbf{V}_{ns}^2(n) - n_{ns}\; \mathbf{m}'^2_{\mathbf{V}_{ns}}} \tag{5.28}$$

$$b' = \mathbf{m}'_{\bar{\mathbf{V}}_{ns}} - a'\,\mathbf{m}'_{\mathbf{V}_{ns}} \tag{5.29}$$

where

$$\mathbf{m}'_{\mathbf{V}_{ns}} = \frac{1}{n_{ns}}\sum_{n=1}^{n_{ns}}\mathbf{V}_{ns}(n); \quad \mathbf{m}'_{\bar{\mathbf{V}}_{ns}} = \frac{1}{n_{ns}}\sum_{n=1}^{n_{ns}}\bar{\mathbf{V}}_{ns}(n) \tag{5.30}$$

Substituting eq. 5.29 into eq. 5.21, the estimate for $\hat{\mathbf{V}}_{ns}(n)$ may be written as:

$$\hat{\mathbf{V}}_{ns}(n) = a'\,\mathbf{V}_{ns}(n) + (\mathbf{m}'_{\bar{\mathbf{V}}_{ns}} - a'\,\mathbf{m}'_{\mathbf{V}_{ns}}) = a'\,(\mathbf{V_{ns}}(n) - \mathbf{m}'_{\mathbf{V}_{ns}}) + \mathbf{m}'_{\bar{\mathbf{V}}_{ns}} \tag{5.31}$$

Moreover, the reduced feature vectors for the normalized images $\hat{\mathbf{V}}_{ns}(n)$ can be expressed according the GMM-based feature reduction for original images $\mathbf{V}_{ns}(n)$ and the intensity normalization parameters as:

$$\hat{\mathbf{V}}_{ns}(n) = \frac{\sum_{n=1}^{n_{ns}}\mathbf{V}_{ns}(n)\bar{\mathbf{V}}_{ns}(n) - n_{ns}\,\mathbf{m}'_{\bar{\mathbf{V}}_{ns}}\mathbf{m}'_{\mathbf{V}_{ns}}}{\sum_{n=1}^{n_{ns}}\mathbf{V}^2_{ns}(n) - n_{ns}\,\mathbf{m}'^2_{\mathbf{V}_{ns}}}\,(\mathbf{V}_{ns}(n) - \mathbf{m}'_{\mathbf{V}_{ns}}) + \mathbf{m}'_{\bar{\mathbf{V}}_{ns}} \tag{5.32}$$

Finally, after having found the optimal linear estimation for $\hat{\mathbf{V}}_{ns}(n)$, we can evaluate the minimum mean-square error using the eqs. 5.23, 5.24 and 5.25:

$$\begin{aligned}\xi'_{\mathbf{min}} &= \frac{1}{n_{ns}}\sum_{n=1}^{n_{ns}} e'(n)\,(a'\,\mathbf{V}_{ns}(n) + b' - \bar{\mathbf{V}}_{ns}(n)) = -\frac{1}{n_{ns}}\sum_{n=1}^{n_{ns}} e'(n)\,\bar{\mathbf{V}}_{ns}(n) \\ &= \frac{1}{n_{ns}}\,(\sum_{n=1}^{n_{ns}}\bar{\mathbf{V}}^2_{ns}(n) - \; b'\sum_{n=1}^{n_{ns}}\bar{\mathbf{V}}_{ns}(n) - a'\sum_{n=1}^{n_{ns}}\mathbf{V}_{ns}(n)\bar{\mathbf{V}}_{ns}(n)\,)\end{aligned} \tag{5.33}$$

In summary, this post-normalization procedure is resumed as:

- Firstly, we apply the GMM-based algorithm for obtaining the underlying Gaussian mixture representation of each functional image and, thereby, each ROI is represented by a single Gaussian with a certain center, shape and weight. Then, a Gaussian selection strategy (see section 5.2.2) is applied in the spatial domain in order to automatically select the clusters of the reference region; that is, the non-specific cortex region, as shown in Figure 5.5.

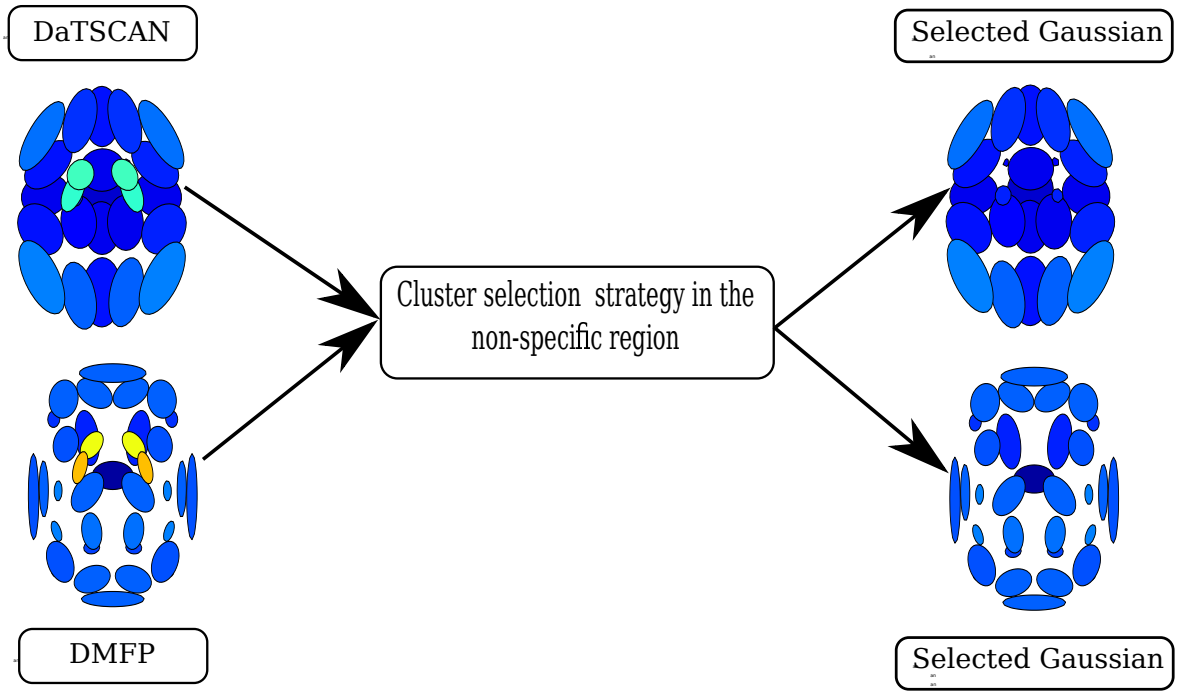

Figure 5.5: Left: the resulting Gaussians from the model-based clustering approach for DaTSCAN and DMFP average normal images. Right: the selected Gaussians in the non-specific region for DaTSCAN and DMFP average images.

- Secondly, we compute the average clusters intensity of the brain $\mathbf{m}'_{\mathbf{V}_{ns}}$ and $\mathbf{m}'_{\bar{\mathbf{V}}_{ns}}$ for the feature vectors of the source and template images, respectively, $\mathbf{V}_{ns}(n)$ and $\bar{\mathbf{V}}_{ns}(n)$ in the NS areas.

- Lastly, we calculate the intensity normalization parameters a' and b' from solving the equations established by differentiating ξ' for each reduced GMM-based feature vectors. Then, we transform linearly all voxel intensity in the brain using eq.5.21 that leads to the minimization of MSE, which tends to zero between the source and the template's images.

5.3 Model-based Multivariate Linear Regression approach for intensity normalization

In this section, a proposed intensity normalization approach based on a predictive modeling using multivariate linear regression (MLR) is presented. Different intensity normalization parameters derived from this model will be used in a linear procedure to perform the intensity normalization of functional brain images. This

new approach is an extension of the mean-squared error normalization method presented in our previous work in the section 5 and in [222]. Thus, this normalization methodology can be applied to the whole medical image, not only in the reference region.

5.3.1 Multivariate linear regression (MLR) model

Multivariate regression analysis is a well-known technique that is widely used in many branches of science and engineering to predict values of D responses from a set of P regressors, where $D \geq 1$ and $P \geq 1$. A MLR is generally based on the following statistical model [226]:

$$\mathbf{Y_i} = \boldsymbol{\beta_0} + \mathbf{B}^{\boldsymbol{T}}\mathbf{x_i} + \boldsymbol{\epsilon_i} \tag{5.34}$$

where the symbol i is used to denote a sample unit; $\mathbf{Y}_i=(Y_{i1},\ldots,Y_{id},\ldots,Y_{iD})^T$ and $\mathbf{x}_i=(x_{i1},\ldots,x_{ip},\ldots,x_{iP})^T$ are the D-dimensional vector of the response variables and the P-dimensional vector of the fixed regressor values for the ith unit, respectively; $\boldsymbol{\beta}_0$ is a D-dimensional vector containing the intercepts for the D responses; $\mathbf{B}$ is a matrix of dimension $P \times D$ whose (p, d)th element, β_{pd}, is the regression coefficient of the pth regressor on the dth response; finally, $\boldsymbol{\epsilon}_i$ denotes the D-dimensional random vector of the error terms corresponding to the ith unit.
To simplify the computation, the multiple regression model in terms of the observations can be written using matrix notation. Using matrices allows for a more compact framework in terms of vectors representing the observations, levels of regressor variables, regression coefficients, and random errors. The model is in the form:

$$\mathbf{Y} = \mathbf{X}\boldsymbol{\beta} + \boldsymbol{\epsilon} \tag{5.35}$$

5.3.2 Intensity normalization using MLR

In this subsection, we apply MLR to a specific pre-processing step of image processing application, that is intensity normalization. The following assumption will be used to perform the normalization task of each image subject:

- Let $\mathbf{Y} \sim \bar{\mathbf{I}}$ be an $N \times 1$ vector of observations on the dependent variable, that is the template image.
- Let $\mathbf{X} \sim \mathbf{I}$ be an $N \times 1$ vector where we have observations on 1 independent variables for N observations, that is the raw data.
- Let the number of observations N be the number of image voxels.

- Let β be an 1×1 vector of unknown parameters that we want to estimate and $\boldsymbol{\epsilon}$ be an $N \times 1$ vector of errors.

Therefore, by estimating the values of β and $\boldsymbol{\epsilon}$ we can easily transform the intensity distribution of $\mathbf{I}$ to $\hat{\mathbf{I}}$ using the following expression:

$$\hat{\mathbf{I}} = \mathbf{I}\ a'' + b'' \tag{5.36}$$

where $\hat{\mathbf{I}}$ is the normalized image, $a'' = \beta$ and $b'' = \bar{\epsilon}$ are the intensity normalization parameters, they represent the scale and offset of the intensity transformation [222]. The used criteria for obtaining our estimates of β is to minimize the residual sums of squares (or error sums of squares) (RSS), which can be defined as:

$$\begin{aligned} \boldsymbol{\epsilon}^T \boldsymbol{\epsilon} = (\bar{\mathbf{I}} - \mathbf{I}\beta)^T (\bar{\mathbf{I}} - \mathbf{I}\beta) &= \bar{\mathbf{I}}^T \bar{\mathbf{I}} - \bar{\mathbf{I}}^T \mathbf{I}\beta - \mathbf{I}^T \beta^T \bar{\mathbf{I}} + \beta^T \mathbf{I}^T \mathbf{I}\beta \\ &= \bar{\mathbf{I}}^T \bar{\mathbf{I}} - 2\beta^T \mathbf{I}^T \bar{\mathbf{I}} + \beta^T \mathbf{I}^T \mathbf{I}\beta \end{aligned} \tag{5.37}$$

To find the β that minimizes the RSS, we need to take the derivative of eq. 5.37 with respect to β. This gives us the following equation:

$$\frac{\partial \boldsymbol{\epsilon}^T \boldsymbol{\epsilon}}{\partial \beta} = -2\mathbf{I}^T \bar{\mathbf{I}} + 2\mathbf{I}^T \mathbf{I}\beta = 0 \tag{5.38}$$

From eq. 5.38, the "normal equations" are:

$$(\mathbf{I}^T \mathbf{I})\beta = \mathbf{I}^T \bar{\mathbf{I}} \tag{5.39}$$

Multiplying both sides of the eq. 5.39 by the inverse $(\mathbf{I}^T \mathbf{I})^{-1}$ gives us the following equation:

$$(\mathbf{I}^T \mathbf{I})^{-1} (\mathbf{I}^T \mathbf{I})\beta = (\mathbf{I}^T \mathbf{I})^{-1} \mathbf{I}^T \bar{\mathbf{I}} \tag{5.40}$$

By definition, $(\mathbf{I}^T \mathbf{I})^{-1} (\mathbf{I}^T \mathbf{I}) = \mathbf{I}_N$, where $\mathbf{I}_N$ is the identity matrix and N is the number of image voxels. As a result, the least square solution of β is :

$$\beta = (\mathbf{I}^T \mathbf{I})^{-1} \mathbf{I}^T \bar{\mathbf{I}} \tag{5.41}$$

The residuals are computed as:

$$\boldsymbol{\epsilon} = \bar{\mathbf{I}} - \mathbf{I}\beta = \bar{\mathbf{I}} - \mathbf{I}(\mathbf{I}^T \mathbf{I})^{-1} \mathbf{I}^T \bar{\mathbf{I}} = (\mathbf{I}_n - \mathbf{I}(\mathbf{I}^T \mathbf{I})^{-1} \mathbf{I}^T) \bar{\mathbf{I}} \tag{5.42}$$

The goal of this approach is to transform linearly all the intensity values for different image subjects using predictive modeling based on MLR. The procedure to perform the intensity normalization is summarized as follows:

- Firstly, the template $\bar{\mathbf{I}}$ is computed as :

$$\bar{\mathbf{I}} = \frac{1}{N_c} \sum_{i \in X_c} (\mathbf{I}_i(x, y, z) + \mathbf{I}_i(-x, y, z)) \tag{5.43}$$

where X_c denotes the subset of control images, N_c the number of control images, $\mathbf{I}_i(x,y,z)$ is the ith image and $\mathbf{I}_i(-x,y,z)$ is its reflected image in the $x=0$ hemisphere midplane.

- Secondly, the different parameters β and $\boldsymbol{\epsilon}$ of the MLR model are estimated using the eqs. 5.41 and 5.42.
- Lastly, the normalized images are computed by linearly transforming the voxel intensity of each image subject using the model in eq. 5.36.

5.4 Conclussion

Three novel intensity normalization approaches are proposed to establish a comparison between specific/non-specific uptake areas. These methodologies are based on the extraction of intrinsic parameters from DaTSCAN SPECT and DMFP PET images, resulting in three automatic procedures for intensity normalization: MSE optimization between the intensity normalized image and the template in the NS region, MSE optimization between the GMM-based extracted features from each subject image and the template in the reference region and finally a normalization method based on predictive modeling using MLR. These methodologies have the advantage of automatically normalizing the 3D functional brain images without using anatomical information. In addition, they can be applied for different image modalities, such as SPECT and PET.

Chapter 6

Experiments and Discussion

This chapter presents an evaluation study of the different proposed intensity normalization approaches when compared to several other normalization methods previously reported in the literature. Thus, quantitative and qualitative image analysis is performed. Furthermore, we carry out experiments to test the ability of the proposed normalization approaches to aid clinicians in diagnosis of DaTSCAN SPECT and ^{18}F-DMFP PET images of Parkinson's disease subjects. All experiments described in this chapter were carried out on the real data.

6.1 Databases description

6.1.1 DaTSCAN SPECT database

To evaluate the proposed methodologies a database consisting of 189 SPECT images from 189 subjects (94 Normal Controls (NCs) and 95 Parkinsonian Syndrome (PS)), was obtained after the injection of 185 MBq (5 mCi) of the radioligand: Ioflupane-I-123 after an extension of time between 3-4 h; during this period, the thyroid was blocked using a Lugols solution. The SPECT images with Ioflupane/123I-FP-CIT were obtained by a using a General Electric gamma camera, Millennium model, equipped with a dual head and general purpose collimator. A 360-degree circular orbit was made around the cranium, at 3-degree intervals, leading to 60 images each 35 seconds per interval and with 128×128 matrix. The brain images were reconstructed using the filtered back projection algorithm, applying a Hanning filter (cut-off frequency equal to 0.7) and were obtained with transaxial slices. To avoid variability from additional image processing, no attenuation or scatter correction was applied in this study. Those images were acquired by the "Virgen de

la Victoria" hospital from January 2003 until December 2008 (see Table 6.1 for demographic details). All the SPECT images were spatially normalized using the SPM 8 software [168] yielding a $73 \times 73 \times 45$ three-dimensional functional activity map for each subject. This method assumes a general affine model with 12 parameters and a Bayesian framework that maximizes the product of the prior function (which is based on the probability of obtaining a particular set of zooms and shears) and the likelihood function, derived from the residual squared difference between the template and the processed image. The template t is computed by registering all control images to a randomly chosen one by affine transformations. This $N_c = 94$ controls and its hemisphere midplane reflected that the images are averaged to create the template [167], providing a symmetric image, as shown in the Figure 3.3. This spatial normalization process ensures that any given voxel in different images refers to the same anatomical position across the brains. This step allows us to compare the voxel intensities of the brain images of the different subjects.

Table 6.1: Demographic details of the DaTSCAN SPECT subjects. μ and σ stand for the average and the standard deviation respectively.

		Sex		Age		
	#	M	F	μ	σ	range
NCs	94	49	45	69.26	10.16	33-89
PS	95	54	41	68.29	9.62	30-87

Once the images have been properly normalized, they were visually labeled by three nuclear medicine specialists from the hospital using only the information contained in the images, without any other medical information [18]. The assessments were done without trying to assign them to different clinical groups within the set of pathological studies. A study was considered to be "normal" when bilateral, symmetrical uptake appeared in caudate and putamen nuclei, and "abnormal" when there were areas of qualitative reduced uptake in any of the striatal structures.

6.1.2 DMFP PET database

This database included 87 subjects showing parkinsonian movement disorders were used for testing the proposed methodologies. Demographic details and groups distribution are gathered in Table 6.2.
These patients with parkinsonism, who underwent $D_{2/3}$ receptor imaging with ^{18}F-DMFP PET to differentiate between idiopathic Parkinsonian syndrome (IPS) and non-IPS (atypical Parkinsonian syndrome (APS)). ^{18}F-DMFP PET scans were acquired according to a standardized protocol.^{18}F-DMFP was injected as a slow intravenous bolus, and the patients were seated in a quiet room. After 55 min, the patients reclined in the scanning bed of the ECAT EXACT HR$^+$ PET tomograph

Table 6.2: Demographic details of the DMFP PET subjects. μ and σ stand for the average and the standard deviation respectively.

		Sex		Age		
	#	M	F	μ	σ	range
IPS	39	22	17	61.38	11.14	35-81
MSA	13	11	2	71.54	9.94	52-85
MSA-C	6	5	1	67.00	7.64	60-81
MSA-P	5	4	1	62.00	14.35	43-79
PSP	24	12	12	69.29	7.33	55-84

(Siemens/CTI), with their head comfortably immobilized within the aperture, using a foam cushion. The scanner acquired 63 contiguous trans-axial planes, simultaneously covering 15.5 cm of the axial field of view. The trans-axial and axial resolutions (FWHM) of the PET system were 4.6 and 4.0 mm, respectively, at the center of the field of view, and 4.8 and 5.4 mm, respectively, at a radial offset of 10 cm. The emission recording began at 60 min after the start of the bolus and consisted of 3 frames of 10 min each, acquired in 3-dimensional mode. Finally, a brief transmission scan was obtained using a rotating ^{68}Ge point source. Images were reconstructed as 128×128 matrices of 2×2 mm voxels by FBP using a Hanning filter with a cutoff frequency of 0.5 Nyquist and corrected for randoms, dead time, and scatter. Images were then transferred to a workstation (Hermes Medical Solutions). After verification of the absence of important head motion between frames, the 3 frames were summed for further analysis [88].
All patients were followed clinically for approximately 2 years after PET examinations, at which time the clinical differential diagnoses were evaluated by clinicians on the basis of observations according to the United Kingdom Parkinson Disease Society Brain Bank Diagnostic Criteria for Parkinson Disease [129] and the second consensus statement on the diagnosis of multiple system atrophy (MSA) [130] as well as the established criteria for the diagnosis of progressive supranuclear palsy (PSP) [227]. According to these criteria and the follow-up clinical examinations, with special attention to the presence or absence of atypical symptoms such as orthostatic hypotension, cerebellar signs, eye movement disorders, and spasticity, 39 patients were labeled as IPS and the remaining 48 subjects either MSA or PSP. It is worth noting that all the images were acquired during the first examinations and, therefore, they correspond to early stages of the disorders.
As in the DaTSCAN images, all the DMFP images were spatially normalized using the template matching approach implemented in SPM [168]. In order to build the DFMP template, the control images, i.e. idiopathic Parkinson, were first registered to a randomly chosen one. The resulting images and their hemisphere midplane reflections (ensuring a symmetric template) were then averaged and smoothed before being used to spatially normalize the whole set of images. As a result, we got brain

volumes with $79 \times 95 \times 68$.

6.2 DaTSCAN experiments

In order to evaluate the improvements provided by the proposed intensity normalization (IN) approaches when compared to conventional IN methods adequately adapted to the nature of the Parkinson'disease (PD) images, qualitative and quantitative inter-subject variability measures are performed. For the qualitative evaluation, the resulting intensity-normalized brain images and the mean histogram are depicted and analyzed. Meanwhile, for the quantitative inter-subject variability, the error bars for the mean histogram of the intensity values in the NS region are depicted. Moreover, three statistical analyses, applying the Kullback-Leibler divergence, the Euclidean distance and the Jeffreys divergence are used to study the difference between the probability distributions of each normalized image and the mean normalized brain image for the different IN methods. In addition, a comparison is performed using a classification system for PS detection, that may improve the development of a computer aided diagnosis (CAD) system for PD. Thus, different preprocessing procedures are considered:

- Raw data, for only spatial normalization without intensity normalization procedure.
- BR_{all}-IN approach, for intensity normalization using specific-to-non-specific binding ratio. BR_{all} denotes the binding ratio calculated using all the brain voxels, except those in the striatum [2, 88].
- Gaussian Mixture Model (GMM) reconstruction approach, for modeling the intensity profile of the original image, as shown in section 4.2 and in [228].
- GMM-based image filtering **(FGMM)** approach, for intensity normalization using a normalized probability threshold that discards irrelevant Gaussians in the reference region , as shown in chapter 4 and in [228].
- Mean squared error **(MSE)** optimization approach, for intensity normalization using a linear transformation of intensity by minimizing the MSE between the source and the template image at voxel's level, as shown in section 5.1 and in [229].
- Linear intensity normalization through Gaussians **(MSE-GMM)**. This proposed method is based on minimization of the MSE between the GMM-based extracted features from each subject image and a template in the non-specific (NS) region, as shown in section 5.2 and in [185].

- Model-based Multivariate Linear Regression **(MLR)** approach for intensity normalization. This proposed method is based on predictive modeling, as shown in subsection 5.3.2 and in [113].

- Integral-based intensity normalization (Integral-IN) [1]. This approach is based on the approximation of integral value of the intensity as the sum of all the intensity values in reference region, as shown in section 3.3.2.

- Intensity normalization by minimizing the Kullback-Leibler divergence (MKL-IN) [193]. This normalization technique is based on matching a template histogram to a reference model density by estimating a multiplicative correction field, as shown in section 3.3.3.

- Histogram equalization (Hist-eq-IN). This latter is a non-linear normalization approach. It is used for modifying the dynamic range and contrast of the functional images by altering each individual voxel such that its intensity histogram assumes a desired shape from a reference template, as explained in section 3.3.4.

- Normalization to the maximum intensity values (Max-IN) [1]. This method is based on referring each voxel to the average value of the highest intensity voxels set, as demonstrated in section 3.3.5.

- The α-stable distribution-based intensity normalization (α-stable-IN) [2]. This methodology is based on the fact that the histogram of intensity values can be fitted accurately using a positive skewed α-stable distribution, as illustrated in section 3.3.6.

6.2.1 Qualitative image analysis

6.2.1.1 Raw data

The proposed methodologies have been tested using 127 different DaTSCAN images (68 NCs and 59 PS subjects) from the database described in subsection 6.1.1 which presents a high degree of variability of the intensity level for the specific/non-specific area, as can be seen in Figure 6.1. Furthermore, these images present a relatively low SNR in the non-specific (NS) region provided by the image acquisition system in the nuclear medicine department.

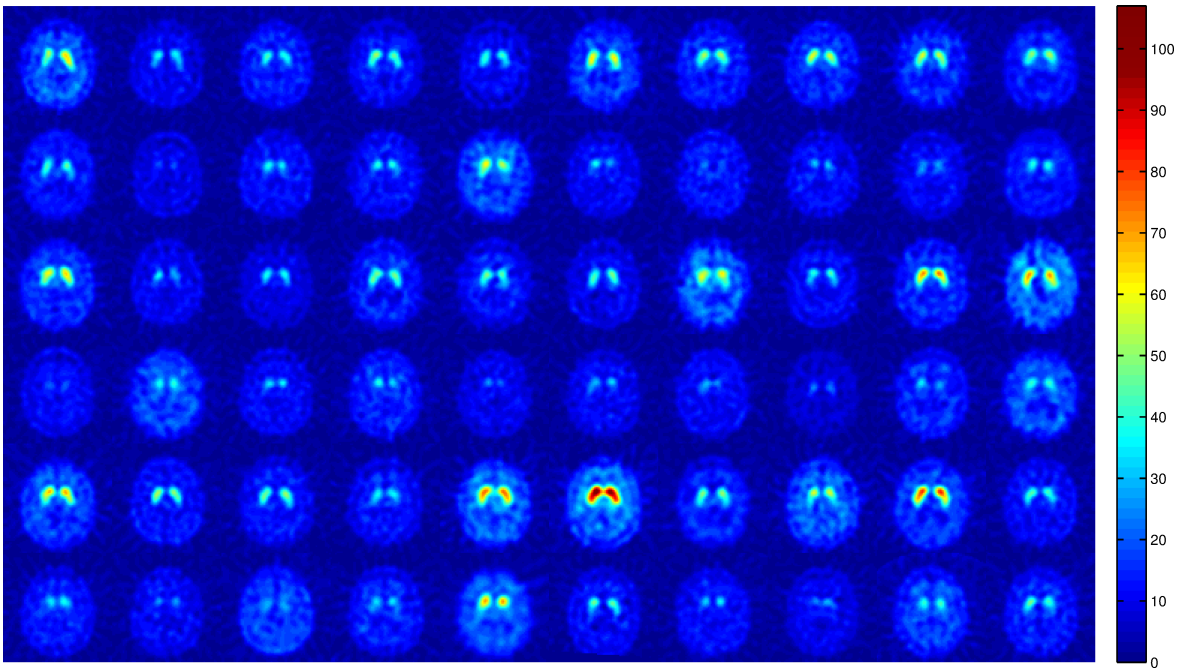

Figure 6.1: A given trans-axial slice of the 60 selected raw DaTSCAN brain images from the database (30 NC + 30 PS): these images present a certain degree of variability between the intensity values before normalization.

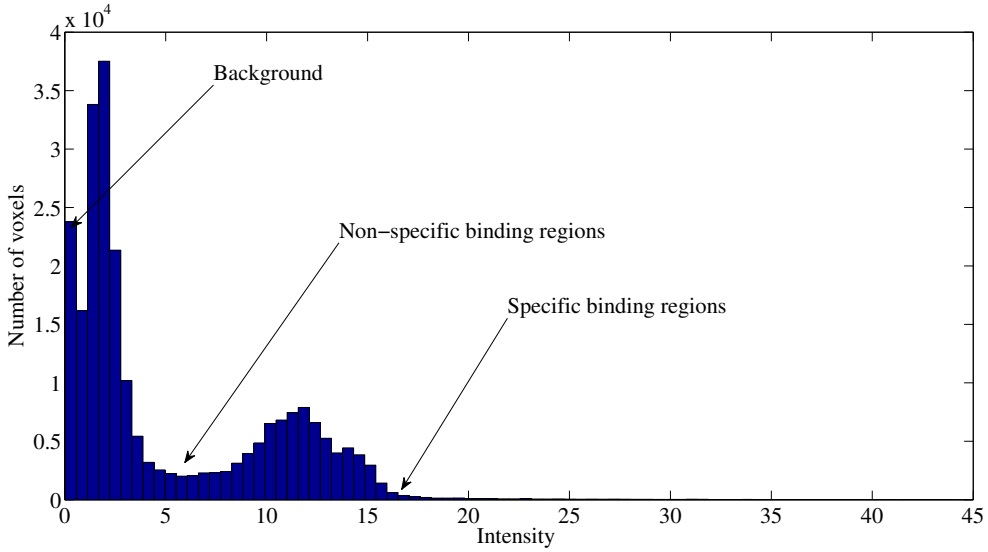

Figure 6.2: Mean histogram of the intensity values for the spatial normalized DaTSCAN images.

Figure 6.2 depicts a scheme of the different parts of the binding values histogram, highlighting the specific and NS areas and their typical intensity values

for original DaTSCAN images. This figure demonstrates that before normalization there is a certain degree of variability between the intensity radioactivity values (from 5.94 to 17.9) in the non-specific binding region due to different noise sources and to an equal supply of tracer from the vascular compartment.

6.2.1.2 The compared IN methods

Linear approaches

The visual inspection of the mean histogram of the raw data, as depicted in Figure 6.2, suggests that this variability in the NS region is not produced by some multiplicative bias in the data [2]. Therefore, a normalization procedure using only a multiplicative parameter, as BR_{all}-IN, MKL-IN, Max-IN and Integral-IN do, could be combined by other procedures for an accurate IN.

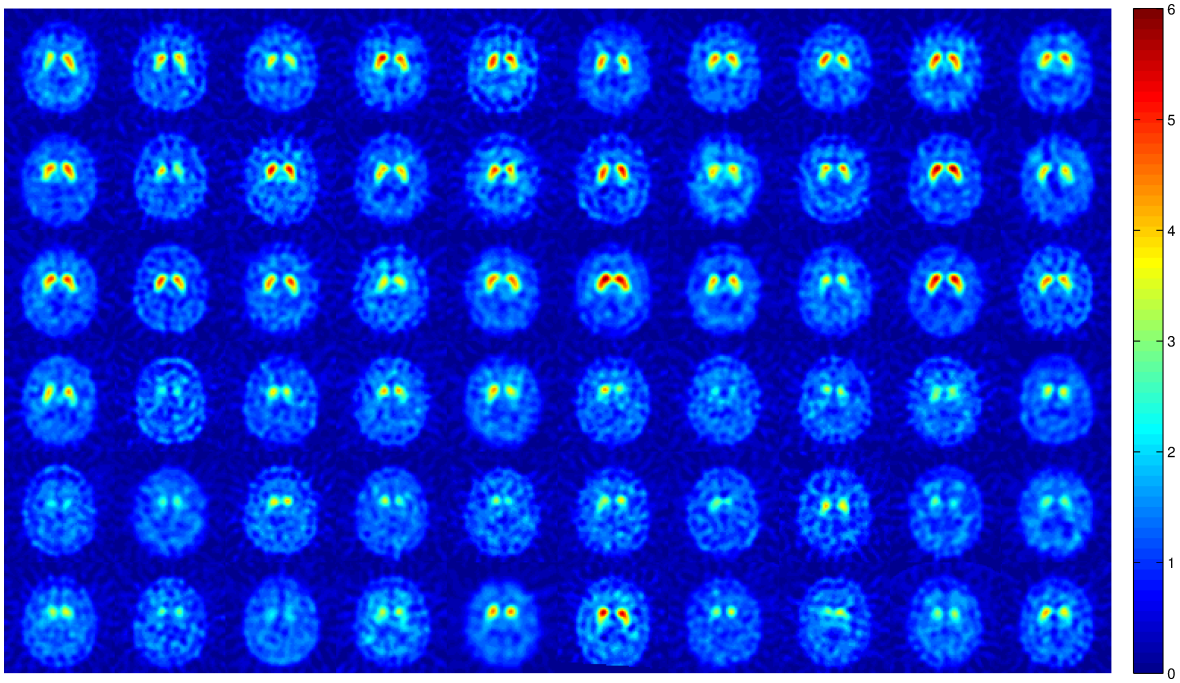

Figure 6.3: A given trans-axial slice of 60 DaTSCAN brain images from the database after normalization by the specific-to-non-specific binding ratio (BR_{all}-IN). In spite of the ability of this approach to normalize the intensity distribution in the NS region, it is not enough for the images in question as it affects the shape and the intensity of the striatal signal.

In figures 6.3 and 6.4, BR_{all}-IN method entails the normalization of the intensity

in the NS region. However, it is not enough for the images in question as it affects the shape and the intensity of the striatal signal.

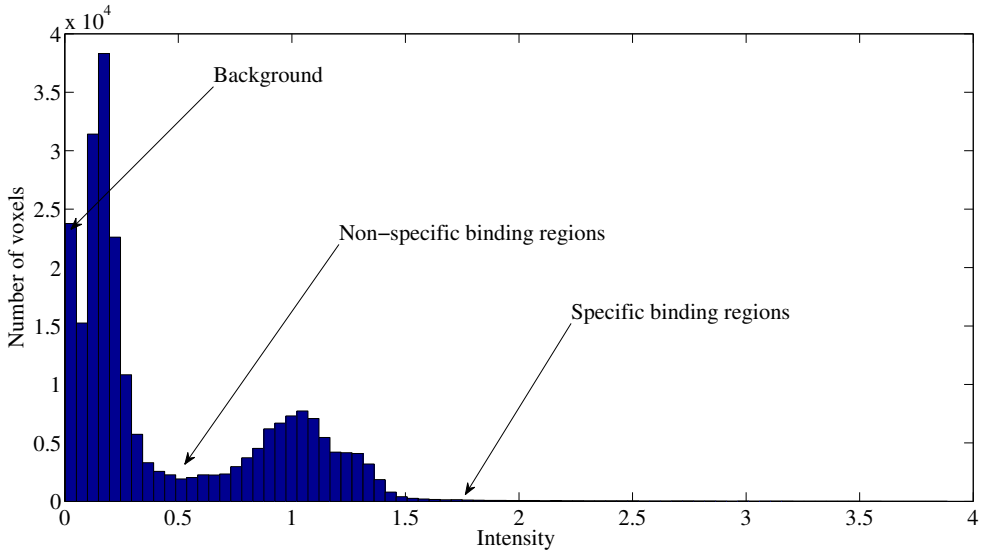

Figure 6.4: Mean histogram of the intensity values for intensity normalized DaTSCAN images by BR_{all}-IN.

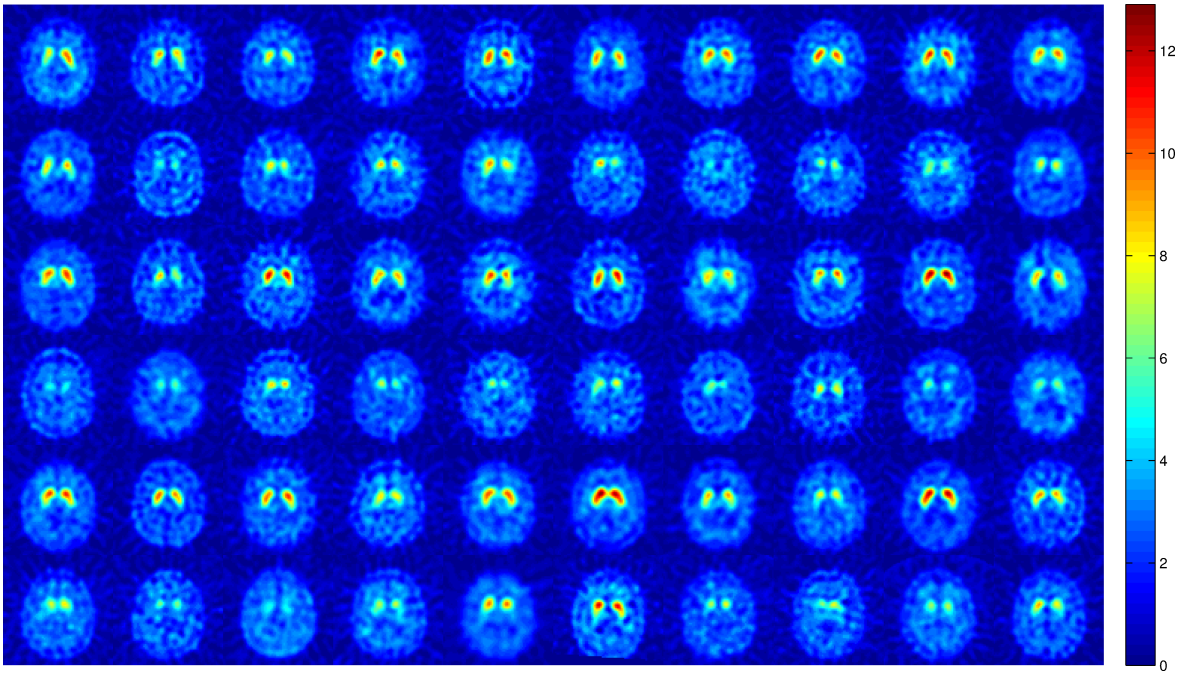

Figure 6.5: A given trans-axial slice of 60 DaTSCAN brain images from the database after normalization by the Integral-based intensity normalization approach (Integral-IN).

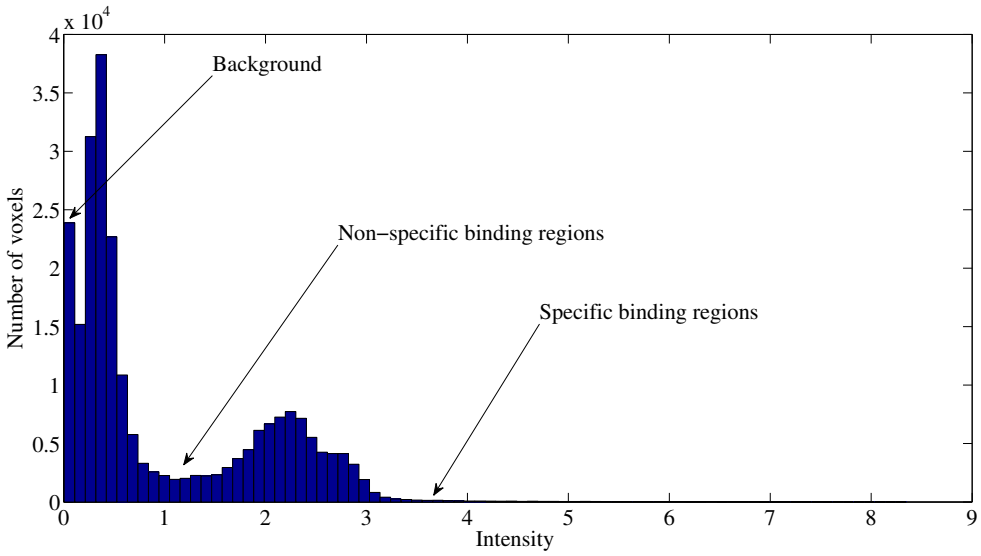

Figure 6.6: Mean histogram of the intensity values for intensity normalized images by Integral-IN.

Integral-IN preserves absolute differences in the uptake of the tracers. Thus, it produces a similar measure for NS regions.

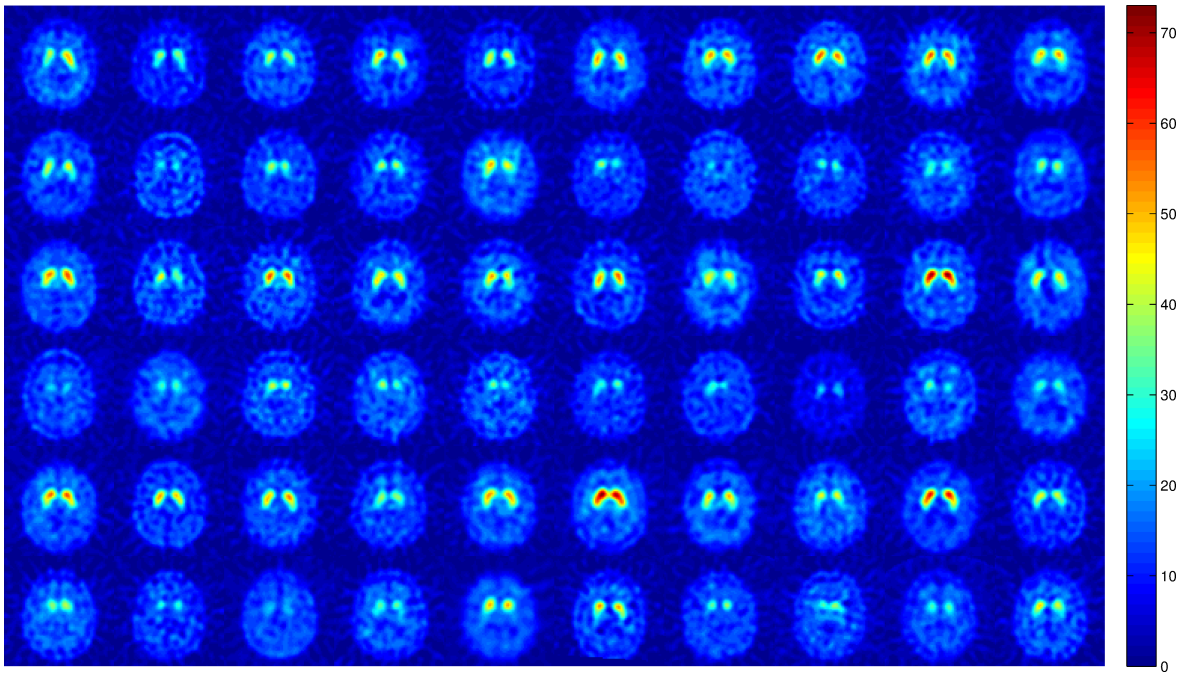

Figure 6.7: A given trans-axial slice of 60 DaTSCAN brain images from the database after normalization by minimizing the Kullback-Leibler divergence (MKL-IN).

In addition, after normalization using the Integral-IN method, there is a noticeable difference in striatal structures with highest intensity counts, as can be seen in figures 6.5 and 6.6. This method is inexact and more sensitive to extreme values. For instance subjects with severe loss of dopamine receptors, high intra-subject differences in the binding potential, or outlier characteristics.

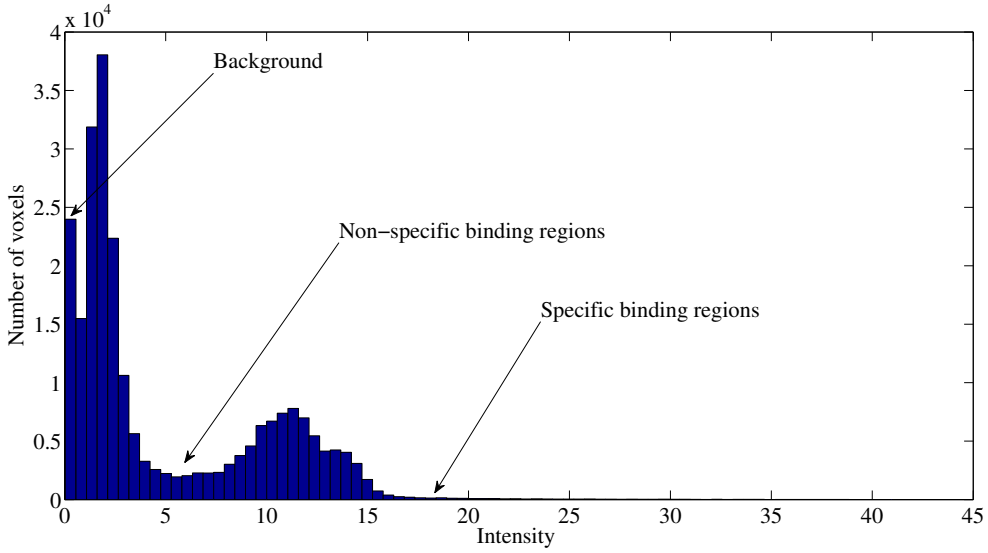

Figure 6.8: Mean histogram of the intensity values for intensity normalized images by MKL-IN.

As in BR_{all}-IN approach, MKL-IN entails a fair intensity normalization in NS region, despite that the striatal signal is affected, as shown in figures 6.7 and 6.8.
For the normalization to the maximum scheme, the uptake of the tracer in the striatal structures is matched for both classes; controls and patients. This could affect the relation between the loss of dopamine receptors and decreased count numbers, which can be lost. Thus, the interpretation in terms of absolute uptake values is lost, as depicted in figures 6.9 and 6.10. The objective of this approach is to extend the size of discriminative regions (striatal structures) by interchanging the roles of specific/nonspecific areas of activity. This may lead to a fault diagnosis.

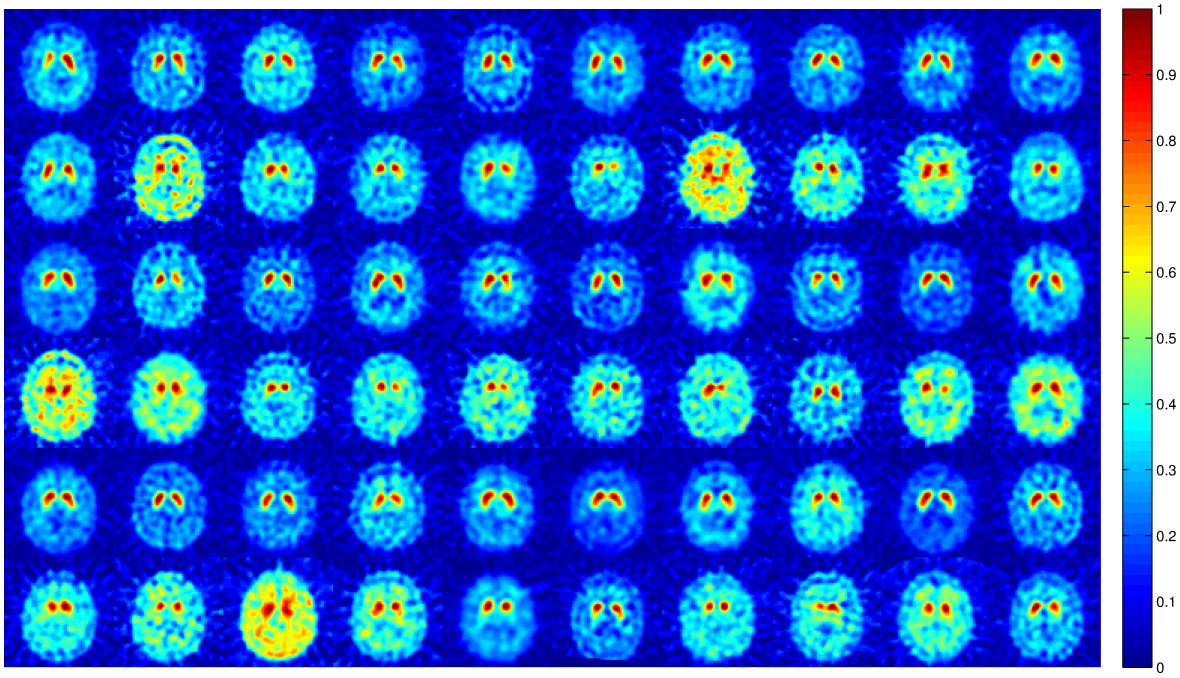

Figure 6.9: A given trans-axial slice of 60 DaTSCAN brain images from the database after normalization by the maximun intensity values (Max-IN).

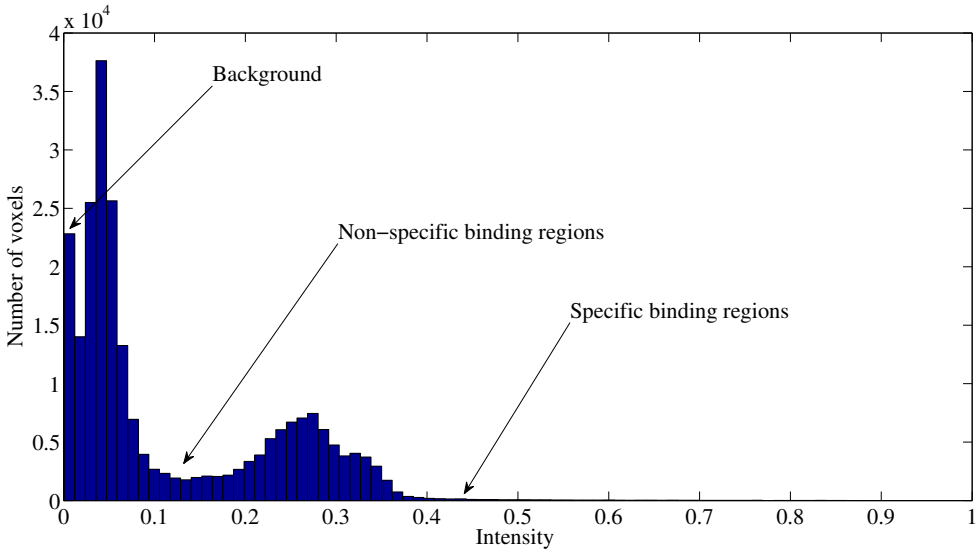

Figure 6.10: Mean histogram of the intensity values for intensity normalized images by Max-IN.

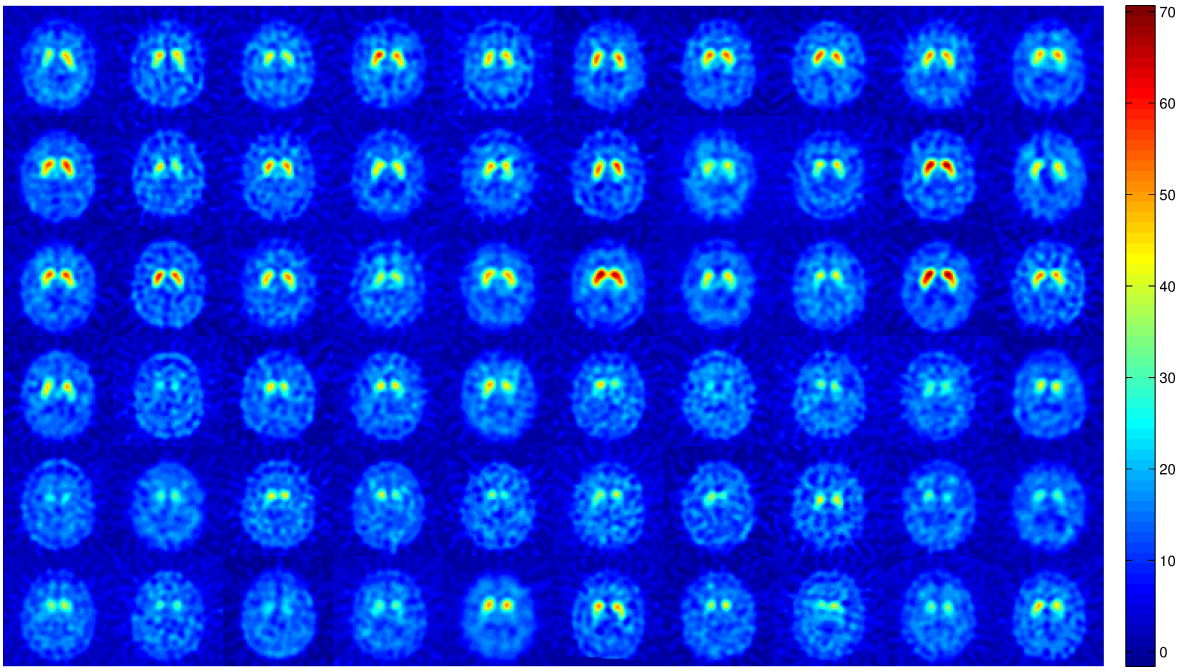

Figure 6.11: A given trans-axial slice of 60 DaTSCAN brain images from the database after normalization by α-stable distribution (α-stable-IN).

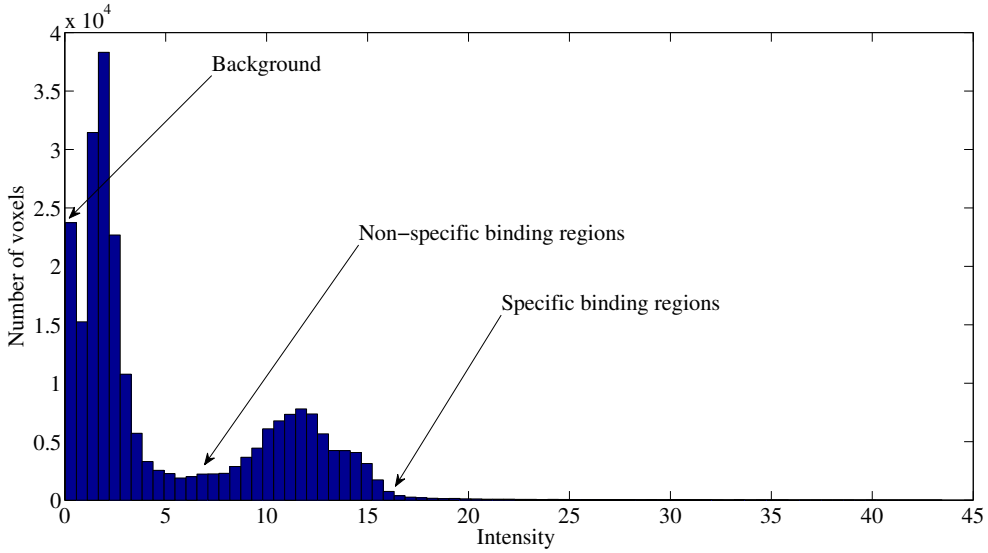

Figure 6.12: Mean histogram of the intensity values for intensity normalized images by α-stable approach.

The α-stable distribution approach is based on the fact that the shape of the distribution of intensity values is skewed and heavy-tailed, and therefore, it can be

modeled in a parsimonious way using the α-stable distribution [2]. The location-scale property is used to transform linearly the intensity values in each voxel. After normalization, the α-stable location and the scale parameters of the NS voxels in each of the DaTSCAN brain images are the same. Thus, the inter-subject differences in intensity values in the NS region is clearly mitigated after normalization, as illustrated in figures 6.11 and 6.12.

Nonlinear approach

The histogram equalization methodology is a nonlinear intensity transformation, which is based on the cumulative distribution function of values in each brain image. Since this technique is operationally equivalent to a ranking procedure, this robustness should be expected. Ranked data underlie many nonparametric statistical procedures that are robust to oddly shaped distributions and outlying observations. Thus, after applying this method, the intensity normalization affects the whole image, as shown in figures 6.13 and 6.14. Moreover, the tracer uptake in the striatum is matched for NC and PS subjects and the differentiation between these two classes becomes difficult. For this reason, we tried to apply the Hist-eq-IN only in the reference region, as illustrated in figures 6.15 and 6.16.

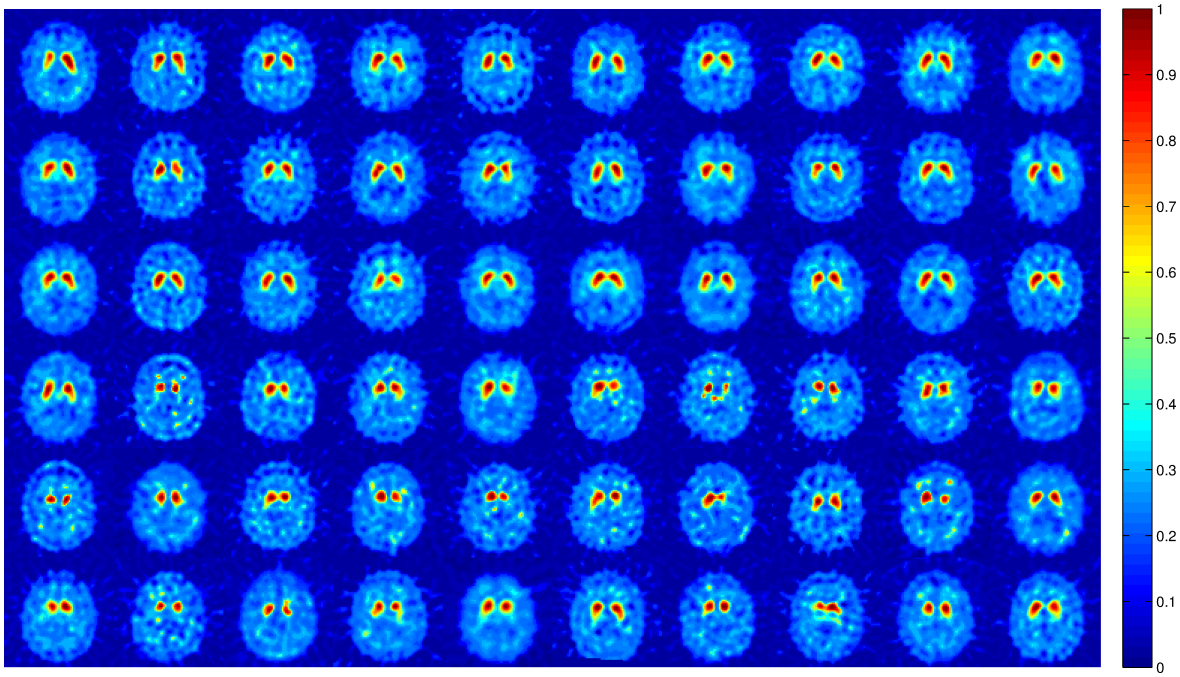

Figure 6.13: A given trans-axial slice of 60 DaTSCAN brain images from the database after normalization by the Histogram equalization method (Hist-eq-IN).

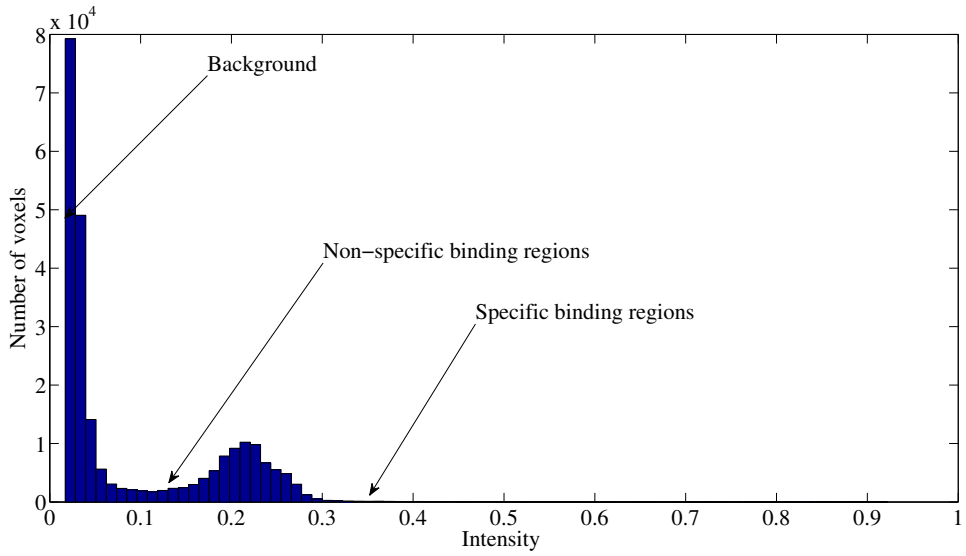

Figure 6.14: Mean histogram of the intensity values for intensity normalized images by Hist-eq-IN approach.

In Figure 6.15, the brain images became with similar intensity distribution in the reference region. Moreover, the intensity in the specific region is preserved after applying the Hist-eq-IN approach only in the NS region.

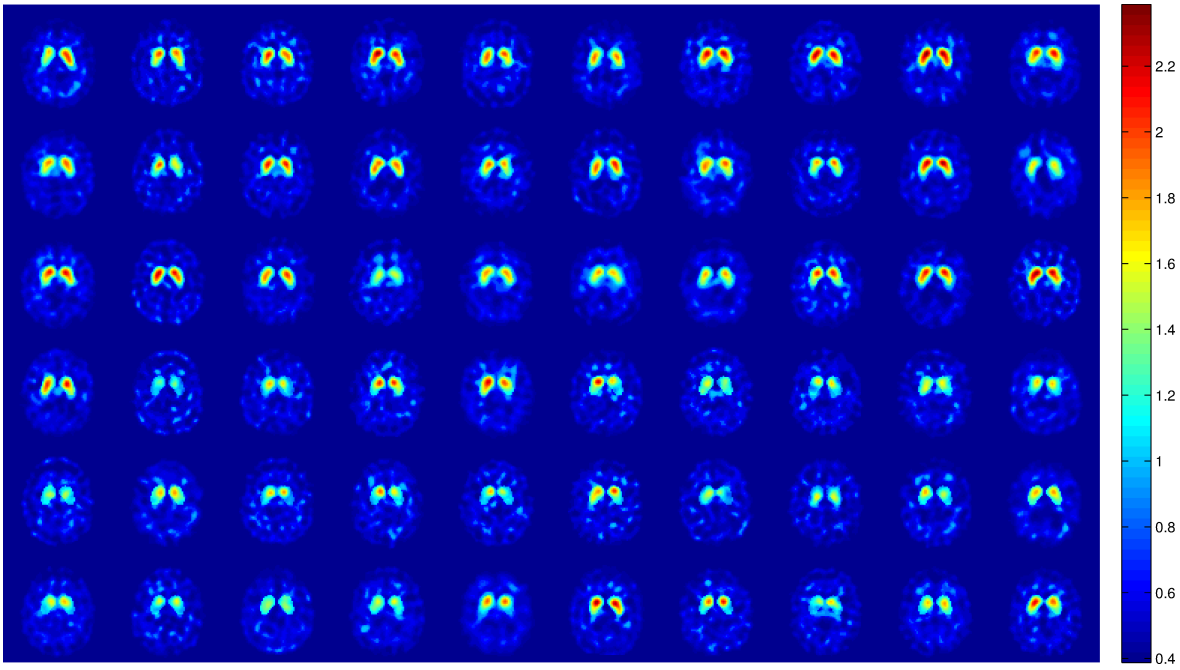

Figure 6.15: A given trans-axial slice of 60 DaTSCAN brain images from the database after normalization by the Hist-eq-IN in the NS region.

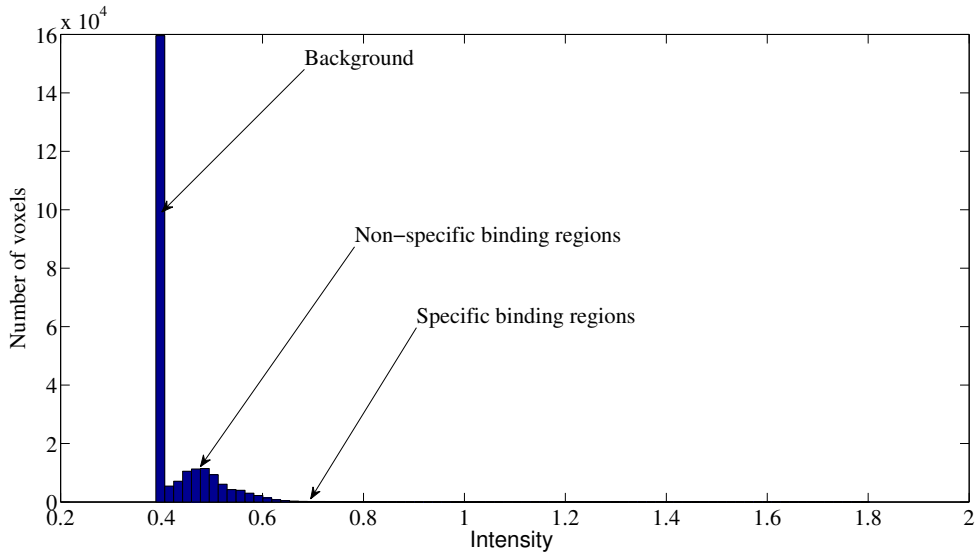

Figure 6.16: Mean histogram of the intensity values for intensity normalized images by Hist-eq-IN approach in the NS region.

6.2.1.3 Proposed approaches

As can be observed in the previous figures, these widely used normalization approaches for this low-resolution image modality where anatomical details in the NS region are lost, can alter the shape and the intensity of the striatal structures. For this purpose a different IN methods based on GMMs, MSE and MLR are proposed in order to acquire brain images with similar intensity distribution in the reference region and to increase the separation between the different binding regions.

GMM-based image filtering (FGMM)

We tested the GMM method for image modeling and cluster selection using the DaTSCAN database. The number of Gaussians used for modeling ROIs (parameter k in (4.3)) is selected according to an information criterion for model selection (see section 4.2.3), such as the one based on the minimization of the MSE between the original and the GMM-reconstructed images as shown in [211].
For our experiments we used machines running Intel® Xeon® processors with 2.67 GHz CPU frequency and having 48 GB of memory. In fact with this workstation, the computational time can reach 4-5 hours of a GMM model with $k = 125$ clusters for a reconstructed image subject.
In Figure 6.17 there a stability of the reconstruction error when the number of Gaussians increases. In this Thesis, we have used a model with $k = 64$ Gaussians that

leads to a good representation of FP-CIT SPECT images. Since the reconstruction error is small and due to the smoothness of the DaTSCAN images, a number of clusters equal to 64 is enough for achieving such a trade-off between the size of feature vectors and the ability of reconstruction (related with the model adjustment).

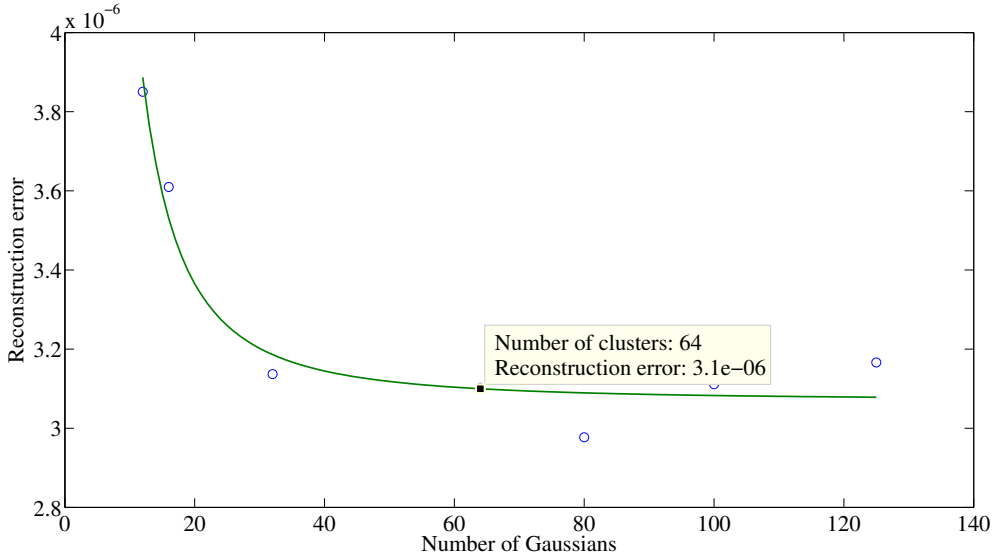

Figure 6.17: Reconstruction error of DaTSCAN SPECT images as a function of the number of Gaussians used in the model.

Thus, by applying the GMM approach, an accurate model is obtained by the superposition of 64 Gaussians with a similar mean of intensity distribution histogram, as can be seen on Figure 6.18.
The intensity radioactivity values of the GMM-reconstructed images, both in the specific and non-specific region approximate the intensity distribution of the raw data. Thus, the intensity profile of each image is conserved (similar to Figure 6.1).

The resulting mixture model for each functional subject image is used for IN according to a cluster selection strategy, as explained in section 4.3 and the appendix A.1.

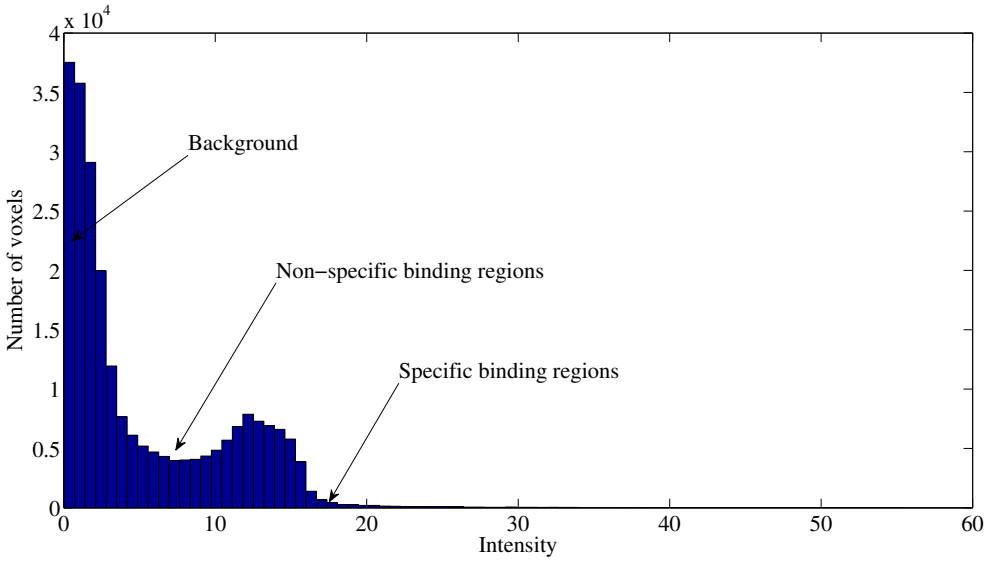

Figure 6.18: Mean histogram of the intensity values for reconstructed images by the GMM method: the GMM histogram approximates the intensity distribution in the original DaTSCAN images.

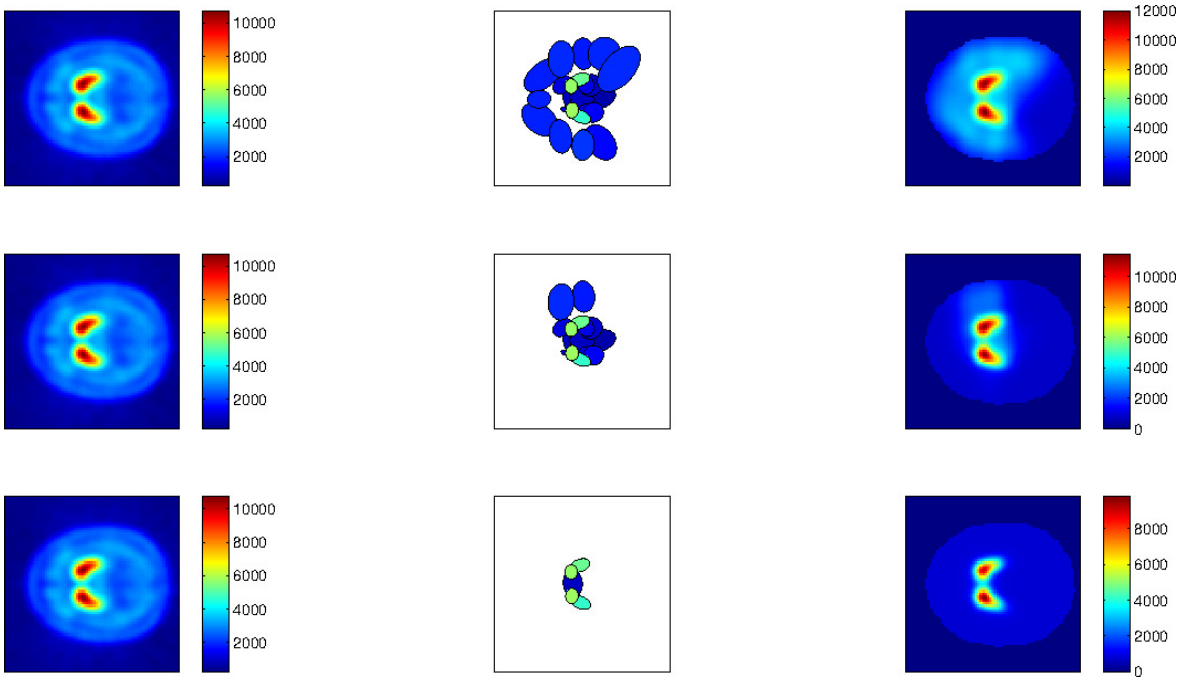

Figure 6.19: Left column: DaTSCAN image of average normal subjects. Central column: different location and intensity of relevant clusters for different normalized probability threshold values $\eta = 4 \cdot 10^{-6}$, $4 \cdot 10^{-5}$ and $4 \cdot 10^{-4}$. Right column: filtered GMM image reconstruction according to eq. 4.16), which remove the irrelevant clusters in the occipital region.

Figure 6.19 shows a normalized average image after the filtering process by means of GMM (right column). Different normalized probability threshold values can be used to obtain the intensity normalization in the NS region. According to these normalized thresholds, the relevant clusters that contribute to the intensity of the striatal region are preserved (central column) and the remaining ones are removed.
In accordance with this procedure, we provided a filtered GMM image reconstruction that: *i*) preserves the intensity in the specific region, and *ii*) automatically normalizes the intensity in the NS areas such that the inter-subject intensity differences are reduced and the irrelevant clusters that may represent different noise sources are automatically removed.

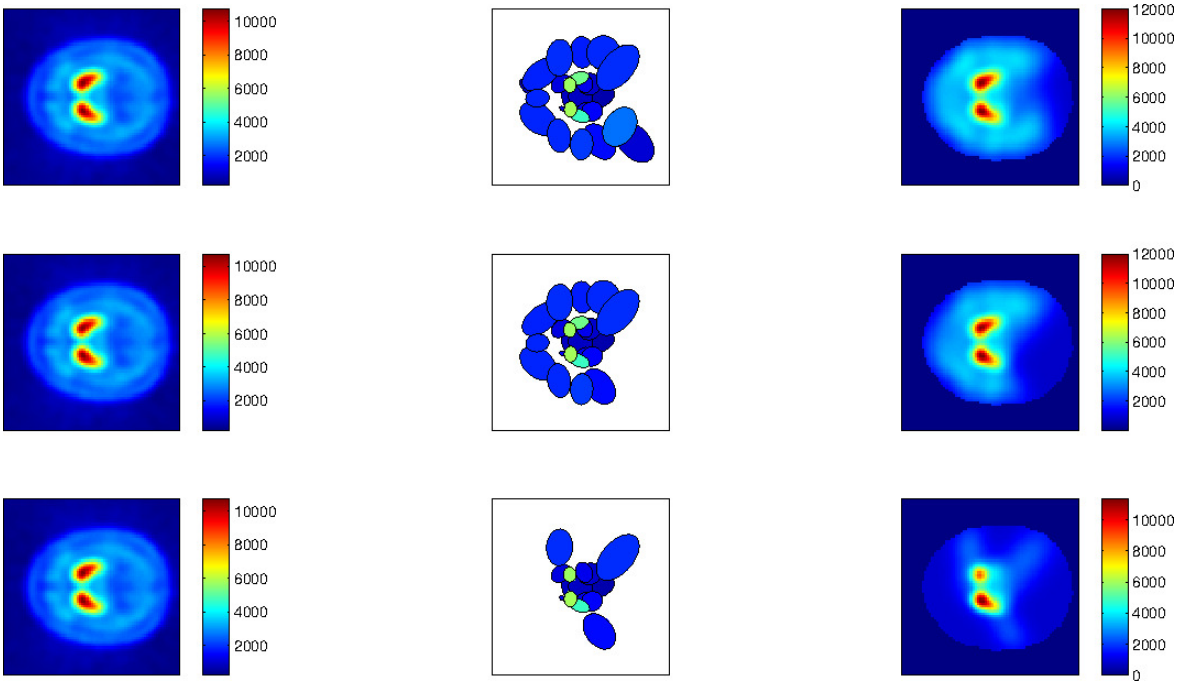

Figure 6.20: Left column: DaTSCAN image of average normal subjects. Central column: different location and intensity of relevant clusters for different fraction of N_s, α = 95%, 75% and 50%. Right column: filtered GMM image reconstruction according to eqs. 4.16 and 4.17, which remove the irrelevant clusters in the occipital region.

Figure 6.20 illustrates the effect of α on the filtering process, specifically for a value less then 75% of N_s which affects the striatal signal. For the filtering stage, we choose $\alpha = 75\%$.
Thus, the proposed GMM-based image filtering approach entails noise reduction and the increase of the difference between the average intensities in the striatal and NS regions, as depicted in Figure 6.21. Furthermore, the proposed nonlinear image

filtering provides an IN with respect to the reference region (NS region) and maintains the original intensity values in the striatum (specific region). This permitted a fair comparison between subjects based only on DaTSCAN activity distribution in the striatal structures.

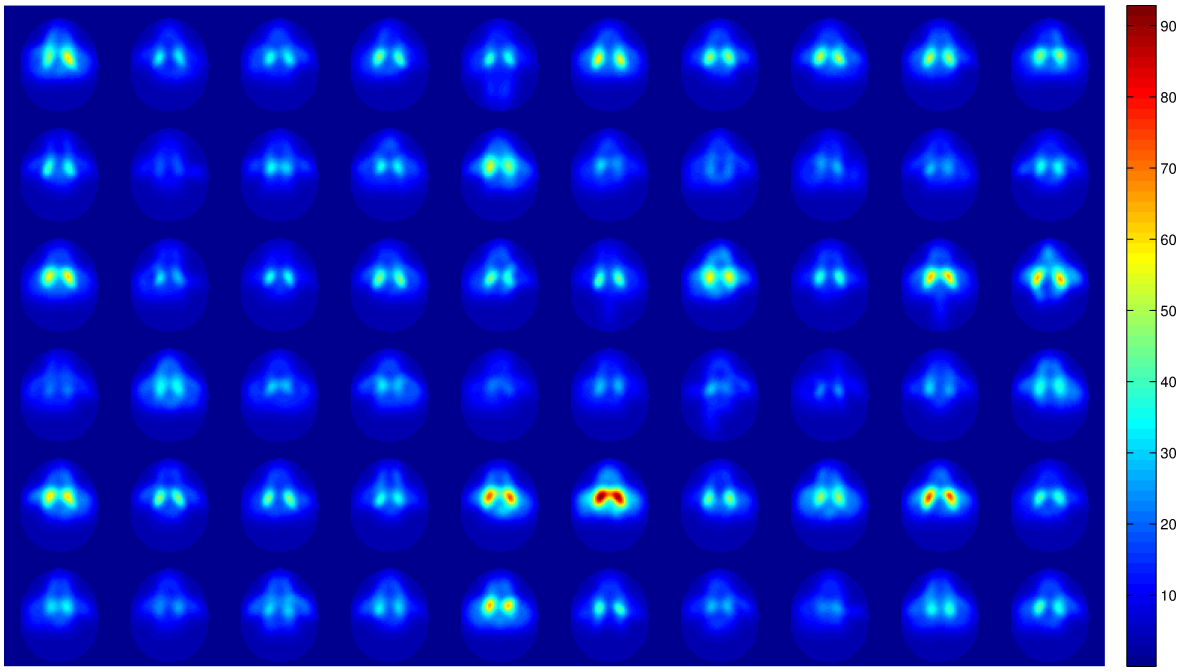

Figure 6.21: A given trans-axial slice of 60 FGMM, post-normalization DaTSCAN brain images: 30 NC + 30 PS.

Figure 6.21 shows one trans-axial slice for the 60 intensity-normalized DaTSCAN brain images using the proposed FGMM method.

Figure 6.22 shows the post-normalization mean histogram of FGMM approach for the DaTSCAN dataset. Observe that there is a high concentration of low-intensity voxels in the background (on the far left). This makes sense as we assume that the removed Gaussians according to a normalized probabilistic threshold do not contribute to the intensity in the NS region, reducing its variance.

These figures prove that, after applying IN, the inter-subject intensity differences in the NS region are clearly reduced. In this sense, relevant information in the striatum, as well as in the NS region affecting the striatum area, is also preserved. This is the key area used to perform a visual diagnosis of PD.

The complexity of the proposed system depends on the number of Gaussians

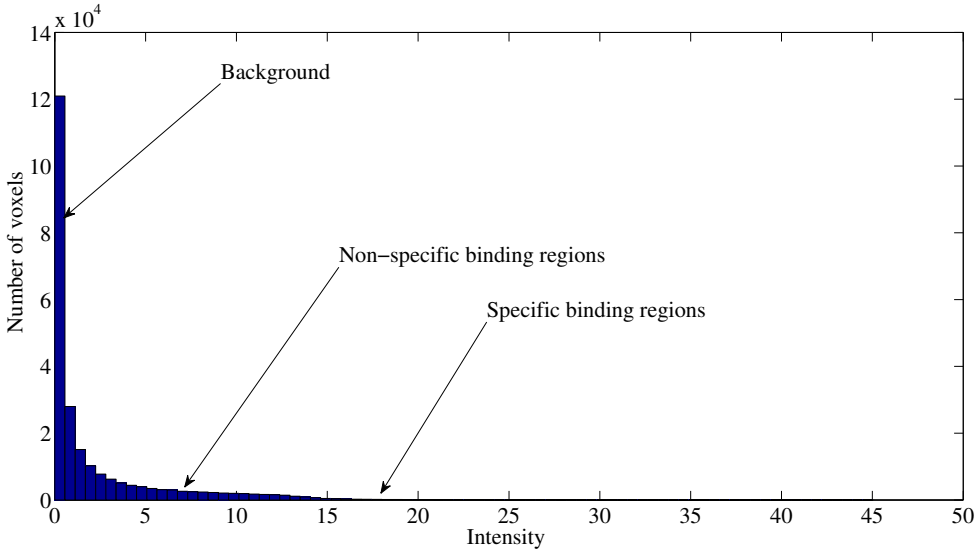

Figure 6.22: Mean histogram of the intensity values for FGMM, post-normalization DaTSCAN images. Take note that the intensity radioactivity values (from 3.94 to 11.8) for all the images are very similar after normalization. The histogram is passed through a nonlinear filtering process to eliminate the Gaussian noise and an expected blood supply presented in the reference region of the original images.

which are used to model the brain data set as well as on the number of voxels in the image [230]. The main implementation problem is the large number of Gaussians, that leads to high computational complexity of the EM algorithm, as shown in section 4.2.3 and in [231]. In previous works, such as in [212] and in section 4.2.2, the computation of the EM algorithm is discussed.

Mean Squared Error (MSE) Optimization at voxel level

By applying this proposed intensity normalization method detailed in the methodological section 5.1, the intensity heterogeneity in the NS region is reduced and the difference between the striatum and the background uptakes is increased as shown in Figure 6.23.
In Figure 6.24, The intensity radioactivity values for all the images are very similar after normalization in NS binding regions (its intensity values are between 14.93 and 15.5). The histogram is passed through a linear transformation that eliminates the Gaussian noise and an expected blood supply presented in the reference region of the original images. Therefore, this normalization method is suitable for preprocessing of ^{123} I-ioflupane brain images for diagnosis purposes.

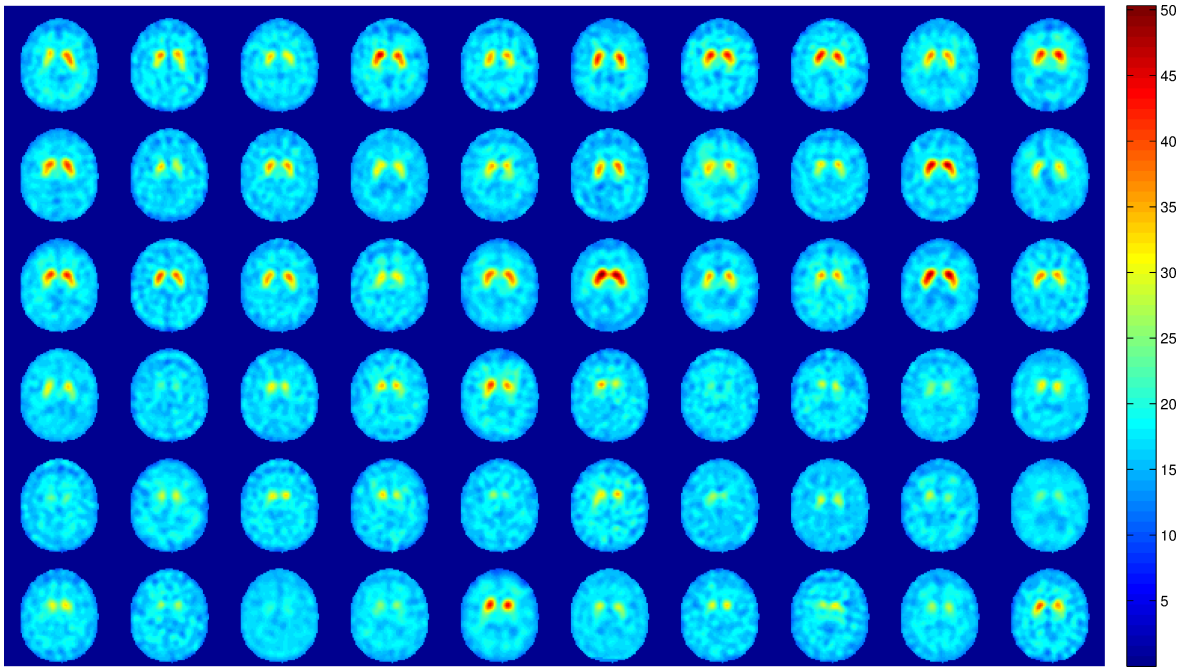

Figure 6.23: A given trans-axial slice of 60 normalized DaTSCAN brain images: 30 NC + 30 PS by MSE approach.

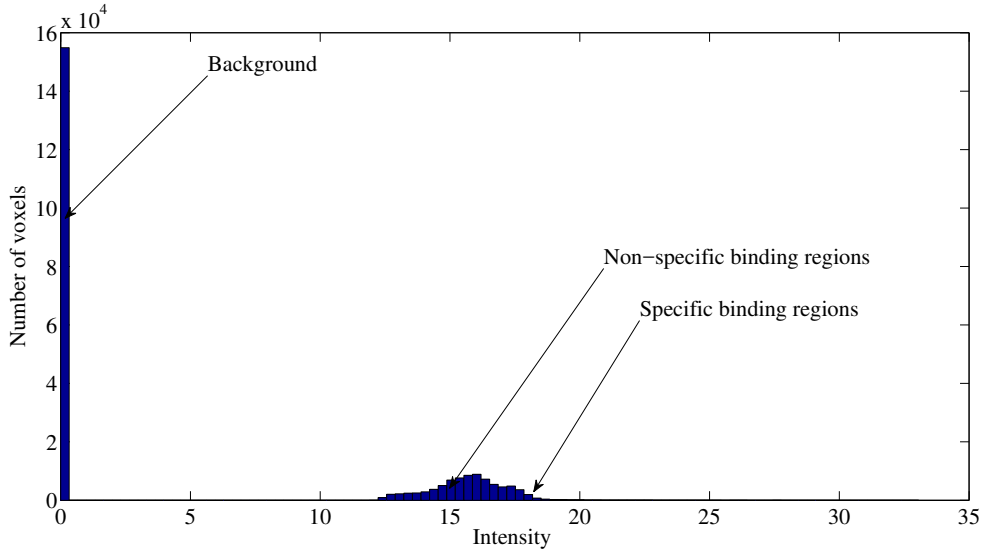

Figure 6.24: Mean histogram of the intensity values for MSE, post-normalization DaTSCAN images.

Mean Squared Error (MSE) Optimization at Gaussian level

This normalization scheme is a combination between the two previous proposed approaches, i.e., the GMM and the MSE.

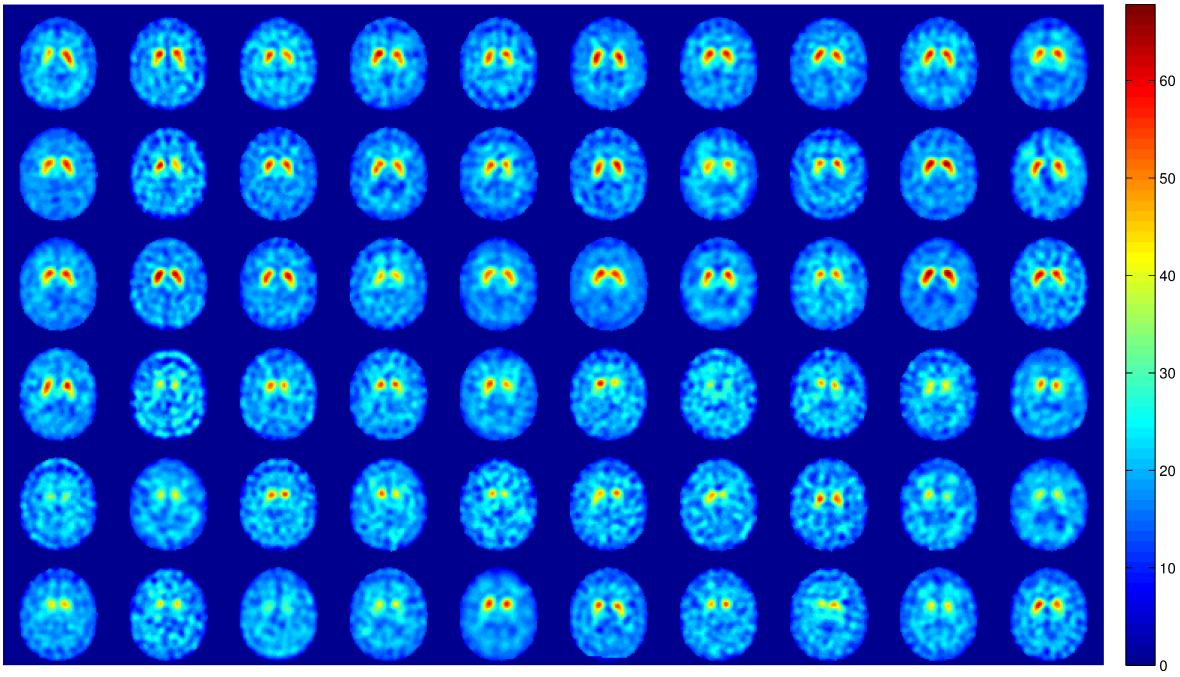

Figure 6.25: A given trans-axial slice of 60 normalized DaTSCAN brain images: 30 NC + 30 PS by MSE-GMM approach.

The motivation behind this new intensity normalization method is to overcome the computational cost of the image preprocessing stage using the GMM-based algorithm. Thus, the linear transformation of the intensity values is applied on the cluster level.
The qualitative effects can be seen more clearly at the image level in the results of Figure 6.25. Moreover, this figure proves that, post-normalization, the contrasts of relevant features in the striatum are improved and the inter-subject intensity differences in the NS region (between 14.7 and 17) are clearly reduced, as illustrated in Figure 6.26.

Model-Based Multivariate Linear Regression (MLR) Approach

This new method is an extension of the MSE normalization approach presented in section 5.1. The major advantage of this normalization methodology is that it can

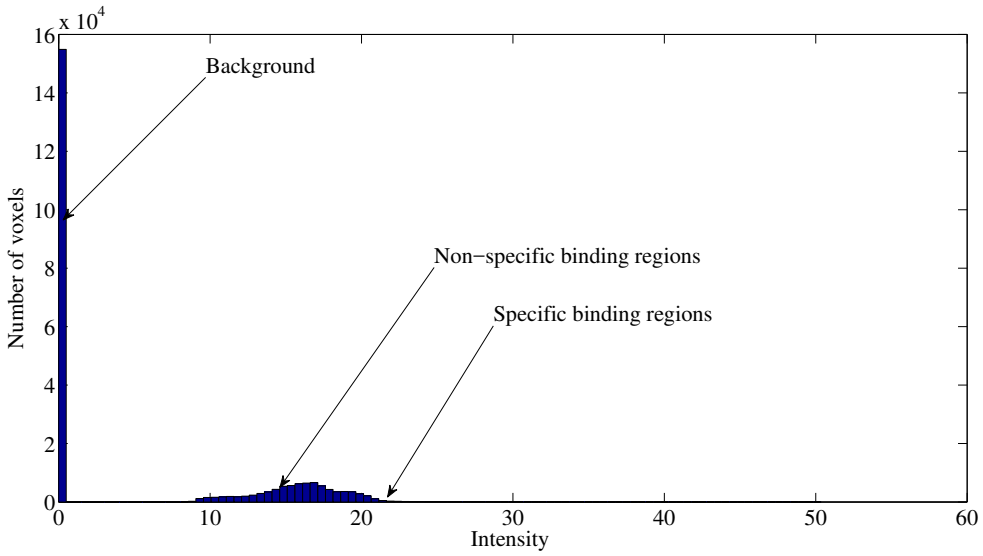

Figure 6.26: Mean histogram of the intensity values for MSE-GMM, post-normalization DaTSCAN images.

be applied to the whole medical image, not only in a NS region. Thus, it is independent from the reference region. The qualitative effect of this method is presented in figures 6.27 and 6.28.
In conclusion, these figures demonstrate that the inter-subject intensity differences in the NS region due to several effects [30, 31, 156] are clearly reduced after the normalization using our proposed methods. Unlike those ones shown in compared approaches, the processed images are smoothed and preserve the relevant information in the striatum region. In addition, the proposed normalization schemes allow us to guarantee that the inter-subject differences in the DaTSCAN image database (NC and PS subjects) are due only to the uptake of the tracer in the discriminant region (striatum) and not due to the baseline calibration of the gamma camera used for the acquisition.

6.2.2 Quantitative image analysis

In order to quantitatively measure the efficiency of the proposed intensity normalization methods, we compare them with the spatial normalized DaTSCAN brain images (before intensity normalization) and several widely used normalization methods. The comparison is carried out by depicting the error bars, which are estimated using 25th and 75th percentile of the mean histogram in the NS region, as in [2] (see figures 6.29 and6.30). These error bars present the inter-subject intensity variability that is clearly reduced by our normalization methods based on the nonlin-

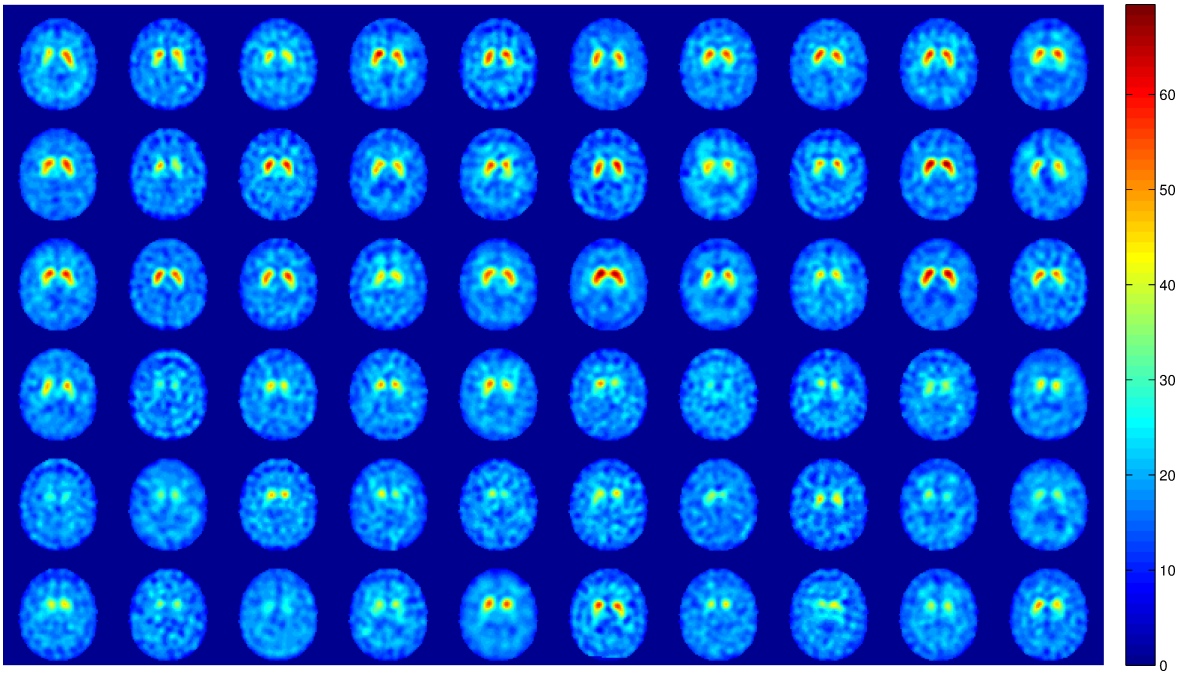

Figure 6.27: A given trans-axial slice of 60 normalized DaTSCAN brain images: 30 NC + 30 PS by MLR approach.

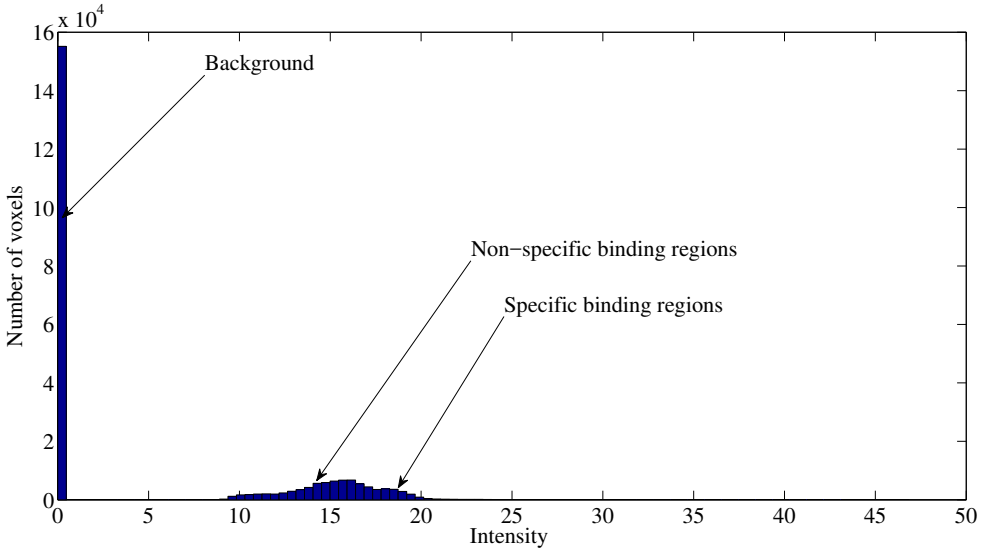

Figure 6.28: Mean histogram of the intensity values for MLR, post-normalization DaTSCAN images. The inter-subject variability is reduced in the NS region (its intensity values are between 14 and 16).

ear filtering process (FGMM approach) and a linear intensity transformation (MSE, MSE-GMM and MLR approaches), as displayed in figures 6.29.b, 6.29.c, 6.29.d and

6.29.e. Thus, these methodologies entail a greater degree of homogeneity in the intensity values of the NS region, which is in fact the main goal of our intensity normalization procedures.
Figure6.30 depicts the inter-subject intensity variability that is quietly reduced by the compared methods in the reference region.
The proper adjustment of the resulting normalized set of images can be evaluated by means of some defined metrics that provide a measure of the difference between two sets of samples, such as the Kullback-Leibler divergence (KL) [194], the Euclidean distance (ED) and the Jeffreys divergence (JD) measure [232]. In this particular case, the set of samples to be evaluated with these metrics is the histogram of the normalized 3D image, referred to the histogram of a reference target 3D image (typically, the mean image of the healthy subjects) in the NS region. Lower values of these divergences represent less difference between the two distributions of histograms. Thus, the difference between the probability distribution of each image denoted by Q and the probability distribution of the mean brain image denoted by P is evaluated for all subjects before and after intensity normalization using KL, ED and JD divergences are defined as:

$$KL\ (P\|Q) = \sum_{i=1}^{n} \ln\left(\frac{P(i)}{Q(i)}\right)\ (P(i)) \tag{6.1}$$

$$ED\ (P\|Q) = \sum_{i=1}^{n} |P(i) - (Q(i)| \tag{6.2}$$

$$JD\ (P\|Q) = \int_{-\infty}^{+\infty} P(i)\ \ln\left(\frac{P(i)}{Q(i)}\right)\ d(i) + \int_{-\infty}^{+\infty} Q(i)\ \ln\left(\frac{Q(i)}{P(i)}\right)\ d(i) \tag{6.3}$$

where n is a fixed number of bins. We use the discretized approximation of JD by replacing the integrals with the summations over a fixed number of bins. The inter-subject distance is calculated quantitatively between these two distributions, both before normalization, for raw images and after normalization, using the proposed and the compared methods.
The lowest KL, ED and JD values and the lowest error are obtained (in terms of the standard deviation) by the proposed normalization methods based on linear intensity normalization by MSE optimization at voxel and Gaussian levels, the GMM-based image filtering and the MLR approach as presented in tables 6.3, 6.4 and 6.5. This experimental result suggests that the proposed methods outperform the compared methods, in entailing more intensity homogeneity in the NS region for the different classes.

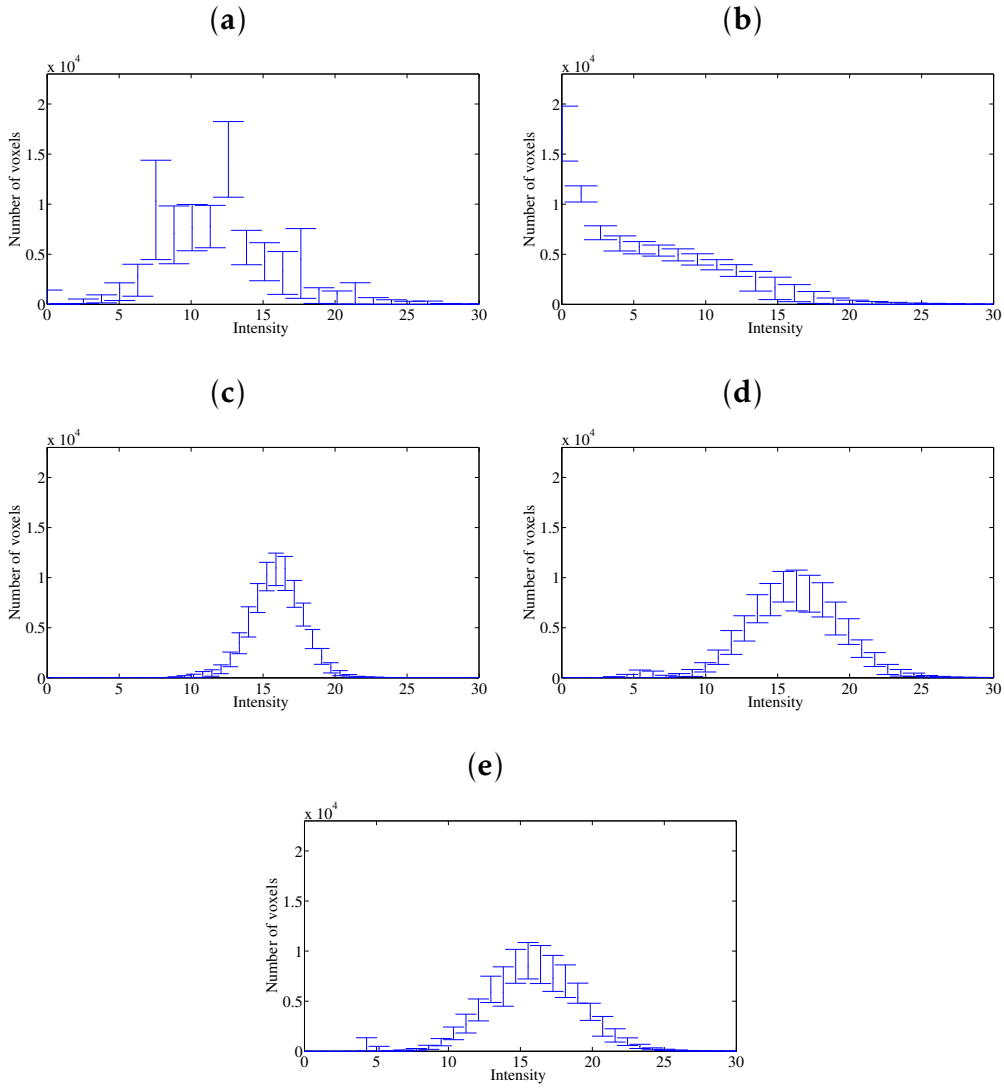

Figure 6.29: Error bars for the mean histogram of the intensity values in the NS region for DaTSCAN images before and after normalization using the proposed approaches. (a): Raw images, (b): FGMM images, (c): MSE images, (d): MSE-GMM images and (e) MLR images. Error bars are calculated considering 25th and 75th percentiles.

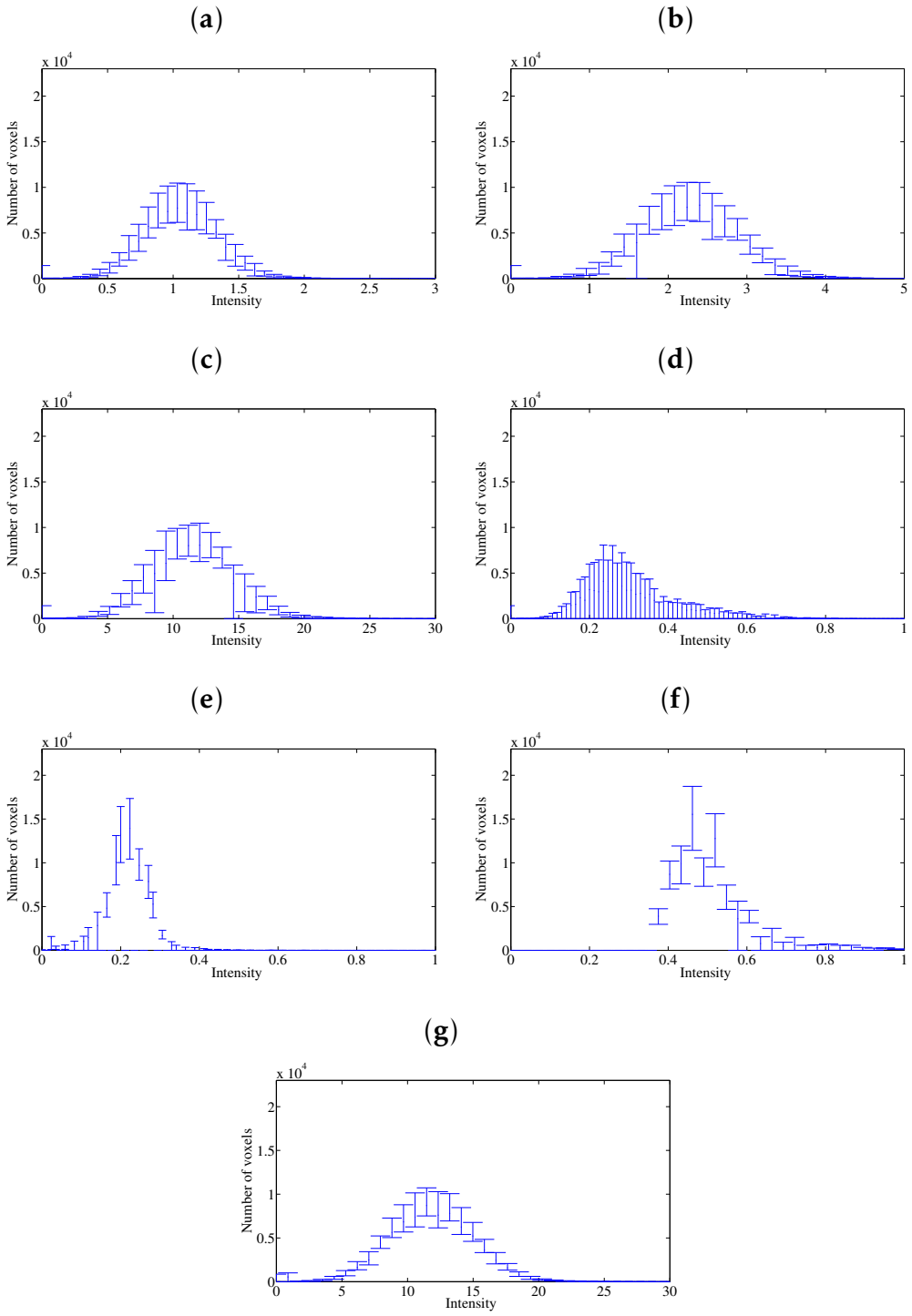

Figure 6.30: Error bars for the mean histogram of the intensity values of DaSCAN images in the NS region for the different compared approaches. (a): BR_{all} images, (b): Integral-IN images, (c): MKL-IN images, (d): Max-IN images, (e): Hist-eq-IN images, (f): Hist-eq-IN (NS region) images and (g): α-stable-IN images. Error bars are calculated considering 25th and 75th percentiles.

Table 6.3: Mean Kullback-Leibler distance and standard deviation for DaTSCAN SPECT images before and after intensity normalization methods in the non-specific region.

Normalization approach	Class	Kullback-Leibler distance
Raw data (spatial normalization)	NCs	0.3021±0.2342
	PS	0.2882±0.2412
	NCs+PS	0.2957±0.2367
$BR_{all} - IN$	NCs	0.2549±0.1681
	PS	0.3308±0.2279
	NCs+PS	0.2902±0.2009
Integral-IN	NCs	0.2498±0.1611
	PS	0.3238±0.2034
	NCs+PS	0.2842±0.1850
MKL-IN	NCs	0.2180±0.1443
	PS	0.2875±0.2716
	NCs+PS	0.2503±0.2150
Max-IN	NCs	0.6931±0.2988
	PS	2.1852±1.2460
	NCs+PS	1.3863±1.1490
α-stable-IN	NCs	0.2075±0.1496
	PS	0.2836±0.1792
	NCs+PS	0.2428±0.1678
Hist-eq-IN	NCs	0.1986±0.1388
	PS	0.2632±0.1808
	NCs+PS	0.2286±0.1623
Hist-eq-IN in NS region	NCs	0.2004±0.1389
	PS	0.2902±0.2441
	NCs+PS	0.2421±0.1993
FGMM	NCs	**0.0671±0.0588**
	PS	**0.0777±0.0575**
	NCs+PS	**0.0720±0.0582**
MSE	NCs	**0.1025±0.0588**
	PS	**0.1196±0.0928**
	NCs+PS	**0.1105±0.0766**
MSE-GMM	NCs	**0.1523±0.0789**
	PS	**0.1754±0.0894**
	NCs+PS	**0.2421±0.1993**
MLR	NCs	**0.1618±0.0670**
	PS	**0.1600±0.0866**
	NCs+PS	**0.1610±0.0764**

Table 6.4: Mean Jeffreys Divergence and standard deviation for original DaTSCAN images and intensity normalized images in the non-specific region.

Normalization approach	Class	Jeffreys Divergence
Raw data	NCs	0.7408±0.5743
(spatial normalization)	PS	3.2127±0.6336
	NCs+PS	0.7422±0.5943
BR_{all}	NCs	0.1634±0.0927
	PS	2.8289±0.2387
	NCs+PS	0.1860±0.1432
Integral-IN	NCs	0.1655±0.0867
	PS	2.8100±0.2320
	NCs+PS	0.1873±0.1276
MKL-IN	NCs	0.1981±0.1443
	PS	2.9990±0.4418
	NCs+PS	0.2484±0.3831
Max-IN	NCs	0.5482±0.2807
	PS	2.7281±0.2533
	NCs+PS	1.3048±1.2823
α-stable-IN	NCs	0.1670±0.1240
	PS	0.7154±0.1504
	NCs+PS	0.1755±0.1637
Hist-eq-IN	NC	0.1671±0.0800
	PS	0.4729±0.2499
	NC+PS	0.1916±0.1450
Hist-eq-IN in NS region	NCs	0.1717±0.0596
	PS	2.7416±0.0971
	NCs+PS	0.1789±0.0803
FGMM	NCs	**0.1095±0.0525**
	PS	**2.1166±0.1819**
	NCs+PS	**0.1270±0.0604**
MSE	NCs	**0.1211±0.0685**
	PS	**2.8498±0.2440**
	NCs+PS	**0.1429±0.1203**
MSE-GMM	NCs	**0.1511±0.0690**
	PS	**0.4166±0.1959**
	NCs+PS	**0.1657±0.0974**
MLR	NCs	**0.1469±0.1267**
	PS	**0.7645±0.2727**
	NCs+PS	**0.1633±0.1394**

Table 6.5: Mean Euclidean distance and standard deviation for original DaTSCAN images and intensity normalized images in the non-specific region.

Normalization approach	Class	Euclidean distance
Raw data	NCs	0.5761±0.2567
(spatial normalization)	PS	1.2363±0.0757
	NCs+PS	0.5601±0.2479
$BR_{all} - IN$	NCs	0.5058±0.2220
	PS	1.2621±0.0363
	NCs+PS	0.5430±0.2303
Integral-IN	NCs	0.4998±0.2068
	PS	1.2592±0.0361
	NCs+PS	0.5394±0.2153
MKL-IN	NCs	0.4758±0.1838
	PS	1.2655±0.0706
	NCs+PS	0.4978±0.2095
Max-IN	NCs	0.9680±0.2312
	PS	1.4916±0.1181
	NCs+PS	1.1773±0.3286
α-stable-IN	NCs	0.4241±0.2000
	PS	1.2657±0.0332
	NCs+PS	0.4529±0.2012
Hist-eq-IN	NCs	0.4477±0.1909
	PS	1.3116±0.0240
	NCs+PS	0.4830±0.1982
Hist-eq-IN in NS region	NCs	0.4356±0.1918
	PS	1.3141±0.0257
	NCs+PS	0.4680±0.2044
FGMM	NCs	**0.2166±0.0974**
	PS	**0.7235±0.1038**
	NCs+PS	**0.2218±0.0961**
MSE	NCs	**0.3091±0.1012**
	PS	**1.3057±0.0185**
	NCs+PS	**0.3022±0.1294**
MSE-GMM	NCs	**0.3790±0.0899**
	PS	**1.2688±0.0189**
	NCs+PS	**0.3703±0.0867**
MLR	NCs	**0.3332±0.1139**
	PS	**1.2613±0.0140**
	NCs+PS	**0.3605±0.1218**

Tables 6.3, 6.4 and 6.5 reveal that the inter-subject differences in intensity values in the NS region are quantitatively mitigated after the intensity normalization using the proposed methodologies.
Moreover, Figure 6.31 shows the inter-subject intensity variability in the striatum for NC subjects (first row) and PS subjects (second row) in terms of mean histogram and error bars. Notice that the intensity distributions obtained by our approaches are clearly different in shape and variability for NC and PS subjects (specifically the first row versus the second row of Figure 6.31. b and Figure 6.31. c.
Figures 6.32 and 6.33 depict the error bars for the mean histogram of the intensity values in the striatum region for the different compared approaches.
When the Hist-eq-IN approach is applied in the whole image, the intensity distribution of the striatum region is deeply affected in both classes, as shown in Figure 6.33.a compared to Figure 6.31.a. For this reason, we tried to apply this method also in the reference region (NS region).
In order to further analyze these results, we propose the following sections in which these distributions are considered in classification tasks.

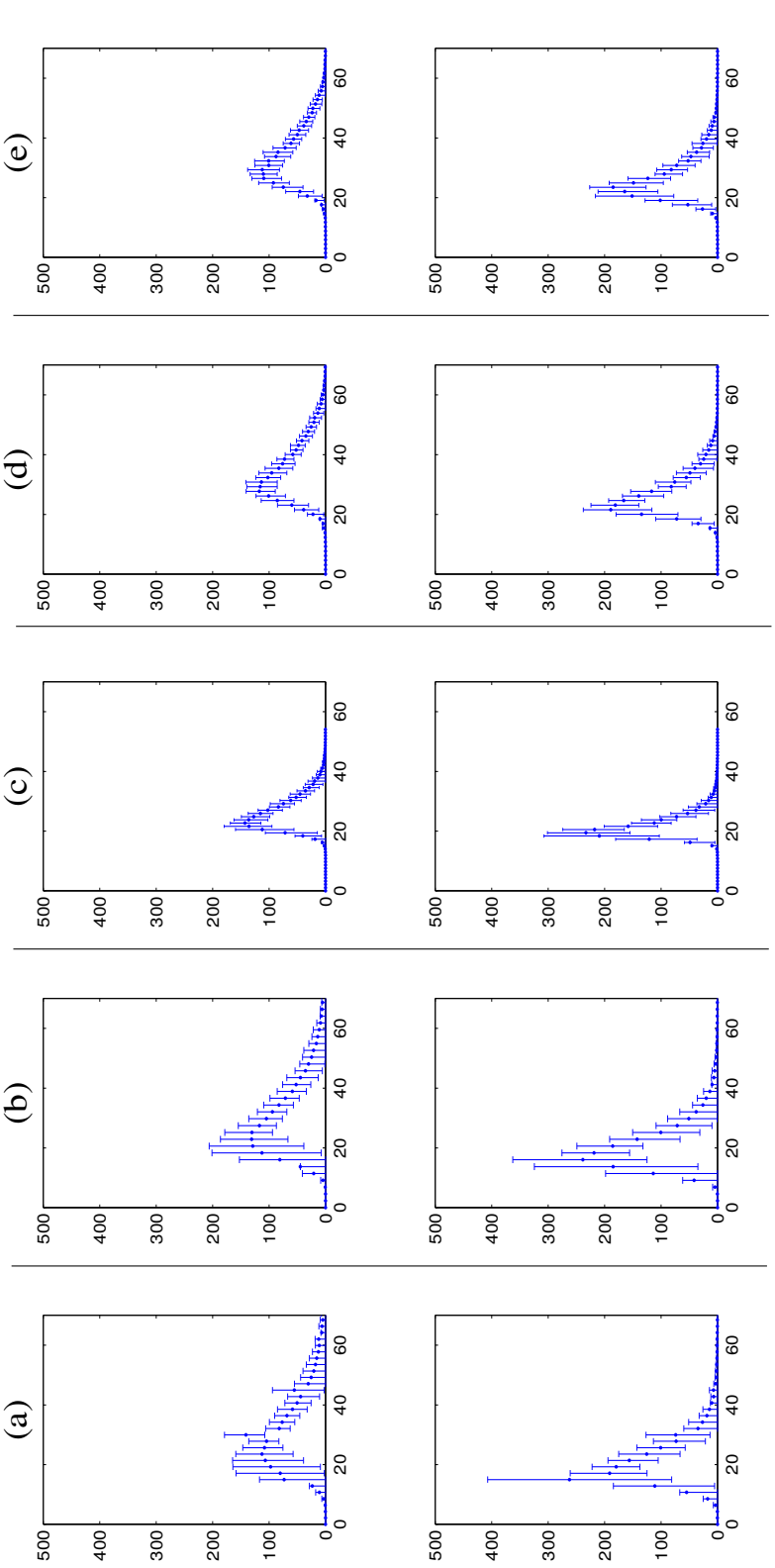

Figure 6.31: Mean histograms and error bars in the striatum region for 127 DaTSCAN images before and after intensity normalization using the proposed approaches and keeping separate distributions for the two different classes. The first row is for NC subjects and the second row is for PS subjects. (a): Original DaTSCAN images, (b): FGMM images, (c): MSE images, (d): MSE-GMM images and (e): MLR images. Error bars are calculated considering 25th and 75th percentiles. The x-axis represents the intensity. The y-axis indicates the number of voxels with a given level in the striatum region.

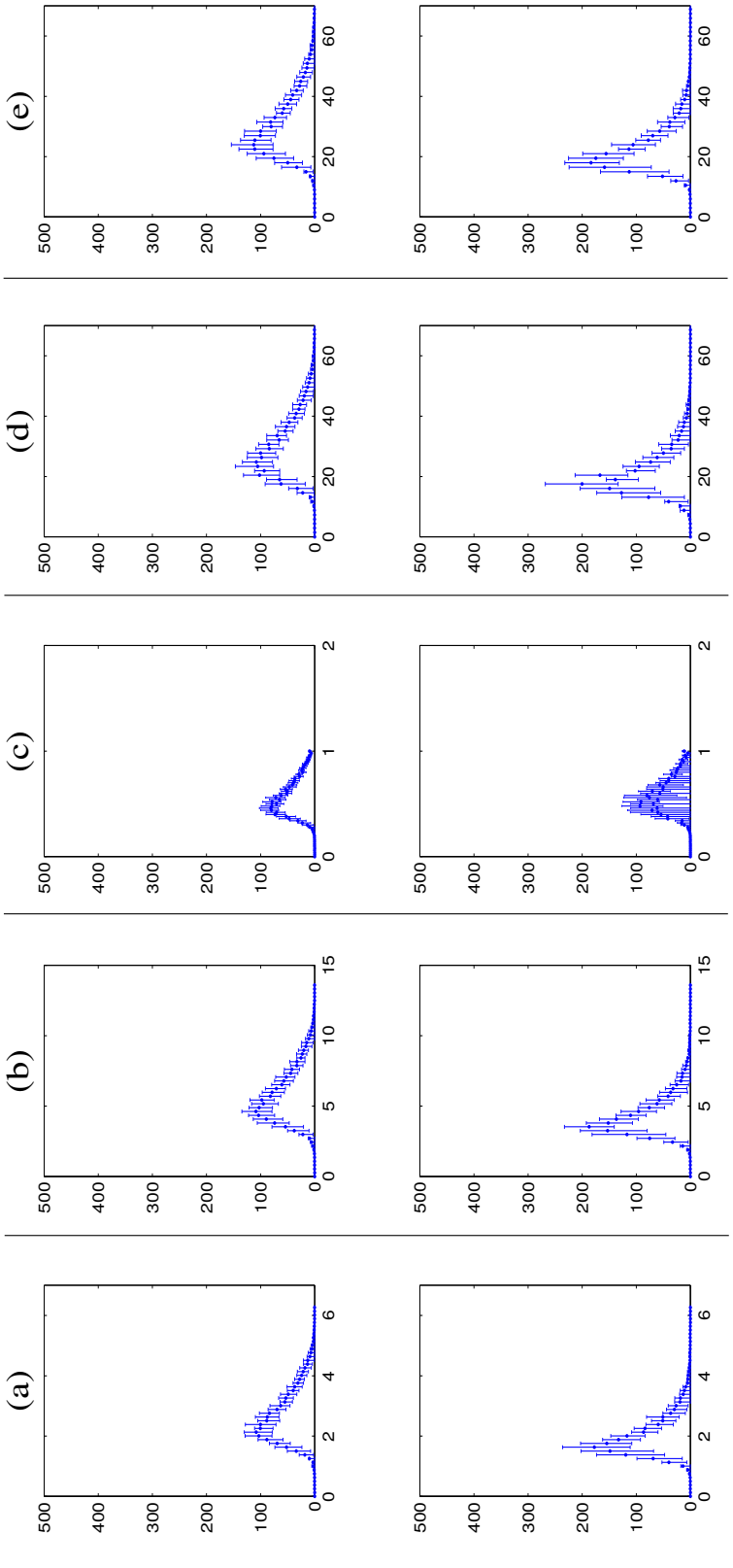

Figure 6.32: Mean histograms and error bars in the striatum region for 127 intensity normalized DaTSCAN images using the compared approaches and keeping separate distributions for the two different classes. The first row is for NC subjects and the second row is for PS subjects. (a): BR_{all} images, (b): Integral-IN images, (c): Max-IN images, (d): MKL-IN images and (e): α-stable-IN images. Error bars are calculated considering 25th and 75th percentiles. The x-axis represents the intensity. The y-axis indicates the number of voxels with a given level in the striatum region.

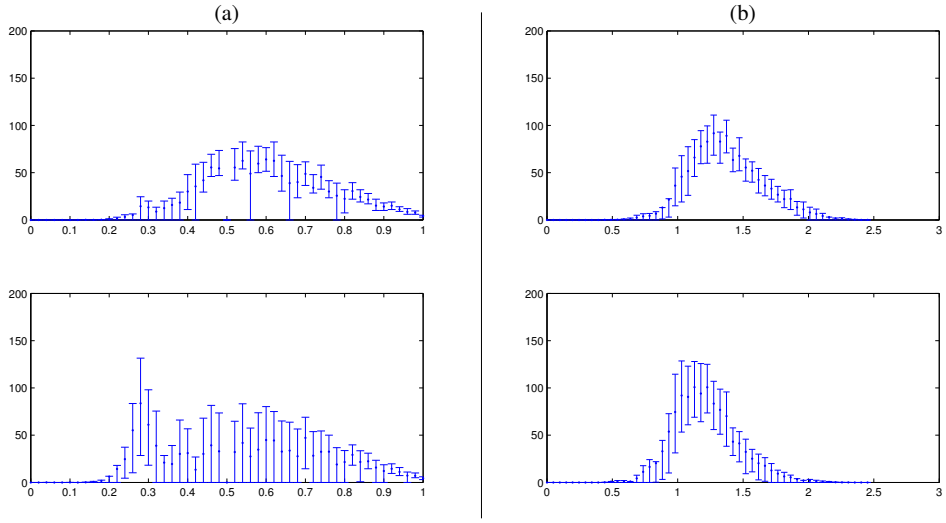

Figure 6.33: Mean histograms and error bars in the striatum region for 127 intensity normalized DaTSCAN images using the histogram equalization method and keeping separate distributions for the two different classes. The first row is for NC subjects and the second row is for PS subjects. (a): Hist-eq-IN images and (b): Hist-eq-IN (NS region) images. Error bars are calculated considering 25th and 75th percentiles. The x-axis represents the intensity. The y-axis indicates the number of voxels with a given level in the striatum region.

6.2.3 Quantitative classification performance of Parkinsonism

The benefits of the proposed intensity normalization methods are evaluated also for PS detection. Several experiments were performed on the previously described database in section 6.1.1. The proposed methods are assessed on the task of discriminating PS from NC and compared to widely used IN techniques. Thus, each intensity normalization procedure leads to a different dataset. For each dataset, the performance of the Support Vector Machines (SVM) classifier was studied. This classifier is described in detail in appendix B.1.
Only linear SVM has been used to compute the results, due to the large number of input features to the classifier, to obtain more generalizable results and to avoid the small sample size problem [19]. In this Thesis, the accuracy estimation of the different datasets is performed following a Leave-One-Out (LOO) cross-validation strategy (see appendix B.2).

6.2.3.1 Selection of the Region of Interest (ROI)

The ^{123} I-ioflupane radiopharmaceutical provides brain images with higher activation in the striatum, a region of high interest for the diagnosis of PS [107]. Figure 6.34 reveals that most of the activity is gathered in the striatum. However, the images contain a lot of information (a large number of voxels) that is not relevant for the diagnosis of the disorder. For this purpose, a required binary mask is applied to each image for the different datasets in order to select only the high-intensity voxels of the striatum area. Once the images of the different datasets are ready for the classification process, the relevant information has to be extracted. Only the voxels that contain relevant information in terms of discrimination ability should be chosen. In the case of Parkinson's disease, this region is, as previously mentioned, the striatum. For this purpose, we need to apply a binary mask for each image which is computed as follows:

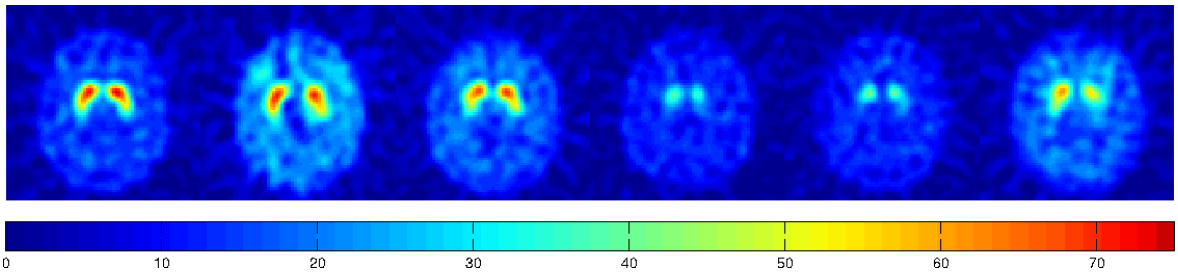

Figure 6.34: A given trans-axial slices of 6 selected brain images; 3 healthy subjects (left) and 3 PS patients (right) of raw DaTSCAN brain images.

$$m_i = \begin{cases} 1 & \text{if} \quad c_i \geqslant 0.45\ max\ c_i \\ 0 & \text{otherwise} \end{cases} \tag{6.4}$$

where $m_i, i = 1...n$ are the n voxels of the mask with value (0 or 1), $c_i, i = 1...n$ are the intensity of n voxel at position i of an intermediate image, c, and $max\ c_i$ is the highest intensity of c. The image c is computed by using the average of all NCs in each dataset. Applying this mask allows to select the voxels whose intensity is high (compared with the maximum intensity) in healthy subjects. In practice, this is equivalent to select the voxels of the striatum.
Thus, after voxel selection, a set of intensity values is obtained for each subject, arranged in a 1D array. This array is the key data to be processed in classification between NCs and PS.

6.2.3.2 Statistical performance measures of the different IN approaches

Voxels-as-Features (VAF)

The first applied method to the datasets is the simple VAF approximation [233]. VAF is considered as a baseline in many works like MRI analysis for AD or autism diagnosis, as many studies suggest that this method is, at least, comparable with the visual exam performed by experts [233]. This approximation uses all voxels in each image as a feature vector, which is used as an input to the classifiers. This baseline has been applied to different datasets using the raw images (spatially normalised ^{123} I-ioflupane-SPECT images) and intensity normalized images by the different proposed approaches.
A significant improvement of the performance results is carried out by the proposed approaches, as shown in Table 6.6. For instance, the accuracy gain is 10.18%, the sensitivity and the specificity gains are 13.64% and 8.57% compared to unnormalized intensity images (raw data). Compared to the other intensity normalization methods, the accuracy gain is up to 11.02%, the sensitivity and the specificity gains are up to 9.57% and 12.62%. The underlying reason for these improvements is the reduction of inter-subject intensity variability between different images of the same class, and between images of different classes as shown in the previous section.

Table 6.6: Comparison between the accuracy rates achieved with the different intensity normalization methodologies based on VAF approach and linear SVM classifier.

Normalization approach	Accuracy	Sensitivity	Specificity
Raw data	79.58%	78.95%	80%
$BR_{all} - IN$	85.83%	88.68%	83.78%
Integral-IN	85.04%	88.46%	82.66%
MKL-IN	81.10%	83.02%	79.73%
Max-IN	85.03%	87.03%	83.66%
α-stable	85.05%	87.04%	83.56%
Hist-eq-IN	78.74%	83.33%	75.95%
Hist-eq-IN in NS region	85.83%	85.96%	85.71%
FGMM	**88.98**%	**90.91**%	**87.50**%
MSE	**88.97**%	**89.47**%	**88.57**%
MSE-GMM	**89.76**%	**92.59**%	**87.67**%
MLR	**88.19**%	**90.74**%	**86.30**%

The accuracy rates for different normalization methods using the voxel intensity in the striatum are presented in Table 6.7. In this Table, the use of the proposed intensity normalization approaches on DaTSCAN images show a significant improve-

ment of the performance results over the same VAF approach (up to 91.34% for the Acc, 92.59% for the Sens and 92.54% for the Spec) compared to unnormalized intensity images (raw data) and the widely used IN approaches, used here as a baselines. The behavior of the computer aided diagnosis (CAD) system with these strategies of preprocessing highlights the benefits of using an intensity normalization, which allow us to compare the striatum area of each image voxel to voxel, assuming that a similar value of intensity in two different subjects corresponds to a similar value of the drug uptake. As well they show their ability and robustness in PS pattern detection.

Table 6.7: Comparison between the accuracy rates achieved with the different intensity normalization methodologies based on VAF approach and linear SVM classifier in the striatum regions.

Normalization approach	Accuracy	Sensitivity	Specificity
Raw data	87.40%	86.44%	88.23%
$BR_{all} - IN$	88.19%	87.93%	88.40%
Integral-IN	88.18%	87.90%	88.25%
MKL-IN	88.98%	87.93%	88.57%
Max-IN	88.97%	94.12%	85.53%
α-stable	86.61%	85%	88.06%
Hist-eq-IN	88.98%	89.47%	87.67%
Hist-eq-IN in NS region	84.25%	88.23%	81.57%
FGMM	**91.34**%	**90**%	**92.54**%
MSE	**90.55**%	**88.52**%	**92.42**%
MSE-GMM	**89.77**%	**88.33**%	**91.04**%
MLR	**89.76**%	**92.59**%	**88.58**%

Principal Component Analysis (PCA)

The second system tested for the diagnosis of PS for different datasets is based on the PCA feature extraction method [234–237]. Further details about this technique are given in appendix B.3. As it is shown in tables 6.8 and 6.9, the proposed methodologies to analyze ^{123} I-ioflupane images provide high accuracy rates for PS diagnosis with peak values over 92% for MSE and FGMM approaches and over 89% for MLR and MSE-GMM approaches in the striatum region. However, taking into account all the image voxels, the accuracy rates for the proposed approaches with the PCA feature extraction method are up to 90.55%. They represent a significant improvement in the incrementation of the accuracy compared with the results obtained by raw images and the compared methods. The improvements in accuracy rates are due to the ability of PCA to extract patterns explaining the greatest variance in the

data. In addition, the dimensionality reduction of PCA is very effective in classification because a higher number of features will easily lead the classifier into the problem of overfitting [235, 236]. However, the VAF approach considers the raw information included in the ROI.
To sum up, the proposed methods for intensity normalization deserve much attention in the diagnosis of PS. They demonstrate also their ability and robustness to improve computer aided diagnosis performance in DaTSCAN SPECT imaging in combination with SVM classification, as may be seen from Tables 6.6,6.7, 6.8 and 6.9 and supported by Figure 6.31.
An important observation is that intensity normalization using the proposed approaches can prove to be a reasonable trade-off of computational complexity in favor of having an uniform cross-subject distribution of the intensities in the non-specific area and the diagnostic ability of PS detection. For instance, the FGMM outperforms the MSE in the sense of entailing intensity normalization in the non-specific region as it leads to a less difference between the images of the same class, and between images of different classes as shown in Tables 6.3, 6.4 and 6.5. However, MSE approach obtains higher classification results with a peak value of 92.91% for the accuracy and 94.64% for the sensitivity using the PCA system as shown in Table 6.9. In addition, Figure 6.31.c reveals that the intensity normalization using MSE deeply affects the voxel information in the striatum region which leads to a better sensitivity using the PCA system. Otherwise, FGMM preserves the information in that region. Finally, taking into account the computational load, the MSE approach is less demanding with a computation time of 7 seconds, as can be seen in equation 5.13, than the FGMM method which requires a model estimation stage [212]. For our experiments we used machines running Intel® Xeon® processors with 2.67 GHz CPU frequency and having 48 GB of memory. In fact, with this workstation, the computational time for the model estimation stage can reach 1-2 hours of a GMM model with $k = 64$ clusters. However, for the filtering stage, it takes about 281.06 seconds. For the remaining proposed approaches, the computation time of MLR is 1487 seconds and for MSE-GMM is 465.50 seconds. For the baseline approaches, the computation time varies between 2 and 570.87 seconds.
As a conclusion, the proposed intensity normalization procedures lead to comparable generalization estimations and perform substantially better than the baseline methods.

Table 6.8: Comparison between the accuracy rates achieved with the different intensity normalization methodologies based on PCA feature extraction method and linear SVM classifier.

Normalization approach	Accuracy	Sensitivity	Specificity
Raw data	84.25%	81.96%	86.36%
$BR_{all} - IN$	88.18%	86.66%	89.55%
Integral-IN	85.83%	82.54%	89.06%
MKL-IN	85.03%	83.33%	86.56%
Max-IN	87.40%	85.24%	89.39%
α-stable	87.40%	86.44%	88.24%
Hist-eq-IN	83.46%	83.93%	83.1%
Hist-eq-IN in NS region	86.61%	86.21%	86.96%
FGMM	**88.98**%	**90.91**%	**87.5**%
MSE	**90.55**%	**89.83**%	**91.18**%
MSE-GMM	**88.98**%	**88.14**%	**89.71**%
MLR	**88.97**%	**89.47**%	**88.57**%

Table 6.9: Comparison between the accuracy rates achieved with the different intensity normalization methodologies based on PCA feature extraction method and linear SVM classifier in the striatum regions.

Normalization approach	Accuracy	Sensitivity	Specificity
Raw data	89.76%	92.59%	87.67%
$BR_{all} - IN$	90.34%	91.22%	90%
Integral-IN	89.76%	87.93%	88.73%
MKL-IN	87.40%	87.72%	87.14%
Max-IN	86.61%	86.21%	86.96%
α-stable	88.19%	89.29%	87.32%
Hist-eq-IN	87.40%	90.38%	84%
Hist-eq-IN in NS region	85.04%	87.04%	83.56%
FGMM	**92.13**%	**91.53**%	**92.65**%
MSE	**92.91**%	**94.64**%	**91.55**%
MSE-GMM	**90.55**%	**91.23**%	**90**%
MLR	**89.77**%	**89.66**%	**89.86**%

6.3 DMFP experiments

The same experiments were also performed on another independent database which is described in section 6.1.2. The use of another independent dataset is a major strength of our study, which keeps the research findings more objective as contrast

to the other studies conducted on one dataset. Qualitative and quantitative image analysis are performed, using the resulting intensity-normalized brain images and the mean histogram of the intensity values for each normalized neuroimage. In addition, the inter-subject variability is depicted using the error bars for the mean histogram of the intensity values in the NS region. Furthermore, it is measured by three statistical analyses, applying the KL divergence, the ED and the JD to study the difference between the probability distributions of each normalized image and the mean normalized brain image for the different IN methods. Finally, a comparison is performed using a classification system to separate IPS from APS patients, that may improve the development of a computer aided diagnosis (CAD) system for PD. Thus, the following preprocessing procedures are considered:

- Raw data.
- BR_{all}-IN [2, 88].
- **MSE** [229].
- **MSE-GMM** [185].
- **MLR** [113].
- Integral-IN [1].
- Max-IN [1].
- Hist-eq-IN in all binding regions.
- Hist-eq-IN in NS region.
- α-stable-IN [2].

The GMM-based image filtering **(FGMM)** approach is not applied to this database because the high computational load of the model estimation stage. It can reach more than 69 hours for just a one GMM model. In addition, a present lack of this database of control subjects presents limitations, such that we are unable to consider the MKL-IN approach for comparison. However, the Hist-eq method is applied, firstly, taking into account all the image voxels and, secondly, taking into account only the NS region.

6.3.1 Qualitative image analysis

6.3.1.1 Raw data

We tested the different IN methods using 87 raw ^{18}F-DMFP images from the database described in section 6.1.2, as shown in Figure 6.35. This figure reveals that there is

a high degree of variability in the intensity level for the specific/non-specific area before normalization. Thus, the cause of this variability is the machine artifact that is a direct result of the spacing of the detectors in the tomographic ring. This last issue also introduces an axial point-spread resulting from the width of the detector, or the thickness of the ring of detectors [238].
The visual image analysis of the striatal ^{18}F-DMFP uptake showed good spatial discrimination between caudate nucleus and putamen, and generally, the striatal tracer uptake was clearly reduced in the APS patients compared with the IPS patients. In addition, with this decrease of the striatal tracer uptake, there is a lowest uptake in the left striatum. Thus, APS patients show reduced postsynaptic tracer binding, indicating a decreased receptor density due to neuronal cell loss.

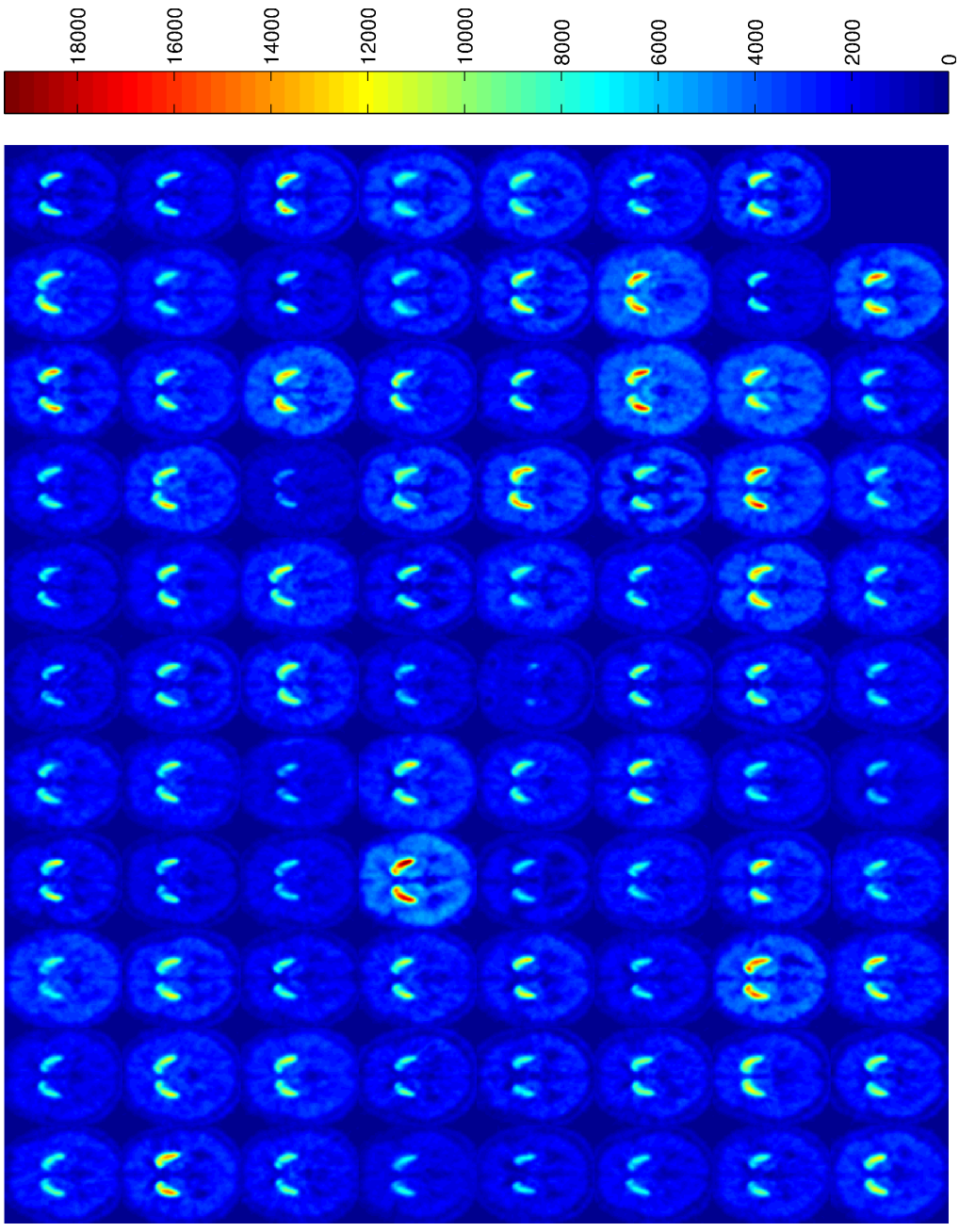

Figure 6.35: A given trans-axial slice of the 87 selected raw DMFP brain images from the database (39 IPS + 48 APS): these images present a certain degree of variability between the intensity values before normalization.

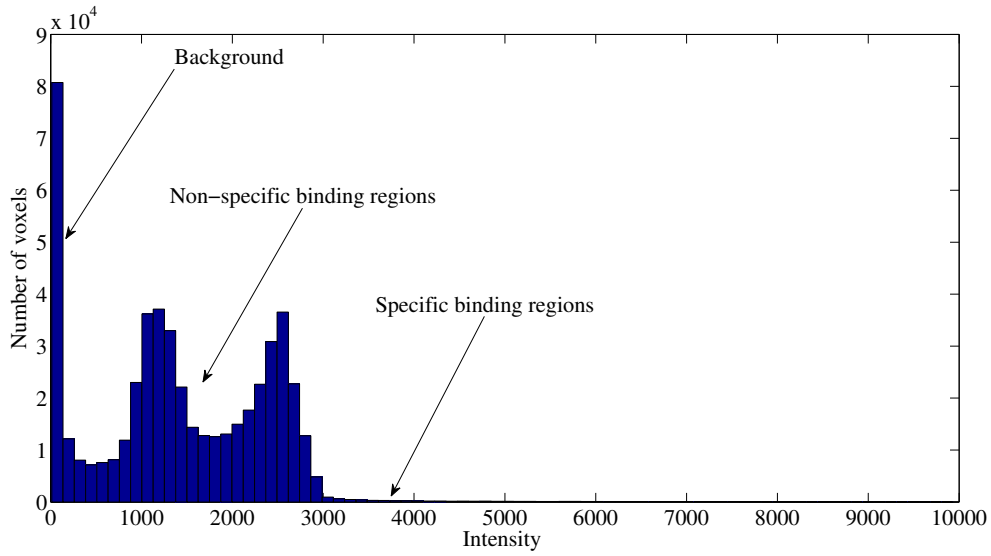

Figure 6.36: Mean histogram of the intensity values for the spatial normalized DMFP images.

Figure 6.36 depicts a scheme of the different parts of the binding values histogram, highlighting the specific and NS regions and their typical intensity values for original ^{18}F-DMFP images. Observe in this figure how the histogram corresponding to these data has two similar peaks at large intensities. Moreover, this figure shows that in the intensity profile, there is a large amount of the total intensity, which is located in the specific region. However, in other region, i.e. NS region (from $1.1 \cdot 10^3$ to $3.79 \cdot 10^3$) have also intensity values large enough to allow the inter-subject discrimination due to the machine artifact.
In summary, DMFP-based neuroimages contain a small region, the striatum, of great importance for the differential diagnosis, and other regions of lower importance, that are not significant for the diagnosis. These regions are considered as a reference region for normalization.

6.3.1.2 The compared IN methods

Linear approaches

The specific-to-non-specific binding ratio (BR_{all}-IN) is the most widely used normalization method [189] and it can be used for removing individual differences from brain activity measures, as illustrated in figures 6.37 and 6.38. However, this ratio method has substantially lower reliability in the striatum region, since, the variability in the NS region might bias the intensity radioactivity values in the specific binding region.

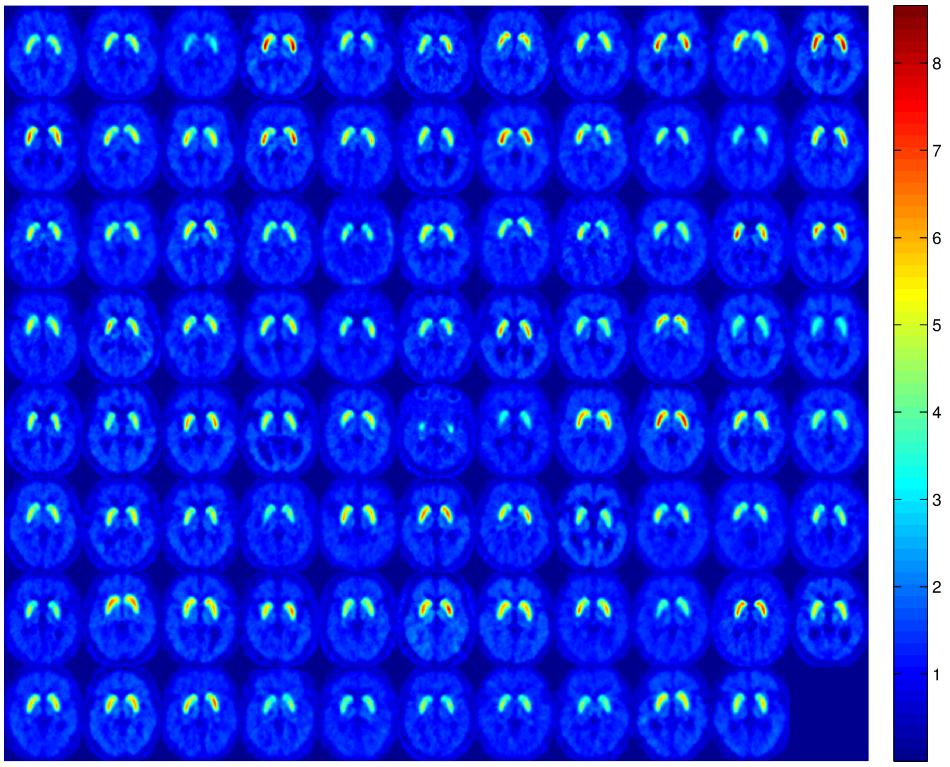

Figure 6.37: A given trans-axial slice of 87 DMFP brain images from the database after normalization by the specific-to-non-specific binding ratio (BR_{all}-IN).

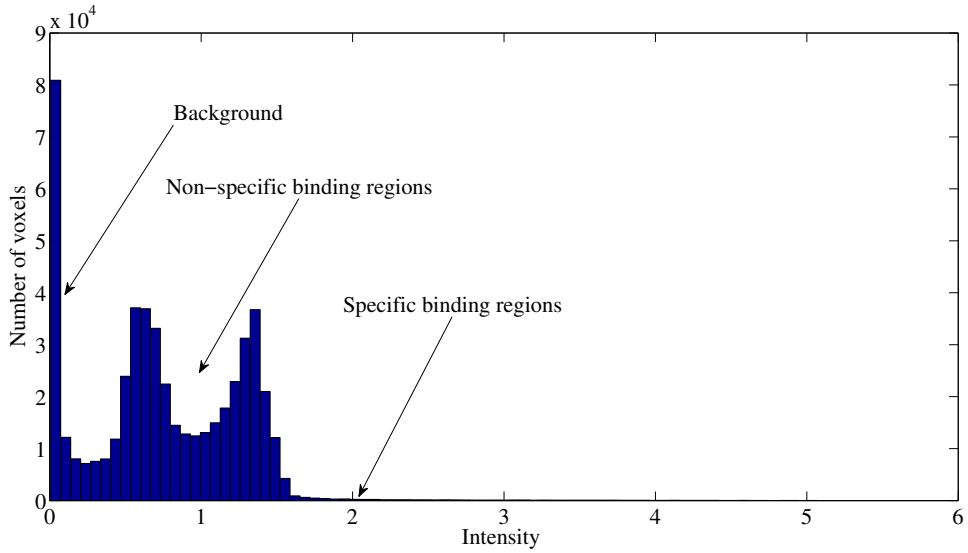

Figure 6.38: Mean histogram of the intensity values for intensity normalized DMFP images by BR_{all}-IN.

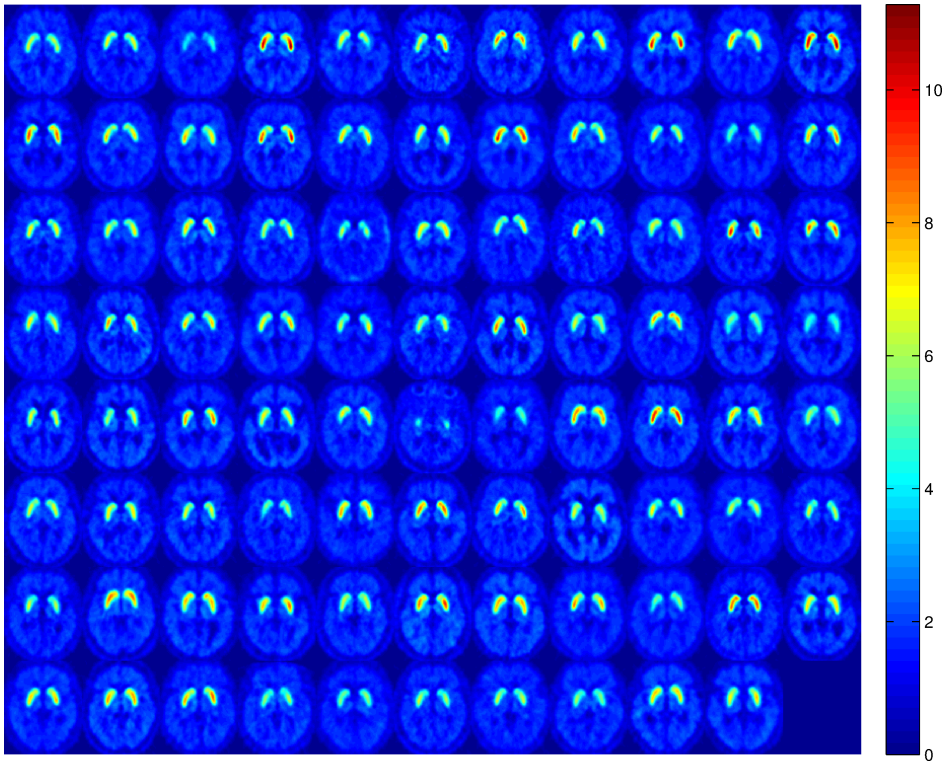

Figure 6.39: A given trans-axial slice of 87 DMFP brain images from the database after normalization by the integral-based intensity normalization approach (Integral-IN).

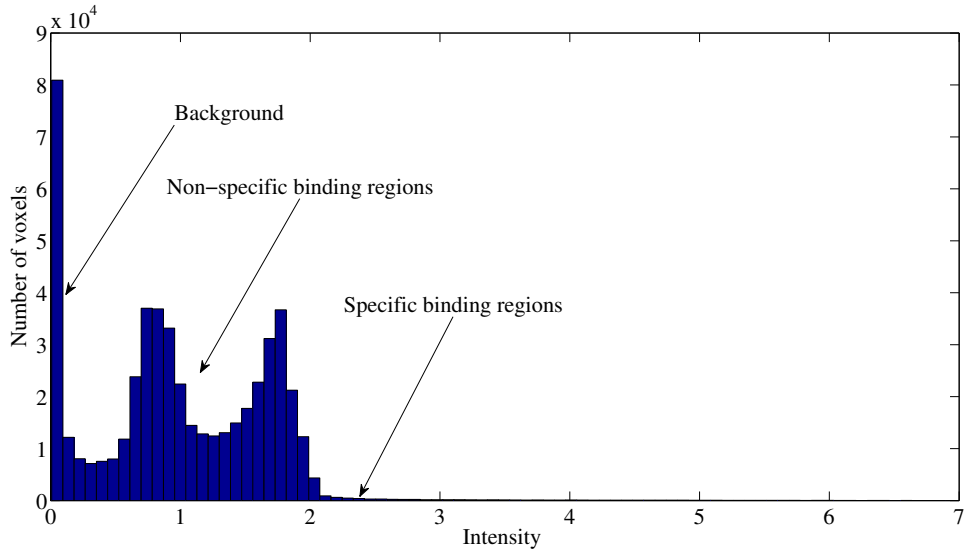

Figure 6.40: Mean histogram of the intensity values for intensity normalized DMFP images by Integral-IN.

In figures 6.39 and 6.40, Integral-IN preserves absolute differences in the uptake of the tracers. Thus, it produces a similar measure for NS regions, and there is a noticeable difference in striatal structures, where the contrasts of relevant features in the striatum are improved compared to unnormalized DMFP images.
According to figures 6.41 and 6.42, the intensity of the DMFP images was normalized to a maximum value, obtained by averaging the 0.1% of the highest intensities per image, as described in [239]. Similar to DaTSCAN scans, the Max-IN method has unfortunate effects on IPS and APS scans. For the reason that the discriminative regions are extended by interchanging the roles of specific/nonspecific areas of activity. Thus, the uptake of the tracer in the striatal structures is matched for both classes; IPS and APS. As a consequence, this scaling approach affects areas that show atrophy from the disease, i.e. the striatum. This may lead to a fault diagnosis.

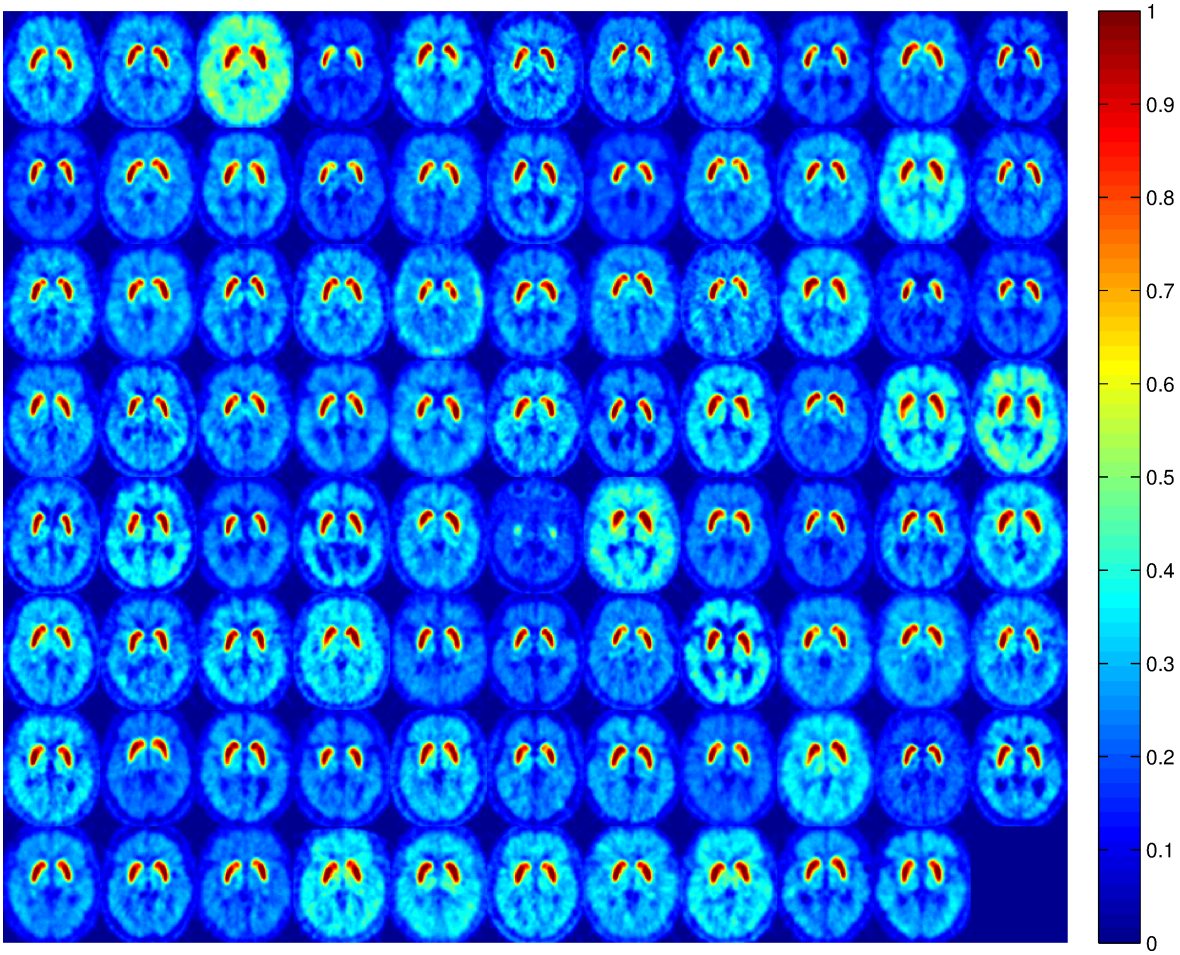

Figure 6.41: A given trans-axial slice of 87 DMFP brain images from the database after normalization to the maximum scheme (Max-IN).

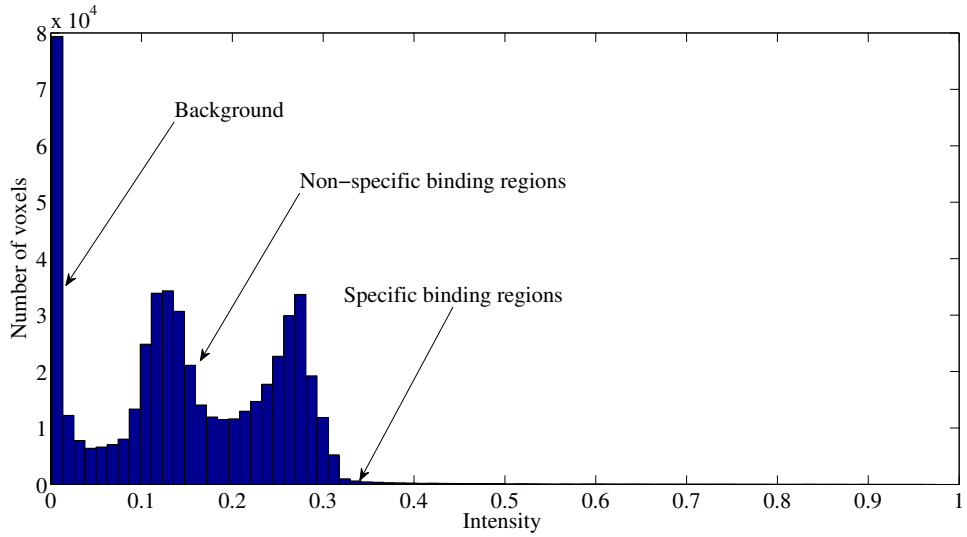

Figure 6.42: Mean histogram of the intensity values for intensity normalized DMFP images by Max-IN.

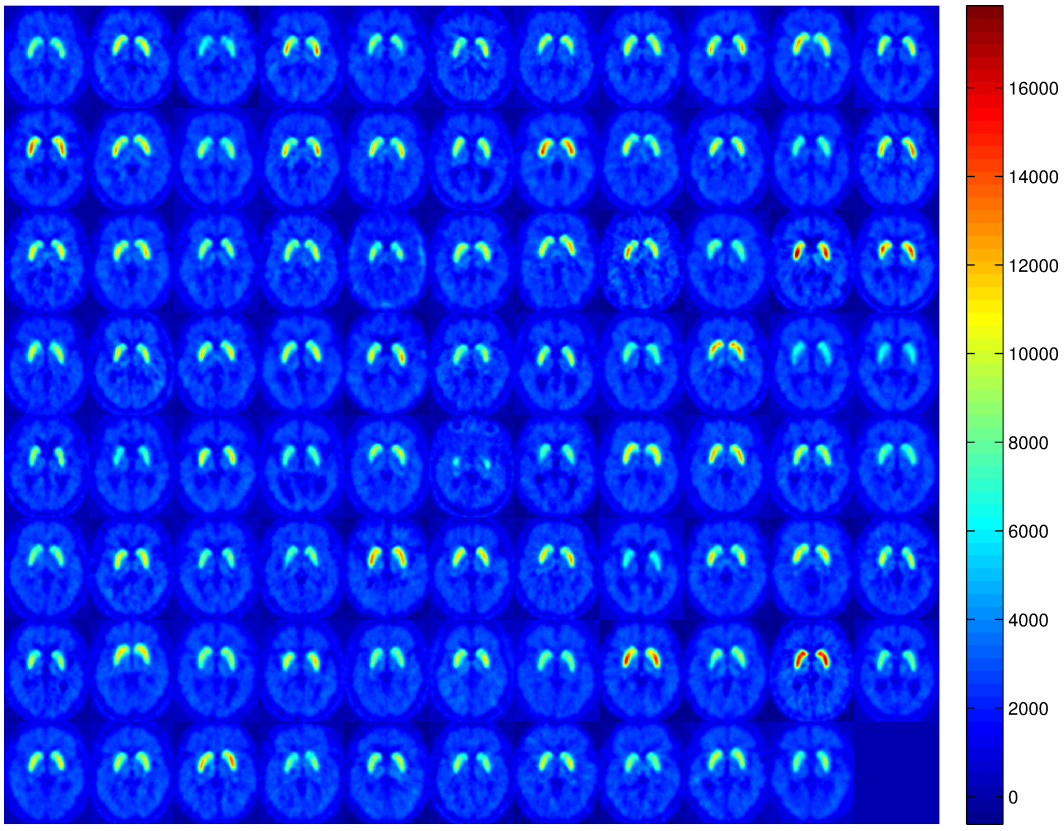

Figure 6.43: A given trans-axial slice of 87 DMFP brain images from the database after normalization by α-stable distribution (α-stable-IN).

Moreover, the intensity of ^{18}F-DMFP images is normalized by a linear procedure using the α-stable distribution, as illustrated in figure 6.43. This methodology is based on the fact that the histogram of intensity values can be fitted accurately using a positive skewed α-stable distribution. Then, the predicted α-stable parameters and the location-scale property are used to linearly transform the intensity values in each voxel. Figure 6.44depicts the mean histogram of the normalized DMFP images using the α-stable-IN method.

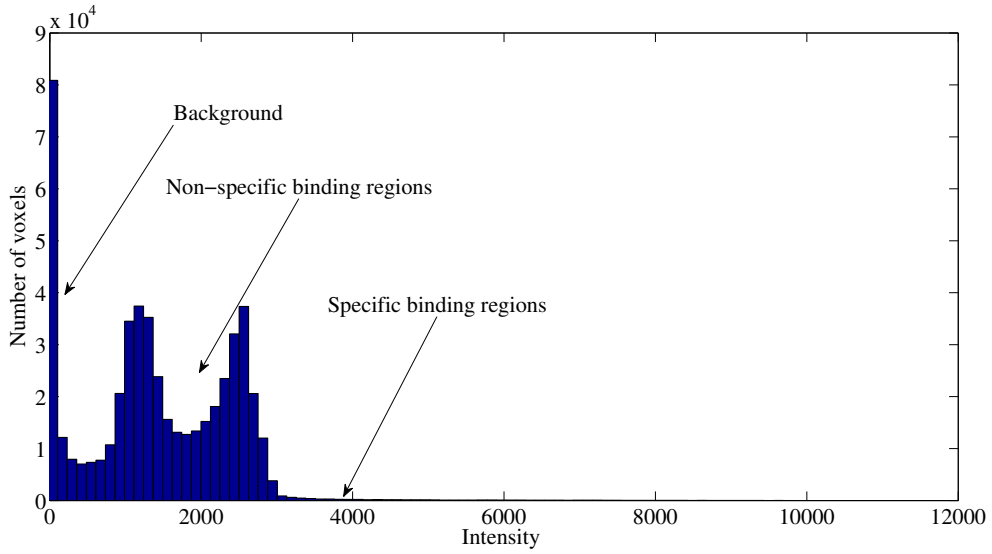

Figure 6.44: Mean histogram of the intensity values for intensity normalized DMFP images by α-stable-IN method.

Nonlinear approach

We used the histogram equalization methodology as a nonlinear approach that will be compared to our proposed methods. This method is based on a histogram matching; the intensity values in the original DMFP image are pre-adjusted using the information of the histogram of the reference template, as shown in Figure 6.45. The histograms of intensity values of each DMFP images are superimposed in the first row of Figure 6.45. This figure reveals that there is a certain degree of variability between the intensity values before normalization. The second row of the Figure 6.45 depicts the grayscale transformation that maps gray levels in the unmormalized DMFP image to gray levels in the normalized DMFP image. The third row of Figure 6.45 shows the histograms with the intensity values for each of the DMFP images after performing the normalization procedure. Take note that the bulk of the histograms of all the images are very similar after normalization.

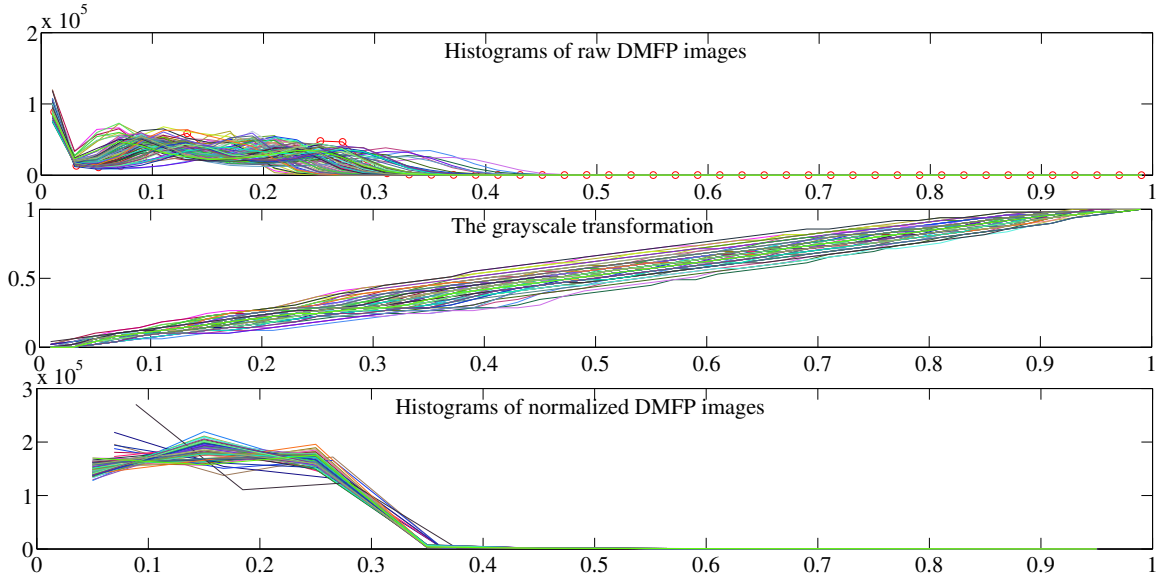

Figure 6.45: Histograms of each DMFP image before and after normalization using the Hist-eq-IN approach. The intensity values in the source images are adjusted to the intensity of the reference template (the red line with red circles).

Figure 6.46 shows the mean histogram of normalized DMFP images by Hist-eq-IN method and the different parts of the binding values histogram, highlighting the specific and NS regions.

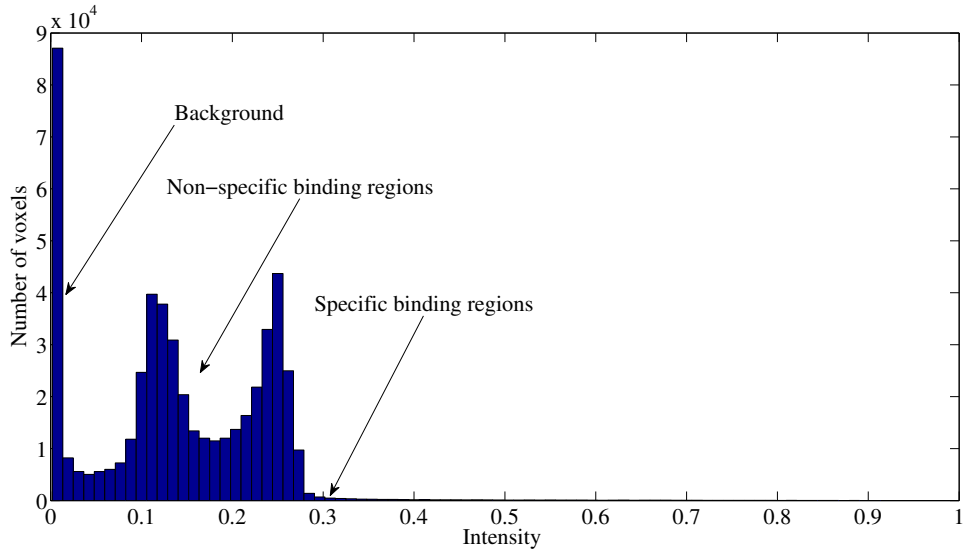

Figure 6.46: Mean histogram of the intensity values for intensity normalized DMFP images by Hist-eq-IN method.

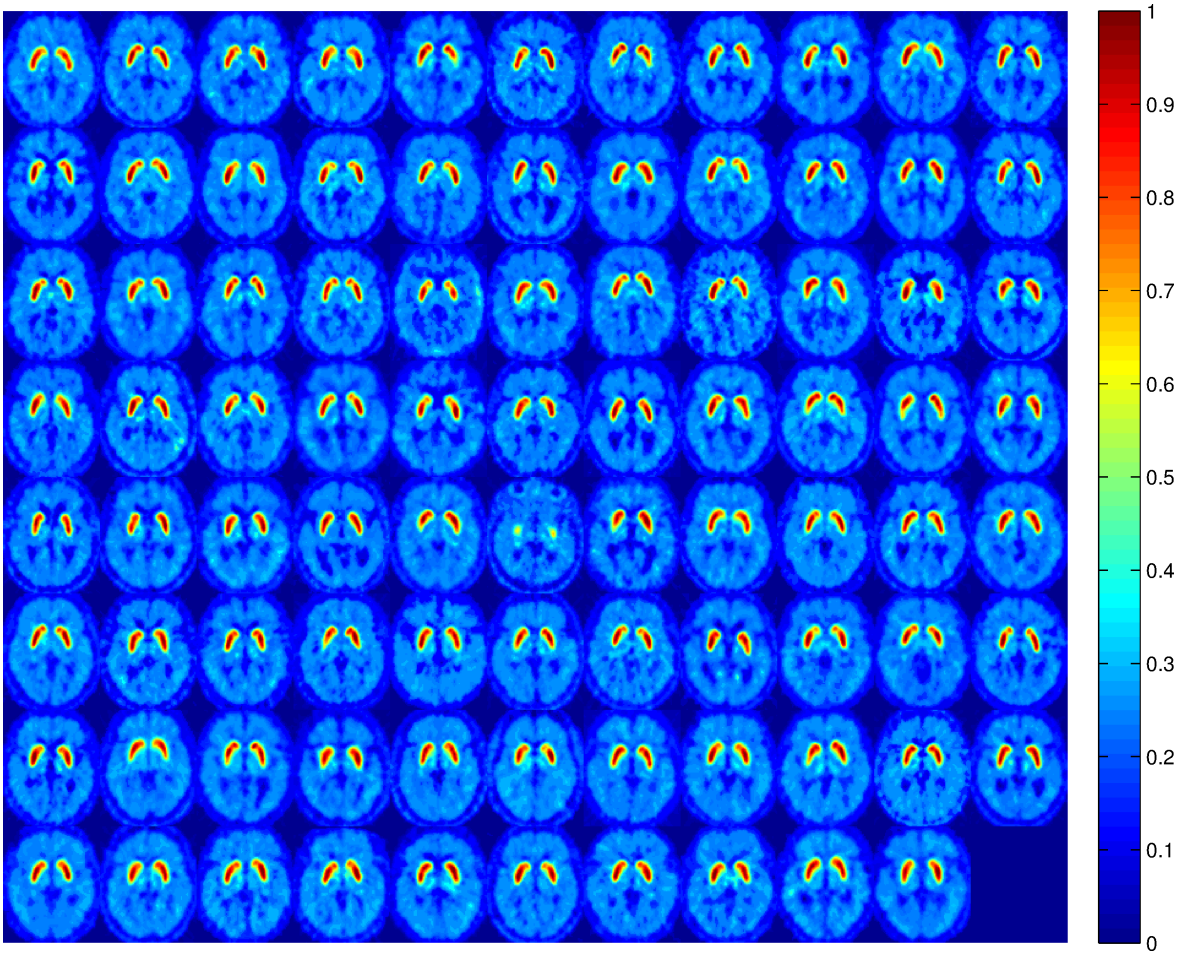

Figure 6.47: A given trans-axial slice of 87 DMFP brain images from the database after normalization by the Histogram equalization method (Hist-eq-IN). The striatal tracer uptake was clearly increased in both, the IPS and APS patients. There were no visually detectable differences in striatal tracer binding between IPS and APS patients.

Figure 6.47 illustrates the resulting intensity-normalized brain images after the Hist-eq-IN. This figure reveals that the inter-subject differences in intensity values in the NS regions is clearly mitigated after IN. However, the tracer uptake in the striatum is matched for IPS and APS subjects and the differentiation between these two classes becomes difficult. For this reason, we tried to apply the Hist-eq-IN only in the reference region, as illustrated in figures 6.48, 6.49 and 6.50.

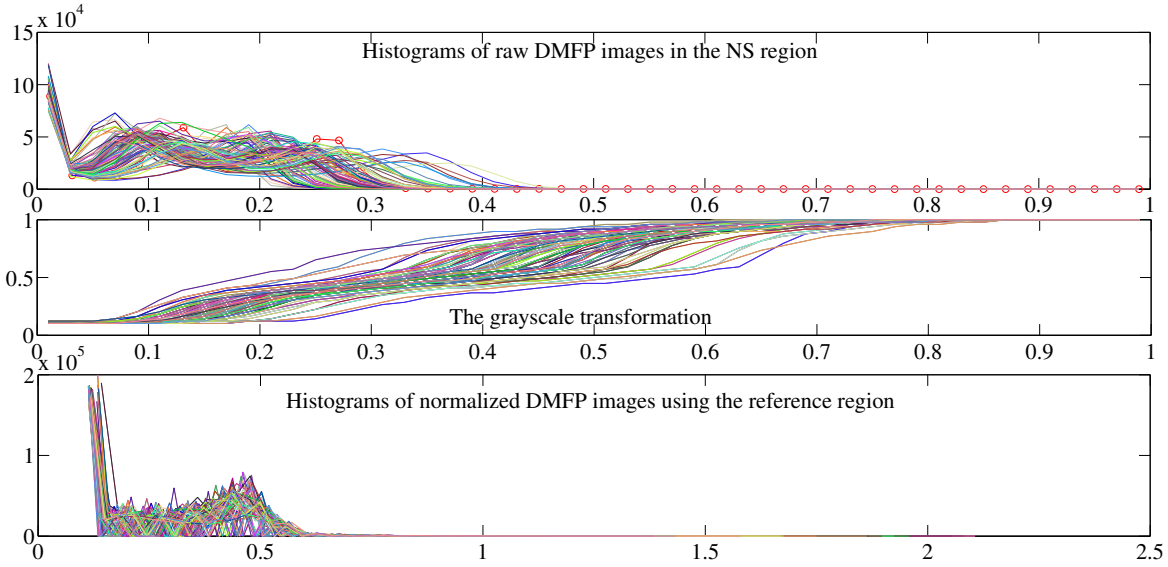

Figure 6.48: Histograms of each DMFP image before and after normalization using the Hist-eq-IN approach in the NS region. The intensity values in the source images are adjusted to the intensity of the reference template (the red line with red circles).

In Figure 6.50, the visual image analysis of the striatal ^{18}F-DMFP uptake showed a difference in the striatal tracer uptake between APS and IPS patients and the matching between the two classes in the discriminative region is avoided.

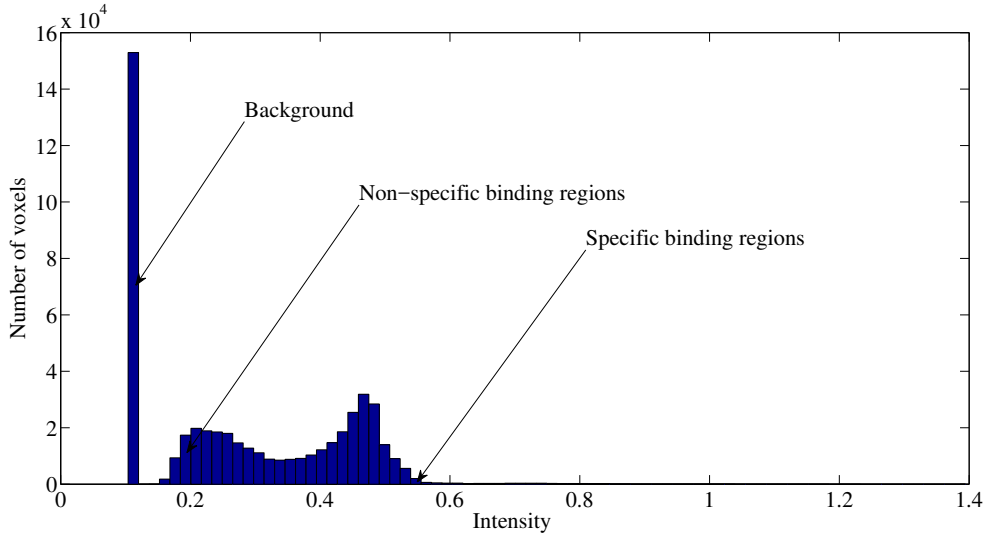

Figure 6.49: Mean histogram of the intensity values for intensity normalized DMFP images by Hist-eq-IN method in the NS region.

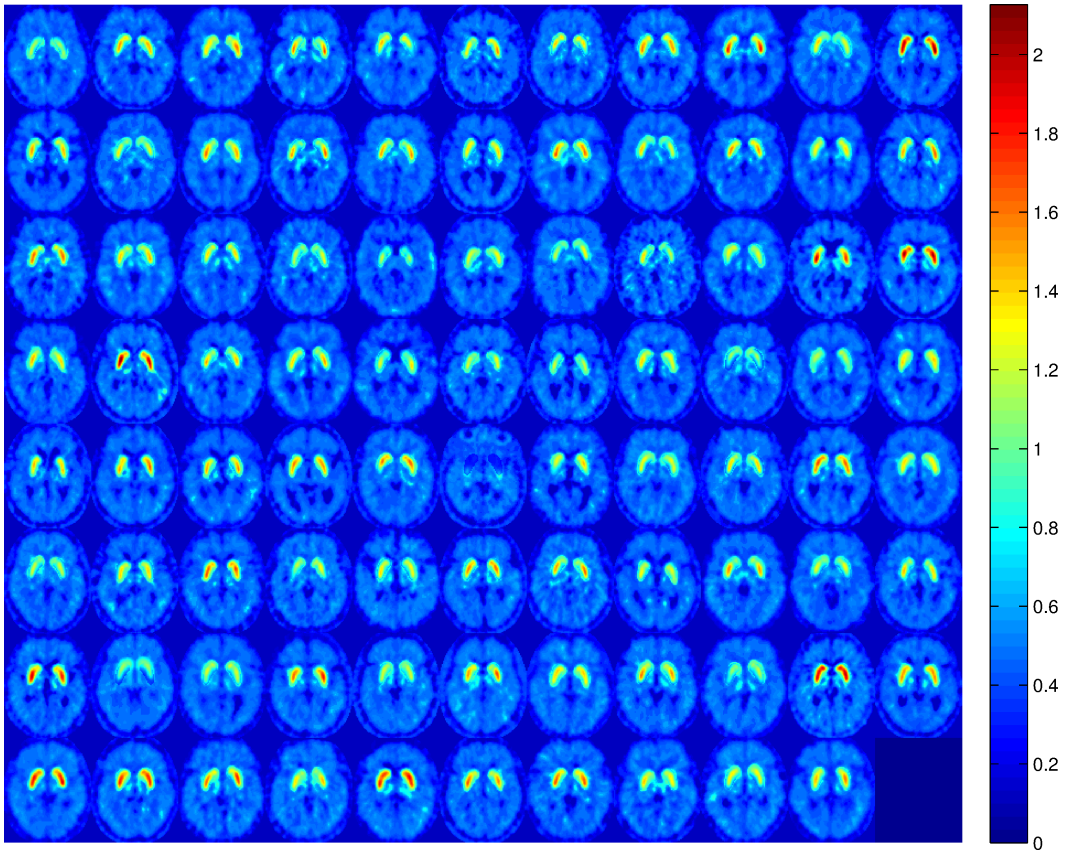

Figure 6.50: A given trans-axial slice of 87 DMFP brain images from the database after normalization by the Histogram equalization method (Hist-eq-IN) in the NS region.

6.3.1.3 Proposed approaches

As mentioned previously, The GMM-based image filtering (FGMM) approach is not applied to this database because of the computational load. Thus, the remaining proposed IN methods based on MSE and MLR are applied to this DMFP database.

Mean Squared Error (MSE) Optimization at voxel level

The minimization of MSE approach between the source image and the template at a voxel level can involve a novel intensity normalization method for ^{18}F-DMFP images.
Figures 6.51 and 6.52 demonstrate that the inter-subject intensity differences in the NS region due to several effects [30] are clearly reduced after normalization using this proposed method.

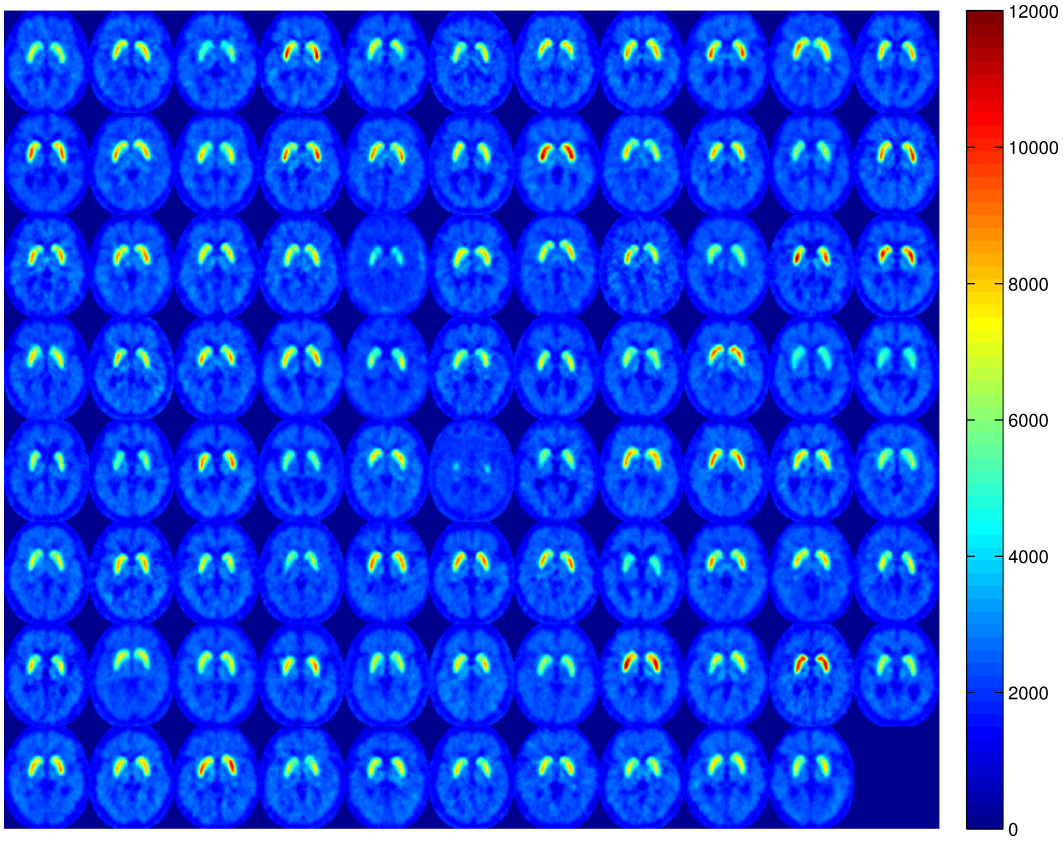

Figure 6.51: A given trans-axial slice of 87 DMFP brain images from the database after normalization by the MSE optimization method in the NS region.

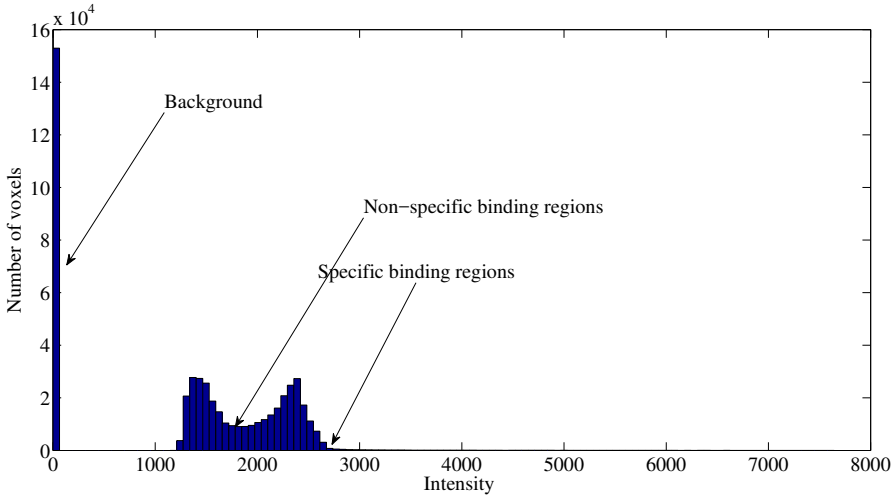

Figure 6.52: Mean histogram of the intensity values for intensity normalized DMFP images by MSE method in the NS region. The inter-subject intensity variability in the NS region between 1900 and 1910 is reduced.

Moreover, unlike those ones shown in the compared approaches, the processed images are smoothed and they preserve the relevant information in the striatum region.

Mean Squared Error (MSE) Optimization at Gaussian level

In order to overcome the computational load of the image preprocessing stage using the GMM-based algorithm in DMFP PET database, this MSE optimization is performed between the GMM-based extracted features from each subject image and the template on the clusters that represent the reference region. Thus, the linear intensity transformation is applied considering the cluster level.
The qualitative effects can be seen more clearly at the image level in the results of Figure 6.53. Moreover, as illustrated in Figure 6.54, the inter-subject variability in the NS region (between 1800 and 2060) are clearly reduced. In addition, ^{18}F-DMFP binding keeps its discriminative aspect between the two groups of patients, given the more prominent nigrostriatal degeneration in the striatum region.

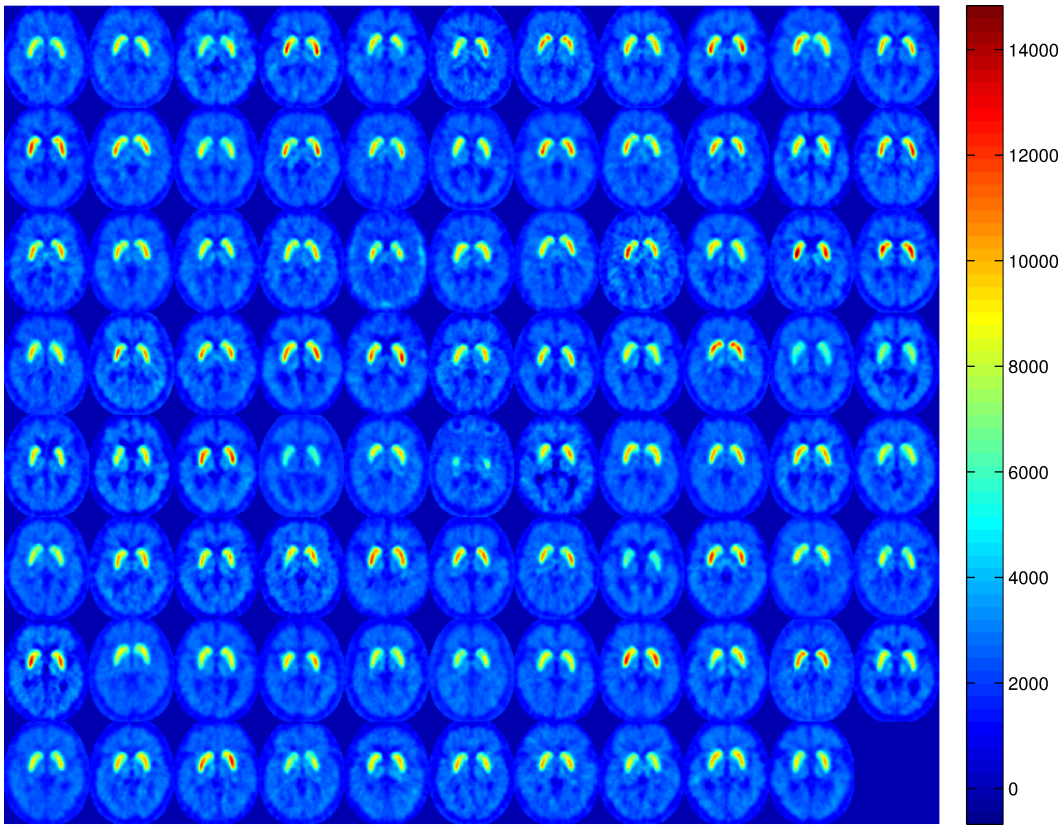

Figure 6.53: A given trans-axial slice of 87 DMFP brain images from the database after normalization by the MSE-GMM optimization method in the NS region.

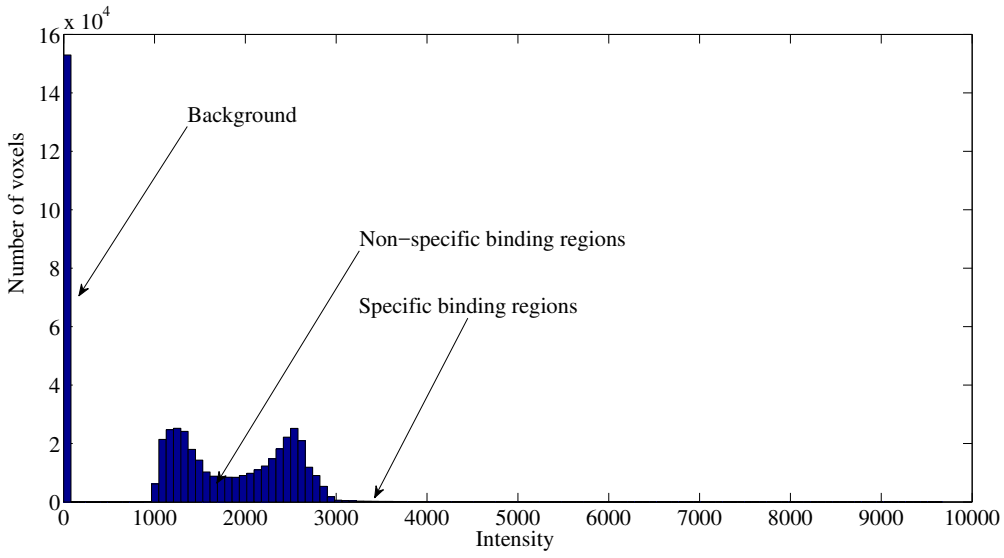

Figure 6.54: Mean histogram of the intensity values for intensity normalized DMFP images by MSE-GMM method in the NS region.

After applying the MSE approach at voxel and cluster level, the resulting brain images show a slight difference on the intensity values of the striatal ^{18}F-DMFP uptake between Figure 6.51 and Figure 6.53. However, both approaches entail a good normalization of intensity in the reference region. This is proved by the uniform part of the mean histogram both in Figure 6.52 and Figure 6.54.

Model-Based Multivariate Linear Regression (MLR) Approach

This normalization methodology can be applied to the whole medical image, not only in a NS region, which represents the major advantage of this proposed method. The goal of this approach is to transform linearly all the intensity values for different image subjects using predictive modeling based on MLR. The qualitative effect of this method is presented in figures 6.55 and 6.56. This figures prove that after applying this proposed approach, the intensity heterogeneity in the NS region (its values of intensity are between 1830 and 1930) is reduced and the separation between the striatum and the NS region is increased. In addition the noise and the artifact that may affect the raw data are clearly reduced.

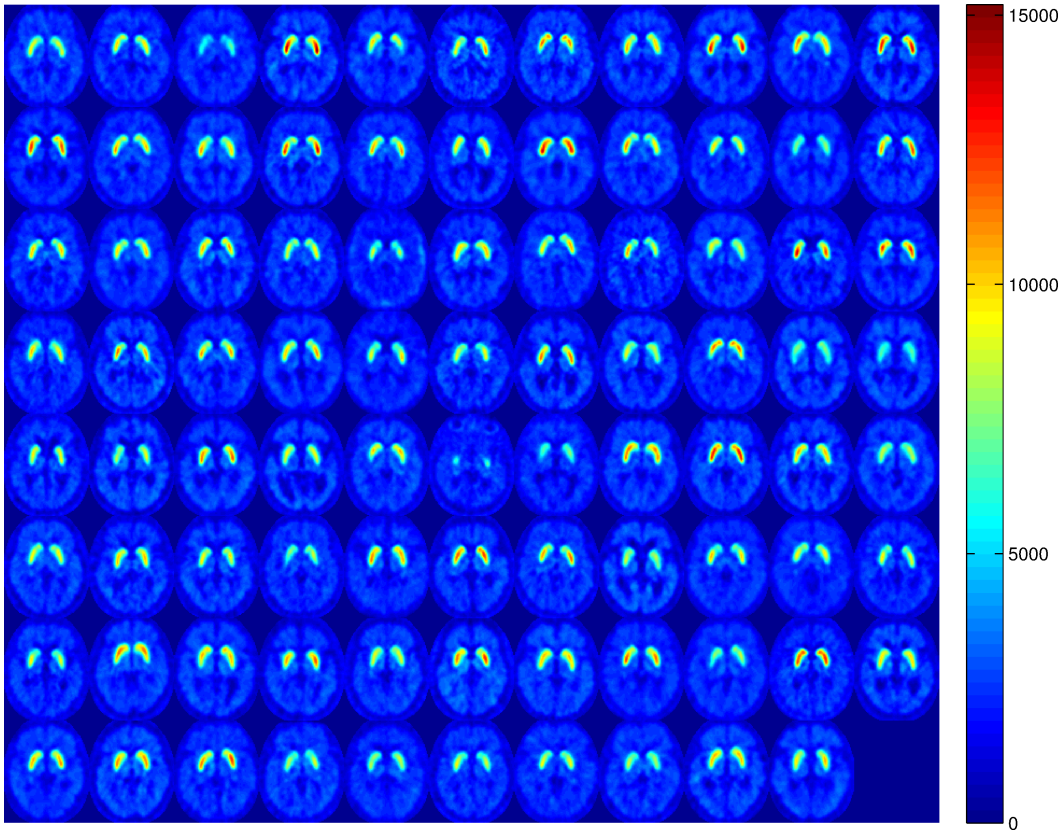

Figure 6.55: A given trans-axial slice of 87 DMFP brain images from the database after normalization by the MLR method.

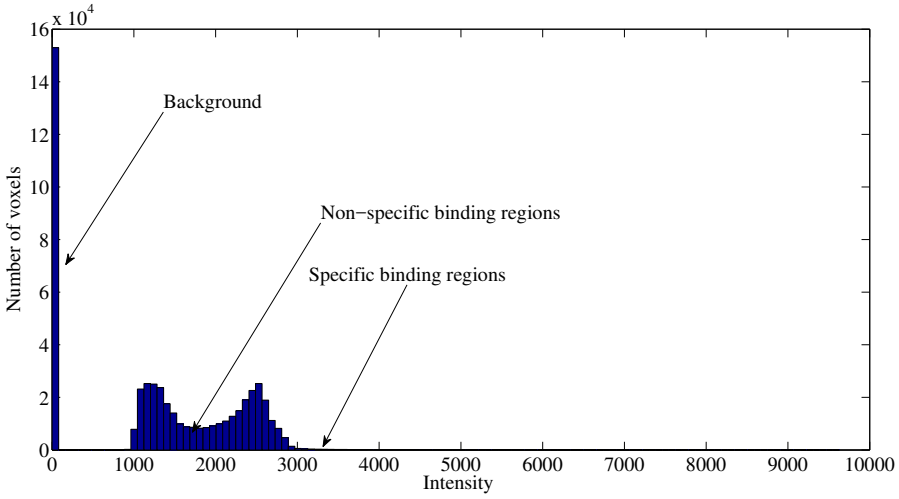

Figure 6.56: Mean histogram of the intensity values for intensity normalized DMFP images by MLR method.

6.3.2 Quantitative image analysis

The proposed intensity normalization methods are compared quantitatively to many widely used approaches. The comparison is carried out by depicting the error bars, which are estimated using 25th and 75th percentile of the mean histogram in the non-specific region, as depicted in the figures 6.57 et 6.58. The inter-subject intensity variability, presented by error bars, is clearly reduced by our normalization methods. Thus, it yields a greater degree of homogeneity in the intensity values of the NS region.

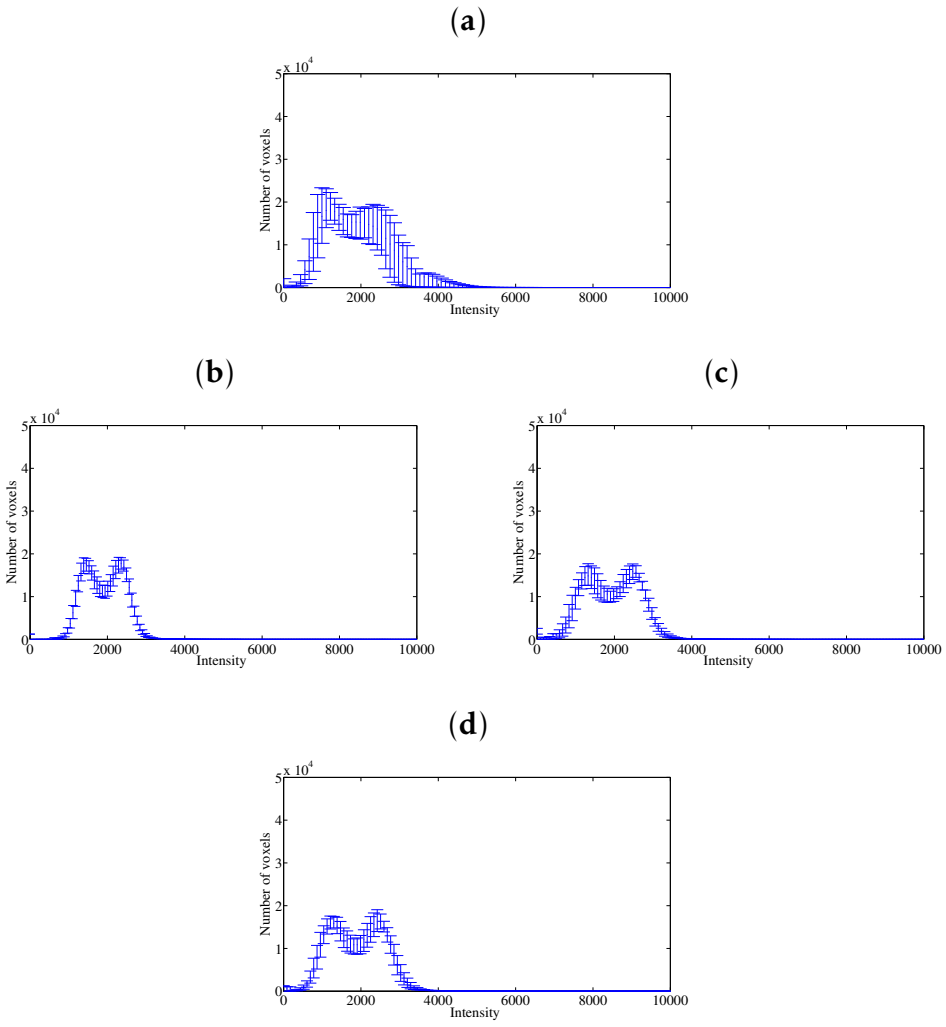

Figure 6.57: Error bars for the mean histogram of the intensity values in the NS region for DMFP images before and after normalization using the proposed approaches. (a): Raw images, (b): MSE images, (c): MSE-GMM images and (d) MLR images. Error bars are calculated considering 25th and 75th percentiles.

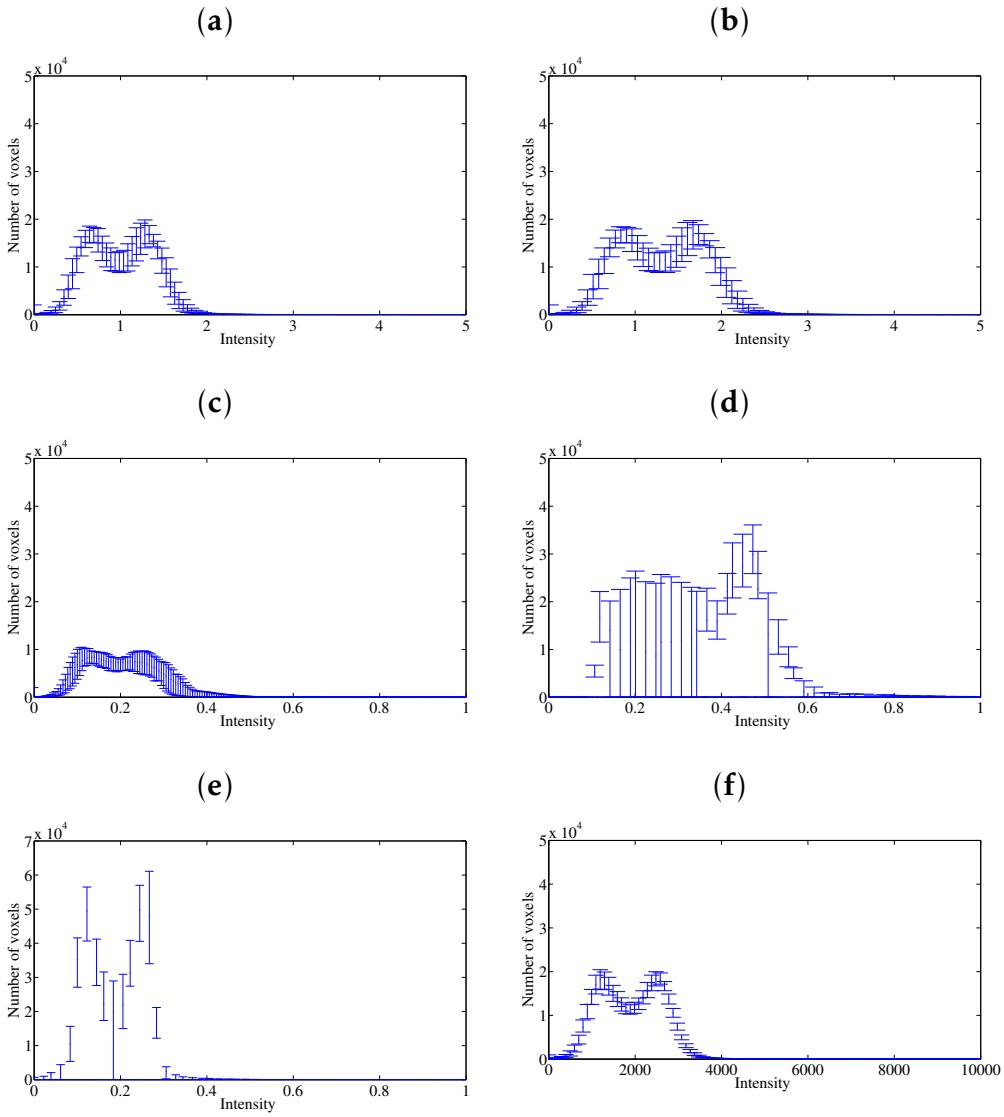

Figure 6.58: Error bars for the mean histogram of the intensity values of DMFP images in the NS region for the different compared approaches. (a): BR_{all} images, (b): Integral-IN images, (c): Max-IN images, (d): Hist-eq-IN images, (e): Hist-eq-IN (NS region) images and (f): α-stable-IN images. Error bars are calculated considering 25th and 75th percentiles.

Moreover, we also evaluate the difference between the probability distribution of each image and the mean brain image for all subjects according to class belonging and using some defined metrics, such as, KL divergence, ED and JD. The inter-subject distance is calculated quantitatively between these two distributions, both before normalization, for raw images and after normalization, using the proposed and the compared methods, as shown in tables 6.10, 6.11 and 6.12.
The lowest KL, ED and JD values and the lowest error are obtained by the proposed normalization methods. Compared to raw data and normalized images using the comparative approaches, its KL, ED and JD mesures represent less difference between adjusted images and target model, both in the same class or in different classes. Thus, these proposed approaches achieve a significant reduction in the DMFP image discrepancy to the normalization reference. This leads to more intensity homogeneity in the reference region.
In addition, the inter-subject intensity variability in the striatum for IPS subjects (first row) and APS subjects (second row) in terms of mean histogram and error bars for the spatial normalized and intensity normalized DMFP images are depicted in figures 6.59,6.60 and 6.61.
Notice that the intensity distributions obtained by our approaches are quite different in shape and variability between the two classes (IPS VS APS; specifically the first row versus the second row of Figure 6.59. b, c and d). However, there is a similarity in these distributions in the compared methods, which will affect the classification tasks. Thus, distinguishing between IPS and APS becomes more difficult.

Table 6.10: Mean Euclidean distance and standard deviation for original DMFP images and intensity normalized images in the NS region.

Normalization approach	Class	Euclidean distance
Raw data (spatial normalization)	IPS	0.4911±0.1792
	MSA+PSP	0.4685±0.1641
	IPS+MSA+PSP	0.4953±0.1776
BR_{all}	IPS	0.2202±0.1103
	MSA+PSP	0.2566±0.1120
	IPS+MSA+PSP	0.2503±0.1109
Integral	IPS	0.2208±0.1092
	MSA+PSP	0.2588±0.1137
	IPS+MSA+PSP	0.2514±0.1111
Max	IPS	0.4098±0.2138
	MSA+PSP	0.4473±0.1310
	IPS+MSA+PSP	0.4499±0.1578
Hist-eq-NS	IPS	0.6296±0.1291
	MSA+PSP	0.6139±0.1691
	IPS+MSA+PSP	0.6286±0.1514
Hist-eq	IPS	0.3421±0.0923
	MSA+PSP	0.3331±0.1049
	IPS+MSA+PSP	0.3409±0.1006
α-stable	IPS	0.1984±0.0929
	MSA+PSP	0.2471±0.1182
	IPS+MSA+PSP	0.2285±0.1082
MSE	IPS	**0.1408±0.0713**
	MSA+PSP	**0.1353±0.0553**
	IPS+MSA+PSP	**0.1430±0.0670**
MSE-GMM	IPS	**0.1998±0.0989**
	MSA+PSP	**0.2298±0.0999**
	IPS+MSA+PSP	**0.2249±0.1010**
MLR	IPS	**0.1786±0.1131**
	MSA+PSP	**0.1771±0.1111**
	IPS+MSA+PSP	**0.1790±0.1169**

Table 6.11: Mean Kullback-Leibler distance and standard deviation for original DMFP images and intensity normalized images in the NS region.

Normalization approach	Class	Kullback-Leibler distance
Raw data (spatial normalization)	IPS	0.2528±0.2366
	MSA+PSP	0.2323±0.1654
	IPS+MSA+PSP	0.2541±0.1862
BR_{all}	IPS	0.0513±0.0570
	MSA+PSP	0.0674±0.0553
	IPS+MSA+PSP	0.0639±0.0541
Integral	IPS	0.0513±0.0565
	MSA+PSP	0.0696±0.0603
	IPS+MSA+PSP	0.0650±0.0564
Max	IPS	0.2014±0.2611
	MSA+PSP	0.2072±0.1348
	IPS+MSA+PSP	0.2151±0.1816
Hist-eq-NS	IPS	0.4282±0.1123
	MSA+PSP	0.4064±0.1627
	IPS+MSA+PSP	0.4234±0.1397
Hist-eq	IPS	0.1499±0.0787
	MSA+PSP	0.1383±0.0863
	IPS+MSA+PSP	0.1456±0.0823
α-stable	IPS	0.0482±0.0498
	MSA+PSP	0.0726±0.0661
	IPS+MSA+PSP	0.0630±0.0594
MSE	IPS	**0.0244±0.0308**
	MSA+PSP	**0.0240±0.0269**
	IPS+MSA+PSP	**0.0263±0.0341**
MSE-GMM	IPS	**0.0422±0.0424**
	MSA+PSP	**0.0564±0.0464**
	IPS+MSA+PSP	**0.0535±0.0457**
MLR	IPS	**0.0356±0.0541**
	MSA+PSP	**0.0388±0.0652**
	IPS+MSA+PSP	**0.0392±0.0641**

Table 6.12: Mean Jeffreys Divergence and standard deviation for original DMFP images and intensity normalized images in the NS region.

Normalization approach	Class	Jeffreys Divergence
Raw data	IPS	0.6073±0.5118
(spatial normalization)	MSA+PSP	0.5825±0.4331
	IPS+MSA+PSP	0.6551±0.4918
BR_{all}	IPS	0.1051±0.1043
	MSA+PSP	0.1415±0.1079
	IPS+MSA+PSP	0.1361±0.1070
Integral	IPS	0.1052±0.1032
	MSA+PSP	0.1455±0.1156
	IPS+MSA+PSP	0.1381±0.1100
Max	IPS	0.4795±0.5834
	MSA+PSP	0.5051±0.3294
	IPS+MSA+PSP	0.5355±0.4477
Hist-eq-NS	IPS	0.7658±0.5473
	MSA+PSP	0.8180±0.8118
	IPS+MSA+PSP	0.8175±0.7078
Hist-eq	IPS	0.1024±0.0390
	MSA+PSP	0.1171±0.0521
	IPS+MSA+PSP	0.1144±0.0478
α-stable	IPS	0.0966±0.0901
	MSA+PSP	0.1459±0.1268
	IPS+MSA+PSP	0.1276±0.1135
MSE	IPS	**0.0464±0.0540**
	MSA+PSP	**0.0431±0.0470**
	IPS+MSA+PSP	**0.0475±0.0583**
MSE-GMM	IPS	**0.0861±0.0791**
	MSA+PSP	**0.1164±0.0883**
	IPS+MSA+PSP	**0.1118±0.0890**
MLR	IPS	**0.0704±0.1085**
	MSA+PSP	**0.0795±0.1488**
	IPS+MSA+PSP	**0.0787±0.1389**

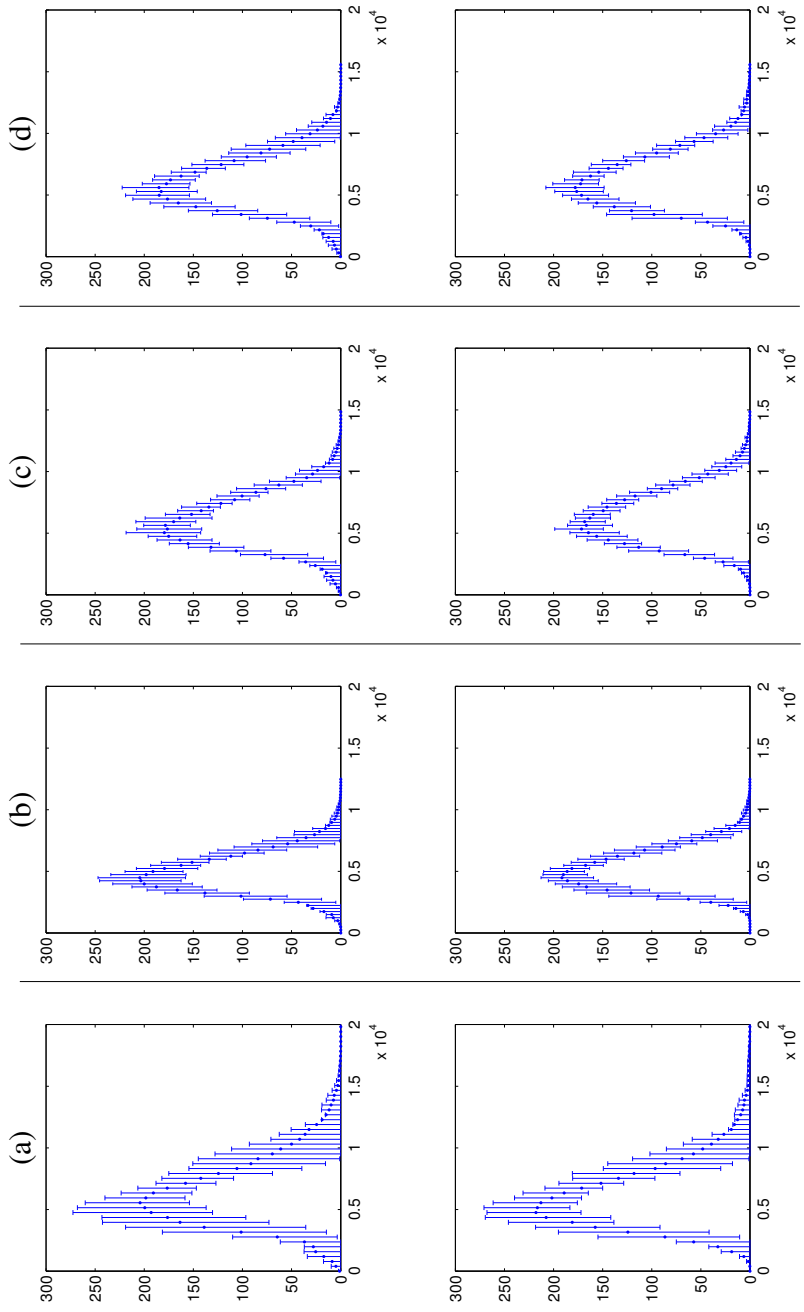

Figure 6.59: Mean histograms and error bars in the striatum region for 87 DMFP PET images before and after intensity normalization using the proposed approaches and keeping separate distributions for the two different classes. The first row is for IPS subjects and the second row is for APS subjects. (a): Original DMFP PET (Spatial normalized images), (b): MSE images, (c): MSE-GMM images and (d): MLR images. Error bars are calculated considering 25th and 75th percentiles. The x-axis represents the intensity. The y-axis indicates the number of voxels with a given level in the striatum region.

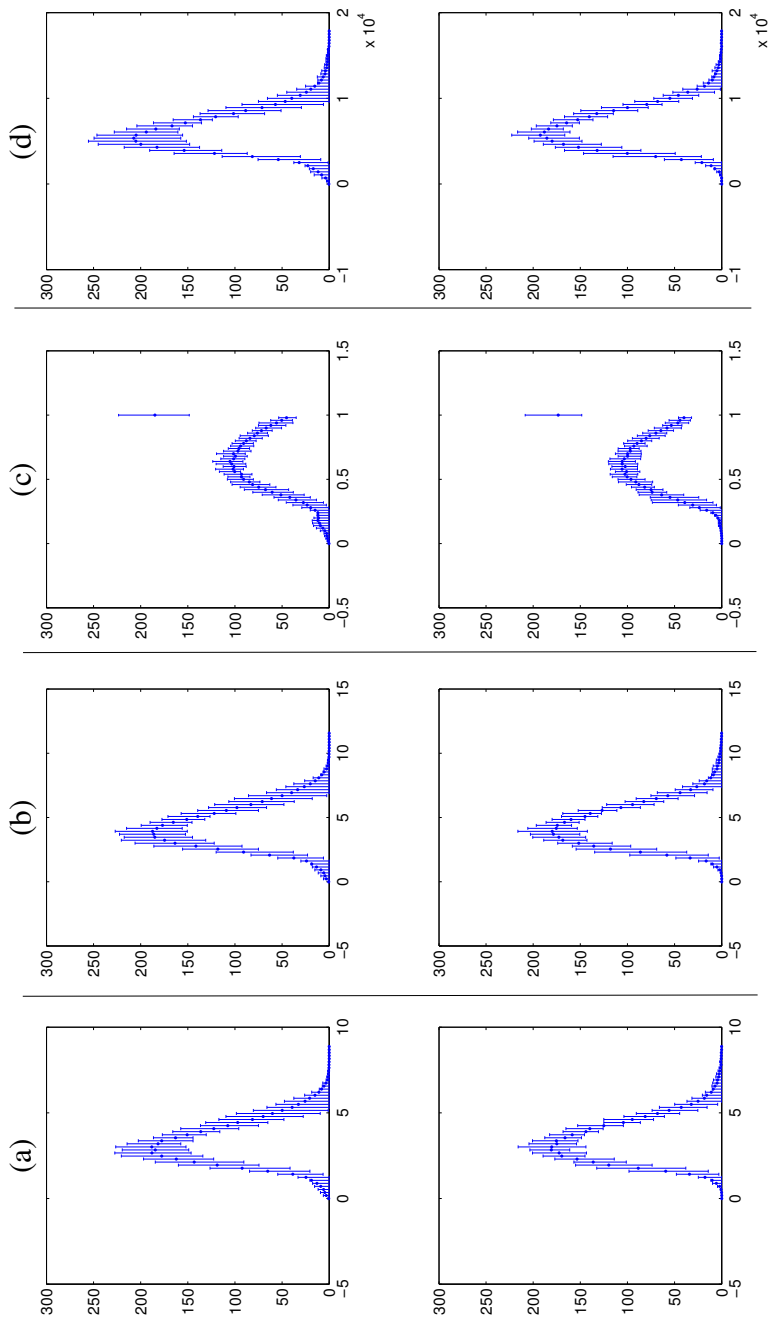

Figure 6.60: Mean histograms and error bars in the striatum region for 87 intensity normalized DMFP PET images using the compared approaches and keeping separate distributions for the two different classes. The first row is for IPS subjects and the second row is for APS subjects. (a): BR_{all} images, (b): Integral-IN images, (c): Max-IN images and (d): α-stable-IN images. Error bars are calculated considering 25th and 75th percentiles. The x-axis represents the intensity. The y-axis indicates the number of voxels with a given level in the striatum region.

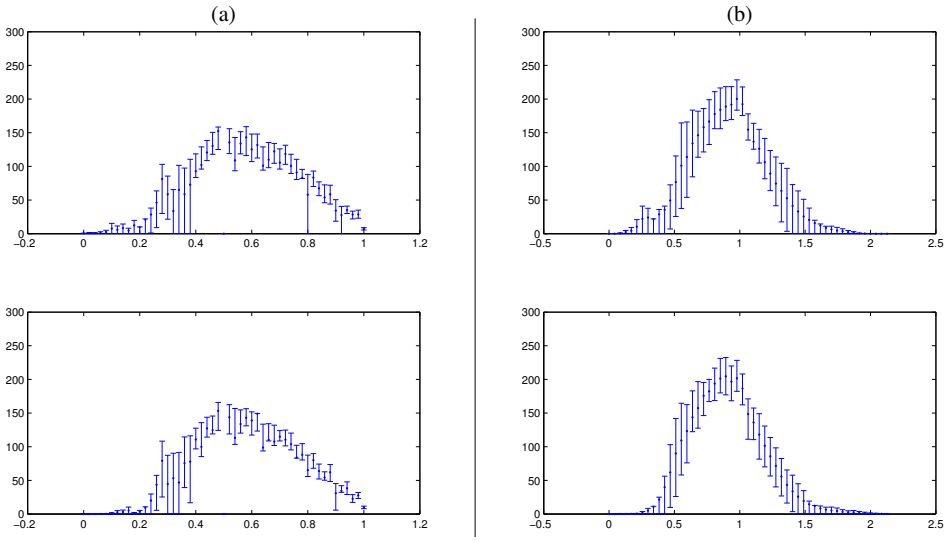

Figure 6.61: Mean histograms and error bars in the striatum region for 87 intensity normalized DMFP PET images using the histogram equalization method and keeping separate distributions for the two different classes. The first row is for IPS subjects and the second row is for APS subjects. (a): Hist-eq-IN images and (b): Hist-eq-IN (NS region) images. Error bars are calculated considering 25th and 75th percentiles. The x-axis represents the intensity. The y-axis indicates the number of voxels with a given level in the striatum region.

6.3.3 Quantitative classification performance of Parkinsonism

The differential diagnosis of IPS (PD) versus APS is clinically important for therapeutic and particularly prognostic reasons. However, the diagnosis of parkinsonian syndromes at early disease stages is difficult because of the initial coexpression of signs and symptoms such as asymmetry of motor symptoms, resting tremor, and positive response to L-DOPA treatment. Thus, distinguishing between IPS and APS is still a challenge due to both disorders have similar symptoms [240, 241].
Since PET imaging provides a more precise quantification of striatal receptor binding owing to its superior imaging properties, the use of positron-emitting radionuclides labelled to appropriate ligands should enable better diagnostic discrimination between IPS and APS patients. Moreover, it should facilitate the diagnosis of early APS stages, especially when ligands are used with higher affinity to D_2-like receptors and with lower unspecific binding.
Since the lack of studies using DMFP data in terms of classification accuracy and there are still no data on the suitability of ^{18}F-DMFP in the diagnosis of parkin-

sonism, this study aims to investigate the diagnostic performance of ^{18}F-DMFP in patients with different forms of parkinsonism (PD, MSA and PSP), both before and after applying our proposed IN approaches.
Thus, the classification performance of the proposed intensity normalization approaches is tested, firstly, using the classical multivariate approach VAF in combination with the linear SVM kernel. Secondly, using the PCA feature extraction method and the SVM with linear kernel. LOO cross-validation strategy is used in order to estimate several performance parameters, such as, the accuracy rates, the sensitivity and the specificity of the resulting datasets after IN.

Voxels-as-Features (VAF)

The accuracy measures obtained by VAF for the different IN methods are shown in Table 6.13. The proposed approaches outperform the raw data, as they achieved a gain of 3.45% for the accuracy, 5.18% for the sensitivity and a gain of 1.88% for the specificity. Moreover, the accuracy again of our approaches is up to 9.2% compared to the widely used IN and it is up to 11.16% and to 8.12% for the sensitivity and the specificity gains.
^{18}F-DMFP has a high binding affinity for dopamine transporters in the striatal region of the brain. For this reason, neuroimaging studies based on it usually focuses on that region. Thus, a binary mask is applied to each image for the different datasets in order to select only the high-intensity voxels of the striatum area. The accuracy rates for different normalization methods using only the voxel intensity in the striatum are presented in Table 6.14.

Table 6.13: Comparison between the performance (%) achieved with the proposed intensity normalization methodologies, the raw data and the other normalization approaches **in the whole brain image** using **VAF** approach and linear SVM classifier.

Normalization approach	Accuracy	Sensitivity	Specificity
Raw data	64.37%	60.53%	67.35%
$BR_{all} - IN$	62.07%	58.82%	64.15%
Integral-IN	63.22%	60%	65.38%
Max-IN	63.21%	59.46%	66%
Hist-eq-IN	66.66%	64.70%	67.92%
Hist-eq-NS-IN	58.62%	54.55%	61.11%
α-stable-IN	62.07%	60%	63.16%
MSE	**67.82%**	**65.71**%	**69.23**%
MSE-GMM	**64.37%**	**62.50**%	**65.45**%
MLR	**66.67%**	**64.71**%	**67.93**%

There is a significant improvement of the performance results over the same VAF approach after the ROI selection for the different IN methods. However, The MSE methodology, proposed in this work, achieved an accuracy rate of 71.27% and outperformed other previous approaches in a fair comparison (using the same data and classification approach).

Table 6.14: Comparison between the performance (%) achieved with the proposed intensity normalization methodologies, the raw data and and the other normalization approaches **in the striatum** using the **VAF** approach and linear SVM classifier.

Normalization approach	Accuracy	Sensitivity	Specificity
Raw data	70.11%	67.57%	71.15%
$BR_{all} - IN$	67.82%	67.74%	67.86%
Integral-IN	62.06%	58.33%	64.70%
Max-IN	63.21%	59.45%	66%
Hist-eq-IN	65.52%	62.86%	67.31%
Hist-eq-NS-IN	62.07%	60%	63.15%
α-stable-IN	64.37%	62.50%	65.45%
MSE	**71.27%**	**70.59%**	**71.70%**
MSE-GMM	**68.97%**	**67.65%**	**69.81%**
MLR	**67.82%**	**67.74%**	**67.86%**

Principal Component Analysis (PCA)

In addition, we evaluated the proposed IN approaches using the PCA feature extraction method in computer systems to distinguish between idiopathic and non-idiopathic Parkinsonism. The reported accuracy rates of the proposed IN methods vary from 70.12% up to 72.41%, using the PCA in the whole image and taking into account all the binding regions. Thus, they outperform the unormalized DMFP images (raw data) whose its accuracy rate is 65.52% and the remaining IN approaches whose their accuracy rates vary from 60.91% up to 68.96%. Taking into account the striatum region, the accuracy rates of the proposed IN approaches reach a peak value of 72.41% and they demonstrate a good trade-off between sensitivity and specificity, as shown in tables 6.15 and 6.16. They outperform the raw data and the compared methods in spite of their accuracy improvement after ROI selection. Comparing the results obtained from the DaTSCAN SPECT database, the relatively low accuracy rates obtained from DMFP database could be explained by the used neuroimages, which correspond to early stages of the PD. Observe that the neuroimaging data were acquired during the first visit, 2 years before assigning the final diagnosis that was used to label the data. Furthermore, it is worth noting that the database was clinically labeled, what introduced an error due to the intrinsic

limitations of the clinical assessment [242], and the generalization of the classification procedure should be interpreted from this perspective. As a conclusion, the obtained results suggest that the proposed intensity normalization procedures lead to comparable generalization estimations and perform substantially better than the baseline methods. Moreover, the proposed approaches demonstrate also their ability and robustness to develop an accurate computer aided diagnosis system based on DMFP-based data in combination with SVM classification.

Table 6.15: Comparison between the performance (%) achieved with the proposed intensity normalization methodologies, the raw data and the other normalization approaches **in the whole brain image** using **PCA** approach and linear SVM classifier.

Normalization approach	Accuracy	Sensitivity	Specificity
Raw data	65.52%	60.98%	69.57%
$BR_{all} - IN$	68.96%	67.64%	69.81%
Integral-IN	68.97%	67.65%	69.82%
Max-IN	65.52%	61.54%	68.75%
Hist-eq-IN	60.91%	57.14%	63.46%
Hist-eq-NS-IN	60.92%	57.58%	62.96%
α-stable-IN	67.82%	65.71%	69.23%
MSE	**72.41%**	**72.73%**	**72.22%**
MSE-GMM	**70.12%**	**67.57%**	**72%**
MLR	**71.27%**	**68.42%**	**73.47%**

Table 6.16: Comparison between the performance (%) achieved with the proposed intensity normalization methodologies, the raw data and and the other normalization approaches **in the striatum** using the **PCA** approach and linear SVM classifier.

Normalization approach	Accuracy	Sensitivity	Specificity
Raw data	67.81%	64.86%	70.37%
$BR_{all} - IN$	68.96%	66.66%	70.58%
Integral-IN	64.37%	60.53%	67.34%
Max-IN	67.81%	62.79%	69.56%
Hist-eq-IN	66.66%	63.15%	69.38%
Hist-eq-NS-IN	63.22%	58.97%	66.66%
α-stable	67.81%	64.86%	70%
MSE	**72.41%**	**69.23%**	**75%**
MSE-GMM	**70.11%**	**65.85%**	**73.91%**
MLR	**68.97%**	**65.79%**	**71.43%**

6.4 Conclusion

Nowadays, the visual examination of the neuroimages is combined with modern computer systems that automatically analyze the data and are able to estimate their class (pathological or not). In the case of PD diagnosis, the classical approach addresses the problem directly, i.e., by quantifying the loss of striatal dopamine. However, modern computer systems examine the images, looking for the patterns that characterize the studied disease.
In this sense, the present chapter evaluates the impact of different intensity normalization methods for the development of a computer aided diagnosis system for PS detection based on DaTSCAN and DMFP image analysis and classification. Four novel alternatives are proposed to establish a comparison between specific/non-specific uptake areas. These methodologies are based on the extraction of intrinsic parameters from ^{123} I-ioflupane-SPECT and ^{18}F-DMFP PET images without using anatomical information, resulting in four automatic procedures for intensity normalization: GMM-based image filtering, MSE optimization (under voxel and cluster levels) and predictive modeling using MLR. Further analysis reveals that, the proposed normalization methods outperform many widely used approaches. Since, the proposed ones improve the normalization, increase the the difference between the striatum and the background uptakes. In addition, the inter-subject intensity differences are quantitatively reduced in the non-specific region, and the artifacts and noise affecting the source images are removed. This allows us to guarantee that the differences between the different DaTSCAN (NC and PS subjects) and DMFP (IPS and APS subjects) brain images are due only to the uptake of the tracer in the striatum region. Finally, These proposed automatic intensity normalization methods demonstrate also its ability and robustness in PS pattern detection as they provide good values of accuracy compared to other approaches.

Chapter 7

Conclusions and Future Work

This chapter shows the conclusions of the Thesis and highlights the scientific contributions that have been made. These contributions are divided into two groups. On the one hand, the development of new intensity normalization algorithms that improve the precision of computer aided diagnosis (CAD) systems for neurodegenerative diseases such as Parkinson's disease (PD). On the other hand, a comparison with many conventional intensity normalization (IN) methods adequately adapted to the nature of the PD is performed. Furthermore, several proposals for the continuation of this work are proposed, as future research lines.

7.1 Conclusions

Advances in clinical medical imaging have brought about the routine production of vast numbers of medical images that need to be analyzed. As a result, an enormous amount of computer vision research effort has been targeted at achieving automated medical image analysis. This has proved to be an elusive goal in many cases. Several factors degrade the medical image quality, some of which are due to physical factors, such as Compton scattering and photon attenuation, and system parameters, such as intrinsic and extrinsic spatial resolution of the gamma camera system. These factors result in blurred and noisy images. A high noise level will obscure the contrast and reduce the image quality, resulting in less accurate diagnosis or even in a fault diagnosis. The complexity of this problem encountered in analyzing these images has prompted considerable interest in the use of a relevant pre-processing step for such applications.
Hence, intensity normalization is a significant preprocessing step for functional imaging. It guarantees that the differences between subjects or scans are due to physiological reasons and brain functioning, and not due to the baseline calibration

of the gamma camera applied for the acquisition.
In this sense, new intensity normalization schemes are proposed, firstly, for analyzing functional tomographic images. Secondly, for improving the accuracy of the CAD systems used for the diagnosis of neurodegenerative diseases, such as, PD, MSA and PSP. These novel IN approaches are based on GMM, MSE and MLR.
The first normalization approach is based on a nonlinear image filtering by means of GMM. It is called the GMM-based image filtering approach. The voxels in the non-specific region, i.e., the reference region are intensity normalized by removing clusters whose likelihood is negligible. This process is based on a probability threshold that measures the weight of each kernel or cluster on the specific region, i.e., the striatum.
The second normalization method is based on the MSE optimization which is performed by a linear intensity transformation at a voxel level. This approach is based on predicting jointly different intensity normalization parameters that leads to the joint minimization of the squared sum errors between the template image and the optimal linear estimated image (normalized image).
The third approach is a combination between the two previous methods. Thus, it is based on the minimization of the MSE between the GMM-based extracted features from each subject image and a template in the non-specific region at the cluster (of voxels) level.
The fourth and the last proposed intensity normalization approach is based on a predictive modeling using MLR. Different intensity normalization parameters derived from this model will be used in a linear procedure to perform the intensity normalization of the brain images.
The methodologies developed for the normalization of 3D images were essentially applied to normalize DaTSCAN SPECT images. Furthermore, they are successfully applied to other modalities of images, such as, DMFP PET imaging. Further analysis reveals that, the proposed methods are characterized by stability and repeatability of performance, speed of execution, independence of clinical protocol and robustness.
The main motivations of using these approaches are *i)* to perform an automatic intensity normalization of brain images, *ii)* to eliminate operator-dependent manipulations [203], *iii)* to avoid the manual preselection of relevant information by means of statistical analysis [176] and *iiii)* to improve CAD systems.
Throughout the experiments on two independent datasets, we not only demonstrate the merits of our methods that outperform most state-of-the-art methods. Although, we also show that the intensity normalization have a significant role in discriminating NC from PD images and in distinguishing PD from APS for an accurate computer aided diagnosis systems.
As a final conclusion of this PhD project, the initial goals were successfully reached. This is confirmed by the fact that the works developed were published in several international journals and presented at international conferences.

7.2 Future Work

As future lines of the research developed throughout this work, we present the following proposals:

- Improvements in the MKL-IN approach, which is based on the minimizing of the Kullback-Leibler divergence. This normalization scheme is more demanding, as it is based on an iterative algorithm (SPSA). In order to overcome this computational load, this algorithm needs the optimization of many parameters, such as, the gain sequences, the maximum number of iterations, the initial intensity adjustment parameter, ext.
- The use of a multiple kernel learning procedure along with a SVM classifier to improve the the relatively low accuracy rates obtained from DMFP database.
- The use of the Multiclass classification that allows to categorize the images in more than two classes and therefore to distinguish different stages of the progressive diseases.
- The use of the well-known Automated Anatomical Labeling (AAL) [243] atlas in order to automatically parcel the neuroimaging data. This procedure allows isolating specific regions such as the striatum.
- Field Programmable Gate Array (FPGA) Implementation of the GMM-based image filtering (FGMM) approach for DMFP database in order to decrease the computational time for the model estimation stage. It can reach more than 69 hours for just a one GMM model.

Appendices

Appendix A

Appendix

A.1 Cluster selection strategy

The local averaged intensity in the ROI for each image subject can be computed by:

$$I_{\mathcal{R}} = \int_{\mathcal{R}} \mathrm{d}^3\mathbf{x}\, I(\mathbf{x}) f_n(\mathbf{x}) \tag{A.1}$$

where I(x) is is the global intensity of the image. In terms of a-priori probabilities, the eq (A.1) can be expanded to:

$$I_{\mathcal{R}} = \int_{\mathcal{R}} \mathrm{d}^3\mathbf{x}\, I(\mathbf{x}) p(\mathbf{x}) \tag{A.2}$$

where p(x) is the probability density function (pdf) which is given by [200]:

$$p(\mathbf{x}) = \sum_{n=1}^{k} P_n p(\mathbf{x}|\theta_n) \tag{A.3}$$

The parameter $P_n = \omega_n$ denotes the a priori probability of class "n" and $p(\mathbf{x}|\theta_n)=f_n(\mathbf{x}|\theta_n)$ is the conditional density of class "n". As a result the local averaged intensity can be expressed as follows:

$$I_{\mathcal{R}} = \sum_{n=1}^{k} P_n \int_{\mathcal{R}} \mathrm{d}^3\mathbf{x}\, I(\mathbf{x}) p(\mathbf{x}|\theta_n) = \sum_{n=1}^{k} P_n I_n \tag{A.4}$$

If the striatum is selected as ROI and we assume that the intensity $I_{\mathcal{S}}$ holds almost constant in this region, the contribution of every cluster to the striatum intensity can be computed as:

$$I_n = I_{\mathcal{S}} \int_{\mathcal{S}} \mathrm{d}^3\mathbf{x}\, p(\mathbf{x}|\theta_n) \tag{A.5}$$

Moreover the condition for activation (>) or non-activation (<) for every single voxel in Γ is:

$$f_n(\mathbf{x_j^s}|\theta_\mathbf{n}) \gtrless \eta \quad n \in \Omega \tag{A.6}$$

If a region is "probable" or activated then, its probability $P(X^\mathbf{S})$ must be higher that the one assigned by the uniform pdf of the same region:

$$P(X^\mathbf{S}) > P_u(X^\mathbf{S}) \tag{A.7}$$

where $P(X^\mathbf{S})$ is evaluated as:

$$P(X^\mathbf{S}) = \sum_{n=1}^{k} P_n \int_\mathcal{S} \mathrm{d}^3\mathbf{x}\ p(\mathbf{x}|\theta_n) = \sum_{n=1}^{k} P_n P(\mathbf{x^s}|\theta_n) \tag{A.8}$$

And $P_u(X^\mathbf{S})$ is calculated as:

$$P_u(X^\mathbf{S}) = \int_\mathcal{S} \mathrm{d}^3\mathbf{x}\ p_u(\mathbf{x}) = \eta \cdot V_\mathcal{S} \tag{A.9}$$

Following the eq (A.6), the contribution of each relevant cluster to the whole probability for all the voxels:

$$P(\mathbf{x^s}|\theta_n) = \int_\mathcal{S} \mathrm{d}^3\mathbf{x}\ p(\mathbf{x}|\theta_n) \simeq \sum_{j=1}^{N_s} v_s\ p(\mathbf{x_j^s}|\theta_n) > \sum_{j=1}^{N_s} v_s \eta = P_u(X^\mathbf{S}) \tag{A.10}$$

where v_s is the volume element, i.e. the voxel resolution. Thus the condition for activation is:

$$\mu_s = \frac{1}{N_s} \sum_{j=1}^{N_s} p(\mathbf{x_j^s}|\theta_n) > \eta \tag{A.11}$$

Hence, the sample mean of the random variable $p(\mathbf{x_j^s}|\theta_n)$ must be higher than η. In order to relax the condition in eq (A.6) for cluster selection we allow just a fraction α of voxels to satisfy this condition, i.e. a fraction equal or greater than 75%. If this fraction is large enough, the probability that the sample mean is bigger than η is quite large, thus the eq (A.7) is fulfilled by a single cluster.
To assess this probability, lets assume for the set of N_s trials that $p(\mathbf{x_j^s}|\theta_n)$ is distributed normally and independently with mean μ and variance $\sigma^2 \sim \mathcal{N}(\mu, \sigma^2)$. Under the null hypothesis H_0 that the both means are equal, i.e. $\mu = \eta$, the probability $P(p(\mathbf{x_j^s}|\theta_n) \gtrless \eta)$=$p$=0.5. Moreover, the probability of getting N_b samples greater than the mean η in N_s trials follows a binomial distribution is given by :

$$P(X = N_b) = \frac{N_s!}{N_b!M!}\ p^{N_b}(1-p)^M = \frac{N_s!}{N_b!M!}\ p^{N_s} \tag{A.12}$$

where M= N_s–N_b stands for the samples of the probability less than the mean. Given $N_s \cong 1000$, N_b= $0,75 \cdot N_s$ and M= $0,25 \cdot N_s$, $P(X = 0,75 \cdot N_s) = 4.5 \cdot 10^{-59}$. Thus the false alarm rate $P(X \geq 750) = \sum_{i=750}^{1000} P(X = i) = 1 - P(X \leq 750) = 0$. As a conclusion, our selection criterion is enough to fulfill the condition of relevance.

A.2 MKL-IN

The Simultaneous Perturbation Stochastic Approximation (SPSA) [244, 245] is used in this normalization approach to calculate an approximation of the objective function gradient at each iteration and then adjusts the current solution estimate according to the gradient estimate. Moreover, for generating the gradient estimate, finite differences are used. Thus, the SPSA method incorporates two "gain" sequences that serve to shrink, as illustrated in eq. A.13 . Whereas the iterations progress, the distance over which the finite differences are calculated as well as the size of the adjustment step taken.
For the calculation of an approximation of the objective function, SPSA generates a gradient estimate $\hat{\boldsymbol{g}}_{\boldsymbol{i}}$, at each iteration i, as follows:

$$\hat{\boldsymbol{g}}_{\boldsymbol{i}}(\boldsymbol{F_s}) = \frac{\boldsymbol{u}(\boldsymbol{F_s} + \boldsymbol{c_i}\boldsymbol{\Delta_i}) - \boldsymbol{u}(\boldsymbol{F_s} - \boldsymbol{c_i}\boldsymbol{\Delta_i})}{2\boldsymbol{c_i}\boldsymbol{\Delta_i}} \tag{A.13}$$

where $u(F_s) = KL(h(F_sI), M)$ is the objective function, $h(F_sI)$ is the histogram of the adjusted image $\hat{I}$ (the original image I multiplied by the current estimate of the adjustment field F_s), M is the model histogram to which we are matching, and KL is the Kullback-Leibler divergence. The gradient estimate is made across a perturbation of the parameter field F_s by $\pm\, \boldsymbol{\Delta_i}$. The convergence over a number of iterations is guaranteed by the selection of $\boldsymbol{\Delta_i}$. Spall suggests in [244] that sampling the elements of $\boldsymbol{\Delta_i}$ from a Bernoulli ± 1 distribution with +1 and -1 equally likely, as we have used here. Therefore, $c_i\boldsymbol{\Delta_i}$ is a vector of $\pm\, c_i$.
The gain sequences are defined as follows:

$$c_i = \frac{c}{i^{\gamma}} \tag{A.14}$$

$$a_i = \frac{a}{(i + A)^{\alpha}} \tag{A.15}$$

where c_i controls the distance over which the gradient estimate is made and a_i controls the size of the resulting step taken. A is an added parameter that allows for a more aggressive value of a, while avoiding instability during early iterations. The decay parameters, α and γ, are set to 0.602 and 0.101, which was the starting point recommended in [244].
After each iteration, the estimate of the solution parameter field F_i is updated as:

$$F_{i+1} = F_i - a_i g_i \tag{A.16}$$

Appendix B

Quantification of the intensity normalization methods

The classification performances of our proposed approaches are tested using support vector machines-based supervised learning and the Leave-One-Out (LOO) cross-validation strategy. The LOO strategy is often computationally expensive because of the large number of times the training process is repeated, although it gives insight into the ability of the classification method since all the available information is included in the learning process. In addition, in order to extract the most significant features from the datasets, the PCA based feature extraction is used.

B.1 Support vector machines classifier (SVM)

SVM are a set of related supervised learning methods widely used in pattern recognition, voice activity detection, classification and regression analysis [246–249]. It is introduced in order to separate a set of binary labelled training data with a hyperplane that is maximally distant from the two classes (called maximal margin hyperplane). The objective is to build a function f: $\mathbb{R}^N \rightarrow \pm 1$ using training data, that is, n-dimensional patterns $\mathbf{x_i}$ and class labels y_i, so that f will correctly classify new examples $(\mathbf{x}, y)$:

$$(\mathbf{x_1}, y_1), (\mathbf{x_2}, y_2), ..., (\mathbf{x_N}, y_N) \in \mathbb{R}^N \times \pm 1 \tag{B.1}$$

Linear discriminant functions define decision hyperplanes in a multidimensional space, that is:

$$\mathbf{g}(\mathbf{x}) = \mathbf{w}^T\mathbf{x} + w_0 \tag{B.2}$$

where $\mathbf{w}$ is the weight vector that is orthogonal to the decision hyperplane and w_0 is the threshold. The optimization task consists of finding the unknown parameters

$\mathbf{w_i}$, i =1,...,N and w_0 that define the decision hyperplane. Let $\mathbf{x_i}$, i =1,...,n be the feature vectors of the training set, $\mathbf{x}$. These belong to either of the two classes, w_1 or w_2. If the classes were linearly separable, the objective would be to design a hyperplane that classifies correctly all the training vectors. The hyperplane is not unique, and the selection process is focused on maximizing the generalization performance of the classifier, that is, the ability of the classifier, designed using the training set, to operate satisfactorily with new data. Among the different design criteria, the maximal margin hyperplane is usually selected since it leaves the maximum margin of separation between the two classes. Since the distance from a point $\mathbf{x}$ to the hyperplane is given by z =|g ($\mathbf{x}$)|/||$\mathbf{w}$||, scaling w and $\mathbf{w_0}$ so that the value of g ($\mathbf{x}$) is +1 for the nearest point in w_1 and -1 for the nearest points in w_2, reduces the optimization problem to maximizing the margin: 2/||$\mathbf{w}$|| with the constraints:

$$\mathbf{g}(\mathbf{x}) = \mathbf{w^T x} + \mathbf{w_0} \geqslant 1, \forall \mathbf{x} \in w_1 \tag{B.3}$$

$$\mathbf{g}(\mathbf{x}) = \mathbf{w^T x} + \mathbf{w_0} \leqslant 1, \forall \mathbf{x} \in w_2 \tag{B.4}$$

When no linear separation of the training data is possible, SVM can work effectively in combination with kernel techniques such as quadratic, polynomial or radial basis function (RBF), so that the hyperplane defining the SVM corresponds to a non-linear decision boundary in the input space[250]. A kernel function is defined as:

$$K(\mathbf{x_i}, \mathbf{x_j}) = \varphi(\mathbf{x_i})\varphi(\mathbf{x_j}) \tag{B.5}$$

The use of kernel functions avoids directly working in the high dimensional feature space, thus the training algorithm only depends on the data through dot products in Euclidean space, i.e., on terms of the form $\varphi(\mathbf{x_i})\varphi(\mathbf{x_j})$.

B.2 Cross validation

In cross validation, we randomly split the set of labeled training samples into two parts: one is used as the traditional training set for adjusting model parameters in the classifier. The other set is the validation set, which is used to estimate the generalization error. Since our ultimate goal is low generalization error, we train the classifier until we reach a minimum of this validation error [251]. The classifier is trained as many times as the size of the database. In each iteration an image is used for the test and the remaining ones for training. The global accuracy is then calculated as the average of the accuracy achieved in each iteration. Thus, the accuracy (Acc), sensitivity (Sens) and specificity (Spec) rates are defined as follows:

$$\text{Acc} = \frac{TP + TN}{TP + TN + TN + FP};\ \text{Sens} = \frac{TP}{TP + FN};\ \text{Spec} = \frac{TN}{TN + FP} \tag{B.6}$$

where *TP* is the number of true positives (number of PS patients correctly classified), *TN* is the number of true negatives (number of control subjects correctly classified), *FP* is the number of false positives (number of control subjects classified as PS patients and *FN* is the number of false negatives (number of PS patients classified as control subjects).

B.3 Principal Component Analysis

Principal component analysis (PCA)[235] has been called one of the most important and valuable results from applied linear algebra. PCA is used frequently in all forms of analysis because it is an efficient tool for extracting the most significant features from a dataset. It is often used in neuroimaging in order to reduce the original high dimensional space of the brain images to a lower dimensional subspace [236, 252]. Furthermore, it has been successfully applied for neuroimage classification problems [237]. Mathematically, PCA generates an orthonormal basis vector that maximizes the scatter of all the projected samples. After the preprocessing steps, the n remaining voxels for each subject are rearranged into a vector form. Let $\mathbf{X} = [\mathbf{x}_1, \mathbf{x}_2 ..., \mathbf{x}_N]$ be the sample set of these vectors, where N is the number of patients. After normalizing the vectors to unity norm and subtracting the large average, a new vector set $\mathbf{Y} = [\mathbf{y}_1, \mathbf{y}_2 ..., \mathbf{y}_N]$ is obtained, where each $\mathbf{y}_i$ represents an n-dimensional normalized vector, $\mathbf{y}_i = (\mathrm{y_{i1}}, \mathrm{y_{i2}} ..., \mathrm{y_{in}})^t$, $i = 1, 2, .., N$. The covariance matrix of the normalized vectors set is defined as:

$$\Sigma_Y = \frac{1}{\mathrm{N}} \sum_{i=1}^{N} \mathbf{y}_i {\mathbf{y}_i}^t = \frac{1}{\mathrm{N}} \mathbf{Y}\mathbf{Y}^t \tag{B.7}$$

and the eigenvector and eigenvalue matrices $\mathbf{\Phi}$ and $\mathbf{\Lambda}$ are computed as:

$$\Sigma_Y \mathbf{\Phi} = \mathbf{\Phi}\mathbf{\Lambda} \tag{B.8}$$

Note that $\mathbf{Y}\mathbf{Y}^t$ is an $n \times n$ matrix while $\mathbf{Y}^t\mathbf{Y}$ is an $N \times N$ matrix. If the sample size N is much smaller than the dimensionality n, then diagonalizing $\mathbf{Y}^t\mathbf{Y}$ instead of $\mathbf{Y}\mathbf{Y}^t$ reduces the computational complexity [253].

$$(\mathbf{Y}^t\mathbf{Y})\mathbf{\Psi} = \mathbf{\Psi}\mathbf{\Lambda_1} \tag{B.9}$$

$$\mathbf{T} = \mathbf{Y}\mathbf{\Psi} \tag{B.10}$$

where $\mathbf{\Lambda}_1 = \mathrm{diag}\{\lambda_1, \lambda_2, ..., \lambda_N\}$ and $\mathbf{T} = [\mathbf{\Phi}_1, \mathbf{\Phi}_2, ..., \mathbf{\Phi}_N]$. In short, we use PCA to transform the data into a set of a few intermediate linear latent variables (components) and then, these new variables are used for dimension reduction.

Appendix C

Introducción

C.1 Introducción General

La imagen tomográfica ha sido seleccionada como uno de los grandes logros del siglo XX por la Academia Nacional de Ingeniería [7] debido a su impacto en la medicina y la biología [8]. En el campo médico, los datos de imagen se utilizan de forma ubicua en la práctica clínica, así como en los estudios científicos para inferir detalles sobre el proceso objeto de la investigación, bien sea de un proceso de enfermedad o un proceso fisiológico. Por lo tanto, la información proporcionada por las imágenes médicas se ha convertido en una parte vital para la salud del paciente de hoy.
Más allá de esto, las imágenes no solo han mejorado la calidad de la atención al paciente, sino también la reducción de los costes del cuidado de la salud. De hecho, la imagen es una herramienta complementaria para las pruebas neuropsicológicas que pueden evaluar las anomalías estructurales y funcionales para mejorar el diagnóstico precoz. Además, muchas enfermedades pueden ser diagnosticadas en una etapa mucho más temprana en la progresión de la enfermedad, ya que no es necesario que los síntomas sean evidentes en el exterior del cuerpo humano, como solía ocurrir. Por otra parte, si se detecta una enfermedad, los procedimientos que se pueden utilizar para ello resultan mucho menos invasivos.
A diferencia de las imágenes producidas en las aplicaciones industriales, las imágenes generadas en aplicaciones médicas son complejas y muy diferentes de una aplicación a otra.
La medicina nuclear es la sección de la ciencia que utiliza las características de los fármacos radiactivos con el fin de obtener información clínica y bioquímica de la fisiología humana. De acuerdo con el examen necesario para cada paciente, una pequeña cantidad de material radiactivo, es decir, un radionúclido se fija a un fármaco (trazador). Esta combinación se llama radiofármaco o radiotrazador. En-

tonces, todo el complejo se administra al paciente por vía intravenosa. Por lo tanto, el marcador radiactivo sigue su vía fisiológica y se concentra en un lugar específico en el cuerpo del paciente dónde puede haber enfermedad o una anomalía durante cortos períodos de tiempo. A continuación, la radiación emitida por el producto radiofarmacéutico en el cuerpo humano se detecta usando una cámara especial que se llama cámara gamma, dando como resultado imágenes de la biodistribución del radiotrazador. Por lo tanto, las imágenes de medicina nuclear muestran información característica acerca de las propiedades fisiológicas del tejido u órgano investigado. En las últimas décadas, los sistemas de imágenes médicas han avanzado considerablemente. Se han producido unas mejoras sustanciales en sus características como sensibilidad, resolución y velocidad de adquisición. Por lo tanto, las técnicas avanzadas de procesamiento y análisis de imágenes encuentran un amplio uso en la medicina. Los métodos de procesamiento de imágenes están en continuo desarrollo con el fin de mejorar aún más la calidad de las imágenes médicas que se utilizan para un diagnóstico fiable.

El reto del procesamiento y análisis de imágenes aplicado a las aplicaciones médicas permite la mejora de la calidad de la imagen adquirida y extraer información cuantitativa (es decir, característica) de los datos médicos de imagen de una manera eficiente y exacta.

La calidad de la imagen juega un papel importante en la formación de imágenes de medicina nuclear con el fin de proporcionar una imagen fiable del órgano proyectado para un diagnóstico o terapia precisa. Las características físicas que se utilizan para describir la calidad de la imagen son la resolución espacial, el contraste y el ruido.

La resolución espacial se define como la capacidad de la técnica de imagen para reproducir los detalles de una distribución no uniforme del trazador radiactivo en el paciente [21]. Por lo tanto, se refiere a la capacidad del instrumento de formación de imágenes para proporcionar la nitidez o detalle del objeto. La resolución espacial se separa en la resolución intrínseca (centelleador, tubos fotomultiplicadores y un circuito electrónico) y la resolución del sistema (colimador, centelleo, tubos fotomultiplicadores y circuito electrónico) [22]. La resolución intrínseca depende del espesor del cristal de centelleo, mientras que la resolución del sistema depende principalmente de la distancia de la fuente emisora del colimador (la geometría del colimador) y en cierta medida por el grosor del tabique. Además, la resolución de una cámara gamma está limitada por varios factores, tales como, el movimiento del paciente, la fluctuación estadística de la distribución de fotones visibles detectada, la geometría del colimadores, el ruido de Poisson en la producción de fotones de centelleo, el número de tubos fotomultiplicadores, los algoritmos de localización de posición utilizados y la visualización de la imagen o sistemas de registro [3].

Por lo tanto, las resoluciones espaciales intrínsecas y de la cámara son parámetros que afectan inherentemente a la calidad de la imagen y la precisión cuantitativa. La mayoría de las cámaras gamma modernas tienen valores similares para estos parámetros, y la mayoría de los valores están cerca óptima para el presente coli-

mador / centelleador de cristal / tecnología fotodetector [3].
La segunda característica física para describir la calidad de la imagen es el contraste de la imagen. Se puede definir como la diferencia en intensidad correspondiente a la diferente concentración de la actividad en el paciente [22]. Las imágenes de medicina nuclear deben ser de alto contraste para una buena precisión diagnóstica. El contraste de la imagen se ve afectado por varios factores, tales como, el producto radiofarmacéutico que se utiliza para formación de imágenes, el efecto Compton, coincidencias aleatorias o accidentales, y el detector de tiempo muerto [3]. Por lo tanto, es preferible utilizar un fármaco radiactivo que permita una alta absorción en el órgano diana. El efecto Compton [23] puede ser reducido por las ventanas de energía. Sin embargo, para mantener una alta sensibilidad, la resolución de energía y la fracción de los fotones deben ser altas [3].Para resolver coincidencia se requiere un cristal de centelleo rápido brillante o un detector de bajo nivel de ruido y electrónica [3]. El azar en la coincidencia y los efectos de tiempo muerto pueden reducirse si se implementan detectores rápidos [25, 26].
Por último, la tercera característica física es el ruido, que es el factor principal en la degradación de la calidad de imagen. El ruido de la imagen puede dividirse en ruido aleatorio y estructurado [22, 27]. El ruido aleatorio, también conocido como ruido estadístico, es el resultado de las variaciones estadísticas en los recuentos de ser detectado, que puede ser bastante significativo en los estudios de imagen de la tomografía computarizada por emisión de positrones (PET)[28]. El ruido estructurado se deriva de la falta de uniformidad en la cámara de centelleo y estructuras superpuestas en el cerebro del paciente. El ruido estructurado puede surgir de la propia distribución de radionucleido o causado por artefactos del sistema [29]. Por lo tanto, el ruido proviene principalmente de las variaciones aleatorias inherentes en el conteo de fotones. Por otra parte, está relacionado con el número de fotones detectados y utilizados para la generación de la imagen [29, 30]. Por ejemplo, la tomografía por emisión de un sólo fotón (SPECT), que permite obtener imágenes con un menor número de fotones, tiene niveles de ruido de alrededor de 10% [30].
En consecuencia, el ruido puede ser causado por un lado, por incertidumbres aleatorias no correlacionadas, incluyendo el ruido de fotones, ruido electrónico y el ruido debido a la radiación dispersa. Por otro lado, el ruido puede ser generado por incertidumbres sistemáticas correlacionadas, incluyendo la distorsión geométrica, detector de la no linealidad, los errores debidos a muestrear una imagen continua en un conjunto discreto de píxeles y errores de cálculo cuando una imagen se reconstruye a partir de datos indirectos [31].
El campo del procesamiento y análisis de imágenes tiene que hacer frente a un conjunto diverso y complejo de problemas. Debido a su gran extensión, nos centramos en ciertos temas que consideramos importantes en el campo de la medici-na, tales como el desarrollo de sistemas de diagnóstico asistido por ordenador (CAD, del inglés “computer aided diagnosis”) de enfermedades neurodegenerativas. CAD es un concepto amplio que integra el procesamiento de imágenes, visión artificial, las matemáticas, la física y las estadísticas en gráficos computarizados. Estas

técnicas ayudan a los radiólogos en el proceso de toma de decisiones médicas, tal como se representa en la figura C.1. Sirve como una segunda opinión en la detección de anomalías, clasificación de las lesiones, cuantificación de la enfermedad y de las estructuras anatómicas, evaluación de riesgos y la evaluación fisiológica. Por otra parte, CAD es una tecnología interdisciplinaria relativamente joven que combina elementos de la inteligencia artificial y procesamiento de imágenes digitales en el campo de la imagen de medicina nuclear y radiológica. Una aplicación típica es la detección de un tumor. Por ejemplo, algunos hospitales utilizan CAD para apoyar su examen médico preventivo en la mamografía (diagnóstico de cáncer de mama), la detección de pólipos en el colon y cáncer de pulmón. Esto parece indicar que los sistemas CAD están empezando a ser aplicado ampliamente en la detección y diagnóstico diferencial de los diferentes tipos de anomalías en las imágenes médicas obtenidas en diversos exámenes mediante el uso de diferentes modalidades de imagen. De hecho, los sistemas CAD se han convertidos en uno de los principales temas de investigación en imagen médica y el diagnóstico radiológico [9–11]. Últimamente, algunos métodos basados en el paradigma de aprendizaje automático [12, 13] y redes neuronales [14] se han aplicado a los procedimientos de análisis de imagen, dando lugar a la construcción de sistemas CAD para varias enfermedades neurodegenerativas, como la enfermedad de Alzheimer (AD, del inglés Alzheimer's Disease) [15–17]o la enfermedad de Parkinson (PD, del inglés Parkinson's Disease) [1, 18–20]. Estos sistemas no solo procesan y analizan datos de la imagen, sino también pueden determinar si una imagen pertenece a la clase de imágenes normales (sujetos sanos) o imágenes patológicas (pacientes), realizando de esta manera un diagnóstico automático. Por lo tanto, un sistema CAD típico puede estar compuesto de cuatro módulos principales, como se muestra en la Figura C.1. El pre-procesamiento de las imágenes mejora la calidad de imagen de entrada y así permite la segmentación de la imagen para la extracción precisa de las regiones de interés. La extracción y selección de características identifican un pequeño número de características matemáticas que son utilizadas por las técnicas de reconocimiento de patrones y de aprendizaje automático para la identificación de la enfermedad y la clasificación. Además, los sistemas CAD se pueden aplicar a diferentes imágenes en medicina nuclear.

C.2 Motivación

A pesar de los enormes progresos realizados en la tecnología de adquisición de imágenes, muchos problemas graves en el uso de estos dispositivos están relacionados con los artefactos de imágenes médicas para el diagnóstico y la planificación del tratamiento. Así, la calidad de las imágenes adquiridas se encuentra degradada por factores físicos, tales como el efecto Compton y la atenuación de fotones, y los parámetros del sistema (la resolución espacial intrínseca y extrínseca del sistema

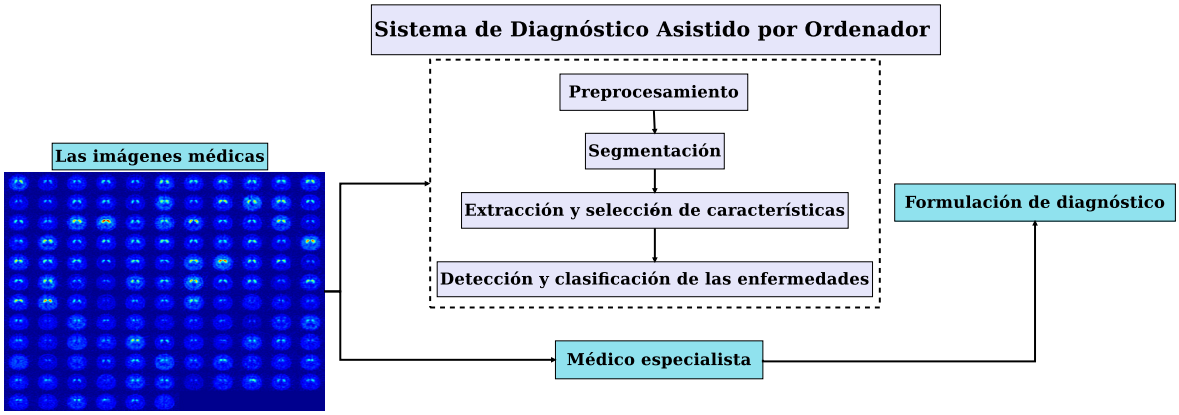

Figure C.1: Arquitectura general de los sistemas CAD para las imágenes médicas.

de cámara gamma). El principal problema es que estas imperfecciones de imagen pueden influir en el diagnóstico o, en el peor de los casos, pueden incluso dar lugar a malas decisiones médicas. Por lo tanto, las fuentes de los artefactos deben ser comprendidas y eliminan durante el proceso de adquisición. Sin embargo, en muchos casos, esto no se puede lograr debido a problemas físicos, financieros o de tiempo. Por lo tanto, tienen que utilizar los métodos de corrección retrospectivos [32]. Por otra parte, con el fin de superar la influencia de la variabilidad interindividual, las imágenes se procesan con pasos de registro y de normalización de intensidad. Estos pasos están dedicados para normalizar los volúmenes cerebrales, alinear espacialmente las regiones anatómicas, y calibrar la intensidad en escala de grises, de modo que las imágenes puedan ser comparadas una con otra. En esta tesis, investigaremos la posibilidad de proporcionar a los médicos herramientas que proporcionen información útil acerca de las imágenes de tomografía computarizada por emisión, tales como, SPECT y PET para el proceso de diagnóstico. Para ello, se concentrará principalmente en una parte muy importante del sistema de CAD, la normalización de la intensidad con el fin de mejorar el rendimiento general en la detección temprana de la enfermedad de PD y otras enfermedades neurodegenerativas, tales como el síndrome de Shy-Drager o atrofia multisistémica (MSA, del inglés “multiple system atrophy”) y la parálisis supranuclear progresiva (PSP, del inglés “progressive supranuclear palsy”). El diagnóstico inicial de la PD realizado por neurólogos generales ha demostrado ser incorrecto entre el 24 % y 35 % de los casos [33]. Una prueba de diagnóstico fiable, que se pudiera utilizar para diferenciar diferentes trastornos de temblor, por lo tanto sería de gran valor. Como una característica de la PD es una marcada reducción de las neuronas dopaminérgicas en la región estriatal, técnicas de imagen cerebral (SPECT o PET) con ligandos específicos se pueden utilizar como una herramienta valiosa para evaluar pacientes con PD [34]. Estos radio-ligandos específicos se unen a los transportadores de dopamina en el cuerpo estriado y han evolucionado como marcadores en vivo de la pérdida progresiva de neuronas dopaminérgicas en la PD. Previo a cualquier tipo de procesamiento

de imágenes, las imágenes cerebrales funcionales tienen que ser normalizadas en cuanto a intensidad. Por lo tanto, el paso de la normalización de la intensidad es esencial, ya que corresponde a la etapa inicial en cualquier análisis posterior por ordenador. Garantiza que las diferencias entre imágenes de temas diferentes son debidas a razones fisiológicas y al funcionamiento del cerebro, entre otros factores y no debido a la calibración de referencia de la cámara gamma que se usa para la adquisición [35]. Las principales ventajas de los sistemas CAD podrían ser la reducción de la carga de trabajo de los médicos, así como la obtención de resultados fiables, reproducibles e independientes del observador. Teniendo en cuenta los estudios y tratamiento de pacientes longitudinales, los sistemas CAD pueden ser capaces de detectar y llamar la atención en las primeras etapas de los casos prodrómicos.

C.3 Objetivos

El objetivo principal de esta tesis es presentar cuatro metodologías totalmente automatizadas de la normalización de la intensidad con el fin de ayudar a los médicos en el análisis de las imágenes tomográficas funcionales del cerebro, tales como las imagenes de DaTSCAN SPECT y DMFP PET. Estos nuevos enfoques se basan en el modelo de mezcla gaussiana (GMM, del inglés "Gaussian mixture model"), el error cuadrático medio (MSE, del inglés "mean-squared error") y el modelado predictivo, utilizando la regresión lineal multivariante (MLR, del inglés "multivariate linear regression"). El método de filtrado de imágenes basado en GMM se consigue de acuerdo con un umbral de probabilidad que elimina los grupos cuya probabilidad son insignificantes en la región no específica (los voxels del cerebro, excepto los de la zona del estriado). El método de optimización de MSE consistirá en una transformación lineal que se obtiene reduciendo al mínimo el error cuadrático medio en la región no específica entre la intensidad de la imagen normalizada y la plantilla. Para el enfoque MLR, las imágenes normalizadas se calculan mediante la transformación lineal de la intensidad en el voxel de cada imagen del objeto, utilizando un modelo predefinido, como en el enfoque MSE. Los métodos de normalización de intensidad propuestos serán comparados con los enfoques ampliamente utilizados, como por ejemplo, la relación de unión específica y no específica, la normalización de la intensidad integral, la ecualización del histograma, la normalización de intensidad lineal utilizando la distribución de α-*stable*, la normalización de intensidad utilizando los valores máximos y la normalización de la intensidad, reduciendo al mínimo la divergencia de Kullback-Leibler. Esta comparación se realiza en dos bases de datos de imagen diferentes que comprenden las etapas de análisis y de clasificación para el desarrollo de sistemas CAD para la detección de síndrome de Parkinson (PS, del englés "Parkinsonian syndrome") idiopático y atípico. Además, estos métodos propuestos serán evaluados en la corrección de artefactos espacialmente variables que modulan la intensidad de las imágenes.

C.4 Estado del arte en la normalización de la intensidad

Hay diferentes métodos de normalización disponibles en la literatura para la normalización de las imágenes de PD [187–190]. Estos enfoques se basan en la normalización general de las imágenes funcionales 3D y se pueden adaptar para la normalización de un tipo particular de imágenes, tales como las imágenes SPECT o PET, utilizadas en esta tesis para el diagnóstico de la enfermedad de Parkinson. En esta sección, vamos a tratar de presentar algunos de los métodos convencionales de la normalización de intensidad adecuadamente adaptados a la naturaleza de las imágenes de PD. Además, se tendrán en cuenta para la comparación con los enfoques propuestos.

- Relación de unión específica y no específica (BR_{all}-IN): este enfoque de normalización se basa en el cálculo de la relación de unión (BR, del inglés "Bin - ding Ratio") del producto radiofarmacéutico en cada voxel entre el flujo sanguíneo alto y bajo como una función de la concentración de marcador en el flujo de sangre [156, 176]. Este BR puede ser utilizado para la normalización de las imágenes funcionales del cerebro [191]. El proceso de normalización se basa en la división de cada intensidad de voxel por el valor medio de intensidad en la región no específica en una forma defineda en [2]. BR $_{all}$, como se muestra en la ecuación 3.4, indica la relación de la unión calculada utilizando todos los voxels del cerebro, excepto los de la zona del estriado como región no específica. El principal motivo de esta elección es que esta región se encuentra desprovista de sitios de unión del transportador de dopamina. La relación de unión específica y no específica y la densidad del transportador de dopamina pueden ser afectadas por una serie de factores y pueden no ser lineales a menos que el trazador logre un equilibrio estable durante el período de formación de imágenes [156].
  Este enfoque se usa comúnmente para eliminar el efecto de los valores globales en varias aplicaciones de imagen [190]. Además, supera a varios enfoques, como, *ANCOVA*, *z score*, *residual* y *subject residual profile* [189]. Por estas razones, se consideró que este enfoque como *baseline* para la comparación con los enfoques propuestos. Sin embargo, este método de normalización depende de mucho tiempo, trabajo y experiencia del operador y también de su habilidades en colocar manualmente las regiones de interés (ROI, del inglés "Regions of interest"). Además, este enfoque supone que la concentración de trazador en la sangre sea estacionaria sobre toda la volumen de la imagen.
  También, el tamaño de los volúmenes de interés, en particular, tiene un impacto directo en la medición de la concentración de recuento. Esto es principalmente una consecuencia de la baja resolución espacial de las modalidades de imagen funcional (respecto a la estructural), lo que provoca que los recuen-

tos sean borrosos fuera del volumen físico de la estructura, es decir, el efecto de volumen parcial [192], y por lo tanto hace que sea difícil evaluar las concentraciones de recuento con precisión [181].

- La normalización de la intensidad integral [1](Integral-IN): la normalización de intensidad basada en Integral consiste en el cálculo de un parámetro intrínseco de la imagen, I_p. Esta normalización se realiza mediante la estimación de la actividad de unión:

$$\hat{I} = \frac{I}{I_p} \tag{C.1}$$

donde I denota la imagen espacialmente normalizada, $\hat{I}$ indica la imagen normalizada en la intensidad e I_p es el valor de la integral de intensidad. Se puede aproximarse como la suma de todos los valores de intensidad de la imagen, dando un valor integral de la intensidad de [19]:

$$I_p = \int I(x,y,z) \approx \sum I(x,y,z) \tag{C.2}$$

Por lo tanto, I_p puede ser visto como la intensidad media de la imagen [1]. El cálculo de este valor de intensidad integral se puede estimar en un volumen de referencia particular en el cerebro para cada imagen cerebro de 3D . En el caso particular de la PD, el volumen de referencia tiene que ser adecuadamente definido y seleccionado. En esta tesis, se propone fijar la región de referencia al volumen total del cerebro sin la región del estriado, como se mencionó anteriormente.
El método Integral-IN preserva las diferencias absolutas en los valores de captación, produciendo una medida similar para la región no específica, y las diferencias en las estructuras del estriado con conteos más altos de intensidad [1]. Este método es inexacto y más sensible a los valores extremos, por ejemplo, en los sujetos con pérdida severa de los receptores de dopamina, las altas diferencias intra-sujeto en el potencial de unión, o las características atípicas [1].

- La normalización de la intensidad, reduciendo al mínimo la divergencia de Kullback-Leibler (MKL-IN): La idea básica del método presentado en [193] es estimar un campo de corrección multiplicativa con el fin de que coincida con un histograma de la plantilla a una densidad de modelo de referencia. La imagen observada I se puede expresar como:

$$I = F\hat{I} + n \tag{C.3}$$

donde F es un campo de la corrupción multiplicativo de la intensidad, n es el ruido de adquisición adicional y $\hat{I}$ es la imagen correcta deseada. Después de despreciar el efecto de la variable n, por tener poca influencia sobre el problema de la normalización de la intensidad, la solución de la ecuación C.3 para

$\hat{I}$, se obtiene como $\hat{I} \approx F^{-1}I$. El parámetro de ajuste de intensidad F^{-1} tiene que ser elegido de manera que se minimiza la divergencia de Kullback-Leibler (KL) [194] entre los conjuntos de datos de origen y de destino. La aproximación nestocástica de perturbación simultánea (SPSA, del inglés "Simultaneous Perturbation Stochastic Approximation") se utiliza para generar la estimación de gradiente y a continuación para ajustar la estimación actual de la solución de acuerdo con la estimación del gradiente, como se muestra en el Apéndice A.2. Este enfoque tiene las siguientes ventajas [193]: *i*) Se pueden combinar con un modelo histograma suministrado que puede ser generado por cualquier sujeto representativo. Esto permite proceder sin suposiciones acerca de la forma del histograma o la contribución específica de una determinada clase de tejido. *ii*) Dado que puede ser resuelto para un campo de normalización espacialmente variable, no es necesaria la participación de un paso separado para la corrección de la falta de homogeneidad de campo. Sin embargo, teniendo en cuenta la carga computacional, este esquema de normalización es más exigente, ya que se basa en un algoritmo iterativo (SPSA) y necesita la optimización de muchos parámetros, tales como, las secuencias de ganancia, el número máximo de iteraciones, el parámetro de ajuste de la intensidad inicial, etc. Además, se limitan necesariamente a las estimaciones de F^{-1} que sean de baja frecuencia espacial. Esto proporciona una solución que mejora la agrupación de estadísticas de imagen globales, preservando el contraste local que define los límites anatómicos de interés.

- La ecualización del histograma (Hist-eq-IN): mediante técnicas de modelado de histograma, es decir, la ecualización de histograma proporcionan un método sofisticado para modificar el rango dinámico y el contraste de una imagen mediante la alteración individual de cada voxel de tal manera que su histograma de intensidad asume una forma deseada [195]. Un mapeo monotónico, no lineal se emplea por el enfoque de ecualización del histograma que re-asigna los valores de intensidad de voxels en la imagen de entrada de manera que la imagen de salida contiene una distribución uniforme de las intensidades [196]. A través de este ajuste, este método se utiliza en los procesos de comparación de la imagen (debido a que es eficaz en la mejora de los detalles), y en la corrección de los efectos no lineales introducidos por un digitalizador o un sistema de visualización [197]. Los niveles de gris en una imagen pueden ser vistos como variables aleatorias en el intervalo [0, 1]. Uno de los descriptores más fundamentales de una variable aleatoria es su función de densidad de probabilidad (PDF, del inglés "probability density function").
  Supongamos que el histograma normalizado deseado o especificado es $p_d(t)$,, con la imagen deseada se representa como d, que tiene el nivel de gris normalizado $t = 0, 1, 2, ..., L-1$. La imagen dada f con el PDF $p_f(r)$ puede ser igualada

en los histogramas con la transformación:

$$C_1(r) = \int_0^r p_f(w)dw \quad 0 \leqslant r \leqslant 1 \tag{C.4}$$

donde C_1 es la suma acumulada de la imagen f para todas las intensidades r, r es los niveles de gris de las imágenes a ser mejoradas y w es una variable ficticia de la integración [198].
El histograma de ecualización para transformar la imagen deseada puede ser también conducido como:

$$C_2(t) = \int_0^t p_d(w)dw \quad 0 \leqslant t \leqslant 1 \tag{C.5}$$

donde C_2 es el histograma acumulado de la imagen de referencia.
Para imágenes empleamos variables discretas aproximando probabilidades e sumatorias en lugar de probabilidades de funciones de densidad e integrales. La probabilidad de ocurrencia de nivel de gris r_k en una imagen se aproxima por:

$$p_f(r_k) = \frac{n_k}{n} \quad k = 0, 1, 2, ..., L-1 \tag{C.6}$$

donde n es el número total de voxels en la imagen, n_k es el número de voxels que tienen gris nivel de r_k y L es el número total de posibles niveles de gris de la imagen. La versión discreta de la función de transformación dada en la ecuación C.4 es

$$C_1(r_k) = \sum_{j=0}^{k} p_f(r_j) = \sum_{j=0}^{k} \frac{n_j}{n} \quad k = 0, 1, 2, ..., L-1 \tag{C.7}$$

Por lo tanto, una imagen procesada se obtiene mediante la asignación de cada voxel con el nivel r_k de la imagen de entrada en un voxel correspondiente con el nivel $C_1(r_k)$ de imagen de salida a través de la ecuación C.7.
Matemáticamente, cuando se suministra un histograma deseado, la ecualización del histograma consiste en elegir la transformación $\mathbf{T}$ de escala de grises para minimizar

$$\| C_1(\mathbf{T}(t)) - C_2(t) \| \tag{C.8}$$

Esta reducción está sujeta a las restricciones de que $\mathbf{T}$ debe ser monótona y $C_1(\mathbf{T}(a))$ no puede sobrepasar $C_2(a)$ en más de la mitad de la distancia entre el recuento de histograma a un valor de intensidad dado a [106]. Entonces, la transformación $\mathbf{T}$ se utiliza para asignar los niveles de gris de la imagen f (o el mapa de colores) a sus nuevos valores.
Este enfoque de normalización no lineal se lleva a cabo para la normalización de la intensidad de imágenes funcional, tal como, imágenes SPECT y PET como sigue:

  - En primer lugar, una máscara se aplica en las imágenes de origen con el fin de tener en cuenta únicamente los voxels con valores de intensidad superior a un umbral determinado. Este paso se realiza para descartar aquellos voxels de imagen que se encuentran fuera del cerebro.
  - En segundo lugar, se calcula el histograma de la imagen de la plantilla.
  - Por último, la ecualización del histograma se lleva a cabo y los valores de intensidad en las imágenes fuente se ajustan a los valores de intensidad de la plantilla de referencia.

  El enfoque de ecualización del histograma es un enfoque robusto y versátil en muchos trabajos anteriores, como por ejemplo en [190]. Por esta razón, los utilizaremos para la comparación con los enfoques propuestos. Además, vamos a tratar de ponerlo en práctica, en una primera etapa, en toda la imagen y en la segunda etapa en la región no específica. Esto podría evitar su efecto en el cuerpo estriado, ya que es un método de normalización no lineal.

- La normalización de intensidad utilizando los valores máximos [1] (Max-IN): este método de normalización se aplica individualmente para cada *scan* del sujeto en referencia de cada voxel al valor medio del conjunto de la más alta intensidad de voxels en [%]. De este modo, se permitiría la comparación estadística entre los diferentes sujetos [186]. Por otra parte, este enfoque tiene como objetivo ampliar el tamaño de las regiones discriminativas para intercambiando los papeles de áreas específicos/no específicos de la distribución de la actividad funcional entre los sujetos [1]. Este enfoque de normalización puede presentar problemas en algunas imágenes que pueden tener valores de intensidad máxima debidos al ruido [186]. Estos errores de normalización pueden ser reparados cuando la normalización de intensidad se refiere a un voxel conjunto con los valores más altos de intensidad. El número de voxels usualmente considerados para esta normalización de intensidad son alrededor de 0,1% voxels [1]. Teniendo en cuenta los niveles de intensidad más bajos, es decir, menor activación en el caso de los pacientes de PD en comparación con sujetos sanos, este método de normalización es propenso a errores. Por otra parte, en la normalización al régimen máximo, la captación del trazador del cuerpo estriado se adapta para todos los sujetos, incluidos los pacientes y los controles normales. Esto podría perder la relación entre la pérdida de los receptores de dopamina y la disminución de contar números. Por lo tanto, en términos de valores absolutos de captación, la interpretación se pierde [1].

- La normalización de intensidad lineal utilizando la distribución α-*stable* [2] (α-stable-IN): la distribución α-*stable* se puede utilizar para el ajuste de las imágenes funcionales [2, 186]. Si se analiza la distribución de intensidad de las imágenes sin la región estriatal, se obtiene una distribución unimodal, pesado de cola y sesgada, con diferente varianza y valores medios. Estas distribu-

ciones de intensidad pueden producirse por un distribución *α-stable* [2].
La distribución *α-stable* está representado por la siguiente ecuación [186, 199]:

$$f_{\alpha,\beta}(y|\gamma,\mu) = \frac{1}{\pi}\Re\left[\int_0^{\inf} e^{jt(y-\mu)}e^{(-\gamma t)^{\alpha}(1-j\beta\tan(\frac{\pi\alpha}{2}))}dt\right] \tag{C.9}$$

Por lo tanto, la función de densidad de probabilidad de *α-stable*, $f_{\alpha,\beta}(y|\gamma,\mu)$ tiene cuatro parámetros: $\alpha \in (0,2]$ es el exponente característico que establece el nivel de impulsividad, es decir, la "cola" de la distribución, $\beta \in [-1,+1]$ es el parámetro de asimetría, ($\beta = 0$, para las distribuciones simétricas y $\beta = \pm 1$ para la familia estable positivo/negativo, respectivamente), $\gamma > 0$ se llama la escala o el parámetro de dispersión, y μ es el parámetro de localización.

La normalización de la intensidad de uso de la *α-stable* se lleva a cabo mediante la transformación del vector de histograma de los datos de intensidad con una distribución *α-stable* con parámetros $I \sim f_{\alpha,\beta}(y|\gamma,\mu)$ a otro distribución *α-stable* con la distribución $\hat{I} \sim f_{\alpha,\beta}(y|\gamma^*,\mu^*)$ mediante el uso de la siguiente expresión

$$\hat{I} = aI + b \tag{C.10}$$

donde $a = \frac{\gamma^*}{\gamma}$ and $b = \mu^* - \frac{\gamma^*}{\gamma}\mu$. Por lo tanto, el objetivo de este enfoque es transformar todos los valores de intensidad para diferentes imágenes i posiblemente con diferentes parámetros de dispersión γ_i y parámetros de localización μ_i a otra distribución *α-stable* con parámetros $\gamma*$ y $\mu*$ utilizando la expresión en la ecuación C.10 [2].

C.5 Contribuciones principales

Las principales contribuciones científicas de la presente tesis doctoral pueden dividirse en tres categorías diferentes: el desarrollo y la aplicación de métodos estándares para la normalización de la intensidad, el desarrollo y la aplicación de nuevos enfoques de la normalización de la intensidad basados en GMM, MSE y MLR, y la utilización del esquema de normalización de intensidad propuesto en una aplicación clínicamente relevante de evaluación asistida por ordenador para la detección temprana de PD. A continuación, vamos a introducir brevemente las principales contribuciones científicas. Para más detalle, en conveniente referimos a los correspondientes capítulos.

- Desarrollo e implementación de los algoritmos del estado del arte presentados en la sección anterior y descritos en el capítulo 3 para la normalización de intensidad, que se llevaron a cabo en dos modalidades de imágen functional (SPECT y PET).

- Desarrollo y aplicación de un enfoque basado en el filtrado no lineal de imágenes utilizando GMM, que considera no sólo los niveles de intensidad, sino también las coordenadas de los voxels dentro de las funciones gaussianas espaciales así definidas. Los voxels en la región de referencia (región no específica) son de intensidad normalizada por la eliminación de las agrupaciones cuya probabilidad es despreciable. Este proceso se basa en un umbral de probabilidad que mide el peso de cada clúster en la región específica, es decir, el cuerpo del estriado, como se muestra en la figura C.2. Con este procedimiento, le ofrecemos una reconstrucción de la imagen filtrada del modelo de GMM que: *i*) conserva la intensidad en la región específica, y *ii*) normalizar de forma automática la intensidad en la región de referencia de manera que las diferencias de intensidad entre los sujetos se reducen y los grupos irrelevantes que pueden representar diferentes fuentes de ruido se eliminan automáticamente.

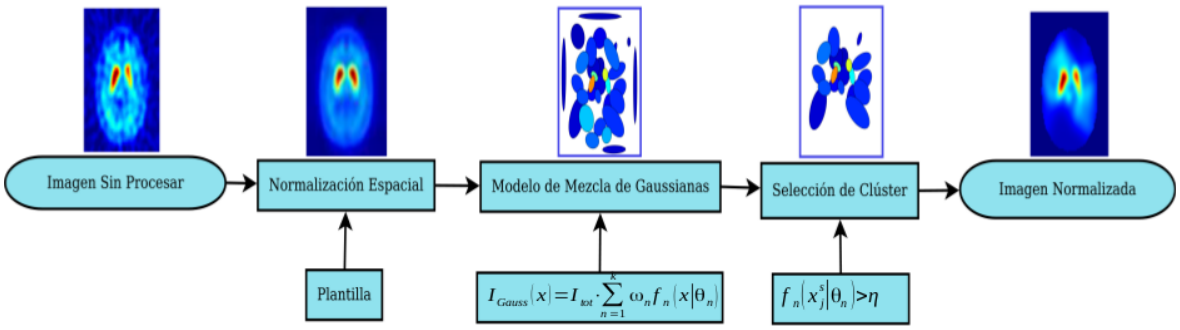

Figure C.2: Diagrama de bloques del procedimiento en las imágenes de SPECT con DaTSCAN.

- Optimización y aplicación de dos metodologías propuestas, que se basan en MSE, como se muestra en la figura C.3. El primer método de optimización del MSE consiste en una transformación lineal en cada voxel de la imagen del cerebro. Esta transformación se obtiene reduciendo al mínimo el MSE entre la intensidad de la imagen norma-lizada y la plantilla en la región no específica así definida. El segundo enfoque se basa en la minimización de la MSE entre las características extraídas basados en un GMM de cada imagen del objeto y de la plantilla en la región no específica. Estas metodologías tienen la ventaja de normalizar automáticamente las imágenes funcionales del cerebro en 3D sin necesidad de utilizar la información anatómica. Además, se pueden aplicar para diferentes modalidades de imagen, tales como SPECT y PET.

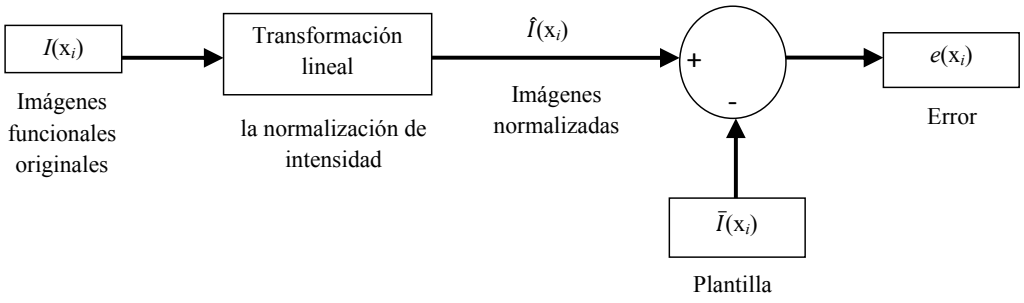

Figure C.3: Esquema general del método lineal de normalización de intensidad para las imágenes funcional utilizando el enfoque MSE.

- Desarrollo e implementación de un nuevo enfoque de la normalización de la intensidad, que se basa en un modelo predictivo utilizando MLR. Diferentes parámetros de normalización en intensidad derivados de este modelo se usan en un procedimiento lineal para normalizar en intensidad las imágenes funcionales cerebrales. Este nuevo enfoque es una extensión del método de normalización que se basa en la minimizacíon del error cuadrático medio presentado anteriormente. Por lo tanto, esta metodología de normalización se puede aplicar a cualquier imagen médica, no sólo a regiones específicas/no específicas en determinadas modalidades funcionales como DaTSCAN.
- Se utilizan medidas cualitativas y cuantitativas, tales como las imágenes del cerebro, el histograma media, las barras de error para el histograma media de los valores de intensidad en la región no específica, las divergencias de Kullback-Leibler y Jeffreys y la distancia euclídea, de variabilidad entre individuos para evaluar las mejoras proporcionadas por los enfoques propuestos en comparación con el estado del arte de los algoritmos.
- Desarrollo de algoritmos de normalización que sean independientes del protocolo clínico o del experto explorador.
- Implementación de algoritmos eficientes en cuanto al cómputo necesario para su aplicación. Mejora del tiempo de cálculo,la estabilidad y la repetibilidad de los resultados usando los diferentes esquemas de normalización de intensidad.
- Integración de los métodos desarrollados en los llamados sistemas CAD (de ayuda al diagnóstico basado en computador) para proporcionar sistemas más

precisos en la detección precoz de PS con modalidades de imágenes tan diferentes como SPECT o PET.

C.6 Trabajos publicados

Parte del trabajo que aquí se presenta ha sido publicado y ya está disponible para la comunidad científica.

Artículos en revistas indexadas:

1. A. Brahim, J. M. Górriz, J. Ramírez, L. Khedher, 'Intensity normalization of DaTSCAN SPECT imaging using a model-based clustering approach'. Journal of Applied Soft Computing, 37 (2015): 234–244, 2015, doi: 10.1016/j.asoc.2015.08.030.

2. A. Brahim, J. Ramírez , J. M. Górriz, L. Khedher and D. Salas-Gonzalez, 'Comparison between Different Intensity Normalization Methods in ^{123}I-Ioflupane Imaging for the Automatic Detection of Parkinsonism'. Journal of Plos One, 10 (6): 1–20, 2015, doi:10.1371/journal.pone.0130274.

Conferencias internacionales:

1. A. Brahim, J. M. Górriz, J. Ramírez, L. Khedher, 'Linear intensity normalization of DaTSCAN images using Mean Square Error and a model-based clustering approach', International Conference on Innovation in Medicine and Healthcare, San Sebastian, Spain, July 2014. vol.207, pp 251-260, ISBN: 978-1-61499-473-2,

2. A. Brahim, J. Ramírez , J. M. Górriz, L. Khedher, 'Linear intensity normalization of DaTSCAN images using Mean Square Error and a model-based clustering approach', 2014 IEEE International Conference on Image Processing (ICIP14), Paris, France, October 2014. vol.207, pp 3617–3621, ISBN: 978-1-4799-5751-4,

3. A. Brahim, J. M. Górriz, J. Ramírez, L. Khedher, 'Intensity Normalization of ^{123}I-ioflupane-SPECT Brain Images Using a Model-Based Multivariate Linear Regression Approach', 6th. INTERNATIONAL WORK-CONFERENCE on the INTERPLAY between NATURAL and ARTIFICIAL COMPUTATION, Elche, Spain, June 2015. vol. 9107, pp 68-77, ISBN: 978-3-319-18913-0.

Por otra parte, frutos de varias colaboraciones se han publicado otros artículos en diferentes revistas indexadas y conferencias internacionales:

1. L. Khedher, J. Ramírez, J. M. Górriz, A. Brahim and F. Segovia, 'Early diagnosis of Alzheimer's disease based on partial least squares, principal component analysis and support vector machine using segmented MRI images'.Journal of Neurocomputing, 151 (1): 139–150, 2014, doi:10.1016/j.neucom.2014.09.072.

2. L. Khedher, J. Ramírez, J. M. Górriz , A. Brahim. , 'Automatic classification of segmented MRI data combining Independent Component Analysis and Support Vector Machines', International Conference on Innovation in Medicine and Healthcare (Inmed14), San Sebastian, Spain, July 2014. vol.207, pp 271–279, ISBN: 978-1-61499-473-2,

3. L. Khedher, J. Ramírez, J. M. Górriz, A. Brahim and I.A. Illán, 'Independent Component Analysis-Based Classification of Alzheimer's Disease from Segmented MRI Data', 6th. INTERNATIONAL WORK-CONFERENCE on the INTERPLAY between NATURAL and ARTIFICIAL COMPUTATION, Elche, Spain, June 2015. vol. 9107, pp 78-87, ISBN: 978-3-319-18913-0.

C.7 Estructura del documento

El contenido de la tesis se organiza de la siguiente manera:

- El capítulo 2 presenta una introducción a la SPECT y la PET, sus radiotrazadores y la aplicación clínica, así como una visión general acerca de los diversos artefactos de imagen que influyen en la calidad de la misma. Además, contiene información de referencia médica sobre las enfermedades neurodegenerativas que son consideradas a lo largo de la tesis: PD, PSP y MSA. Esta introducción familiariza al lector con estas modalidades de imagen, algunas de sus posibilidades y limitaciones en la detección de estos tipos de enfermedades. Esta familiaridad le ayuda a comprender las dificultades encontradas, sobre todo en las cuestiones de normalización de intensidad.

- El capítulo 3 revisa los preparativos de preprocesamiento previos para las modalidades de datos SPECT y PET que han sido tratadas. Además, se presenta el estado del arte sobre la normalización de la intensidad adecuadamente adaptado a la naturaleza de las imágenes de PD.

- El capítulo 4 presenta un nuevo método para la normalización automática de intensidad de las imágenes funcionales del cerebro. La metodología propuesta se basa en GMMs que se utilizan en primer lugar para la estimación de la densidad del perfil de intensidad de cada imagen médica funcional. Nos aproximamos al perfil de intensidad de las imágenes de SPECT por una suma de gaussianas que satisface un criterio de máxima verosimilitud (ML, del inglés

Maximum Likelihood). A continuación, el modelo de mezcla resultante se utiliza para la normalización de intensidad de acuerdo a una estrategia de selección de clúster. Los clústers se seleccionan por medio de un umbral de probabilidad normalizada que mide el peso de cada *kernel* en la zona del área del estriado y la normalización de intensidad se lleva a cabo en realidad sólo por la adición de los grupos relevantes en la reconstrucción de la imagen.

- El capítulo 5 se ocupa de la corrección de las variaciones de intensidad de la señal entre la imagen, mediante la propuesta de tres nuevos enfoques de normalización de la intensidad. Estas metodologías se basan en la extracción de parámetros intrínsecos de imágenes DaTSCAN SPECT y PET DMFP, lo que resulta en tres procedimientos automáticos para la normalización de intensidad: la optimización de MSE entre la imagen normalizada de intensidad y la plantilla en la región no específica, la optimización de MSE entre las características extraídas basadas en GMM a partir de cada imagen del objeto y de la plantilla en la región de referencia, y finalmente un método de normalización sobre la base de modelos de predicción utilizando MLR.

- El capítulo 6 muestra un estudio de evaluación de los enfoques de la normalización de la intensidad propuestos cuando se comparan con los métodos convencionales adecuadamente adaptados a la naturaleza de la PD. De este modo, se llevan a cabo medidas cualitativas y cuantitativas de variabilidad interindividual. Además, se realiza una comparación utilizando un sistema de clasificación para la detección de síndromes de Parkinson, que puede mejorar el desarrollo de un sistema CAD para PD.

- La tesis se concluye en el capítulo 7 dónde también se discuten algunos posibles caminos para la investigación futura.

Bibliography

[1] I. A. Illán, J. M. Górriz, J. Ramírez, F. Segovia, J. M. Jimenez-Hoyuela, and S. J. Ortega Lozano. Automatic assistance to parkinson's disease diagnosis in DaTSCAN SPECT imaging. *Medical Physics*, 39(10):5971–5980, 2012.

[2] D. Salas-Gonzalez, J. M. Górriz, J. Ramírez, I. A. Illán, and E. W. Lang. Linear intensity normalization of FP-CIT SPECT brain images using the α-stable distribution. *NeuroImage*, 65:449–455, 2013.

[3] M.N. Wernick and J.N. Aarsvold. *Emission Tomography: The Fundamentals of PET and SPECT*. Elsevier Academic Press, 2004.

[4] Available at http://hyperphysics.phy-astr.gsu.edu/hbase/nucene/nucmed.html.

[5] J. Hodler, G. K. von Schulthess, and Zollikofer. C. L. *Diseases of the Brain, Head & Neck, Spine*. Springer Milan Berlin Heidelberg New York, 2008.

[6] L. G. Harsing Jr. *Handbook of Neurochemistry and Molecular Neurobiology*, chapter Dopamine and the Dopaminergic Systems of the Brain, pages 149–170. Springer US, 2008.

[7] US National Academy of Engineering. Available at www.nae.edu.

[8] O. Demirkaya, M. H. Asyali, and P. K. Sahoo. *Image Processing with MATLAB: Applications in Medicine and Biology*. 2008.

[9] Bartholmai B. Erickson, B. J. Computer-aided detection and diagnosis at the start of the third millennium. *Journal of digital imaging*, 15(2):59–68, 2002.

[10] R. M. Summers. Road maps for advancement of radiologic computer-aided detection in the 21 st century. *Radiology*, 229:11–13, 2003.

[11] K. Doi. Diagnostic imaging over the last 50 years: Research and development in medical imaging science and technology. *Physics in Medicine and Biology*, 51(13):R5–R27, 2006.

[12] V. N. Vapnik. *Statistical Learning Theory*. John Wiley and Sons, Inc., New York, 1998.

[13] E. Corchado, A. Abraham, and A. Carvalho. Hybrid intelligent algorithms and applications. *Information Sciences*, 180 (14):2633–2634, 2010.

[14] W. Pedrycz and R. Aliev. Logic-oriented neural networks for fuzzy neurocomputing. *Neurocomputing*, 73 (1–3):10–23, 2009.

[15] G. Fung and J. Stoeckel. SVM feature selection for classification of SPECT images of Alzheimer's disease using spatial information. *Knowledge and Information Systems*, 11 (2):243–258, 2007.

[16] I. A. Illán, J. M. Górriz, J. Ramírez, D. Salas-Gonzalez, M. M. López, F. Segovia, R. Chaves, M. Gómez-Rio, and C. G. Puntonet. ^{18} F-FDG PET imaging analysis for computer aided Alzheimer's diagnosis. *Information Sciences*, 181(4):903–916, 2011.

[17] F. J. Martínez-Murcia, J.M. Górriz, J. Ramírez, C. Puntonet, and D. Salas-González. Computer aided diagnosis tool for Alzheimer's disease based on Mann–Whitney–Wilcoxon U–test. *Expert Systems with Applications*, 39 (10):9676–9685, 2012.

[18] F. Segovia, J. M. Górriz, J. Ramírez, I. Alvarez, J. M. Jimenez-Hoyuela, and S. J. Ortega. Improved parkinsonism diagnosis using a partial least squares based approach. *Medical Physics*, 39 (7):4395–4403, 2012.

[19] F.J. Martínez-Murcia, J.M. Górriz, J. Ramírez, I.A. Illán, and A. Ortiz. Automatic detection of parkinsonism using significance measures and component analysis in datscan imaging. *Neurocomputing*, 126(0):58–70, 2014.

[20] F.J. Martínez-Murcia, J.M. Górriz, J. Ramírez, M. Moreno-Caballero, and M. Gómez-Río. Parametrization of textural patterns in ^{123}I-ioflupane imaging for the automatic detection of Parkinsonism. *Medical physics*, 41(1):012502, 2014.

[21] Y. M. Y. Abdallah, A. Hayder, and E. Wagiallahm. Automatic Enhancement of Mammography Images using Contrast Algorithm . *International Journal of Science and Research*, 3 (9):1885–1889, 2014.

[22] H. N. Moulick and M. Ghosh. IMAGE COMPRESSION USING K-MEANS CLUSTERING AND NUCLEAR MEDICINE IMAGE PROCESSING. *International Journal of Innovative Research in Computer and Communication Engineering*, 1(4):869–877, 2013.

[23] J. S. Smith and S. Desgreniers. Exploiting area detectors to reduce measured Compton scattering via energy selection. *Nuclear Instruments and Methods in Physics Research Section A: Accelerators, Spectrometers, Detectors and Associated Equipment*, 668:9–13, 2012.

[24] H. Zaidi. *Molecular Imaging of Small Animals: Instrumentation and Applications*. 2014.

[25] D. L. Bailey, D. W. Townsend, P. E. Valk, and M. N. Maisey. *Positron Emission Tomography: Basic Sciences*. 2006.

[26] P. Lecoq, E. Auffray, S. Brunner, H. Hillemanns, P. Jarron, A. Knapitsch, T. Meyer, and F. Powolny. Factors Influencing Time Resolution of Scintillators and Ways to Improve Them. *IEEE TRANSACTIONS ON NUCLEAR SCIENCE*, 57(5):2411–2416, 2010.

[27] K. M. Hanson. *Radiology of the Skull and Brain, Vol. V: Technical Aspects of Computed Tomography*. C. V. Mosby, 1981.

[28] H. Hsu, N. M. Alpert, B. T. Christian, A. A. Bonab, E. Morris, and A. J. Fischman. Noise properties of a graphical assay of receptor binding. *Journal of Nuclear Medicine*, 38:204P, 1997.

[29] S. R. Cherry, J. A. Sorenson, and M. E. Phelps. *Physics in Nuclear Medicine*. 2012.

[30] P. Razifar, M. Sandström, H. Schnieder, B. Langström, E. Maripuu, E. Bengtsson, and M. Bergström. Noise correlation in PET, CT, SPECT and PET/CT data evaluated using autocorrelation function: a phantom study on data, reconstructed using FBP and OSEM. *BMC Medical Imaging*, 5(5):1–23, 2005.

[31] P. T. Krishna Kumar, Vir. V. Phoha, S. S. Iyengar, and Puneeth Iyengar. Reduction of noise due to systematic uncertainties in ^{113m} in SPECT imaging using information theory. *Computers in Biology and Medicine*, 39(5):482–488, 2009.

[32] U. Vovk, F. Pernus, and B. Likar. A Review of Methods for Correction of Intensity Inhomogeneity in MRI. *IEEE TRANSACTIONS ON MEDICAL IMAGING*, 26 (3):405–421, 2007.

[33] J. Jankovic, A.H. Rajput, M.P. McDermott, D.P. Perl, and for the Parkinson Study Group. The evolution of diagnosis in early parkinson disease. *Archives of Neurology*, 57(3):369–372, 2000.

[34] K. D. Seifert and J. I. Wiener. The impact of DaTscan on the diagnosis and management of movement disorders: A retrospective study. *American journal of neurodegenerative disease*, 2(1):29–34, 2013.

[35] K. J. Friston, C. D. Frith, P. F. Liddle, R. J. Dolan, A. A. Lammertsma, and R. S. J. Frackowiak. The Relationship Between Global and Local Changes in PET Scans. *Journal of Cerebral Blood Flow & Metabolism*, 10:458–466, 1990.

[36] R. A.J.O. Dierckx, A Otte, E. F. J. de Vries, A. van Waarde, and K. L. Leenders. *PET and SPECT in Neurology*. Springer, 2014.

[37] J Illes and E. Racine. Imaging or Imagining? A Neuroethics Challenge Informed by Genetics. *Am J Bioeth*, 5(2):5–18, 2005.

[38] R. A.J.O. Dierckx, A Otte, E. F. J. de Vries, A. van Waarde, and P.G. M. Luiten. *PET and SPECT of Neurobiological Systems*. Springer, 2014.

[39] J. Ramírez, J.M. Górriz, D. Salas-González, A. Romero, M. López, I. Álvarez, and Gómez-Río. Computer-aided diagnosis of Alzheimer's type dementia combining support vector machines and discriminant set of features. *Information Sciences*, 237 (2013):59–72, 2009.

[40] J. I. Agbinya, E. Biermann, and Y. Hamam. *Biomedical and Environmental Sensing*. River Publishers, 2009.

[41] S. S. Kety and C. F. Schmidt. The Nitrous Oxide Method for the Quantitative Determination of Cerebral Blood Flow in Man: Theory, Procedure and Normal Values. *Journal of Clinical Investigation*, 27(4):476–483, 1948.

[42] H. I. Glass and A. M. Harper. Measurement of Regional Blood Flow in Cerebral Cortex of Man through Intact Skull. *British Medical Journal*, 1:593, 1963.

[43] D. H. Ingvar and N. A Lassen. Quantitative Determination of Regional Cerebral Blood-Flow. *Lancet*, 2:806–807, 1961.

[44] D. E. Kuhl and Edwards R. Q. Image Separation Radioisotope Scanning. *Radiology*, 80:653–661, 1963.

[45] M. M. Khalil, J. L. Tremoleda, T. B. Bayomy, and W. Gsell. Molecular SPECT Imaging: An Overview. *International Journal of Molecular Imaging*, 2011:1–15, 2011.

[46] C. Asbury. Brain Imaging Technologies and Their Applications in Neuroscience. Technical report, The Dana Foundation, 2011.

[47] S. Vallabhajosula. *Molecular Imaging: Radiopharmaceuticals for PET and SPECT*. Springer-Verlag Berlin Heidelberg, 2009.

[48] S. H. A. ALehyani. Application of single photon emission computed tomography (SPECT) parameters for bone scintigraphy. *Journal of King Saud University - Science*, 21 (1):109–117, 2009.

[49] M. King and T. Farncombe. An overview of attenuation and scatter correction of planar and SPECT data for dosimetry studies. *Cancer Biother Radiopharm*, 18(2):181–190, 2003.

[50] J. A. Sorenso and M. E. Phelps. *Physics in Nuclear Medicine*, chapter The Anger Camera: Performance Characteristics, pages 331–345. Harcourt Brace Jovanovich, Inc., 1987.

[51] M. Analoui, J. D. Bronzino, and D. R. Peterson. *Medical Imaging: Principles and Practices*. CRC Press, 2012.

[52] J. D. Bronzino and D. R. Peterson. *Biomedical Signals, Imaging, and Informatics*. CRC Press, 2014.

[53] K. Van Laere, M. Koole, I. Lemahieu, and R. Dierckx. Image filtering in single-photon emission computed tomography: principles and applications. *Computerized Medical Imaging and Graphics*, 25 (2001):127–133, 2000.

[54] M. Lyra and A. Ploussi. Filtering in SPECT Image Reconstruction. *International Journal of Biomedical Imaging*, 2011:14, 2011.

[55] K. Kacperski. Attenuation correction in SPECT without attenuation map. In *IEEE Nuclear Science Symposium conference record Nuclear Science Symposium*, pages 1–8, 1997.

[56] A. Brahme. *Comprehensive Biomedical Physics*. Newnes, 2014.

[57] Atam P. Dhawan. *Medical Image Analysis, 2nd Edition*. 2011.

[58] F. Kharfi. *Imaging and Radioanalytical Techniques in Interdisciplinary Research - Fundamentals and Cutting Edge Applications*, chapter Principles and Applications of Nuclear Medical Imaging: A Survey on Recent Developments, pages 1–29. InTech, 2013.

[59] T. VIK. *Non-Gaussian Statistical Appearance Models. Application to the Creation of a Probabilistic Atlas of Brain Perfusion in Medical Imaging*. PhD thesis, University of Louis Pasteur - Strasbourg I, 2004.

[60] J. Nuyts, B. De Man, J. A. Fessler, W. Zbijewski, and F. J. Beekman. Modelling the physics in iterative reconstruction for transmission computed tomography. *Phys Med Bio*, 58 (12):R63–R96, 2013.

[61] S. Clare. *Functional Magnetic Resonance Imaging: Methods and Applications* . PhD thesis, University of Nottingham, 1997.

[62] M. M. Ter-Pogossian, M. E. Phelps, E. J. Hoffman, and N. A Mullani. A positron-emission transaxial tomograph for nuclear imaging (PETT). *Radiology*, 114 (1):89–98, 1975.

[63] M. E. Phelps, E. J. Hoffman, N. A. Mullani, and M. M Ter-Pogossian. Application of annihilation coincidence detection to transaxial reconstruction tomography. *Journal of Nuclear Medicine*, 16 (3):210–224, 1975.

[64] G. Koukourakis, G. Maravelis, S. Koukouraki, P. Padelakos, and V. Kouloulias. Overview of positron emission tomography chemistry: clinical and technical considerations and combination with computed tomography. *Journal of Balkan Union of Oncology*, 14 (4):575–580, 2009.

[65] A. P. Dhawan, H. K. Huang, and Dae-Shik. Kim. *Principles and Advanced Methods in Medical Imaging and Image Analysis*. World Scientific, 2009.

[66] J. L. Semmlow. *Biosignal and Biomedical Image Processing*. Marcel Dekker, Inc., 2004.

[67] L. Mehta and S. Thomas. The role of PET in dementia diagnosis and treatment. *Applied Radiology*, 41 (5):8–15, 2012.

[68] M. A. Deli, S. Veszelka, B. Csiszár, A. Tóth, A. Kittel, M. Csete, A. Sipos, A. Szalai, L. Fülöp, B. Penke, C. S. Abrahám, and M. Niwa. Protection of the blood-brain barrier by pentosan against amyloid-β-induced toxicity. *Journal of Alzheimer's Disease*, 22 (3):777–794, 2010.

[69] L. L. Weyandt. *The Physiological Bases of Cognitive and Behavioral Disorders*. Routledge, 2006.

[70] J.-F. Démonet, C. Price, R. Wise, and R. S. J. Frackowiak. A PET study of cognitive strategies in normal subjects during language tasksInfluence of phonetic ambiguity and sequence processing on phoneme monitoring. *Brain*, pages 671–682, 1994.

[71] C. Loane and M. Politis. Positron emission tomography neuroimaging in Parkinson's disease. *American Journal of Translational Research*, 3 (4):323–341, 2011.

[72] T. Eckert, A. Barnes, V. Dhawan, S. Frucht, M.F. Gordon, A.S. Feigin, and D Eidelberg. FDG PET in the differential diagnosis of parkinsonian disorders. *Neuroimage*, 26:912–921, 2005.

[73] K. L. Poston and D. Eidelberg. FDG PET in the Evaluation of Parkinson's Disease. *PET Clin*, 5 (1):55–64, 2010.

[74] M. Niethammer, A. Feigin, and D. Eidelberg. Functional Neuroimaging in Parkinson's Disease. *Cold Spring Harbor Perspectives in Medicine*, 2 (5):a009274, 2012.

[75] A. Rahmim and H. Zaidi. PET versus SPECT: strengths, limitations and challenges. *Nuclear Medicine Communications*, 29(3):193–207, 2008.

[76] D. R. Owen, P. Piccini, and P. M. Matthews. Towards molecular imaging of multiple sclerosis. *Journal of Multiple Sclerosis*, 17(3):262–272, 2011.

[77] R. Tadeusiewicz. *Modern Computational Intelligence Methods for the Interpretation of Medical Images*. Springer, 2008.

[78] G. B. Saha. *Basics of PET Imaging*. Springer New York, 2005.

[79] A. K. Shukla and Â¡. Kumar, U. Positron emission tomography: An overview. *J Med Phys*, 31 (1):13–21, 2006.

[80] W. W. Moses. Fundamental Limits of Spatial Resolution in PET. *Nucl Instrum Methods Phys Res A*, 648:S236–S240, 2011.

[81] S. E. Derenzo and T. F. Budinger. Resolution limits for positron imaging devices. *Journal of Nuclear Medicine*, 18:491–492, 1977.

[82] S.E. Derenzo. Precision measurement of annihilation point spread distributions for medically important positron emitters. In *Proceedings of the 5th International Conference on Positron Annihilation*, pages 819–824, 1979.

[83] International Atomic Energy Agency. *Quality Assurance for PET and PET/CT Systems*. 2009.

[84] E. J. Hoffman and M. E. Phelps. An analysis of some of the physical aspects of positron axial tomography. *Computers in Biology and Medicine*, 6:345–360, 1976.

[85] C. S. Levin and Hoffman. Calculation of positron range and its effect on the fundamental limit of positron emission tomography system spatial resolution. *Phys. Med. Biol*, 44 (1999):781–799, 1998.

[86] S. Hoffman, E. J. nd Huang, D. Plummer, and M. E. Phelps. Quantitation in positron emission computed tomography: 6 effect of nonuniform resolution. *Journal of Computer Assisted Tomography*, 6(5):987–999, 1982.

[87] F. Segovia. *Análisis de imágenes funcionales cerebrales mediante modelos de mezcla de gaussianas y mínimos cuadrados parciales para el diagnóstico de alteraciones neurológicas*. PhD thesis, Universidad de Granada, 2010.

[88] Christian la Fougere, Gabriele Pöpperl, Johannes Levin, Björn Wängler, Guido Böning, Christopher Uebleis, Paul Cumming, Peter Bartenstein, Kai Bötzel, and Klaus Tatsch. The Value of the Dopamine $D_{2/3}$ Receptor Ligand

^{18}F-desmethoxyfallypride for the Differentiation of Idiopathic and Nonidiopathic Parkinsonian Syndromes. *Journal of nuclear medicine*, 51(4):581–587, 2010.

[89] K. Lange and R. Carson. EM reconstruction for emission and transmission tomography. *Journal of Computer Assisted Tomography*, 8:306–312, 1984.

[90] Y. Vardi, L. A. Shepp, and L. Kaufman. A statistical model for positron emission tomography. *Journal of the American Statistical Association*, 80 (389):8–20, 1985.

[91] E. S. Chornoboy, C. J. Chen, M. I. Miller, T. R. Miller, and D. L. Snyder. An Evaluation of Maximum Likelihood Reconstruction for SPECT. *IEEE Transactions on Medical Imaging*, 9 (1):99–110, 1990.

[92] S. C. Liew, B. H. Hasegawa, J. K. Brown, and T. F. Lang. Noise propagation in SPECT images reconstructed using an iterative maximum-likelihood algorithm. *Physics in medicine and biology*, 38:1713–1726, 1993.

[93] H. M. Hudson and R. S. Larkin. Accelerated Image Reconstruction Using Ordered Subsets of Projection Data. *IEEE Transactions on Medical Imaging*, 13 (4):601–609, 1994.

[94] P. P. Bruyant. Analytic and Iterative Reconstruction Algorithms in SPECT. *The Journal of Nuclear Medicine*, 43 (10):1343–1358, 2002.

[95] R. Chaves, D. Salas-Gonzalez, J. Ramírez, J. M. Górriz, M. López, I. Álvarez, and F. Segovia. *Recent Advances in Biomedical Signal Processing*, chapter Functional Brain Imaging Preprocessing for Computer Aided Diagnosis Systems. Bentham Science Publishers, 2011.

[96] R. M. Chaves. *Un nuevo modelo de la interconectividad funcional cerebral mediante reglas de asociacíon aplicado a la deteccíon de alteraciones neurológicas*. PhD thesis, Universitad de Granada, 2013.

[97] Z. H. Cho, J. P. Jones, and M. Singh. *Foundations of Medical Imaging*. John Wiley & Sons, 1993.

[98] K. Van Laere, M. Koole, I. Lemahieu, and R. Dierckx. Image filtering in single-photon emission computed tomography: principles and applications. *Computerized Medical Imaging and Graphics*, 25(2):127–133, 2001.

[99] M. A. King, S. J. Glick, P. H. Pretorius, R. G. Wells, H. C. Gifford, M. V. Narayanan, and T. Farncombe. *Emission Tomography: The Fundamentals of PET and SPECT*, chapter Attenuation, Scatter, and Spatial Resolution Compensation in SPECT, pages 473–498. 2004.

[100] E. C. Frey, J. L. Humm, and M. Ljungberg. Accuracy and Precision of Radioactivity Quantification in Nuclear Medicine Images. *Semin Nucl Med*, 42 (3):208–218, 2012.

[101] R. E. Henkin, D. Bova, G. L. Dillehay, S. M. Karesh, J. R. Halama, and R. H. Wagner. *Nuclear Medicine 2nd Ed*. Mosby, 2006.

[102] M. L. Pérez. *Nuevos modelos estadísticos para detección de patrones de hipo/perfusión-metabolismo en imágenes de tomografía funcional cerebral*. PhD thesis, University of Granada, 2010.

[103] A. C. Kak and M. Slaney. *Principles of Computerized Tomographic Imaging*. New York: IEEE Press, 1988.

[104] G. L. Zeng. Comparison of a Noise-Weighted Filtered Backprojection Algorithm with the Standard MLEM Algorithm for Poisson Noise. *J Nucl Med Technol.*, 41 (4):283–288, 2013.

[105] Saha. *Basics of PET Imaging: Physics, Chemistry, and Regulations*. Springer Science & Business Media, 2005.

[106] D. Salas-Gonzalez, J. M. Górriz, J. Ramírez, P. Padilla, and I. A. Illán. Improving the Convergence Rate in Affine Registration of PET and SPECT Brain Images Using Histogram Equalization. *Computational and Mathematical Methods in Medicine*, 2013:1–8, 2013.

[107] S. J. O. Lozano, M. D. M. Del Valle Torres, J. M. Jiménez-Hoyuela García, A. L. G Cardo, and V. C. Arillo. Diagnostic accuracy of FP-CIT SPECT in patients with Parkinsonism. *Revista Española de Medicina Nuclear (English Edition)*, 26:277–285, 2007.

[108] V. C. De Cock, M. Vidailhet, and I. Arnulf. Sleep disturbances in patients with parkinsonism. *Nature Clinical Practice Neurology*, 4:254–266, 2008.

[109] N. Granado, S. Ares-Santos, and R. Moratalla. Methamphetamine and Parkinson's Disease. *Parkinson's Disease*, 2013:10, 2013.

[110] L. M. de Lau and M. M. Breteler. Epidemiology of Parkinson's disease. *The Lancet Neurology*, 5(6):525–535, 2006.

[111] A. Samii, J. G. Nutt, and B. R. Ransom. Parkinson's disease. *The Lancet*, 363(9423):1783–1793, 2004.

[112] Available at http://www.pdf.org/.

[113] A. Brahim, J.M. Górriz, J. Ramírez, and L. Khedher. Intensity normalization of ^{123}i-ioflupane-spect brain images using a model-based multivariate linear regression approach. In José Manuel Ferrández Vicente, José Ramón Álvarez-Sánchez, Félix de la Paz López, Fco. Javier Toledo-Moreo, and Hojjat Adeli, editors, *Artificial Computation in Biology and Medicine*, volume 9107 of *Lecture Notes in Computer Science*, pages 68–77. Springer International Publishing, 2015.

[114] A. Abraham, A.K. Muda, and Y.H. Choo. *Pattern Analysis, Intelligent Security and the Internet of Things*. Advances in Intelligent Systems and Computing. Springer International Publishing, 2015.

[115] F.A. Khan. *Biotechnology in Medical Sciences*. CRC Press, 2014.

[116] D. W. Dickson. Parkinson's disease and parkinsonism: neuropathology. *Cold Spring Harbor Perspectives in Medicine*, 2(8):a009258, 2012.

[117] J. Booij, G. Tissingh, G. J. Boer, J. D. Speelman, J. C. Stoof, A. G. M. Janssen, E. C. Wolters, and E. A. Van Royen. [^{123}I]FP-CIT SPECT shows a pronounced decline of striatal dopamine transporter labelling in early and advanced Parkinson's disease. *Journal of Neurology Neurosurgery and Psychiatry*, 62:133–140, 1997.

[118] H. Hou, S. Jia, S. Hu, R. Fan, W. Sun, T. Sun, and H. Zhang. Reduced Striatal Dopamine Transporters in People with Internet Addiction Disorder. *Journal of Biomedicine and Biotechnology*, 2012:1–5, 2012.

[119] N. Pavese and D. J. Brooks. Imaging neurodegeneration in Parkinson's disease. *Biochimica et Biophysica Acta (BBA) - Molecular Basis of Disease*, 1792(7):722–729, 2009.

[120] L. Shen, M. Liao, and Y. Tseng. Recent Advances in Imaging of Dopaminergic Neurons for Evaluation of Neuropsychiatric Disorders. *Journal of Biomedicine and Biotechnology*, 2012:1–14, 2012.

[121] B. Thomas and M.F. Beal. Parkinson's disease. *Human Molecular Genetics*, 16(2):R183–R194, 2007.

[122] C. G. Goetz. The History of Parkinson's Disease: Early Clinical Descriptions and Neurological Therapies. *Cold Spring Harbor Perspectives in Medicine*, 1(1):a008862, 2011.

[123] J. Jankovic. Parkinson's disease: clinical features and diagnosis. *J Neurol Neurosurg Psychiatry*, 79(4):368–376, 2007.

[124] B. Barton, S. E. Zauber, and C. G. Goetz. Movement disorders caused by medical disease. *Semin Neurol*, 29(2):97–110, 2009.

[125] M. A Thenganatt and E. D. Louis. Distinguishing essential tremor from Parkinson's disease: bedside tests and laboratory evaluations. *Expert Rev Neurother*, 12(6):687–696, 2012.

[126] N. C. Palavra, S. L. Naismith, and S. J. G. Lewis. Mild Cognitive Impairment in Parkinson's Disease: A Review of Current Concepts. *Neurology Research International*, 2013:1–8, 2013.

[127] L. Wang, Q. Zhang, H. Li, and Zhang H. SPECT molecular imaging in Parkinson's disease. *Journal of Biomedicine & Biotechnology*, 2012:412486, 2012.

[128] W. Poewe and G. Wenning. The differential diagnosis of Parkinson's disease. *European Journal of Neuroscience*, 9:23–30, 2002.

[129] A. J. Hughes, S. E. Daniel, Y. Ben-Shlomo, and A. J. Lees. The accuracy of diagnosis of parkinsonian syndromes in a specialist movement disorder service. *Brain*, 125 (4):861–870, 2002.

[130] S. Gilman, G. K. Wenning, P. A. Low, D. J. Brooks, C. J. Mathias, J. Q. Trojanowski, N. W. Wood, C. Colosimo, A. D′urr, C. J Fowler, H. Kaufmann, T. Klockgether, A. Lees, W. Poewe, N. Quinn, T. Revesz, D. Robertson, P. Sandroni, K. Seppi, and M. Vidailhet. Second consensus statement on the diagnosis of multiple system atrophy. *Neurology*, 71(9):670–676, 2008.

[131] P. L. Lantos. The definition of multiple system atrophy: a review of recent developments. *Journal of Neuropathology & Experimental Neurology*, 57(12):1099–1111., 1998.

[132] D. Kuzdas-Wood, N. Stefanova, K. A. Jellinger, K. Seppi, M. G. Schlossmacher, W. Poewe, and G. K. Wenning. Towards translational therapies for multiple system atrophy. *Progress in Neurobiology*, 118 (100):19–35, 2014.

[133] L. Ciolli, F. Krismer, F. Nicoletti, and G. K. Wenning. An update on the cerebellar subtype of multiple system atrophy. *Cerebellum & Ataxias*, 1(14):1–14, 2014.

[134] S. Cohen L. Selzer, M. Clarke, G. Kwakkel, and R. Miller. *Textbook of Neural Repair and Rehabilitation*. 2014.

[135] C. Colosimo, A. Albanese, A. J. Hughes, V. M de Bruin, and A. J. Lees. Some specific features differentiate multiple system atrophy (striatonigral degeneration) for Parkinson 's disease. *Arch Neurol*, 52:294–298, 1995.

[136] E. Tolosa, G. Wenning, and W. Poewe. The diagnosis of Parkinson's disease. *The Lancet Neurology*, 5 (1):75–86, 2006.

[137] G. K. von Schulthess. *Molecular Anatomic Imaging: PET-CT and SPECT-CT Integrated Modality Imaging*. Lippincott Williams & Wilkins, 2007.

[138] V. Kramer, P. Chana-Cuevas, C. Juri, R. Pruzzo, A. Amaral, I. Coudeu, F. Rösch, and H. Amaral. 18F-Desmethoxyfallypride PET for differential diagnosis of Parkinson's disease and atypical forms of parkinsonism. *Journal of Nuclear Medicine*, 55:1839, 2014.

[139] S. J. Mo, J. Linder, L. Forsgren, H. Holmberg, A. Larsson, and K. Riklund. Pre- and Postsynaptic Dopamine SPECT in Idiopathic Parkinsonian Diseases: A Follow-Up Study. *BioMed Research International*, 2013:1–14, 2013.

[140] I. Litvan. *Current Clinical Neurology: Atypical Parkinsonian Disorders*, chapter Progressive Supranuclear Palsy, pages 287–308. Humana Press Inc., Totowa, NJ, 2007.

[141] J. J. Hauw, S. E. Daniel, D. Dickson, D. S. Horoupian, K. Jellinger, P. L. Lantos, A. McKee, M. Tabaton, and I. Litvan. Preliminary NINDS neuropathologic criteria for Steele-Richardson-Olszewski syndrome (progressive supranuclear palsy). *Neurology*, 44(11):2015–2019, 1994.

[142] U. Nath, Y. Ben-Shlomo, R. G. Thomson, H. R. Morris, N. W. Wood, A. J. Lees, and D. J. Burn. The prevalence of progressive supranuclear palsy (Steele-Richardson-Olszewski syndrome) in the UK. *Brain*, 124:438–449, 2001.

[143] S. E Daniel, V. M de Bruin, and A. J. Lees. The clinical and pathological spectrum of Steel-Richardson-Olszewski syndrome (progressive supranuclear palsy): a reappraisal. *Brain*, 118:759–770, 1995.

[144] W. J. Weiner, C. G. Goetz, R. K. Shin, and S. L. Lewis. *Neurology for the Non-Neurologist*. Lippincott Williams & Wilkins, 2012.

[145] T. C. Booth, M. Nathan, A. D. Waldman, A. M. Quigley, A. H. Schapira, and J. Buscombe. The Role of Functional Dopamine-Transporter SPECT Imaging in Parkinsonian Syndromes, Part 2. pages 236–244, 2015.

[146] A. Gerhard and D. J. Brooks. *Current Clinical Neurology: Atypical Parkinsonian Disorders*, chapter PET and SPECT Imaging in Atypical Parkinsonian Disorders, pages 459–471. Humana Press Inc., Totowa, NJ, 2007.

[147] A. Winogrodzka, P. Bergmans, J. Booij, E.A van Royen, J.C Stoof, and E.C. Wolters. [^{123}I]Beta-CIT SPECT is a useful method for monitoring dopaminergic degeneration in early stage Parkinson's disease. *Neurology, Neurosurgery & Psychiatry*, 74 (3):294–298, 2003.

[148] I. G. Zubal, M. Early, O. Yuan, D. Jennings, K. Marek, and J.P. Seibyl. Optimized, Automated Striatal Uptake Analysis Applied to SPECT Brain Scans of Parkinson's Disease Patients. *Journal of Nuclear Medicine*, 48 (6):857–864, 2007.

[149] R. A. Hauser and D. G. Grosset. [^{123}I]FP-CIT (DaTscan) SPECT Brain Imaging in Patients with Suspected Parkinsonian Syndromes. *Neuroimaging*, 22 (3):225–230, 2012.

[150] W Reiche, M Grundmann, and G Huber. Dopamine (D2) receptor SPECT with 123I-iodobenzamide (IBZM) in diagnosis of Parkinson syndrome. *Der Radiologe*, 35:838–843, 1995.

[151] SY Bao, JC Wu, WF Luo, P Fang, ZL Liu, and J Tang. Imaging of dopamine transporters with technetium-99m TRODAT-1 and single photon emission computed tomography. *Journal of neuroimaging : official journal of the American Society of Neuroimaging*, 10:200–203, 2000.

[152] General Electric Healthcare. A Technologist's Guide to DaTSCAN Imaging. Technical report, Available at http://www.datscan.cz/stranky/dokumenty-ke-stazeni/firemni-materialy-ge-healthcare.html, 2007.

[153] K. Marek, R. Innis, C. van Dyck, B. Fussell, M. Early, S. Eberly, D. Oakes, and J. Seibyl. [^{123}I]β-CIT SPECT imaging assessment of the rate of Parkinson's disease progression. *Neurology*, 57(11):2089–2094, 2001.

[154] J. Booij, J.B.A. Habraken, P. Bergmans, G. Tissingh, A. Winogrodzka, E.C. Wolters, A.G.M. Janssen, J.C. Stoof, and E.A. Van Royen. Imaging of dopamine transporters with Iodine-123-FP-CIT SPECT in healthy controls and patients with parkinson's disease. *Journal of Nuclear Medicine*, 39(11):1879–1884, 1998.

[155] A. S. Castrejón, A. M. G. Vicente, M. C. Romera, J. V. Cano, S. R. Marina, V. M. P. GarcÃa, S. R. SolÃs, and M. P. T. Rubio. 123-I Ioflupane (DatscanÂ®) presynaptic nigrostriatal imaging in patients with movement disorders. *Brazilian Archives of Biology and Technology*, 48:115–126, 2005.

[156] H. T. S. Benamer, J Patterson, and D. G. Grosset. Accurate Differentiation of Parkinsonism and Essential Tremor Using Visual Assessment of [^{123}I]-FP-CIT SPECT Imaging: The [^{123}I]-FP-CIT Study Group. *Movement Disorders*, 15 (3):503–510, 2000.

[157] A.C. Felicio, M.C. Shih, C. Godeiro-Junior, L.A. Andrade, R.A. Bressan, and H.B. Ferraz. Molecular imaging studies in Parkinson disease: reducing diagnostic uncertainty. *Neurologist.*, 15(1):6–16, 2009.

[158] N. Bajaj, R. A. Hauser, and I. D Grachev. Clinical utility of dopamine transporter single photon emission CT (DaT-SPECT) with (123I) ioflupane in diagnosis of parkinsonian syndromes. *Neurol Neurosurg Psychiatry*, 84(11):1288–1295, 2013.

[159] T. Xie, P. Warnke, and U.J. Kang. Role of DaTSCAN and clinical diagnosis in Parkinson disease. *Neurology*, 79(16), 2012.

[160] J.S. Perlmutter and D. Eidelberg. To scan or not to scan: DaT is the question. *Neurology*, 78(10):688–689, 2012.

[161] M. Schreckenberger, S. Hägele, T. Siessmeier, H.G. Buchholz, H. Armbrust-Henrich, F. Rösch, G. Gründer, P. Bartenstein, and T. Vogt. The dopamine D2 receptor ligand ^{18} F-desmethoxyfallypride: an appropriate fluorinated PET tracer for the differential diagnosis of parkinsonism. *European Journal of Nuclear Medicine and Molecular Imaging*, 31(8):1128–1135, 2004.

[162] C. C. Constantinescu, R. A. Coleman, M. Pan, and J. Mukherjee. Striatal and Extrastriatal microPET Imaging of D2/D3 Dopamine Receptors in Rat Brain with [^{18}F]Fallypride and [^{18}F]Desmethoxyfallypride. *Synapse*, 65(8):778–787, 2011.

[163] Roger P. Woods. Registration. In 2000) I. N. Bankman (Academic, San Diego, editor, *Handbook of Medical Imaging*, pages 421–653, 2000.

[164] K. J. Friston, J. Ashburner, C. D. Frith, J. B. Poline, J.D. Heather, and R. S. J. Frackowiak. Spatial Registration and Normalization of Images. *Human Brain Mapping*, 2:165–189, 1995.

[165] J. L. Lancaster and P. T. Fox. Talairach Space as a Tool for Intersubject Standardization in the Brain. In 2000) I. N. Bankman (Academic, San Diego, editor, *Handbook of Medical Imaging*, volume Chap. 35, pages 555–568, 2000.

[166] Esther Aarts, Rick C. Helmich, Marcel J.R. Janssen, Wim J.G. Oyen, Bastiaan R. Bloem, and Roshan Cools. Aberrant reward processing in parkinson's disease is associated with dopamine cell loss. *NeuroImage*, 59(4):3339 – 3346, 2012.

[167] A. Kas, P. Payoux, M. Habert, Z. Malek, Y. Cointepas, G El Fakhri, P. Chaumet-Riffaud, E. Itti, and P. Remy. Validation of a Standardized Normalization Template for Statistical Parametric Mapping Analysis of ^{123}I FP-CIT Images. *Journal of Nuclear Medicine*, 48(9):1459–1467, 2007.

[168] K. Friston, J. Ashburner, S. Kiebel, T. Nichols, and W. Penny. *Statistical Parametric Mapping: The Analysis of Functional Brain Images*. Academic Press, 2007.

[169] R. P. Woods. Spatial transformation models. In I. N. Bankman, editor, *Handbook of Medical Imaging*, volume Chap. 29, pages 465–490, 2000.

[170] J. Ashburner and K. J. Friston. Nonlinear spatial normalization using basis functions. *Human Brain Mapping*, 7 (4):254–266, 1999.

[171] D. Salas-Gonzalez, J.M. Górriz, Javier Ramírez, I.A. Illán, Pablo Padilla, FranciscoJ. Martínez-Murcia, and ElmarW. Lang. Building a FP-CIT SPECT Brain Template Using a Posterization Approach. *Neuroinformatics*, pages 1–12, 2015.

[172] Qian Wang, Dieter Seghers, Emiliano D'Agostino, Frederik Maes, Dirk Vandermeulen, Paul Suetens, and Alexander Hammers. Construction and Validation of Mean Shape Atlas Templates for Atlas-Based Brain Image Segmentation. In GaryE. Christensen and Milan Sonka, editors, *Information Processing in Medical Imaging*, volume 3565 of *Lecture Notes in Computer Science*, pages 689–700. Springer Berlin Heidelberg, 2005.

[173] Dieter Seghers, Emiliano D'Agostino, Frederik Maes, Dirk Vandermeulen, and Paul Suetens. Construction of a Brain Template from MR Images Using State-of-the-Art Registration and Segmentation Techniques. In Christian Barillot, DavidR. Haynor, and Pierre Hellier, editors, *Medical Image Computing and Computer-Assisted Intervention – MICCAI 2004*, volume 3216 of *Lecture Notes in Computer Science*, pages 696–703. Springer Berlin Heidelberg, 2004.

[174] M. Laruelle, E. Wallace, J.P. Seibyl, R.M. Baldwin, Y. Zea-Ponce, S.S. Zoghbi, J.L. Neumeyer, D.S. Charney, P.B. Hoffer, and R.B Innis. Graphical, Kinetic, and Equilibrium Analyses of In Vivo [^{123}I]β-CIT Binding to Dopamine Transporters in Healthy Human Subjects. *The International Society of Cerebral Blood Flow and Metabolism*, 14:982–994, 1994.

[175] T. Ishikawa, V. Dhawan, K. Kazumata, T. Chaly, F. Mandel, J. Neumeyer, C. Margouleff, B. Babchyck, I Zanzi, and D Eidelberg. Comparative Nigrostriatal Dopaminergic Imaging with Iodine-123-βCIT-FP/SPECT and Fluorine-18-FDOP A/PET. *Journal of Nuclear Medicine*, 37 (11):1760–1765, 1996.

[176] C. Scherfler, K. Seppi, E. Donnemiller, G. Goebel, C. Brenneis, I. Virgolini, GK. Wenning, and W. Poewe. Voxel-wise analysis of [^{123}I]β-CIT SPECT differentiates the Parkinson variant of multiple system atrophy from idiopathic Parkinson's disease. *Brain*, 128 (7):1605–1612, 2005.

[177] G. Andringa, B. Drukarch, J.G. Bol, K. de Bruin, K. Sorman, J.B. Habraken, and J. Booij. Pinhole SPECT imaging of dopamine transporters correlates with dopamine transporter immunohistochemical analysis in the MPTP mouse model of parkinson's disease. *NeuroImage*, 26(4):1150–1158, 2005.

[178] I. Rektorova, H. Srovnalova, R. Kubikova, and J. Prasek. Striatal Dopamine Transporter Imaging Correlates with Depressive Symptoms and Tower of London Task Performance in Parkinson's Disease. *Movement Disorders*, 23(11):1580–1587, 2008.

[179] S. Sharma and M. Ebadi. SPECT neuroimaging in translational research of CNS disorders. *Neurochemistry International*, 52(3):352–362, 2008.

[180] V. Caretti, D. Stoffers, A. Winogrodzka, I.-U. Isaias, G. Costantino, G. Pezzoli, C. Ferrarese, A. Antonini, E.-Ch Wolters, and J. Booij. Loss of thalamic serotonin transporters in early drug-naïve Parkinson's disease patients is associated with tremor: an $[^{123}I]\beta$-CIT SPECT study. *Neural Transmission*, 115 (5):721–729, 2008.

[181] L. Tossici-Bolt, S. M. A. Hoffmann, P. M. Kemp, R. L. Mehta, and J. S. Fleming. Quantification of $[^{123}$I]FP-CIT SPECT brain images: an accurate technique for measurement of the specific binding ratio. *European Journal of Nuclear Medicine and Molecular Imaging*, 33:1491–1499, 2006.

[182] C. Scherfler and M. Nocker. Dopamine transporter SPECT: How to remove subjectivity? *Movement Disorders*, 24(S2):721–724, 2009.

[183] W. Koch, PE. Radau, C. Hamann, and K. Tatsch. Clinical Testing of an Optimized Software Solution for an Automated, Observer-Independent Evaluation of Dopamine Transporter SPECT Studies. *Journal of Nuclear and Medicine*, 46(7):1109–1118, 2005.

[184] M. Soret, P. M. Koulibaly, J. Darcourt, S. Hapdey, and I. Buvat. Quantitative Accuracy of Dopaminergic Neurotransmission Imaging with ^{123} I SPECT. *Journal of Nuclear Medicine*, 44(7):1184–1193, 2003.

[185] A. Brahim, J.M. Górriz, J. Ramírez, and L. Khedher. Linear intensity normalization of DaTSCAN images using Mean Square Error and a model-based clustering approach. *Studies in Health Technology and Informatics*, 207:251–260, 2014.

[186] P. Padilla, J.M. Górriz, J. Ramírez, D. D. Salas-González, and I.A. IllÃ¡n. Intensity normalization in the analysis of functional DaTSCAN SPECT images: The α -stable distribution-based normalization method vs other approaches. *Neurocomputing*, 150:4–15, 2015.

[187] M. Shah, Y. Xiao, N. Subbanna, S. Francis, L. Arnold, D.L Collins, and T. Arbel. Evaluating intensity normalization on MRIs of human brain with multiple sclerosis. *Medical Image Analysis*, 15:267–282, 2011.

[188] P. Borghammer, J. Aanerud, and A. Gjedde. Data-driven intensity normalization of PET group comparison studies is superior to global mean normalization. *NeuroImage*, 46:981–988, 2009.

[189] C.M. Gullion, M.D. Sr. Devous, and A.J. Rush. Effects of four normalizing methods on data analytic results in functional brain imaging. *Biological Psychiatry*, 40:1106–1121, 1996.

[190] S Arndt, T. Cizadlo, D. O'Leary, S. Gold, and NC. Andreasen. Normalizing Counts and Cerebral Blood Flow Intensity in Functional Imaging Studies of the Human Brain. *NeuroImage*, 3:175–184, 1996.

[191] F. P.M. Oliveira and M. Castelo-Branco. Computer-aided diagnosis of Parkinson's disease based on [^{123} I]FP-CIT SPECT binding potential images, using the voxels-as-features approach and support vector machines. *Journal of Neural Engineering*, 12(2):026008, 2015.

[192] Kathleen C Schmidt. Can ROI methodology/normalised tissue activities be used instead of absolute blood flow measurements in the brain? *European journal of nuclear medicine and molecular imaging*, 29(7):948–953, 2002.

[193] N.I. Weisenfeld and S.K. Warfteld. Normalization of joint image-intensity statistics in MRI using the Kullback-Leibler divergence. In *Biomedical Imaging: Nano to Macro, 2004. IEEE International Symposium on*, pages 101–104 Vol. 1, April 2004.

[194] S. Kullback. *Information Theory and Statistics*. Dover Books on Mathematics. John Wiley & Sons, New York, 1959.

[195] Gourav and S. R. Singh. Image Enhancement Based on Transform Wavelet Coefficient by Histogram Shifting and Shaping. *International Journal of Engineering Research & Technology*, 3(3):1109–1111, 2014.

[196] S. Venkatesan and S. Rao madane. PRE PROCESSING HIERARCHY DESIGNED FOR ENHANCED FACE DETECTION . *Journal of Global Research in Computer Science*, 1 (5):37–39, 2010.

[197] S. K. Singh and M. Gupta. A Multiscale Region-Based Motion Detection And Image Histograms. *International Journal of Engineering Research & Technology*, 2(5):1544–1554, 2013.

[198] R. C. Gonzalez and R. E. Woods. *Digital Image Processing (Second Edition)*. Tom Robbins, 2002.

[199] Gennady Samoradnitsky and M.S. Taqqu. *Stable Non-Gaussian Random Processes: Stochastic Models with Infinite Variance Stochastic Modeling Series*. Chapman and Hall, London, UK, 1994.

[200] K. Fukunaga. *Introduction to Statistical Pattern Recognition*. Academic Press, New York, 1990.

[201] J. Goldberger, S. Gordon, and H. Greenspan. Unsupervised image-set clustering using an information theoretic framework. *IEEE Transactions on Image Processing*, 15 (2):449–458, 2006.

[202] G. McLachlan and D. Peel. *Finite Mixture Models*. John Wiley & Sons, New York, 2000.

[203] W. Pirker, S. Asenbaum, G. Bencsits, D. Prayer, W. Gerschlager, L. Deecke, and T. Brücke. $[^{123}I]\beta$-CIT SPECT in multiple system atrophy, progressive supranuclear palsy, and corticobasal degeneration. *Movement Disorders*, 15:1158–1167, 2000.

[204] K. S. Tamilselvan, G. Murugesan, and M. Vinothsaravanan. A Histogram based Hybrid Approach for Medical Image Denoising using Wavelet and Curvelet Transforms. *International Journal of Computer Applications*, 74(21):6–11, July 2013.

[205] J. Ashburner and K.J. Friston. Unified segmentation. *NeuroImage*, 26(3):839–851, 2005.

[206] M. Aladjem. Projection pursuit mixture density estimation. *IEEE Transactions on Signal Processing*, 53 (11):4376–4383, 2005.

[207] J. Banfield and A. Raftery. Model-based gaussian and non-gaussian clustering. *Biometrics*, 49:803–821, 1993.

[208] J. P Nolan. Levy processes: theory and applications. maximum likelihood estimation of stable parameters. *Birkhäuser, Boston*, pages 379–400, 2001.

[209] J. Neumann, D. Y. von. Cramon, and G. Lohmann. Model-Based Clustering of Meta-Analytic Functional Imaging Data. *Human Brain Mapping*, 29(2):177–192, 2008.

[210] G. J. McLachlan and P. N. Jones. Fitting Mixture Models to Grouped and Truncated Data via the EM Algorithm. *Biometrics*, 44:571–578, 1988.

[211] F. Segovia, J.M. Górriz, J. Ramírez, D. Salas-Gonzalez, I. Álvarez, M. López, and R. Chaves. A comparative study of feature extraction methods for the diagnosis of Alzheimer's disease using the ADNI database. *Neurocomputing*, 75(1):64–71, 2012.

[212] J. M. Górriz, F. Segovia, J. Ramírez, A. Lassl, and D. Salas-Gonzalez. GMM based SPECT image classification for the diagnosis of Alzheimer's disease. *Applied Soft Computing*, 11 (2):2313–2325, 2011.

[213] T.K. Moon. The expectation-maximization algorithm. *IEEE Signal Processing Magazine*, 13:47–60, 1996.

[214] A.P. Dempster, N.M. Laird, and D.B. Rubin. Maximum likelihood from incomplete data via the EM algorithm. *Journal of Royal Statistical Society*, 39 (1):1–38, 1977.

[215] C. Fraley and A.E. Raftery. How Many Clusters? Which Clustering Method? Answers Via Model-Based Cluster Analysis. *The computer journal*, 41(8):578–588, 1998.

[216] F. Segovia, J. M. Górriz, J. Ramírez, D. Salas-González, I. A. Illán, M. López, R. Chaves, P. Padilla, and C.G. Puntonet. Automatic selection of ROIs using a model-based clustering approach. *2009 IEEE Nuclear Science Symposium Conference Record (NSS/MIC)*, pages 3194–3198, 2009.

[217] G. Schwarz. Estimating the dimension of a model. *Ann. Statist.*, 6:461–464, 1978.

[218] H. Akaike. A new look at the statistical model identification. *IEEE Transactions on Automatic Control*, 19:716–723, 1974.

[219] Rui Li, Robert Perneczky, Igor Yakushev, Stefan FÃ¶rster, Alexander Kurz, Alexander Drzezga, and Stefan Kramer. Gaussian Mixture Models and Model Selection for [18F] Fluorodeoxyglucose Positron Emission Tomography Classification in Alzheimer's Disease. *PLOS ONE*, pages 1–22, 04 2015.

[220] J. M. Górriz, A. Lassl, J. Ramírez, D. Salas-Gonzalez, C.G. Puntonet, and E.W. Lang. Automatic selection of ROIs in functional imaging using Gaussian mixture models. *Neuroscience Letters*, 460:108–111, 2009.

[221] F. Segovia, J. M. Górriz, J. Ramírez, D. Salas-González, I. A. Illán, M. López, R. Chaves, and P. Padilla. Classification of functional brain images using a GMM-based multi-variate approach. *Neuroscience Letters*, 474:58–62, 2010.

[222] A. Brahim, J.M. Górriz, J. Ramírez, and L. Khedher. Applications of gaussian mixture models and mean squared error within datscan spect imaging. In *Image Processing (ICIP), 2014 IEEE International Conference on*, pages 3617–3621, Oct 2014.

[223] K. Ravi and R. Munish. Analysis Of Various Quality Metrics for Medical Image Processing. *International Journal of Advanced Research in Computer Science and Software Engineering*, 2 (11):137–144, 2012.

[224] Monson H. Hayes. *Statistical Digital Signal Processing and Modeling*. John Wiley & Sons, 1996.

[225] M. Silveira and P. M. Q. Aguiar. Simultaneous Registration and Intensity Normalization of SPECT Perfusion Images. In *Engineering in Medicine and Biology Society, 2008. EMBS 2008. 30th Annual International Conference of the IEEE*, 2008.

[226] G. Galimberti and G. Soffritti. A multivariate linear regression analysis using finite mixtures of t distributions. *Computational Statistics and Data Analysis*, 71:138–150, 2014.

[227] I. Litvan, Y. Agid, D. Calne, G. Campbell, B. Dubois, R. C. Duvoisin, C. G. Goetz, L. I. Golbe, J. Grafman, J. H. Growdon, M. Hallett, J. Jankovic, N. P. Quinn, E. Tolosa, and D. S. Zee. Clinical research criteria for the diagnosis of progressive supranuclear palsy (Steele-Richardson-Olszewski syndrome): report of the NINDS-SPSP international workshop. *ourmal of Neurology*, 47(1):1–9, 1996.

[228] A. Brahim, J.M. Górriz, J. Ramírez, and L. Khedher. Intensity normalization of DaTSCAN SPECT imaging using a model-based clustering approach. *Applied Soft Computing*, 37:234–244, 2015.

[229] A. Brahim, J. Ramírez, J. M. Górriz, L. Khedher, and D. Salas-Gonzalez. Comparison between different intensity normalization methods in ^{123}i-ioflupane imaging for the automatic detection of parkinsonism. *PLoS ONE*, 10(6):1–20, 06 2015.

[230] H. Greenspan, A. Ruf, and J. Goldberger. Constrained Gaussian mixture model framework for automatic segmentation of MR brain images. *Medical Imaging, IEEE Transactions on*, 25(9):1233–1245, Sept 2006.

[231] O. Freifeld, H. Greenspan, and J. Goldberger. Multiple Sclerosis Lesion Detection Using Constrained GMM and Curve Evolution. *International Journal of Biomedical Imaging*, 2009:1–13, 2009.

[232] H. Jeffreys. An invariant form for the prior probability in estimation problems. *Proceedings of the Royal Society of London*, Series A 186:453–461, 1946.

[233] J. Stoeckel, N. Ayache, G. Malandain, P. M. Koulibaly, K.P. Ebmeier, and J. Darcourt. Automatic classification of SPECT images of Alzheimer's disease patients and control subjects. *Lecture Notes in Computer Science*, 3217:654–662, 2004.

[234] L. Khedher, J. Ramírez, J.M. Górriz, A. Brahim, and F. Segovia. Early diagnosis of alzheimer's disease based on partial least squares, principal component analysis and support vector machine using segmented MRI images. *Neurocomputing*, 151, Part 1(0):139–150, 2014.

[235] I.T. Jolliffe. *Principal Component Analysis*. Springer Verlag, 1986.

[236] U. Yoon, J. M. Lee, K. Im, Y. W. Shin, BH. Cho, IY. Kim, JS. Kwon, and S. I. Kim. Pattern classification using principal components of cortical thickness and its discriminative pattern in schizophrenia. *NeuroImage*, 34:1405–1415, 2007.

[237] M.M. López, J. Ramírez, J.M. Górriz, I. Álvarez, D. Salas-Gonzalez, F. Segovia, and R. Chaves. Svm-based CAD system for early detection of the alzheimer's disease using kernel PCA and LDA. *Neuroscience Letters*, 464:233–238, 2009.

[238] K. Najarian and R. Splinter. *Biomedical Signal and Image Processing*. Taylor & Francis Group, 2012.

[239] P. Saxena, D. G. Pavel, J. C. Quintana, and B Horwitz. An automatic threshold-based scaling method for enhancing the usefulness of Tc-HMPAO SPECT in the diagnosis of Alzheimer's disease. In WilliamM. Wells, Alan Colchester, and Scott Delp, editors, *Medical Image Computing and Computer-Assisted Interventation-MICCAI'98*, volume 1496 of *Lecture Notes in Computer Science*, pages 623–630. Springer Berlin Heidelberg, 1998.

[240] I. Litvan. Recent advances in atypical parkinsonian disorders. *Current Opinion in Neurology*, 12 (4):441–446, 1999.

[241] Y. Osaki, Y. Ben-Shlomo, G.K. Wenning, S.E. Daniel, A. Hughes, A.J. Lees, C.J. Mathias, and N. Quinn. Do published criteria improve clinical diagnostic accuracy in multiple system atrophy? *Neurology*, 59:1486–1491, 2002.

[242] K. A. Jobst, L. P. Barnetson, and B. J. Shepstone. Accurate prediction of histologically confirmed Alzheimer's disease and the differential diagnosis of dementia: the use of NINCDS-ADRDA and DSM-III-R criteria, SPECT, X-ray CT, and Apo E4 in medial temporal lobe dementias. Oxford Project to Investigate Memory and Aging. *Int. Psychogeriatr*, 10(3):271–302, 1998.

[243] N. Tzourio-Mazoyer, B. Landeau, D. Papathanassiou, F. Crivello, O. Etard, N. Delcroix, B. Mazoyer, and M. Joliot. Automated anatomical labeling of activations in SPM using a macroscopic anatomical parcellation of the MNI MRI Single-Subject brain. *NeuroImage*, 15 (1):273–289, 2002.

[244] J. C. Spall. Implementation of the Simultaneous Perturbation Stochastic Algorithm for Stochastic Optimization . *IEEE TRANSACTIONS ON AEROSPACE AND ELECTRONIC SYSTEMS*, 34 (3):817–823, 1998.

[245] J. C. Spall. Multivariate Stochastic Approximation Using a Simultaneous Perturbation Gradient Approximation. *IEEE TRANSACTIONS ON AUTOMATIC CONTROL*, 37 (3):332–341, 1992.

[246] V. Vapnik. *Estimation of Dependences Based on Empirical Data*. Springer Verlag, 1982.

[247] Christopher J. C. Burges. A Tutorial on Support Vector Machines for Pattern Recognition. *Data Mining and Knowledge Discovery*, 2(2):121–167, June 1998.

[248] J. Shawe-Taylor and N. Cristianini. *Support Vector Machines and Other Kernel-Based learning methods*. Cambridge University Press, 2000.

[249] B. Schölkopf and AJ. Smola. *Learning with Kernels*. MIT Press, 2001.

[250] R. Chaves, J. Ramírez, J.M. Górriz, M. López, D. Salas-Gonzalez, I. Álvarez, and F. Segovia. SVM-based computer-aided diagnosis of the Alzheimer's disease using t-test NMSE feature selection with feature correlation weighting. *Neuroscience Letters*, 461(3):293–297, 2009.

[251] R. O. Duda, P. E. Hart, and D. G. Stork. *Pattern Classification*. John Wiley & Sons, New York, 2001.

[252] A. Andersen, D. M. Gash, and M. J. Avison. Principal component analysis of the dynamic response measured by fMRI: a generalized linear systems framework. *J.Magn.Reson.Imaging*, 17:795–815, 1999.

[253] M. Turk and A. Pentland. Eigenfaces for recognition. *Journal of Cognitive Neuroscience*, 3 (1):71–86, 1991.